High Spin Gamma-Ray Spectroscopy of N=86 Isotones Around A=150

Thesis submitted in accordance with the requirements of the
University of Liverpool for the degree of Doctor in Philosophy
by

Ishtiaq Ali

Oliver Lodge Laboratory March 1992

To My Mother

Abstract

A study of the single particle excitations of the N = 86 nuclei ^{150}Gd and ^{152}Dy in both the normal and superdeformed potential wells has been carried out. In particular the decay schemes of both ^{150}Gd and ^{152}Dy have been extended around the spins where the superdeformed bands feed into the normal yrast states. Calculations based on the single particle shell model have been performed in order to interpret these level schemes and a comparison between ^{150}Gd and ^{152}Dy and their Z+1 N=86 neighbours (^{151}Tb and ^{153}Ho respectively) has been made.

The reactions ^{130}Te(^{26}Mg, 6n)^{150}Gd at a beam energy of 145 MeV and ^{108}Pd(^{48}Ca, 4n)^{152}Dy at a beam energy of 197 MeV were carried out at the NSF Daresbury using the TESSA3 spectrometer. The level schemes of both nuclei have been extended up to around spin I$\sim$40$\hbar$. The nuclear energy states of the experimental level schemes of both the ^{150}Gd and ^{152}Dy are not only similar up to spin 34$^-$ but also their configurations look similar up to spin 34$^-$.

Furthermore, the single particle structure of ^{150}Gd ,^{151}Tb and ^{152}Dy in the second minimum has also been studied. Excited superdeformed bands have been observed in ^{150}Gd and ^{151}Tb. The moments of inertia of the excited superdeformed bands in ^{150}Gd and ^{151}Tb are quite similar to the yrast SD bands in the neighbouring Z+1 nuclei. This similarity in the moments of inertia implies that these bands are based on the same high-j intruder configurations, which in turn implies that the excited superdeformed bands are based on a low-j particle-hole excitation from the core.

Acknowledgements

First of all I am highly thankful to my supervisor Prof. P. J. Twin for his determination, incisive comments and for providing help, valuable guidance, enthusiasm and continuous encouragement to complete this work.

I am indeed very thankful to the following:

Prof. J. Dudek (Centre de Recherches Nucléar, Strasbourg, France) for allowing me to use his software library and for valuable discussions and help in interpreting the experimental results.

Dr. Paul Fallon and Dr. C. W. Beausang for their help and valuable assistance in the data analysis.

Dr. Paul Fallon for reading this transcript before final submission.

Dr. E. S. Paul for short but always fruitful discussions on almost every aspect of Nuclear Structure Physics.

My thanks also extend to the computing staff at Liverpool for their help during sorting etc..., especially to Dr. J. R. Cresswell and Linda Pratt and also to the crew at N.S.F., Daresbury.

Many thanks to my postgrad. colleagues (A. Alderson, S. A. Forbes, D. M. Cullen, F. Hanna, J. W. Roberts, N. Clarkson, G. Smith, M. Joyce and P. Dagnall) and all those people who have been making my stay at Liverpool enjoyable. I would also like to extend my thanks to all the other members of the Nuclear Structure Group at Liverpool which include Prof. J. F. Sharpey-Schafer, Dr. A. N. James, Dr. P. Nolan, Dr. P. D. Forsyth, Dr. Peter Butler and Dr. G. D. Jones for their guidance during my stay at Liverpool and also to Dr. M. A. Riley for his help during his stay at Liverpool.

Finally, I would extend my thanks to the Ministry of Science and Technology, Government of Pakistan, for providing financial support through "S&T" scholarship award in order to complete this work.

Contents

List of Figures

List of Tables

Chapter 1

Introduction

The atomic nucleus is a many-body quantal system with a large but finite number of nucleons. These nucleons interact via a strong, short range and attractive nuclear force. The interaction between the nucleons is considerably weak to allow them to behave as independent particles, but is strong enough for a few nucleons moving in anisotropic orbits to produce a deformed nucleus. Thus the nucleus shows both collective and non-collective behaviour in the accommodation of its angular momentum. The additional stresses arising from the rapid rotation of the nucleus can cause transitions between prolate, oblate and triaxial shapes. A classic example of nuclear deformation is the nucleus ^{152}Dy, since it contains oblate, low deformation prolate and even superdeformed shapes.

Figure 1.1 illustrates this shape co-existence in ^{152}Dy. The oblate shape is associated with the building up of the spin by single particle configurations (non-collective rotation). The ground-state sequence of stretched quadrupole transitions develops into a rotational band with a low moment of inertia, which is linked with a low deformation prolate (ϵ=0.20) shape. Finally, the superdeformed shape with ϵ=0.6.

The first evidence for superdeformed shapes came from the observation of fission isomers in the very heavy nuclei in the Actinide region. In this case their stability is due to a combination of the shell structure and the

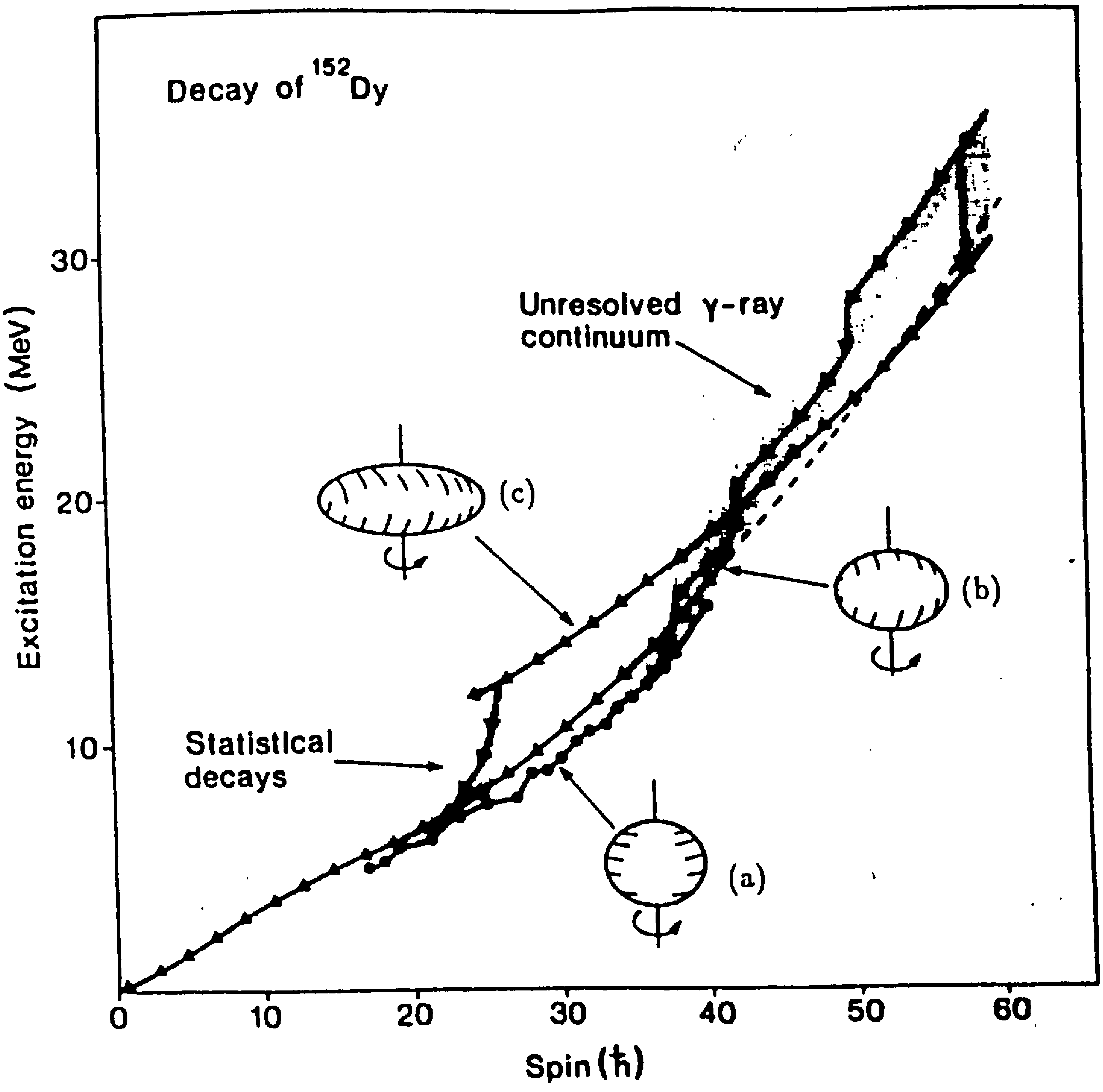

Figure 1.1: *A schematic of the proposed γ-ray decay paths for the nucleus ^{152}Dy. All the three axially symmetric structures i.e., (a) oblate, (b) low deformation prolate, and (c) superdeformed prolate shapes are seen to co-exist over a wide spin range. The major decay flow occurs which is mainly via the E2 transitions in the unresolved gamma ray continuum is also shown. The figure is taken from [NT 88].*

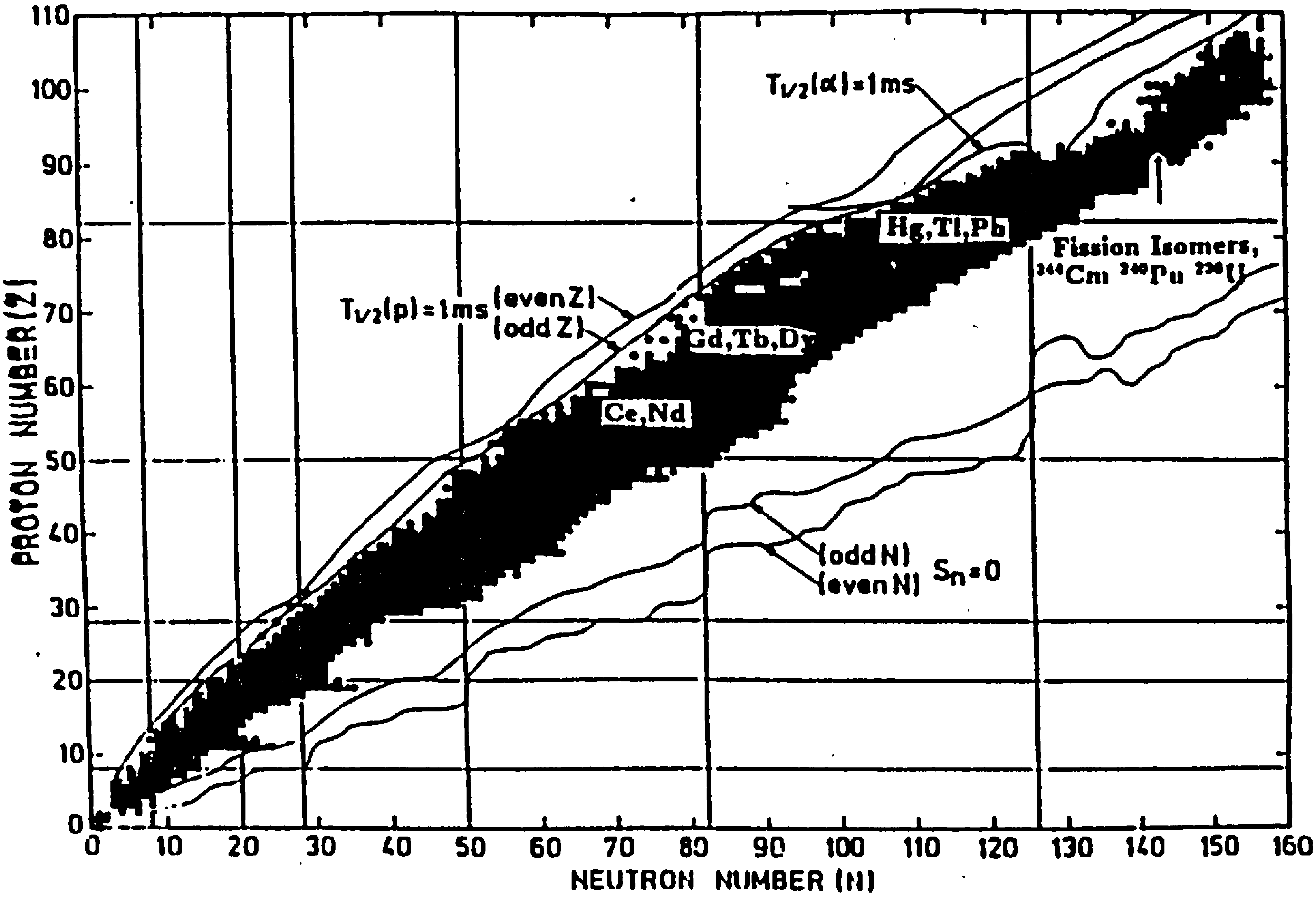

Figure 1.2: *A schematic plot for the N-Z regions where superdeformation has been observed.*

Coulomb energy (due to protons). A similar stability had been predicted to be attained by combining the shell structure with an energy term due to rapid rotation in lighter nuclei. Superdeformed shapes have now also been observed experimentally in many nuclei in the mass A=130,A=150 and A=190 region (figure 1.2). However, no linking transitions between the superdeformed and normal deformed yrast states have been reported so far.

It may be noted that in the mass A=150 region, apart from ^{152}Dy other nuclei such as ^{150}Gd and ^{151}Tb also show collective as well as non-collective behaviour.

This work has been carried out in order to extend the level schemes of ^{150}Gd and ^{152}Dy so as to have as much information as possible on the oblate states in the first minimum. This would give us a greater understanding of the

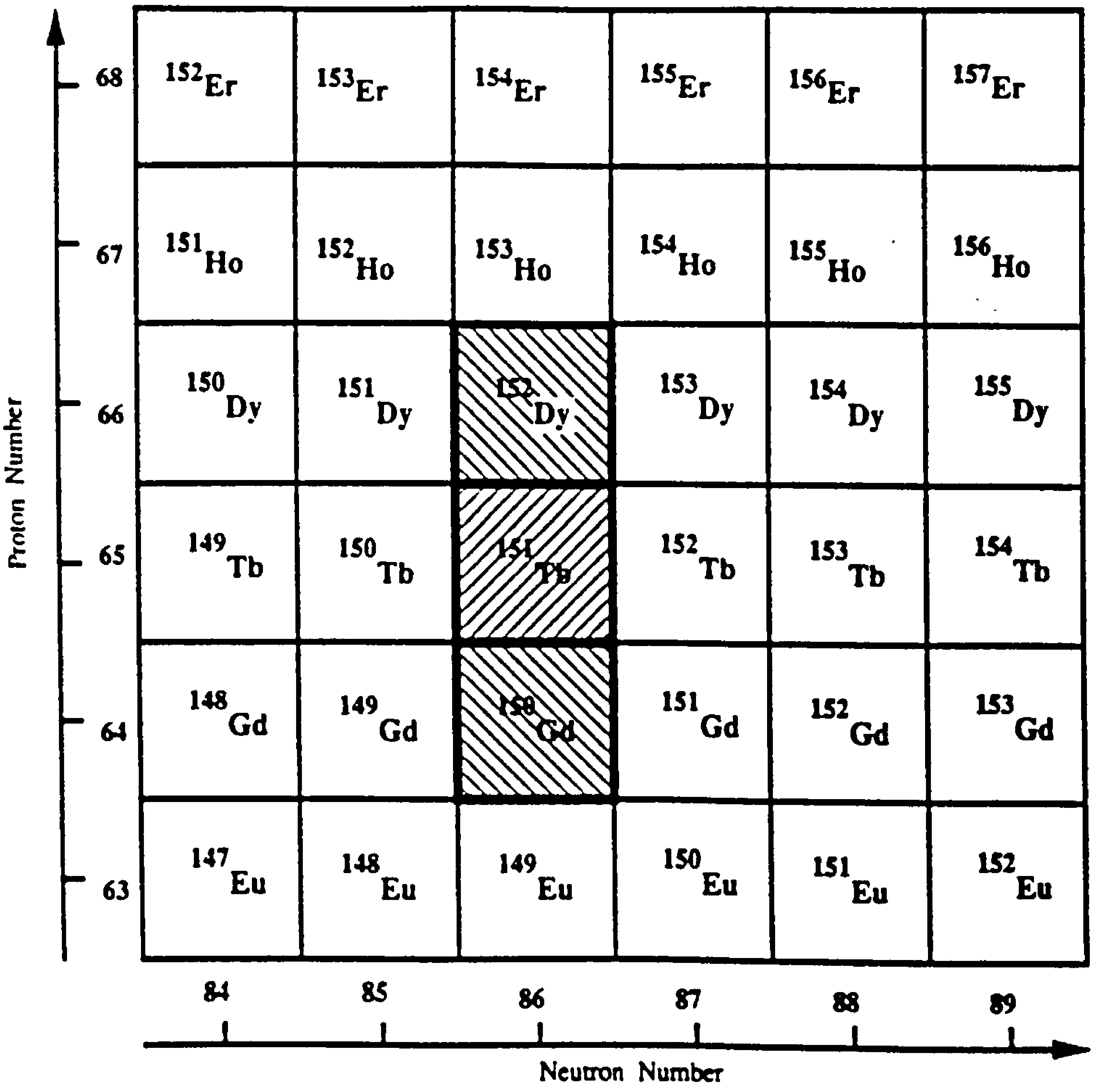

Figure 1.3: *The mass A=150 region in the chart of nuclides. The N = 86 isotones,* ^{150}*Gd,* ^{151}*Tb and* ^{152}*Dy which are the subject of this work are shown with shaded boxes.*

interplay between the superdeformed and normal deformed shapes in the first and second potential energy wells. The configurations for the high spin states of these nuclei are based on the excitations/re-arrangements of the nucleons in the $\nu f_{7/2}h_{9/2}$ and $\pi d_{5/2}h_{11/2}$ orbitals. Furthermore, two new superdeformed bands have been reported in this work, one in ^{150}Gd and the other in ^{151}Tb. These bands have been termed "excited" superdeformed bands as they are proposed to be based on the single proton excitations from the [301]1/2 orbital into the [651]3/2 intruder orbital and are thus the first observation of the proton excitations in the superdeformed nuclei.

The location of the ^{150}Gd, ^{151}Tb and ^{152}Dy in the nuclear mass chart is shown in figure 1.3 and their study in the first and the second potential energy wells is described in the following chapters.

Chapter 2 presents some of the microscopic and macroscopic models and concepts used to describe the atomic nucleus.

Chapter 3 describes nuclear rotation and its characteristic properties. Some general methods used in the calculation of the spectra of non-collective nuclei are also discussed and the chapter ends with a section on superdeformation.

Chapters 4 and 5 discuss the formation and decay of the compound nucleus in a heavy ion fusion evaporation reaction and the detection of the emitted γ-ray radiations from these reactions along with the experimental and analytical techniques used in this work.

The analysis and results from the data for the single particle oblate states presented in chapter 6 are discussed in chapter 7 in terms of the single particle shell model configurations.

Chapter 8 is devoted to the results from the data relating to the occurrence of superdeformed shapes, in particular the observation of excited superdeformed bands and their interpretation are discussed.

Important findings of the study are summarised in chapter 9 and different avenues which need to be pursued in future are also highlighted.

Chapter 2

Nuclear Models

2.1 Introduction

In order to investigate the structure of the nucleus a number of nuclear models have been suggested. Before constructing any theoretical model of the atomic nucleus it is important to consider the properties of the force which binds together nucleons within the nucleus. In an atomic nucleus, the nucleons are held together firmly within a small volume, although there exists a repulsive Coulomb force between the protons. To a good approximation, for a nucleus with atomic mass, A, the number of nucleons per unit volume is constant i.e.,

$$\frac{A}{R^3} \propto constant \tag{2.1}$$

where R is the mean nuclear radius. This implies

$$R = R_o A^{1/3} \tag{2.2}$$

where $R_o \sim$ 1.2 fm. Equation 2.2 shows that the value of the nuclear radius is 10^5 times smaller than the value of the atomic radius. It has also been shown by the experiments on electron scattering [Ja 74] and μ-mesonic x-rays [En 74] that the density of nuclear matter remains constant throughout the nucleus, decreasing rapidly to zero near to the nuclear surface. The density of the nucleus has extremely large values ($\approx 10^{15}$ times greater than the density of matter in bulk) giving some indication of the difficulties that may be involved in the reproduction of the nuclear phenomena by a single theory alone. It has been suggested that there exists an attractive force inside the nucleus which is much stronger than the repulsive Coulomb force and which binds the neutrons and protons together. This strong attractive force has a short range (of the order of 1 fm or less) and is charge independent and is called the nuclear force. Indeed, if only the electromagnetic interaction is considered then the nucleus would fly apart due to the Coulomb repulsion experienced by the protons. However, the nuclear force must also have a repulsive core at very short distances (≈ 0.5 fm) otherwise all nuclei would collapse.

As noted before, it is difficult to develop a single theory to explain the wide variety of nuclear phenomena and the solution of the many body problem is awaited. It is therefore more reasonable to use separate models to interpret various nuclear properties and to describe the interplay between them where applicable.

Among the nuclear models the Liquid drop model (LDM) of the nucleus was historically the first nuclear model to be proposed as an explanation for nuclear properties.

2.2 Liquid Drop Model (LDM)

The analogy between the nucleus and a liquid drop originates from the saturation property of the nuclear force, the very low compressibility of the nucleus and its well defined surface. The nucleus is assumed to have a definite surface tension and the nucleons are expected to behave in a similar manner to water molecules within a liquid. Particle emission corresponds to molecular evaporation from the liquid surface and liquid fission may be viewed as the division of large drops into two smaller ones.

Experiments on nuclear binding energies revealed that the binding energy per nucleon is approximately constant at +7.5 to +8.5 MeV for nuclei with $A \geq$

12. Furthermore, the nuclear force was observed to saturate with increasing nuclear mass (its interaction strength only extends over a few nucleons) and both of these properties are shown in figure 2.1 which shows a plot of the binding energy per nucleon $\frac{B(N,Z)}{A}$ against the mass number A.

2.2.1 The Semi-empirical Mass Formula

The semi-empirical mass formula of Weizsäcker [We 35] and Bethe [BB 36] is a successful approach to describe the total binding energy B(N, Z), where N and Z are the number of neutrons and protons, and is given by,

$$B(N,Z) = a_v A - a_s A^{2/3} - a_c \frac{Z^2}{A^{1/3}} - a_a \frac{(N-Z)^2}{A} + \Delta(A) \qquad (2.3)$$

The five terms on the right hand side of equation 2.3 are called the volume, surface, Coulomb, asymmetry and pairing terms, respectively. The physical meaning of each of them is given below:

- a_vA - the volume term. The volume term arises from B(N, Z) being proportional to A (where A$\propto R^3$, R is the radius of the nucleus and is given as R=$R_0 A^{1/3}$, R_0=1.2 fm).

- $a_s A^{2/3}$ - the surface term. Nucleons near the surface of a nucleus are less bound and contribute less to the binding energy as the nuclear force saturates. The surface term, proportional to R^2 accounts for the reduced total binding energy.

- $a_c\frac{Z^2}{A^{1/3}}$ - the Coulomb term. Protons inside the nucleus experience a Coulomb repulsion. The Coulomb energy is proportional to the square of the number of protons and inversely proportional to the radius of the nucleus.

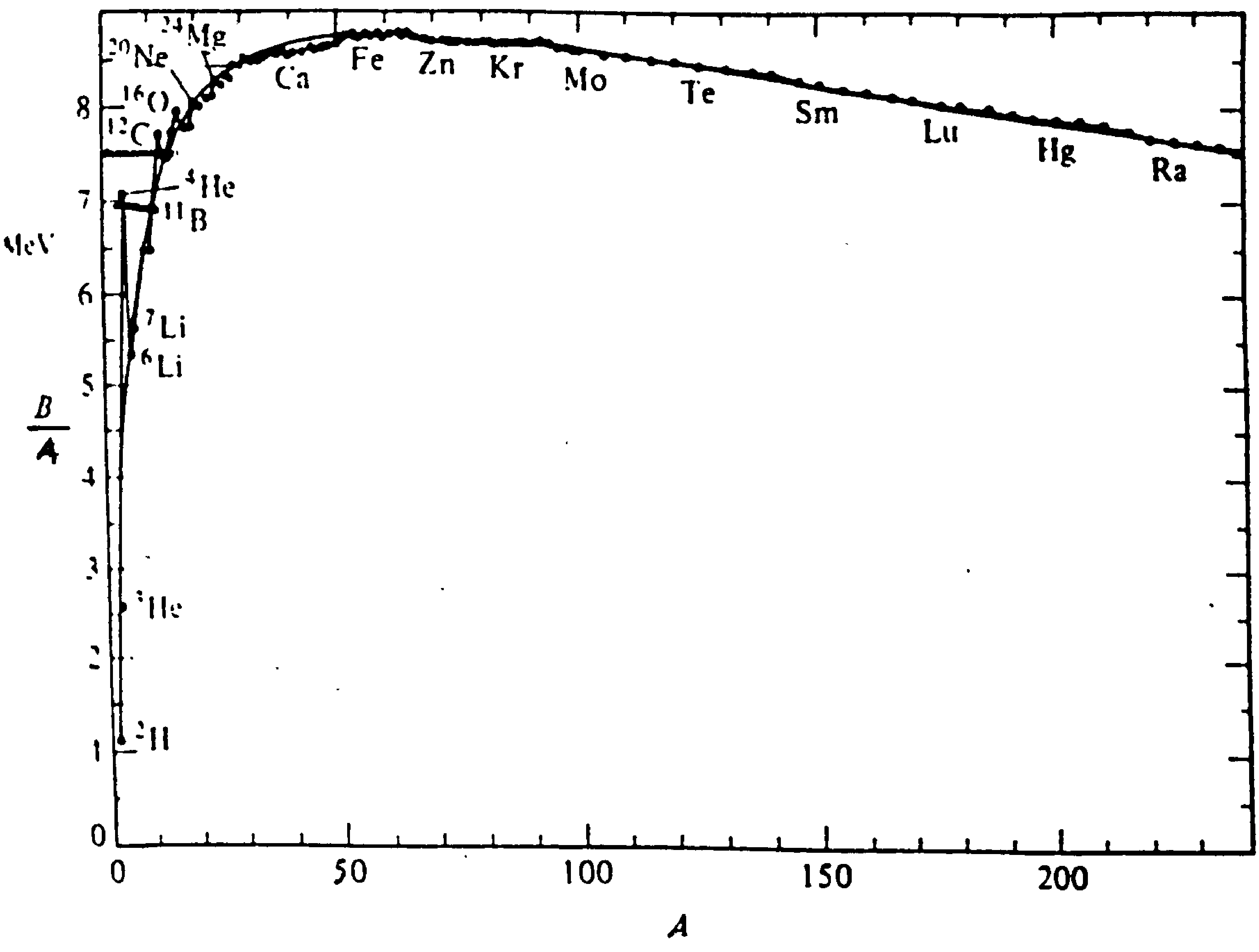

Figure 2.1: *The binding energy per nucleon as a function of mass number A. The smooth curve is from a semi-empirical mass formula similar to 2.3. The figure is taken from [Le 59].*

- $a_a\frac{(N-Z)^2}{A}$ - the asymmetry term. Because nucleons are Fermions they have to obey the Pauli principle. In nuclei, approximately equal numbers of protons and neutrons lead to stable configurations. The asymmetry term is needed to account for the imbalance in most nuclei of the number of neutrons over the number of protons (due to the Coulomb force experienced by protons). For N not equal to Z the reduction in B(N,Z) is proportional to $\frac{(N-Z)^2}{A}$.

- $\Delta(A)$ - the pairing term. The pairing term is due to the pairing force (see later). Conventionally an increase in the binding energy by an amount

Δ is associated with an even-even nucleus compared with an odd-even nucleus. Odd-odd nuclei have both unpaired protons and neutron and have relatively low binding energies.

The Empirical fits to the binding energies give the following values for the coefficients,

$$\left.\begin{array}{l} a_v = 15.7 \\ a_s = 17.8 \\ a_c = 0.7 \\ a_a = 23.7 \end{array}\right\} \text{MeV} \tag{2.4}$$

and

$$\Delta(A) = \left\{\begin{array}{ll} 34A^{-3/4} & \text{for even} - \text{even nuclei} \\ 0 & \text{for even} - \text{odd nuclei} \\ -34A^{-3/4} & \text{for odd} - \text{odd nuclei} \end{array}\right\} \text{MeV} \tag{2.5}$$

The mass of the nucleus can now be written as:

$$M(N,Z) = ZM_P + NM_N - B(N,Z) \tag{2.6}$$

where M_P and M_N are the proton and the neutron masses, respectively. Z and N are the proton and neutron numbers.

2.2.2 The Rotating Liquid Drop Model

The surface of non-spherical (or deformed) nuclei may be described as [Kr 87]

$$R(\theta,\phi) = R_0 C(\alpha_{\lambda\mu}) \left\{ 1 + \sum_{\lambda=0}^{\infty} \sum_{\mu=-\lambda}^{\lambda} \alpha_{\lambda\mu} Y_{\lambda\mu}(\theta,\phi) \right\} \tag{2.7}$$

where $R(\theta,\phi)$ is the distance from the origin, R_0 is the radius of the equivalent sphere (given by equation 2.1), $C(\alpha_{\lambda\mu})$ is a volume conservation factor and $Y_{\lambda\mu}(\theta,\phi)$ are spherical harmonics with coefficients $\alpha_{\lambda\mu}$. For nuclei, the most important deformation is of quadrupole type, for which $\lambda = 2$. For this case, and using the body fixed co-ordinate system (defined by the principal axis of the mass distribution), $\alpha_{22} = \alpha_{2-2}$ and $\alpha_{21} = \alpha_{2-1} = 0$ and so the shape is specified by α_{22} and α_{20} for small deformations. The parameters α_{20} and $\alpha_{22}(\alpha_{2-2})$ can be expressed by another set of parameters, β_2, γ,

$$\left\{ \begin{array}{rcl} \alpha_{20} & = & \beta_2 \cos\gamma \\ \alpha_{22} & = & \frac{1}{\sqrt{2}}\beta_2 \sin\gamma \end{array} \right\} \tag{2.8}$$

where β_2 is the quadrupole deformation parameter and γ is the triaxiality of the system. A representation of the different nuclear shapes in the β_2,γ plane for $-120° \leq \gamma \leq 60°$ is given in figure 2.2 using the Lund convention [An 76]. (Other deformation parameters are also frequently used; for the relationships between the various deformation parameter representation see Löbner *et al.*, [LVH 70].) Rotation is around the shortest, intermediate and largest nuclear axis for $0° \leq \gamma \leq 60°$, $-60° \leq \gamma \leq 0°$ and $-120° \leq \gamma \leq 60°$, respectively. Two types of axially symmetric shapes occur, one at $\gamma = 0°, -120°$ corresponding to prolate (rugby ball) shapes and one at $\gamma = \pm 60°$ corresponding to oblate (earth shaped) shapes. The prolate nucleus may produce rotational states by rotating about the x-axis (defined as an axis perpendicular to the symmetry axis) since this is the axis with the largest moment of inertia. The oblate nucleus may not rotate collectively about its axis of largest moment of inertia (symmetry axis). The nucleons occupy orbitals which have a large projection of spin on the z-axis (symmetry axis). A comprehensive treatment of the classical, rotating, charged liquid drop was carried out by Cohen, Plasil and Swiatecki [CPS 74].

The model addresses the question of the stability of the drop by identifying stationary energy surfaces described by,

$$E_{mac}(\beta,\gamma) = E_{surf}(\beta,\gamma) + E_{coul}(\beta,\gamma) + E_{rot}(\beta,\gamma) \tag{2.9}$$

where the rotational energy is,

$$E_{rot}(\beta,\gamma) = \frac{(\hbar I)^2}{2\Im_{rigid}(\beta,\gamma)} \tag{2.10}$$

and includes the rigid body moment of inertia. Two dimensionless parameters were introduced, the fissility parameter x and the rotational parameter y.

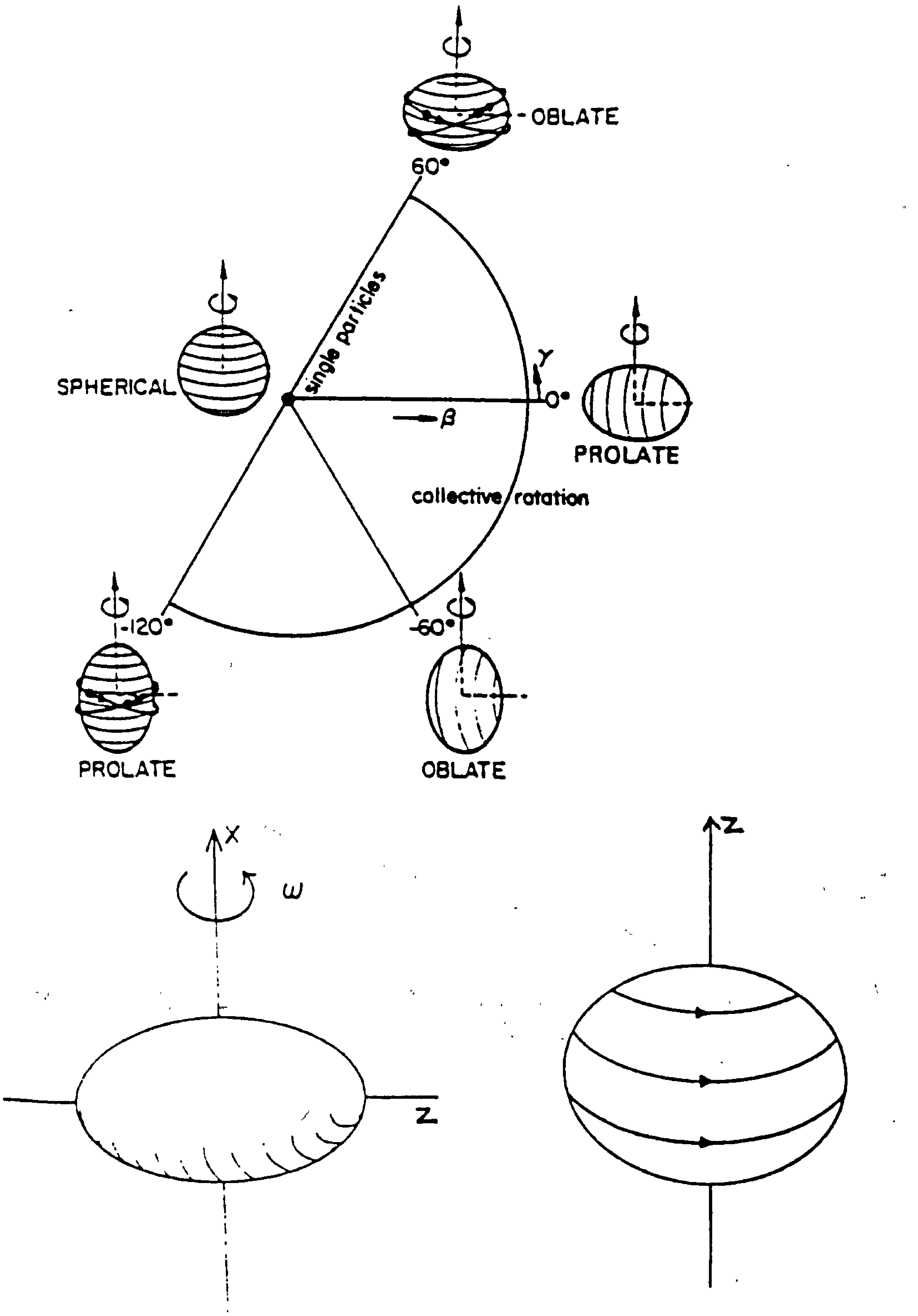

Figure 2.2: *(Upper) The nuclear shapes in the β_2, γ plane as defined by the Lund convention [An 76]. Axially symmetric shapes are shown, the nucleus being triaxial elsewhere. (Lower) A prolate collective nucleus and an oblate single particle nucleus is also shown.*

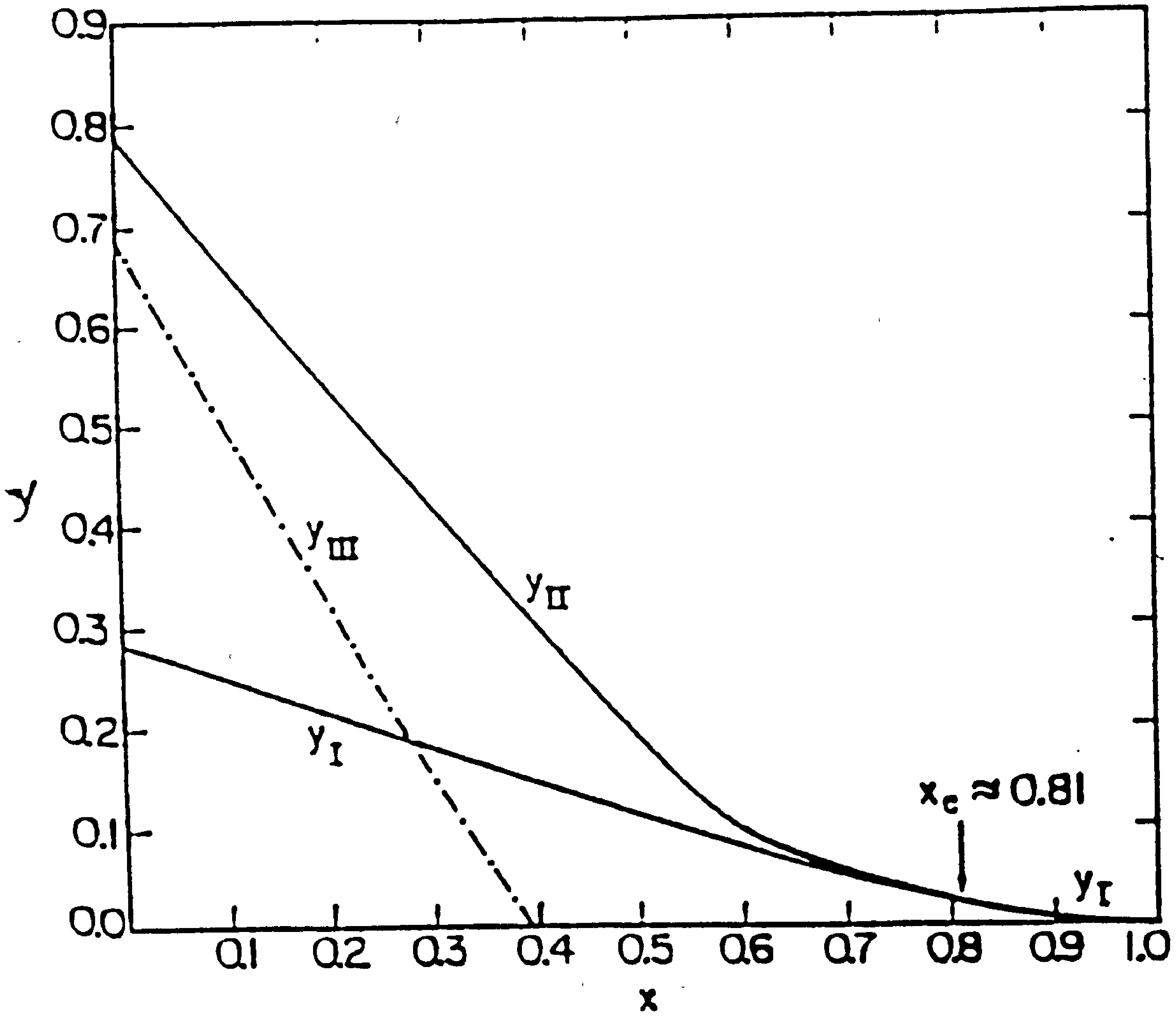

Figure 2.3: *Critical curves of the rotational parameter, y, as a function of the fissility parameter, x. The figure is taken from [CPS 74].*

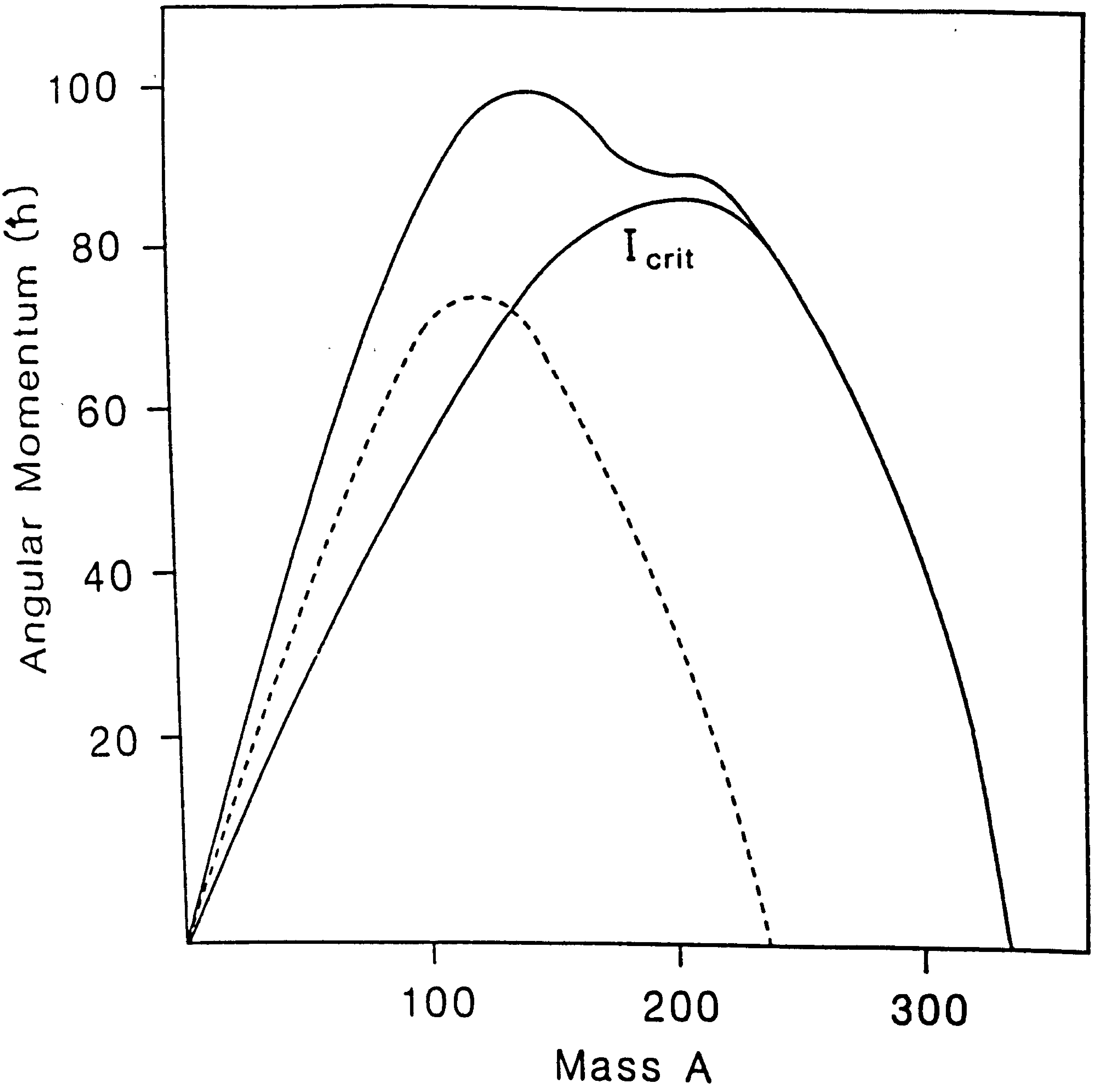

Figure 2.4: *Classical estimate of the maximum angular momentum that can be accommodated in a rotating nucleus. Below the dashed curve the fission barrier is greater than 8 MeV while above the line marked I_{crit} superdeformed shapes are predicted to be stable here. The figure is taken from [CPS 74].*

These are given by,

$$x = \frac{E_{coul}(\beta,\gamma)}{2E_{surf}(\beta,\gamma)} \tag{2.11}$$

and

$$y = \frac{E_{rot}(\beta,\gamma)}{2E_{surf}(\beta,\gamma)} \tag{2.12}$$

The general features of the calculations indicate that at low angular momenta (low y values) the nucleus adopts axially symmetric shapes (oblate) which remain stable up to some critical value y_I and which depend on x (figure 2.3). For $y > y_I$ triaxial shapes are preferred while at higher angular momenta the stable shapes become more axially symmetric (prolate/superdeformed) before fissioning at $y > y_{II}$. When $y > y_{II}$, the nucleus becomes unstable against fission. The model also predicts some physical quantities such as limiting angular momenta, fission barriers and stable ground state deformations for a range of nuclei. The height of a fission barrier is seen to depend on the angular momentum (I), limiting the amount of spin a nucleus can support before fission occurs. Figure 2.4 shows the maximum angular momentum I_{max} as a function of mass A. The line marked I_{crit} is the point above where triaxial/superdeformed shapes are predicted to be the most stable configurations. The dashed line indicates the I_{max} value for a fission barrier of 8 MeV. In general the RLDM is consistent with the experimentally observed limiting values of I, the actual shape of the nucleus is, however, sensitive to the microscopic structure of the nucleus.

2.3 Spherical Shell Models

The liquid drop model of the nucleus is successful in accounting for many properties of the nucleus. However, there is strong experimental evidence for a shell structure in nuclei, analogous to the electron shell structure in atoms. Deviations between the curve described by the semi-empirical mass formula and the experimental data (2.1), as a function of nucleon number, indicate favoured values of neutron and proton numbers where the nucleus is more strongly bound. The existence of especially stable nuclei at well defined magic numbers 2, 8, 20, 28, 50, (64), 82 ..... is indicative of nucleon shells.

2.3.1 The Nuclear Mean field Approximation

The mean-field approximation of the atomic nucleus has been extremely successful in simplifying the complicated interactions inside the nucleus. It was developed in analogy to the atomic model. The situation in the nucleus, however, is very different from the atom. Whereas the atomic electrons are constrained to move in an average repulsive field due to all other electrons, nucleons move in the attractive field of all the other nucleons.

In the mean-field approximation the nucleons of a nucleus produce together an average potential V. The motion of each individual nucleon is regarded as mainly being determined by V. Because of the approximate character of this model an additional potential V_R is assumed. It accounts for any residual interactions which are not included in V. V_R is assumed to be negligible to first order. The Hamiltonian of the mean-field model is given by

$$H = H_{sh} + V_R \tag{2.13}$$

where

$$H_{sh} = \sum_{i=1}^{N} \left\{ \frac{-\hbar^2}{2m_i} \nabla_i^2 + V_{sh}(r_i) \right\} \tag{2.14}$$

The choice of $V_{sh}(r)$ defines a model and contains parameters which can be varied to fit the experimental data. Such models are known as phenomenological models.

2.3.2 The Harmonic Oscillator Potential

The oscillator potential can be expressed as

$$V_{HO} = \frac{-V_0}{1-(R/R_0)^2} \tag{2.15}$$

for $R < R_0$ and zero elsewhere. It can be modified in order to give a better representation of the 'real' potential. In this case it is referred to as the Modified Oscillator potential (MO).

2.3.3 The Woods-Saxon Potential

The Woods-Saxon potential is given as a function of the radius R by

$$V_{WS}(r) = \frac{-V_0}{1 + exp(\frac{r-R}{d})} \tag{2.16}$$

where R accounts for the nuclear radius and 'd' for the diffuseness of the nuclear 'surface' which determines the shape of the potential around R.

2.3.4 Spin-Orbit Coupling

So far, from consideration of a central potential only, it is not possible to predict the correct magic numbers and so it is necessary to introduce a non-central component to the nuclear potential.

Similarly to the situation in the atom, the non central term is given the form of a spin-orbit interaction [Ma 49, HJS 49] although its origin is the nuclear force unlike the electromagnetic force in the case of atoms. The spin-orbit interaction results in a coupling of the intrinsic spin and orbital angular momenta (s and l, respectively) of the nucleon to give a total angular momentum j:

$$\mathrm{j} = \mathrm{l} + \mathrm{s} \tag{2.17}$$

and remembering s=$\pm\frac{1}{2}$ for nucleons, splits a given value of $l(l{\neq}0)$ into two components $j = l + \frac{1}{2}$ and $j = l - \frac{1}{2}$ each containing $2j + 1$ particles. The attractive force means that $j = l + \frac{1}{2}$ lies lowest in energy of the two components. The size of the splitting is proportional to l, hence the states with largest values of l exhibit the greatest splitting. With the inclusion of the spin orbit term and a Coulomb term, the single particle nuclear Hamiltonian has the form

$$h_{SH} = \frac{-\hbar^2}{2m}\nabla^2 + V_{WS} + V_{SO} + V_{Coul} \tag{2.18}$$

where V_{SO} represents the spin-orbit interaction and V_{Coul} is the Coulomb potential for protons and can be derived from the electrostatic potential of a uniformly charged drop. The spin orbit interaction is expressed as

$$V_{SO} = f(r)l.s \tag{2.19}$$

where $f(r)$ is proportional to the derivative of the central potential. The solution of the Schrödinger equation

$$\mathrm{H}_0\Psi = E_0\Psi \tag{2.20}$$

using a mean field potential V_0 with the inclusion of spin-orbit coupling and a V_{Coul} term leads to the shell structure shown in figure 2.5. The levels are now denoted by nl_j. It can be noticed that in this example the negative parity $1\mathrm{h}_{11/2}$ orbital is shifted down into the shell below. The $1\mathrm{h}_{11/2}$ level has opposite parity to the other levels in the shell and is termed a "high j intruder orbital", the other levels being referred to as "normal" parity states.

2.4 Deformed Shell Models

The assumption of essentially independent motion of nucleons in an average field is the basis of the shell model and of all microscopic theories of finite nuclei. This potential is produced by the nucleons themselves and their mutual interactions.

However one has to assume a deformed shell model potential, in order to explain the existence of rotational bands, very large quadrupole moments, strongly enhanced quadrupole transition probabilities and deformation dependent single particle structure.

2.4.1 The Nilsson Potential

One of the simplest deformed shell models is the Nilsson model which employs a modified HO potential as an approximation to the deformed mean-field. The

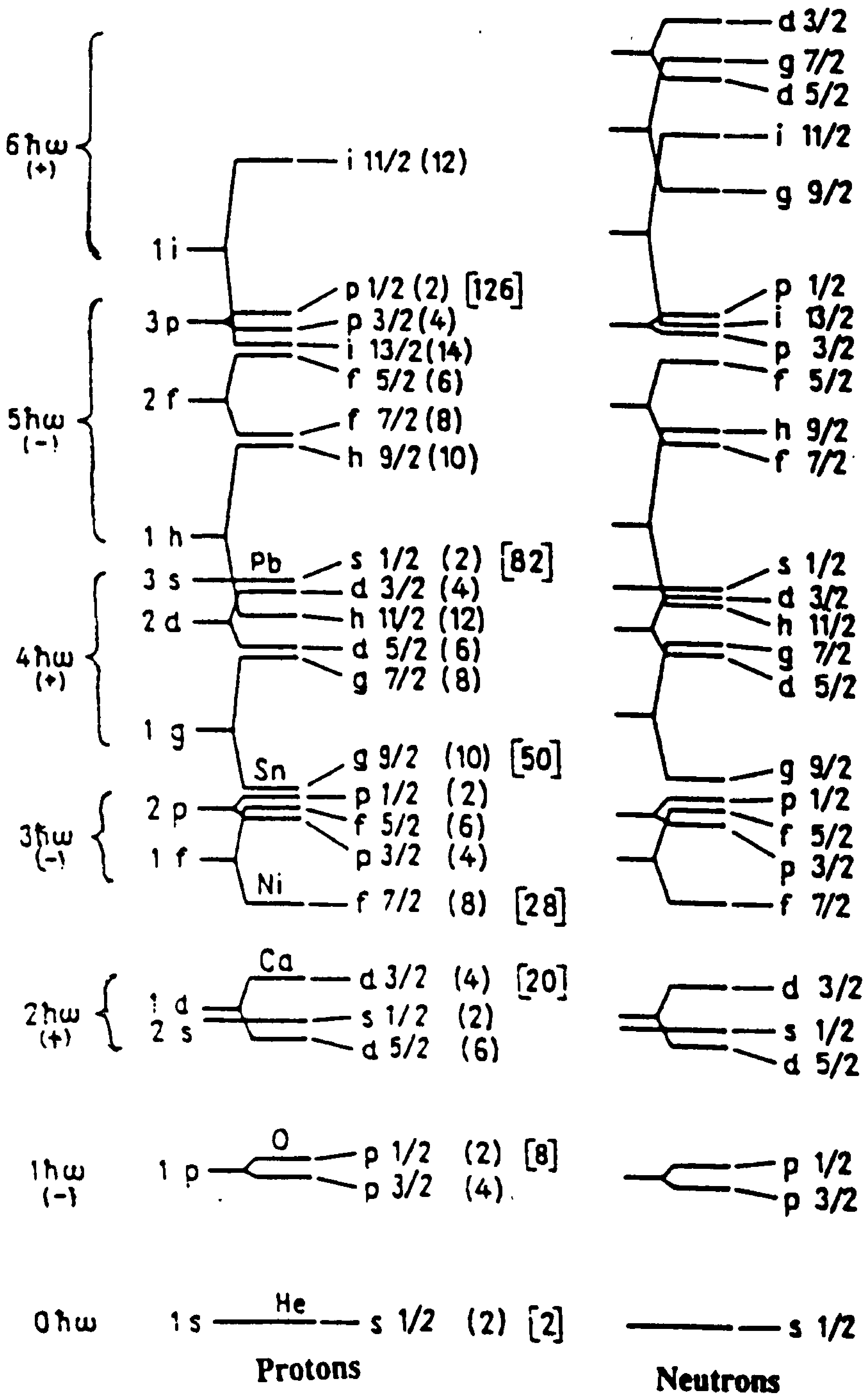

Figure 2.5: *Nucleon energy levels for protons (left) and neutrons (right) deduced using a mean-field potential including a spin-orbit and a Coulomb term. The levels can be assigned as indicated. To the left the corresponding harmonic oscillator quantum numbers and the parity of the levels are indicated. The numbers in squared brackets refer to the magic numbers which correspond to significant shell gaps. The figure is from [Kl 52].*

Nilsson single particle Hamiltonian is given by:

$$h_{Nil} = \frac{-\hbar^2}{2m}\nabla^2 + V_{MHO} - 2\kappa\hbar\omega_o[\mathbf{l}_t.\mathrm{s} - \mu(\mathbf{l}_t^2 - < \mathbf{l}_t^2 >_N)] \tag{2.21}$$

where κ and μ are parameters [Ni 69] varied to fit experimental data and the term $< \mathbf{l}_t^2 >_N$ maintains the average shell energy at a constant value whilst the $\mathbf{l}_t^2$ term moves the levels within the shell [Gu 67], V_{MHO} is the Modified Harmonic Oscillator Potential [Ni 55], $\frac{-\hbar^2}{2m}\nabla^2$ is the usual K.E. operator and $\mathbf{l}_t.\mathrm{s}$ is the spin orbit term.

Plots of the single particle energy levels (usually expressed in the units of $\hbar\omega_0$) versus deformation for protons and neutrons are shown in figures 2.6 and 2.7 (from[BR 85]), respectively and are called Nilsson diagrams. In the spherical region the orbitals are labelled with their l_j values. As the nucleus deforms l_j no longer remains the good quantum number and the so called asymptotic quantum numbers $[Nn_z\Lambda]\Omega$ are used. The asymptotic quantum numbers N, n_z, Λ and Ω are referred to as the principal quantum number, the number of oscillations parallel to the z-axis, the component of the orbital angular momentum of the particle onto the symmetry axis and the component of the total angular momentum onto the symmetry axis, respectively.

2.4.2 The Deformed Woods-Saxon Potential

The Nilsson model has the advantage that the MHO potential is separable into three one-dimensional oscillators and is, therefore, simple, to solve. However, the deformed Woods-Saxon (DWS) potential is a closer estimate to the real deformed nuclear potential and is given by:

$$V_{DWS} = \frac{-V_0}{1 + exp(\frac{dist[r \rightarrow R(\theta)]}{d})} \tag{2.22}$$

where $dist[r \rightarrow R(\theta)]$ denotes the distance from some point R to the nuclear surface, it is defined to be negative for points inside the nuclear surface and positive outside and "d" is the surface diffuseness. The single particle DWS

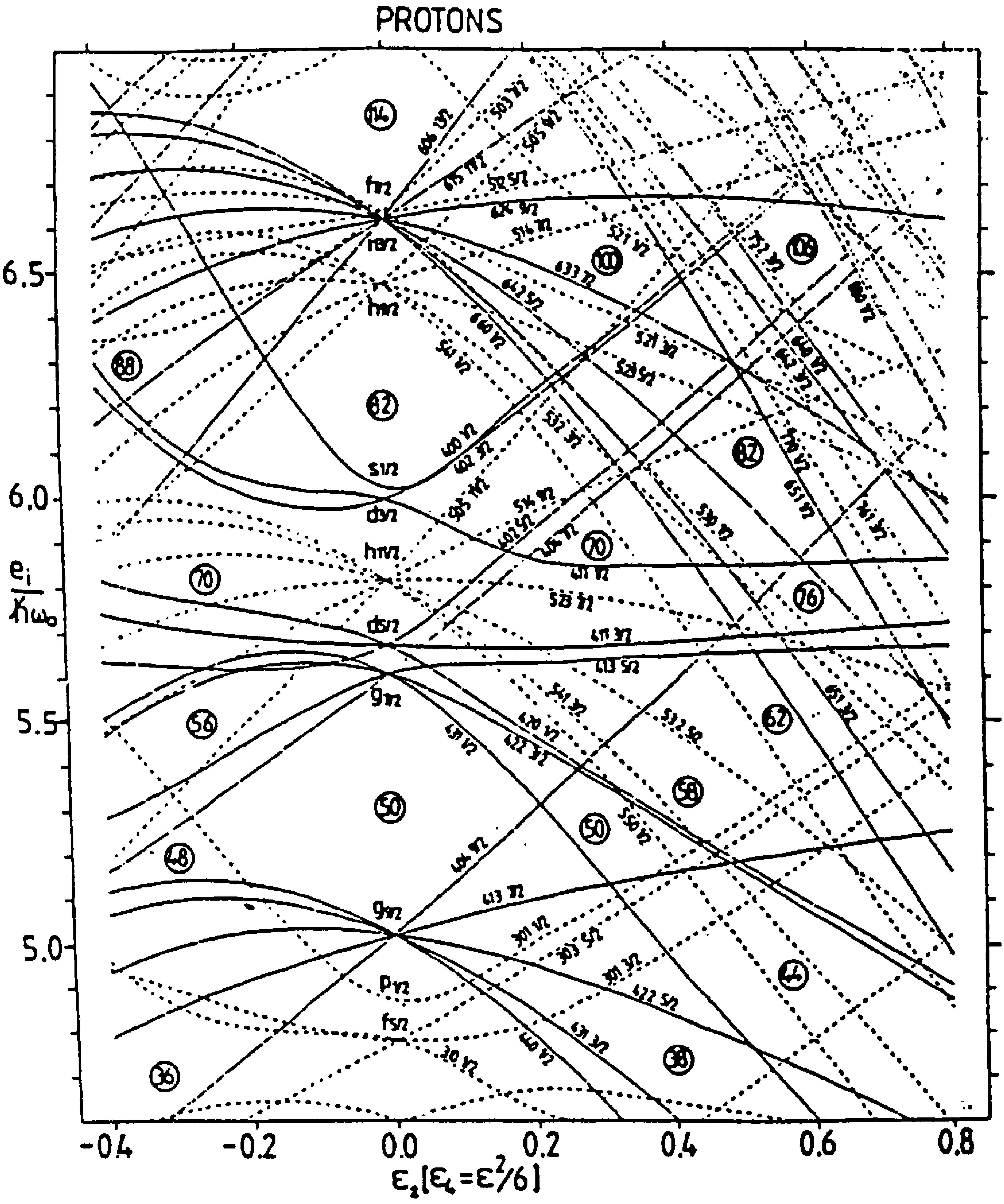

Figure 2.6: *The Nilsson diagram for Protons. For zero deformation the orbitals are labelled by l_j but as the deformation increases the asymptotic quantum numbers are used. The figure is from [BR 85].*

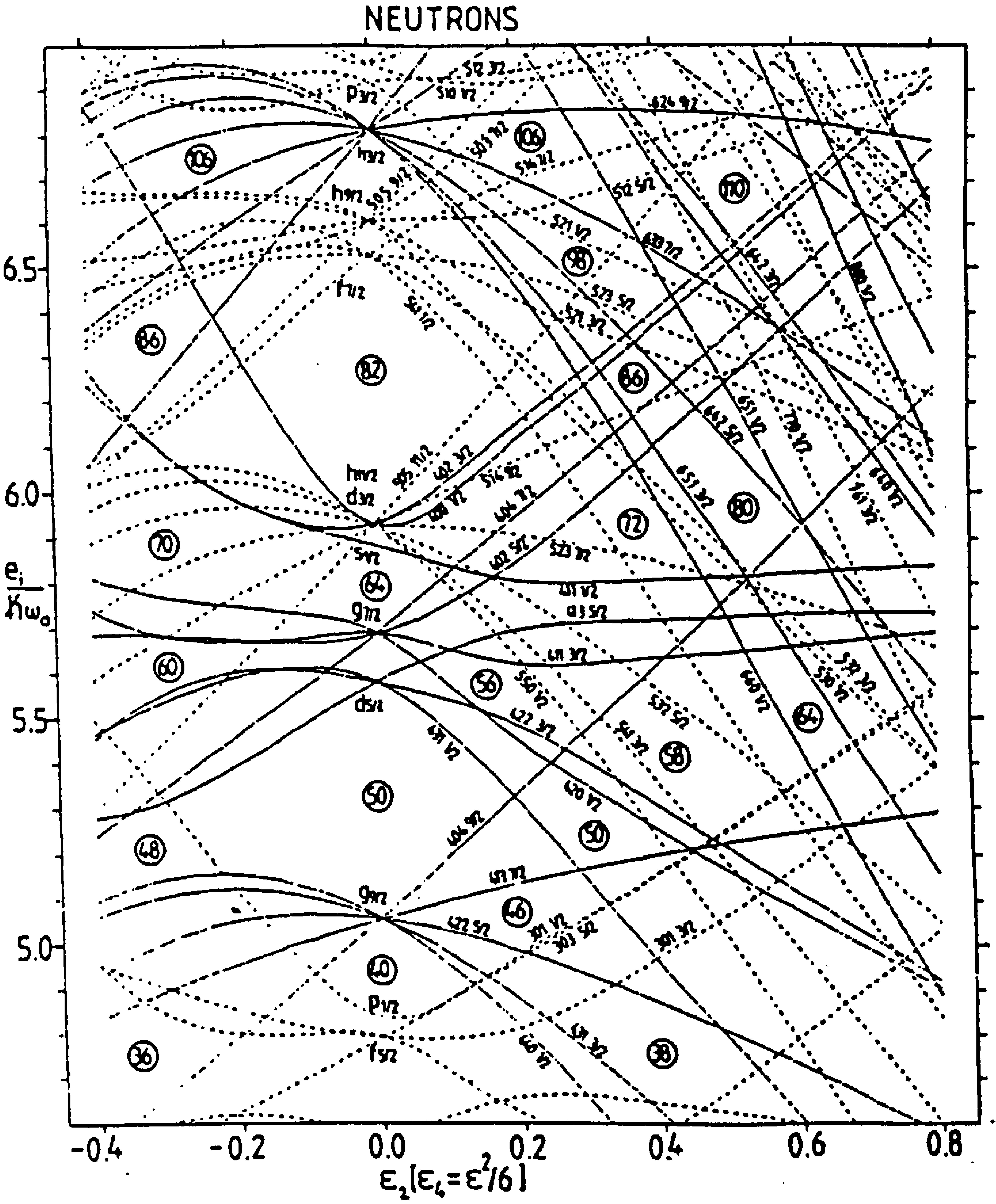

Figure 2.7: *The Nilsson diagram for Neutrons. The figure is from [BR 85]*

Hamiltonian takes a similar form to equation 2.18 and is now written as:

$$h_{DWS} = \frac{-\hbar^2}{2m}\nabla^2 + V_{DWS} + V_{SO} + V_{Coul} \tag{2.23}$$

where the spin orbit term is now given by

$$V_{SO} = -\lambda(\frac{\hbar}{2mc})^2(\nabla V_{DWS} \times p).s, \tag{2.24}$$

where p is the momentum vector and λ a strength parameter.

2.5 The Strutinsky Shell Correction

It follows from the previous discussion that, for a given number of nucleons, the levels which are occupied change as the nucleus deforms. Obviously this is more pronounced for orbits near to the Fermi surface: those levels far from the Fermi surface will tend to remain either occupied or unoccupied. It therefore comes about that the total energy of the system can be written as the sum of two parts; a smooth part due to filled levels below the valence shell, and a rapidly varying part due to levels within the valence shell.

$$E_{tot} = \tilde{E}_{shell} + \delta E_{shell} \tag{2.25}$$

where $\tilde{E}_{shell}$ refers to the smooth part and δE_{shell} is known as the shell correction term.

On the whole the single particle shell model is rather poor at describing the effects due to the bulk of the nucleons far from the nuclear surface, although it does describe the contribution from the valence nucleons rather well. The result is that a pure shell model approach to calculate the total energy is unsatisfactory. Strutinsky[St 65, St 67] proposed that one should replace $\tilde{E}_{shell}$ with a macroscopic term ($E_{macro} \sim E_{LDM}$), usually taken to be the liquid drop or rotating liquid drop (in the rotating case)

$$E_{tot} = E_{macro} + \delta E_{shell} \tag{2.26}$$

One then has the problem of determining the shell correction term, which is the difference between the total shell energy and the 'smooth' shell energy.

$$\delta E_{shell} = \sum_{v=1}^{A} e_v - \tilde{E}_{shell} \tag{2.27}$$

where e_v represents the nucleon single particle eigenvalues. Since this decomposition is entirely a shell model problem, it is useful to define a level density concept, g(e)δe, the number of levels in the energy interval e to e+δe

$$g(e) = \sum_{i} \delta(e - e_i) \tag{2.28}$$

$\delta(e - e_i)$ is a Dirac delta function and in this representation, the particle number, A may be obtained from an integration of g(e) from $-\infty$ to the Fermi energy, λ

$$A = \int_{-\infty}^{\lambda} g(e)\, \delta e \tag{2.29}$$

The Strutinsky renormalisation replaces the discrete density of states by a smooth level density;

$$\tilde{g}(e) = \sum_{i} S(e - e_i) = \frac{1}{\gamma} \int_{-\infty}^{\infty} g(e) f \frac{(e - e')}{\gamma} \delta e \tag{2.30}$$

where $S(e - e_i)$ is a smooth function and $f\frac{(e-e')}{\gamma}$ is Gaussian with width $\gamma \approx \hbar\omega_0$, the energy difference between successive nuclear shells. Hence the particle number A becomes

$$A = \int_{-\infty}^{\tilde{\lambda}} \tilde{g}(e)\, \delta e \tag{2.31}$$

then

$$\tilde{E}_{shell} = \int_{-\infty}^{\tilde{\lambda}} e\tilde{g}(e)\, \delta e \tag{2.32}$$

This average shell energy expression represents a smearing of the Fermi surface and therefore, the occupation probabilities for the unoccupied levels. It restricts the effects of the interactions and crossings which are responsible for the fluctuating behaviour. The results of calculations using the Strutinsky procedure are often given in the form of potential energy surfaces (see later). They are energy contours in an $(\epsilon - \gamma)$ plane. The Strutinsky method may also be applied to rotational nuclei. In this case the method is more complex because the angular momentum also contains a contribution to the total single particle energy and this must be accounted for in an analogous method to above. A detailed account of the extension to include rotation is discussed in section 3.3.

Chapter 3

Nuclear Rotation

3.1 Pairing Correlations

Classically, the most efficient way pairs of nucleons can interact via the short range strong nuclear interaction is for both nucleons to move together in the same orbit. This is forbidden by the Pauli principle, and the occupation of time-reversed orbits is the next most efficient possibility. This so-called pairing interaction is shown schematically in figure 3.1 (a). The angular momenta of the nucleons are now coupled to I=0 via the monopole pairing force. Indeed the observation that even-Z even-N nuclei have a ground state of $I^\pi = 0^+$ is strong evidence for pairing correlations. The paired nucleons have a reduced energy due to the attractive nature of the interaction, leading to the concept of the pairing energy or "pair gap", Δ. It follows therefore that there should be a greater binding energy for even-even nuclei than for their odd-mass neighbours. This effect is observed experimentally, and is often used to estimate the magnitude of the pair gap.

The effect of pairing correlations at low spins is to tend to drive the core to a spherical shape due to the isotropic nature of the interaction. Where the pairing interaction is large in the presence of closely spaced single particle energy levels, the scattering of pairs of nucleons between sets of time-reversed orbits influences the occupation probabilities of the individual single particle

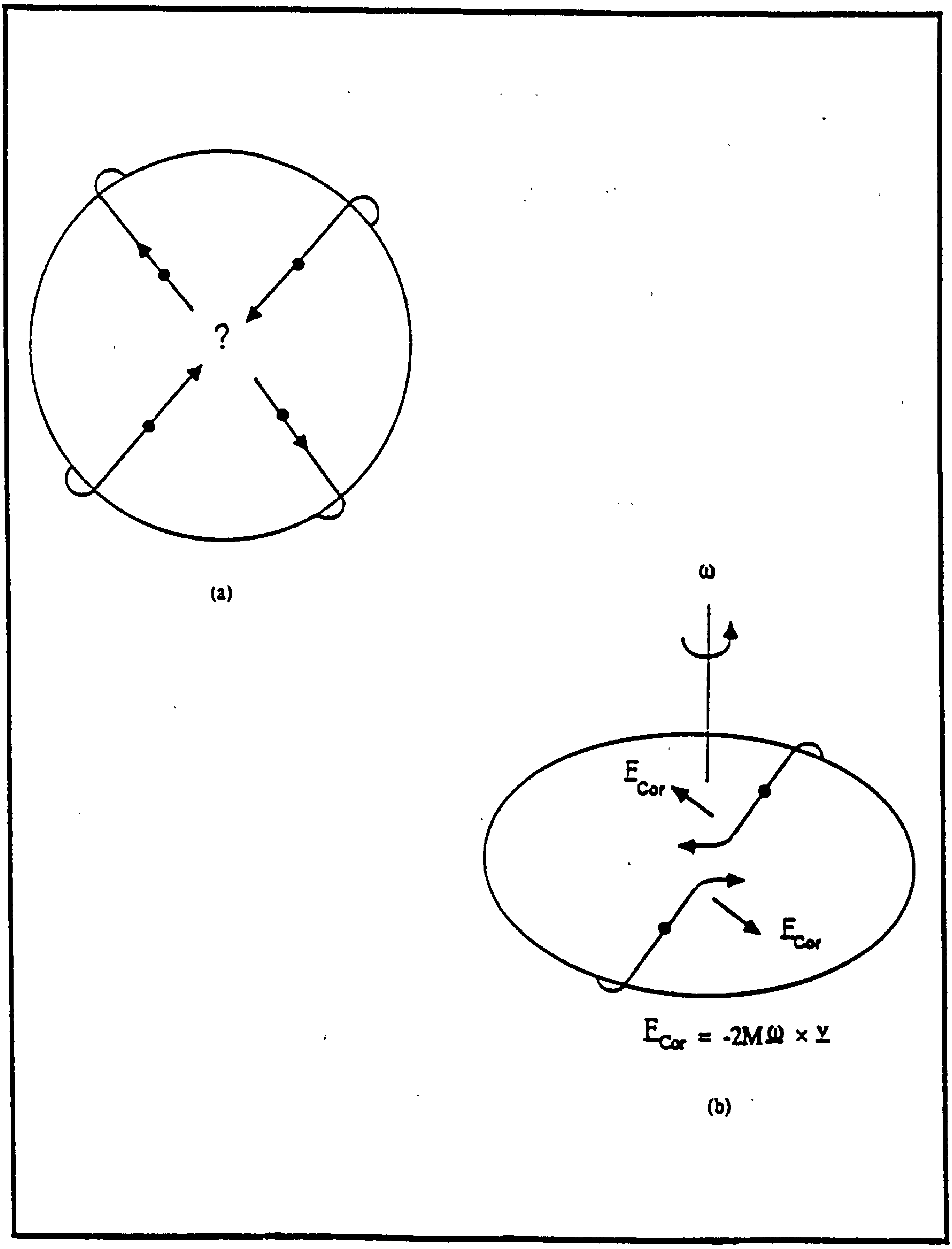

Figure 3.1: *(a) A schematic plot of the pairing interaction between two nucleons and (b) the expected effect of the Coriolis force on the nucleonic motion due to the rotation of the nucleus.*

levels. This has the effect of smearing the Fermi-surface (which for an unpaired system would be well defined). The analogy between these effects and electron correlations in superconductors prompted the suggestion [Bo 58] that this microscopic interaction may be described in terms of Cooper-pairs [BCS 57] and this technique has been applied with some success in the pairing model when considering microscopic two-body interactions.

The effect of nuclear rotation on a pair of particles (a Cooper pair) occupying time reversed orbits is illustrated in figure 3.1 (b). The Coriolis force acts in opposite directions on the two particles and tends to counteract the pairing force and can be pictured as bending the two time reversed orbits away from each other thereby reducing the effectiveness of the short range pairing force. When the Coriolis force overcomes the pairing for a particular pair of nucleons in a high-j orbit, the pair is decoupled from the rotating core and the spin of the pair is aligned parallel to the rotation axis. This effect, leading to a decrease in pairing, is known as Coriolis antipairing (CAP).

3.2 The Cranked Shell Model

3.2.1 Introduction

Some nuclei are deformed in their ground states which enables them to rotate. Due to rotation, centrifugal and Coriolis forces come into play, which are responsible for the generation of the angular momentum, both by the single particles and the core. A microscopic description of nuclear rotations was proposed as long ago as 1954 by Inglis [In 54, In 55]. This procedure, known as the cranking approximation, is frequently used and enables, within the same formulation, a description of both collective rotations and single particle excitations (occasionally referred to as non-collective rotations).

The rotation of a nucleus about an axis perpendicular to a symmetry axis induces a coupling between the individual nucleon orbits and the deformed mean field, partially aligning the nucleon angular momenta with the rotation axis. The total angular momentum can then be considered to be due to a collective contribution from all states.

The rotation of the field introduces explicitly, a time dependence to the Schrödinger equation which can be removed by transforming to the intrinsic (or rotating) frame of reference:

In the laboratory frame the time dependent Schrödinger equation can be written as,

$$i\hbar\frac{\partial\Psi_L}{\partial t} = H_L\Psi_L \tag{3.1}$$

where H_L and Ψ_L are the Hamiltonian and wave function of the system. The laboratory and the intrinsic frame are coupled through a unitary transformation by the rotation operator,

$$R_x = exp(-iJ_x\omega t/\hbar) \tag{3.2}$$

where

$$J_x = \sum_{i=1}^{A} j_{x,i} \tag{3.3}$$

is the component of the total angular momentum along the rotation axis and since the x-axis is taken to be the axis of rotation $J_x{=}J_{x'}$ (prime refer to coordinate in the rotating frame). Hence,

$$\Psi_L = R_x\Psi' \tag{3.4}$$

and

$$H_L = R_xH'R_x^{-1} \tag{3.5}$$

The Schrödinger equation now reads as,

$$i\hbar\frac{\partial\Psi'}{\partial t} = (H' - \omega J_x)\Psi' \equiv H^{\omega}\Psi' \tag{3.6}$$

The Hamiltonian

$$H^{\omega} = H' - \omega J_x \tag{3.7}$$

is called the total cranking Hamiltonian. The second term on the right hand side of equation 3.7 $(-\omega J_x)$ can be considered to play the part of the Coriolis and centrifugal forces. In the case of a single particle, equation 3.7 can be written as

$$h^{\omega} = h' - \omega j_x \tag{3.8}$$

and in this case it is termed the single particle cranking Hamiltonian. The eigen values of h^{ω} are so called routhians and represent the single particle energies of the orbitals in the rotating frame.

The total energy of the rotating system is calculated as the sum of expectation values of the real single particle energies, e_v^{ω}:

$$E = \sum_v < e_v^{\omega} > = E^{\omega} + \hbar\omega < I_x > \tag{3.9}$$

where for a state of spin I belonging to a given K-band (where K is the projection of total angular mometum "I" on the symmetry axis), the value of ω is chosen such that

$$< I_x > = \{I(I+1) - K^2\}^{1/2} \tag{3.10}$$

The sensitivity of an orbit to the rotation of the nuclear mean field can be examined by a direct differentiation of the single particle energies with respect to rotational frequency and is termed as the alignment

$$i_x = \frac{de_v^{\omega}}{d\omega} = - < v^{\omega} | j_x | v^{\omega} > \tag{3.11}$$

The amount to which the orbital is affected by the rotation depends on its j value; high-j, low-Ω orbitals being the most strongly aligned. To illustrate this, figure 3.2 shows the eigenvalues of the single particle Routhians plotted as a function of angular velocity for the Woods-Saxon potential.

3.2.2 Symmetries In The Cranking Hamiltonian

Signature

The cranking Hamiltonian (equation 3.7) does not conserve time reversal or rotational invariance since the J_x operator changes sign under these operations. The only symmetries that remain in H^{ω} are the space reflections (parity) and

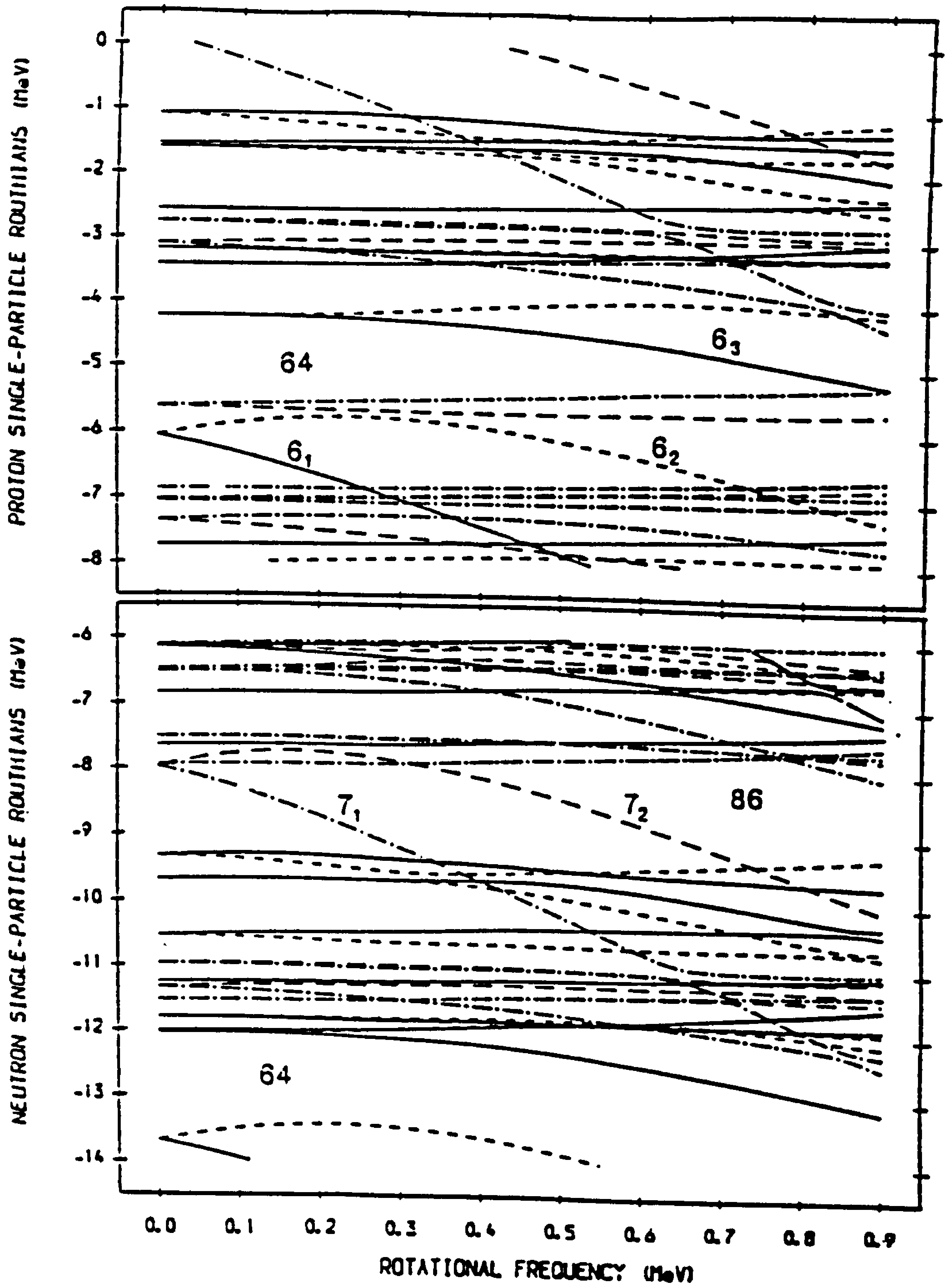

Figure 3.2: *Single-particle Woods-Saxon Routhians for neutrons and protons at β_2=0.575 and β_4=0.88 as a function of rotational frequency. The deformation is characteristic for the SD band in ^{150}Gd. The parity and signature are indicated by solid (π = +, α = 1/2), dotted (π = +, α = -1/2), dot-dashed (π = -, α = 1/2) and long dashed (π = -, α = -1/2) orbitals. The figure is from [NWJ 89].*

the transformation described by the R_x operator, (a rotation about the x-axis by an angle of 180°) which is given by:

$$R_x = \exp(-i\pi j_x) \tag{3.12}$$

For an even system the square of this operator does not alter the wave function while for an odd number of particles (fermions) the wave function changes sign;

$$R_x^2 = (-1)^A \tag{3.13}$$

Therefore, the eigenvalues, e_ν^ω and eigenstates, $|\nu^\omega>$ of the single particle cranking Hamiltonian, h^ω are labelled by the parity of the states, $\pi(\nu)$ and by the eigenvalue, $r_x(\nu)$ of R_x operator, defined as

$$r_x(\nu) = exp[-i\pi\alpha(\nu)] \tag{3.14}$$

The quantum number r_x=r is called the signature of the state $|\nu^\omega>$, and α may be defined as the signature exponent, ($\alpha(\nu)$ is sometimes preferred to $r_x(\nu)$ because α ia an additive quantity).

For nuclei with even mass numbers

$$\begin{aligned} r &= +1 \; or \; \alpha = 0 \Rightarrow I = 0,\ 2,\ 4,\ ... \\ r &= -1 \; or \; \alpha = 1 \Rightarrow I = 1,\ 3,\ 5,\ ... \end{aligned} \tag{3.15}$$

and for odd-mass nuclei

$$\begin{aligned} r &= -i \; or \; \alpha = +\tfrac{1}{2} \Rightarrow I = \tfrac{1}{2},\ \tfrac{5}{2},\ \tfrac{9}{2},\ ... \\ r &= +i \; or \; \alpha = -\tfrac{1}{2} \Rightarrow I = \tfrac{3}{2},\ \tfrac{7}{2},\ \tfrac{11}{2},\ ... \end{aligned} \tag{3.16}$$

Degeneracy

The addition of the cranking term $(-\omega j_x)$ to the single particle Hamiltonians (described in chapter 2) removes the degeneracy of the eigenfunction for ω >0. For example, the Nilsson model eigenfunctions are doubly degenerate with respect to Ω at zero rotational frequency, ($\pm\Omega$). For $\omega \neq 0$, the Coriolis term in the cranking model splits each orbital into two levels of opposite signature exponent, ($\alpha = +\frac{1}{2}$) and ($\alpha = -\frac{1}{2}$). The magnitude of this so called signature splitting depends upon the angular momentum projection onto the rotational axis, j_x and the magnitude of the rotational frequency. For large rotational frequencies, orbits with high-j_x or low Ω projections result in a large signature splitting and are often lowered into the vicinity of the Fermi surface and consequently new sets of magic numbers are seen to occur.

3.3 Cranked Nilsson-Strutinsky Calculations

The description of nuclei at high spins ($30\hbar < I < 60\hbar$ say), requires a model which is self-consistent with respect to the shape degrees of freedom. At high rotational frequencies one may consider the static pair correlations to be negligible, hence in these calculations pairing is neglected and a minimisation of the total energy is carried out with respect to ϵ_2, ϵ_4 and γ (the shape parameters). A successful model employing the above criteria is the Cranked Nilsson-Strutinsky model (CNS).

In the previous chapter, it was observed that the total nuclear energy of a nucleus was inadequately described by a purely microscopic calculation.

Generalising the Strutinsky method to rotations [An 76], the spin (angular momentum) density function $g_2(e^\omega)$ is defined as

$$g_2(e^\omega) = \sum_v < j_x >_v \delta(e^\omega - e_v^\omega) \tag{3.17}$$

analogous to the definition of the level density given by (equation 2.28) i.e.

$$g_1(e^\omega) = \sum_i \delta(e^\omega - e_v^\omega). \tag{3.18}$$

The smearing density function is taken to be (similar to that given by equation 2.30.) :

$$\tilde{g}_1(e^\omega) = \sum_v S(e^\omega - e_v^\omega) \;\; and \;\; \tilde{g}_2(e^\omega) = \sum_v S(e^\omega - e_v^\omega) \tag{3.19}$$

where $S(e^\omega - e_v^\omega)$ is a Strutinsky smearing function. The total angular momentum (I) becomes

$$I = \int_\infty^\lambda g_2(e^\omega)\, de^\omega \tag{3.20}$$

The total single particle energy obtained from the cranking formalism (equation 3.9) can be expressed as;

$$E_{sp}(I) = \int_{-\infty}^{\lambda} e^{\omega} g_1(e^{\omega})\, de^{\omega} + \hbar\omega I \tag{3.21}$$

The energy in terms of the smoothed density functions is given by (as in equation 3.21)

$$\tilde{E}(\omega) = \int_{-\infty}^{\tilde{\lambda}} e^{\omega} \tilde{g}_1(e^{\omega}) + \hbar\omega\, \tilde{g}_2(e^{\omega})\, de^{\omega} \tag{3.22}$$

The cranked Nilsson Strutinsky single particle Hamiltonian also includes hexadecapole deformation (ϵ_4) and the γ-degree of freedom

$$h^{\omega}_{CNS} = h_{Nil}(\epsilon_2, \gamma) + 2\hbar\, \overset{\circ}{\omega}\, \rho^2 \epsilon_4 V_4(\gamma) - \omega j_x \tag{3.23}$$

where ρ is the radius in the stretched coordinate system [Ni 55] and V_4 is the hexadecapole potential [BR 85]. The total energy is defined as the sum of the macroscopic and the shell energies as described in section 2.5.

$$E_{tot}(\epsilon_2, \epsilon_4, \gamma, I) = E_{mac}(\epsilon_2, \epsilon_4, \gamma, I) + \delta E_{shell}(\epsilon_2, \epsilon_4, \gamma, I) \tag{3.24}$$

and the minimisation with respect to E_{tot} is plotted in ϵ versus ω diagrams, for a constant spin, I. The macroscopic energy contribution may be calculated from

$$E_{macro} = E_{surf} + E_{Coul} + \frac{\hbar^2 I^2}{2\Im_{rigid}} \tag{3.25}$$

The cranking term, $-\omega j_x$ causes certain Nilsson orbitals to approach one another in the routhian plots of e^{ω} versus ω.

3.3.1 Potential Energy Surfaces

The potential energy surfaces are calculated by minimising the total energy with respect to the shape parameters (ϵ_2, ϵ_4 and γ) and the resulting energies are usually plotted as contours on ϵ_2, γ maps for fixed values of I. Figure 3.3 illustrates some potential energy surfaces calculated (Anderson *et al.* [An 76]) for the nucleus ^{160}Yb at various values of I.

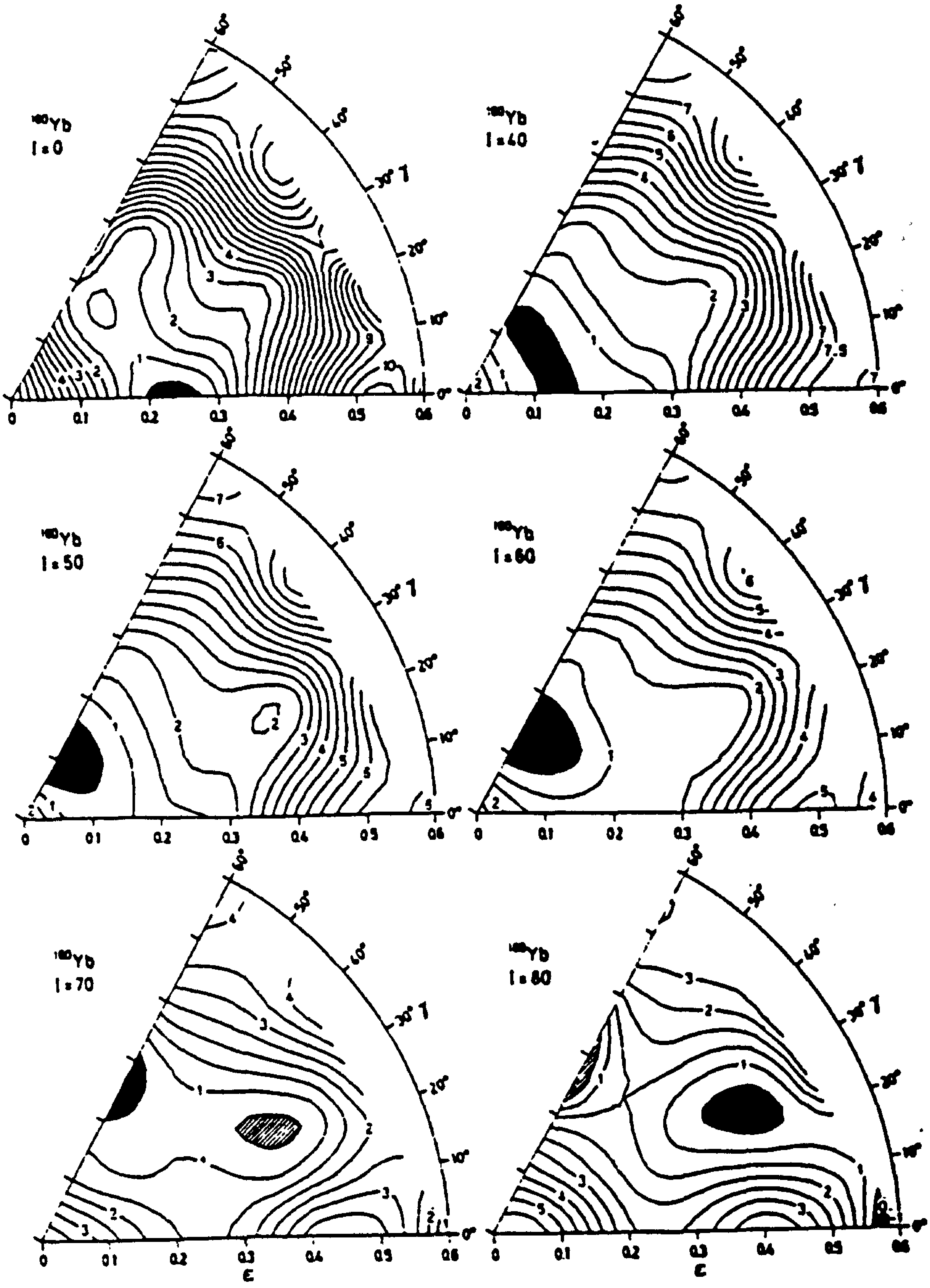

Figure 3.3: *Potential energy surfaces (without pairing) for ^{160}Yb showing how the potential energy minimum is calculated to vary in the ϵ_2,γ plane for I=0, 40, 50, 60, 70 and 80ħ. The figure is from [An 76].*

3.3.2 Total Routhian Surface (TRS) Calculations

Nazarewicz *et al.* [NWJ 89] (and references therein) have studied the behaviour of high deformation rotational bands within the frame work of a model which stresses the importance of both shape changes and pairing correlations.

The cranked Woods-Saxon-Bogolyubov-Strutinsky approach uses a Woods-Saxon single particle potential and a BCS pair field to 'parameterise' the nuclear mean field. The total Routhian of a nucleus as a function of deformation is expressed as,

$$E^{\omega}(Z,N,\hat{\beta}) = E^{\omega}_{macro}(Z,N,\hat{\beta}) + \delta E^{\omega}_{shell}(Z,N,\hat{\beta}) + \delta E^{\omega}_{pair}(Z,N,\hat{\beta}) \quad (3.26)$$

The quantal corrections to the total energy are given by $\delta E^{\omega}_{shell}$ (the single particle shell correction) and by δE^{ω}_{pair} (the pairing correction).

Due to the computational difficulties involved, calculations which treat both the deformation and pair correlations self-consistently are not possible. For this reason two variations of the model are employed. The first, referred to as DSPA (deformation–self-consistent, pairing–average), minimises the total Routhian equation 3.26 with respect to the shape parameters, while approximating the pair correlations by defining the pair gap to be a smooth function of the cranking frequency ω_c (such that the pair gap is reduced by 50% at $\hbar\omega_c=$ 0.7 MeV and 0.6 MeV for protons and neutrons respectively). The second variant, DAPS (deformation–average, pairing–self-consistent), combines the full particle number projection before variation method (keeps track of particle number and eliminates the sharp fluctuations in the pair gap associated with a purely BCS approach to pairing) plus the cranked Hartree-Fock-Bogolyubov (CHFB) equations [PP 80] with an average deformation determined by the DSPA calculations.

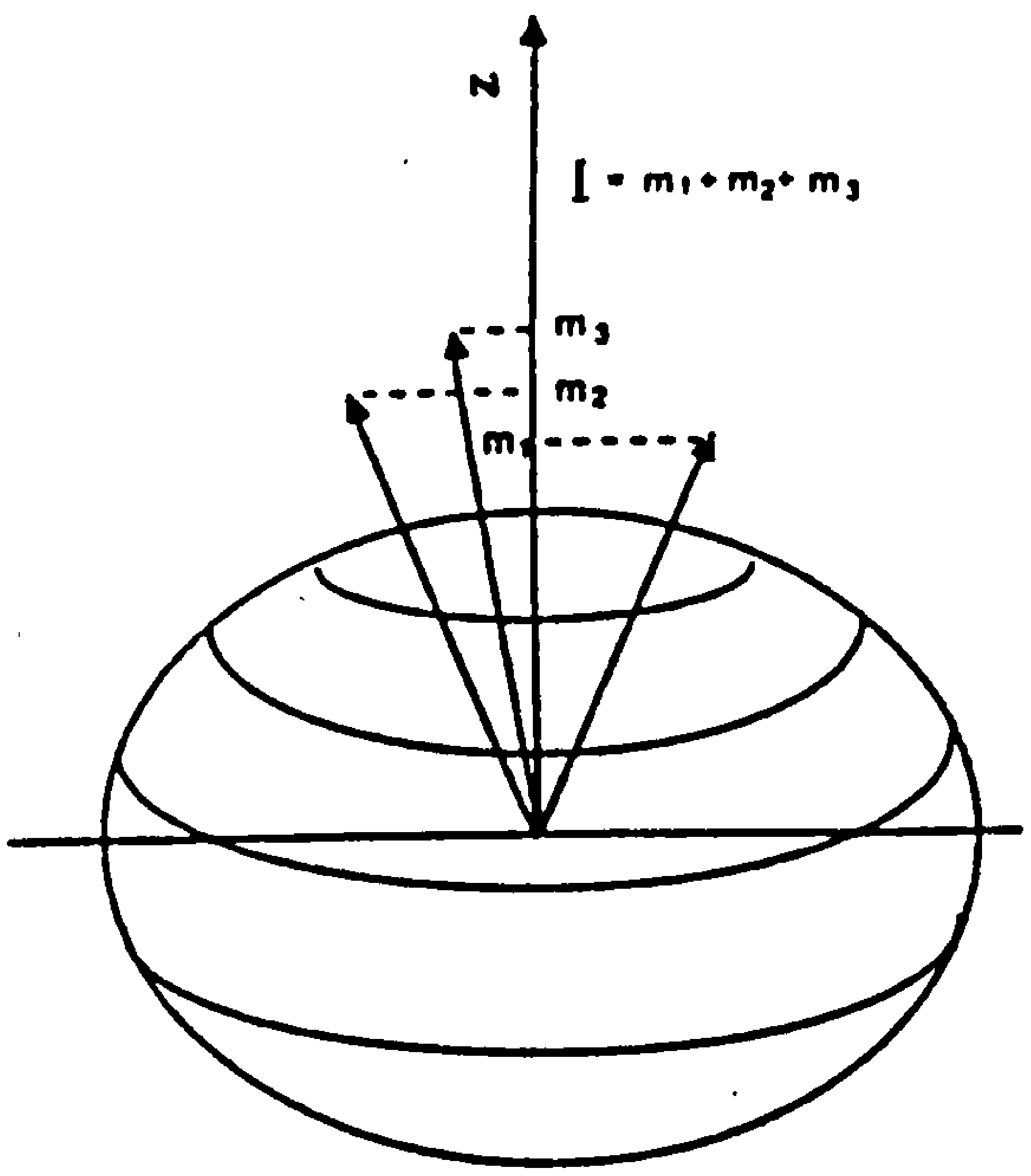

Figure 3.4: *The generation of angular momentum by the single particle excitations where the angular momentum is the sum of the projections on the symmetry axis.*

3.4 Non-Collective (Single Particle) Motion

Angular momentum can be generated by the sum of the contributions from the single particle orbits of the valence nucleons where the angular momenta are not coupled to I=0. The total angular momentum of the nucleus is then the sum of the projections of the intrinsic orbital angular momenta on the axis of symmetry (this is shown schematically in figure 3.4). This is often the method for generating angular momentum for the yrast sequences of spherical (or near closed-shell) nuclei. It can be seen from figure 3.4 that the orbitals which have the largest projection on the symmetry axis (high Ω) are generally lowest in energy for oblate deformations when near a closed shell. This type of generation of angular momentum is therefore most efficient for an oblate shape.

As there is no real contribution to the angular momentum from the core in this picture, this type of excitation is described as "single particle". As each single particle excitation has a very different intrinsic energy associated with it, the resulting decay scheme of a single particle nucleus shows a very irregular energy level pattern. This feature can be seen in the decay schemes of many nuclei such as in mass A=150 region. In this region, the nuclei near to the closed shell have only a few valence particles, they occupy equatorial orbits and are responsible for the generation of nuclear spin. The non-collective nature of these nuclei can be illustrated from a plot of excitation energy versus I(I+1). Such a plot for a single particle nucleus ^{147}Gd is shown in figure 3.5. A close examination of the figure shows that the individual levels do not follow the rotational formula as given by equation 3.35. However, over a fairly large spin interval it can be seen that the level energies do scatter around a linear dependence of excitation energy versus I(I+1). The rotational formula may then be used to define an effective moment of inertia, which is usually close to the moment of inertia of a rigid body with small oblate deformation. The slope of the yrast line is strongly dependent on the neutron number or the number of valence nucleons and gives a measure of the ability of the system to increase its angular momentum by configuration changes. The steep yrast line of a nucleus with few valence nucleons reflects the necessity for excitations across a large shell gap in order to generate high angular momentum states.

3.5 Calculation of the Spectra of the Non-collective Nuclei

Grover and Gilat [GG 67] were the first to construct the high angular momentum states by combining the shell model configuration with the orbitals aligned along the symmetry axis. Present calculations of the level spectra of non-collective nuclei follow two main methods.

- The deformed orbital phenomenological models using either the modified oscillator or Woods-Saxon potential together with the tilted Fermi surface method to define particle configurations to the levels.

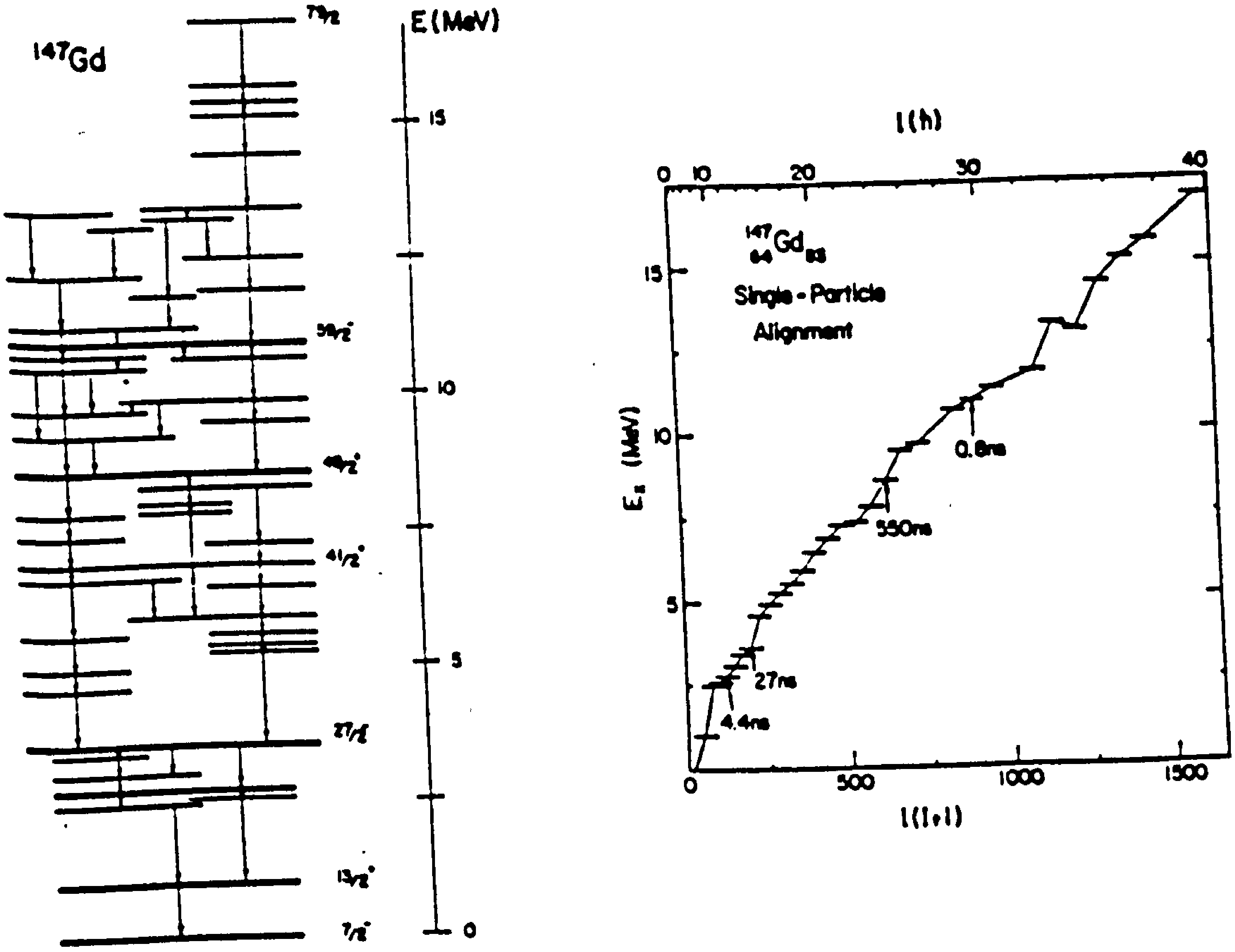

Figure 3.5: *(Left) The decay scheme of* ^{147}*Gd. (Right) Plot of* E_x *versus* $I(I+1)$ *for* ^{147}*Gd.*

- The spherical shell model and two body residual interactions in the calculation of the level sequence.

However, in the calculations of the level sequence of non-collective nuclei the approach of the two body residual interactions used in the shell model influences the orbitals in a similar manner to the deformation used in the phenomenological models.

3.5.1 Deformed Orbital Phenomenological Models

In the calculation of the yrast line of a single particle nucleus the rotational frequency ω may be introduce directly and the same formalism used as that which has been very successful in the description of the states of collective nuclei. Alternatively, ω may be introduced as a parameter in the minimisation of the total energy with constraints on the spin, I, and the number of nucleons, N. This procedure is known as the tilted Fermi surface method.

3.5.2 Cranking Model Approach

The spherical or weakly deformed nuclei at the beginning of the rare earth region, behave similar to the classical liquid drop and up to angular momentum I= 50 -70$\hbar$ they are oblate and rotate around the symmetry axis. To create a large amount of angular momentum the nucleons which lie outside the core must align their angular momentum along the rotational axis (z-axis). Classically speaking these particles have to run in the equatorial plane around the nucleus and produce an oblate density distribution [PP 80]. Since there are only a few particles involved, such a configuration is certainly non-collective and the solution of the cranking Hamiltonian

$$H^{\omega} = H' - \omega J_z \tag{3.27}$$

becomes particularly simple as the rotation is around the symmetry axis. In this case each single particle wave function is an eigenfunction of j_z with the eigen value Ω_i. The component of the total angular momentum in the direction of the symmetry axis is given by

$$< J_z > = \sum_{i=1}^{N} \Omega_i \tag{3.28}$$

To increase the angular momentum one has to change the occupation in the deformed well and to put particles from lower (for instance negative) ω-values into those with higher (positive) ω-values. This can be done by a cranking procedure around the symmetry axis. Since the operator j_z commutes with h (the single particle hamiltonian), we get the single particle energies in the "rotating frame"

$$e_i' = e_i - \omega\Omega_i \tag{3.29}$$

where e_i are the eigenvalues of h in the non rotating frame. These are straight lines as a function of ω, whose slope is given by

$$\frac{de_i'}{d\omega} = -\Omega_i \tag{3.30}$$

This can be seen in figure 3.6(a). The condition to minimize the energy in the rotating frame

$$E' = \sum_{i=1}^{N} (e_i - \omega\Omega_i) \tag{3.31}$$

guarantees that one always occupies the lowest levels e_i'. With increasing frequency ω we thus obtain a stepwise increasing of the angular momentum. This feature is shown in figure 3.6(b). The distance between two steps and the size of the steps is given by the distances of the levels e_i and the angular momentum value Ω_i. Therefore there is a statistical increase of the angular momentum with the frequency ω. The moment of inertia is then defined only on the average (dashed line in figure 3.6(b)).

3.5.3 Tilted Fermi Surface Method

Since the level spacing in the case of a rotation around the symmetry axis has a statistical character, one expects yrast traps, first predicted by Bohr

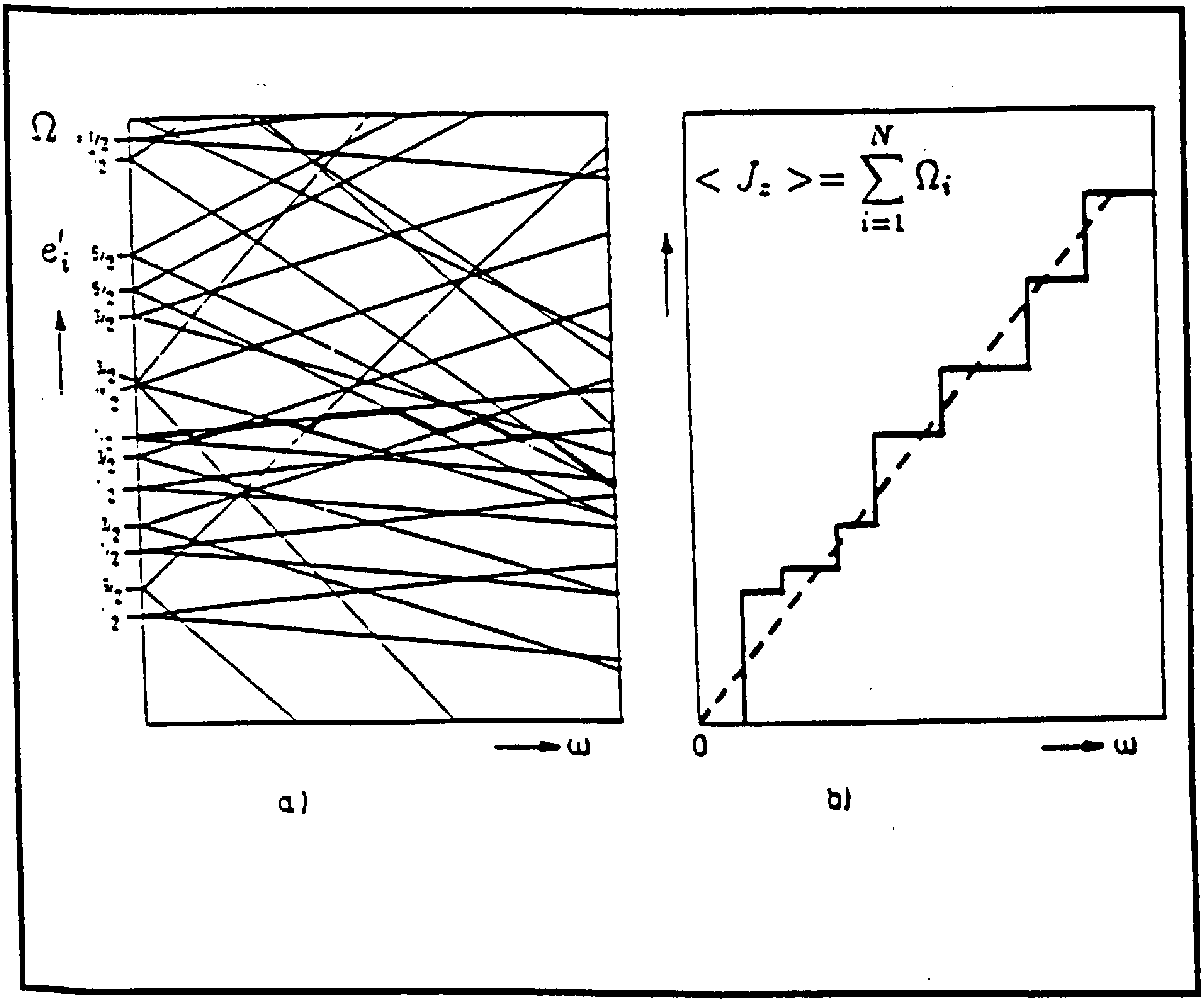

Figure 3.6: (a) A schematic representation of the eigenvalues e_i as a function of cranking frequency (b) The angular momentum $<J_z>$ obtained by increasing values of ω and by always occupying the lowest levels in (a). The figure is from [PP 80].

and Mottelson [BM 74]. Filling the levels in the rotating well always from the bottom, we obtain with increasing angular velocity, jumps in the angular momentum by several units. This can be visualised most easily in a representation of the eigen values e_i in the non-rotating oblate deformed single particle well as a function of the components Ω of the angular momentum along the symmetry axis. This method has been described in detail in chapter 7, while an illustrative example is shown in the next section.

3.5.4 An Illustrative Example

Many authors have performed the calculations to predict the values of spin and parity of the isomers in the oblately deformed nuclei. Among these, one successful attempt was made by Cerkaski *et al.*, [Ce 79]. In the calculation the single particle deformed shell model potential of equation 2.23 is solved by numerical diagonalisation. In order to improve the accuracy in this calculation some parameters used by Rost [Ro 67] were modified by fitting the ground and excited states of 230 odd-A nuclei. Figure 3.7 shows a plot of the single particle energy versus angular momentum component Ω for both protons and neutrons. The optimal spin and parities are $I_n = 0^+, 11^-, 20^+$ and $I_p = 0^+, 5^-, 6^-$ as indicated on the figure. The calculated yrast line is shown in figure 3.8 where the doubly optimal states are indicated by $I_n + I_p$. Several isomers are suggested at $I^\pi = 16^+, 21^-, 30^+$ and also at $I^\pi = 27^-$ which is thought to be a candidate for a structural trap as its structure differs greatly from the states $26^-, 25^-$. No residual interactions have been included in these calculations which makes them unreliable below $I \sim 15$. Experimentally, isomers have been identified at $I^\pi = 17^+, 21^-, 27^-, 30^+$ which means that apart from a possible spin discrepancy of ±1 there is a very good agreement between experiment and theory. The experimentally determined isomers are in fact not true energy traps as predicted in this calculation, so the theory fails in this respect to reproduce the experimental data. The inclusion of two body residual interactions may be expected to make most of the calculated

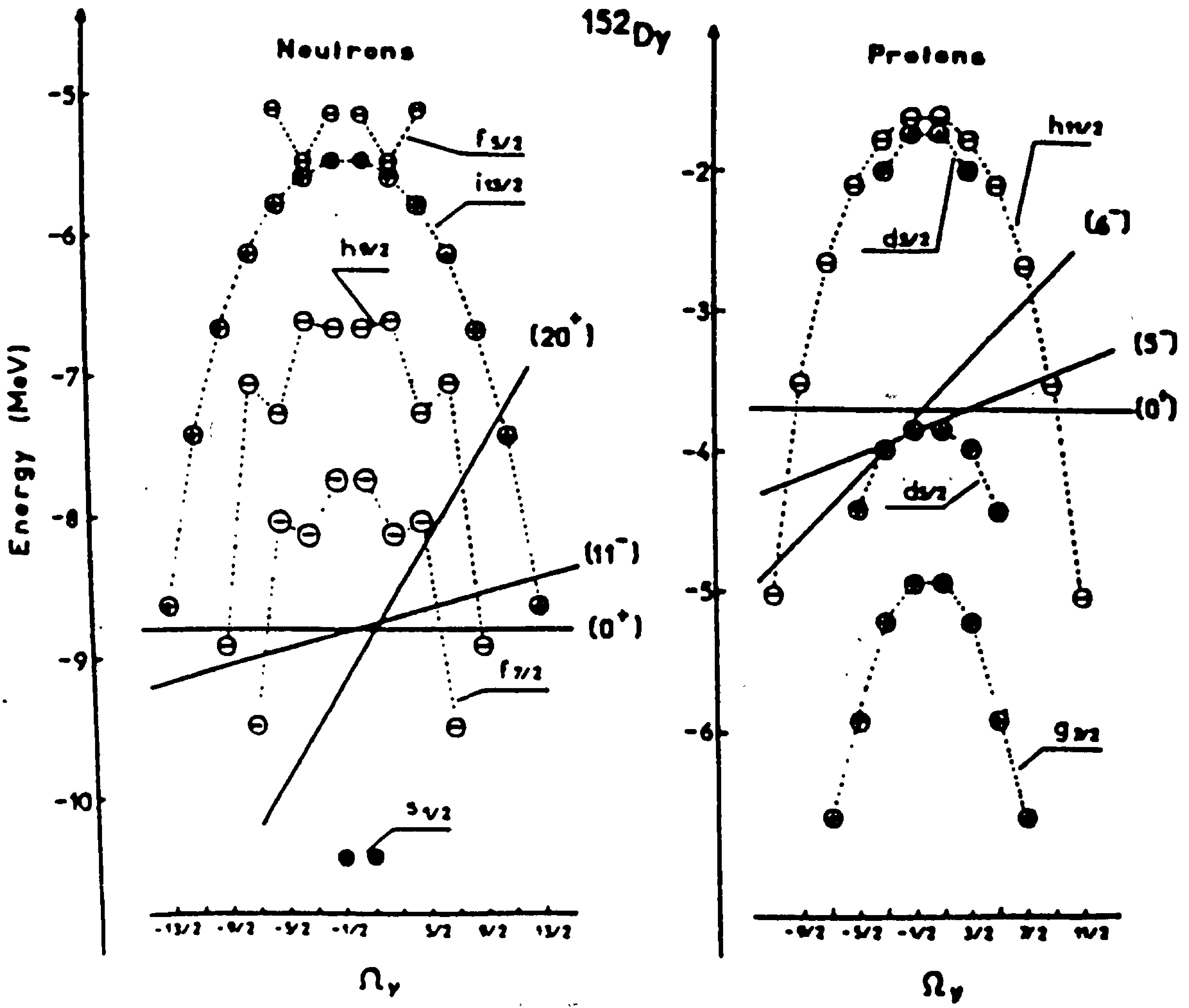

Figure 3.7: *Single Particle orbital energies versus angular momentum component plotted at deformation* $\beta_2 = -0.16$ *and* $\beta_4 = 0.03$ *for* $A=152$ *parameters. The figure is taken from [Ce 79].*

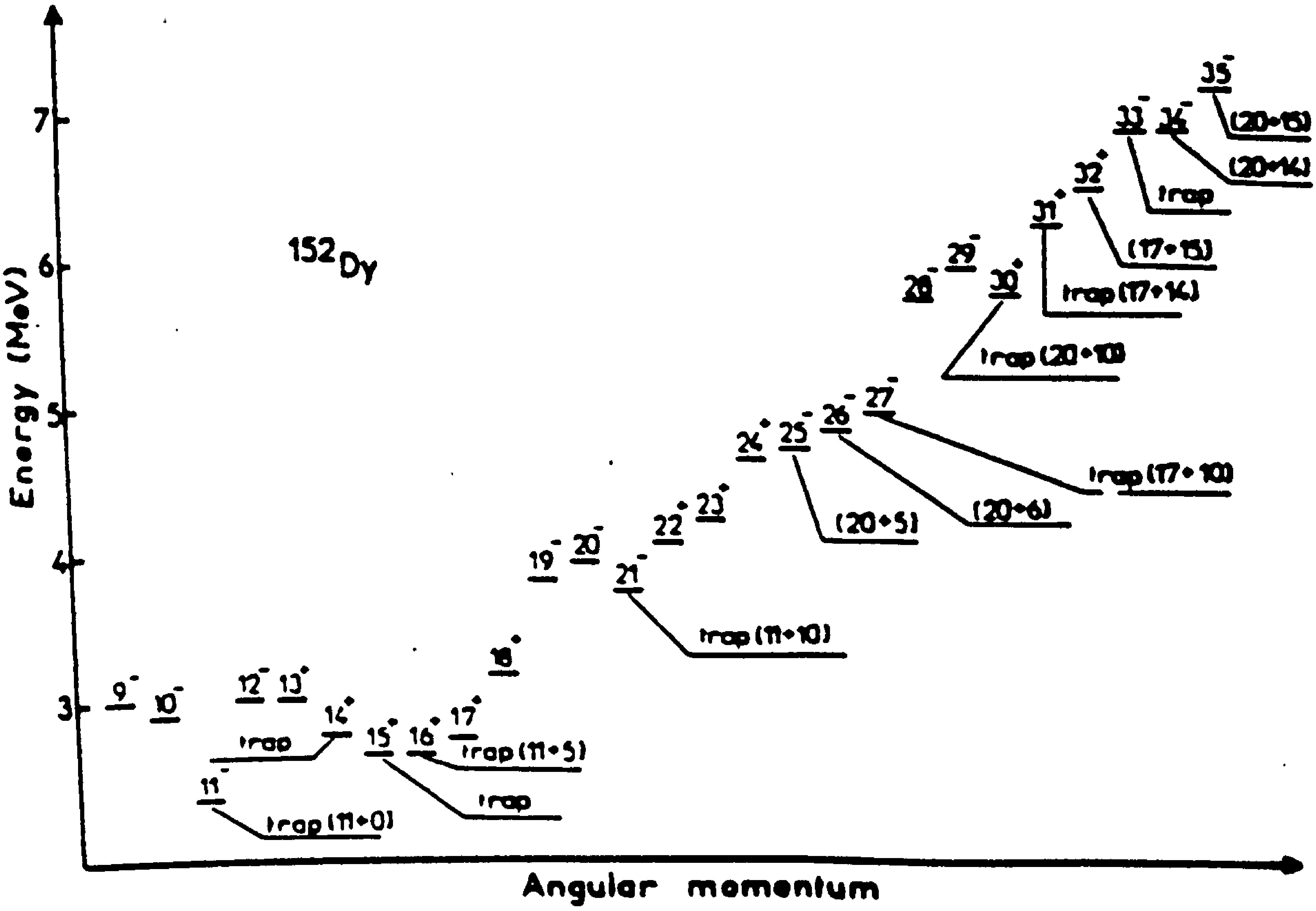

Figure 3.8: *Calculated yrast line for ^{152}Dy. Doubly optimal states are indicated by $I_n + I_p$.*

traps disappear from the yrast line but its irregular character may mean that isomeric states due to a hindrance in the rate of electromagnetic transitions will remain [AK 77]. The calculation of Cerkaski et al [Ce 79] also over estimates the effective moment of inertia by about 40% compared with the experimental value of $2\Im_{eff} = 145\hbar^2 MeV^{-1}$. This may possibly be due to omission of pairing correlations in the calculations, although such correlations are expected to be rather weak for I > 17. Many authors have also performed similar calculations to explain the yrast line of the nucleus ^{152}Dy. Comparison of the calculations with the experimental yrast line for the ^{152}Dy is shown in figure 3.9. These authors used in their calculations

- No pairing, Woods-Saxon levels not adjusted i.e., Cerkaski *et al.* [Ce 79]
- Nilsson levels adjusted, Pairing included i.e., Leander *et al.* [Le 79]
- Spherical shell model plus two body quadrupole forces, Faessler and Ploszajczak [FP 80]
- Woods-Saxon with the new set of levels i.e., Døssing *et al.* [Do 80].

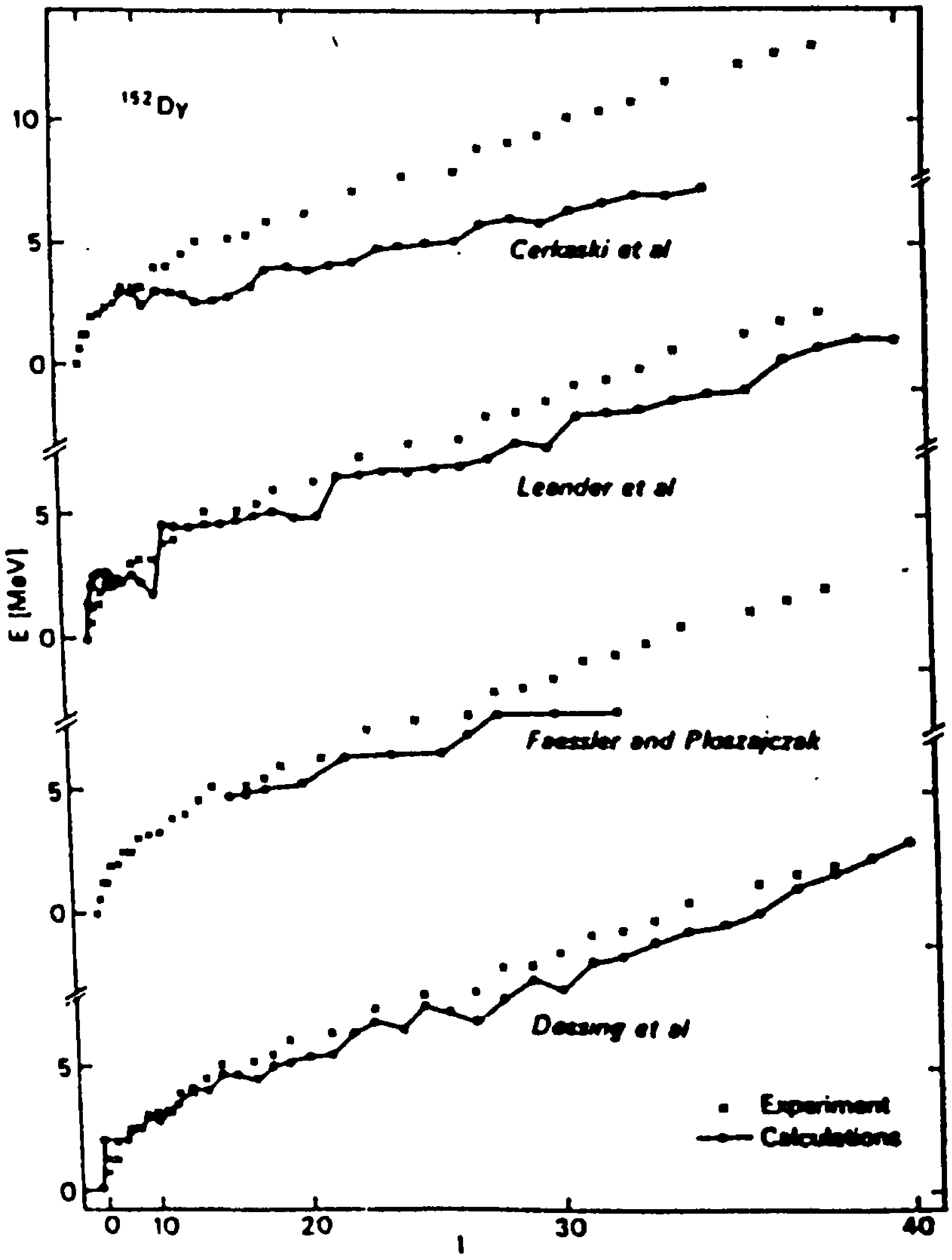

Figure 3.9: *Comparison of many calculations of the yrast line of* ^{152}Dy.

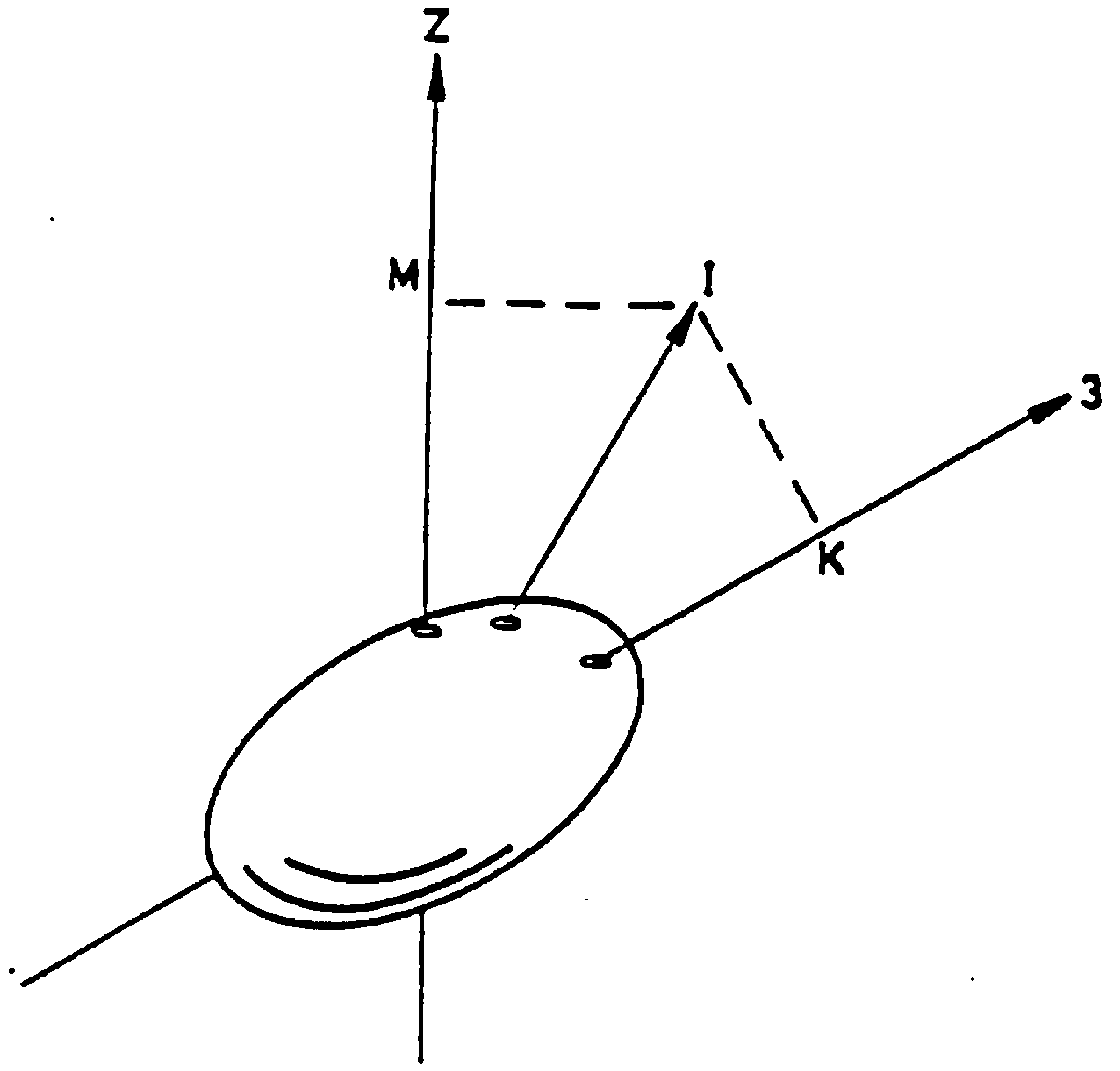

Figure 3.10: *The generation of angular momentum by collective rotation of the nucleus as a whole. The projections, M and K, of the total angular momentum, I, of a rotor onto the laboratory z-axis and the body-fixed 3-axis, respectively, are shown. The figure is taken from [PP 80].*

3.6 Collective Motion

Rather than the angular momentum being generated by the alingment of a few valence nucleons it is possible to create angular momentum from the rotation of the nucleus as a whole about an axis perpendicular to the symmetry axis. For axially symmetric shapes the collective motion of the nucleus may only be considered in the presence of a stable deformation, as rotations about the axis of symmetry for axially symmetric shapes are quantum mechanically indistinguishable from each other.

Figure 3.10 shows, the projections M and K of the total angular momentum "I" onto the laboratory z-axis and the body fixed three axis, respectively. The rotational energy operator is found to be given by [PP 80]

$$T_{rot} = \left(\frac{I_1^2}{2\Im_1} + \frac{I_2^2}{2\Im_2} + \frac{I_3^2}{2\Im_3}\right)\hbar^2 \tag{3.31}$$

where operators I_1, I_2, I_3 are the projections of the total angular momentum "I" onto the body fixed axes and $\Im_1$, $\Im_2$ and $\Im_3$ are the respective moments of inertia. For an axially symmetric case ($\Im_1 = \Im_2$ and $\Im_3$ vanishes) equation 3.32 becomes

$$T_{rot} = (\frac{I^2 - I_3^2}{2\Im})\hbar^2 \tag{3.33}$$

and the spectrum associated with an axially symmetric rotor follows

$$E_{rot} = \frac{I(I+1) - K^2}{2\Im}\hbar^2 \tag{3.34}$$

where I is the total angular momentum, and K is it's projection onto the body fixed three axis. For an even-even nucleus in its ground state rotating about an axis perpendicular to its symmetry axis, K = 0 and equation 3.34 becomes

$$E_{rot}(I) = \frac{\hbar^2 I(I+1)}{2\Im} \tag{3.35}$$

Rotating the system through an angle of π about the 1- or 2- axis leaves the system unchanged resulting in the states with odd values of I missing. The sequence for a pure rotating system with ground state of 0^+ will therefore, have a very regular energy level spacing and hence the resulting spins and parities of the states obeying the above relation are $I^\pi = 0^+, 2^+, 4^+, 6^+$, ...etc. An extremely regular sequence of de-exciting radiation would be expected with transition energies of

$$E_\gamma(I) = \frac{\hbar^2(4I-2)}{2\Im} \tag{3.36}$$

for the specific case of collective stretched quadrupole (Δ I=2, I→I-2) transitions. An example of such a band can be found in [Ny 86] where a low deformation prolate band has been observed in ^{152}Dy up to high spins.

Classically, the energy of a rotor is related to the rotational frequency, ω, by

$$E_{rot}(\omega) = \frac{1}{2}\Im\omega^2 \tag{3.37}$$

where $\Im$ is the moment of inertia of the rotor. Comparing equations 3.35 and 3.37 one get

$$\Im\omega = \hbar[I(I+1)]^{1/2} \tag{3.38}$$

For the specific collective stretched quadrupole transitions, (I+1 to I-1), the transition energy can be shown to be

$$\frac{E_\gamma}{2} = \hbar\omega \tag{3.39}$$

3.6.1 Moments of Inertia

It was suggested by Bohr and Mottelsson [BM 81] that a useful quantity in the study of rotating nuclei would be the moment of inertia, $\Im^{(1)}$ - a quantity measurable from rotational bands. Two quantities are defined (assuming a rotational band) as follows: - the kinematic moment of inertia given by

$$\Im^{(1)} = \left[\frac{1}{\hbar^2}\frac{dE(I)}{dI}\right]^{-1} = \frac{\hbar I}{\omega} \tag{3.40}$$

and the dynamic moment of inertia defined as

$$\Im^{(2)} = \left[\frac{1}{\hbar^2}\frac{d^2E(I)}{d(I)^2}\right]^{-1} = \hbar\frac{dI}{d\omega} \tag{3.41}$$

with the quantities linked by the differential relation

$$\Im^{(2)} = \Im^{(1)} + \omega\frac{d\Im^{(1)}}{d\omega} \tag{3.42}$$

The moments of inertia, $\Im^{(1)}$ and $\Im^{(2)}$, are generally used to describe deformed rotating systems as they are classically linked to the mass and shape of a rotating body. For a rotational sequence of energy levels, the energies of the states are given by equation 3.35 and the moments of inertia for such a band are defined as follows

$$\Im^{(1)} = (\frac{2I-1}{E_\gamma})\hbar^2 \tag{3.43}$$

$$\Im^{(2)} = (\frac{4}{\Delta E_\gamma})\hbar^2 \tag{3.44}$$

where ΔE_γ is the energy difference between adjacent gamma-rays. If the nucleus can be treated as a stiff rotating ellipsoid (or rigid rotor), then the moment of inertia is often estimated from the relation

$$\Im_{rig} = \frac{2}{5}AMR_0^2(1 + 0.31\beta_2) \tag{3.45}$$

For a rigid rotor, both the kinematic and dynamic moments of inertia should equal that of the rigid body value. The quadrupole deformation can therefore be estimated from the measured in-band moments of inertia assuming that the nucleus behaves as a perfect rotor. In practice, however, the moment of inertia can be greatly affected by the nucleonic motion. The dynamic moment of inertia at low spins has been observed in many nuclei to be as low as a third of the rigid body value. This has been attributed to the presence of pairing correlations at low spins, which cause a reduction in the energy of the lowest excited states.

3.7 Particle-plus-Rotor Model

In the previous sections it was shown how the nuclear angular momentum may be generated by both non-collective and collective rotations. These are, clearly, two limiting cases and it might be expected that many nuclei may support some components of both types of angular momentum. To illustrate this Bohr and Mottelson [BM 53] suggested a model where the rotating nucleus may be described as consisting of a few valence particles moving in the deformed potential due to a phenomenological core of particles coupled to a collective rotation of the core itself by the Coriolis force. Known as the Particle-plus-Rotor model (PRM) the total angular momentum of the nucleus, I, is given by

$$I = R + j \tag{3.46}$$

where R is the collective angular momentum and j is the sum of the single particle angular momenta of the valence particles. The PRM Hamiltonian is written as:

$$H_{PRM} = H_{coll} + H_{intr} \tag{3.47}$$

H_{int}, the intrinsic operator, contains a term describing the single particle energies in the deformed potential and a term to account for the interactions between valence particles. The collective part of equation 3.47 can be described in the body fixed coordinate system simply as

$$H_{coll} = (\frac{R_1^2}{2\Im_1} + \frac{R_2^2}{2\Im_2} + \frac{R_3^2}{2\Im_3})\hbar^2 \tag{3.48}$$

where R_i are the body-fixed components of the collective angular momentum of the core. Using equation 3.46 to eliminate R, from equation 3.48, H$_{coll}$ can be decomposed into three parts:

$$H_{coll} = H_{rot} + H_{rec} + H_{cor} \tag{3.49}$$

where

$$H_{rot} = (\frac{I_1^2}{2\Im_1} + \frac{I_2^2}{2\Im_2} + \frac{I_3^2}{2\Im_3})\hbar^2 \tag{3.50}$$

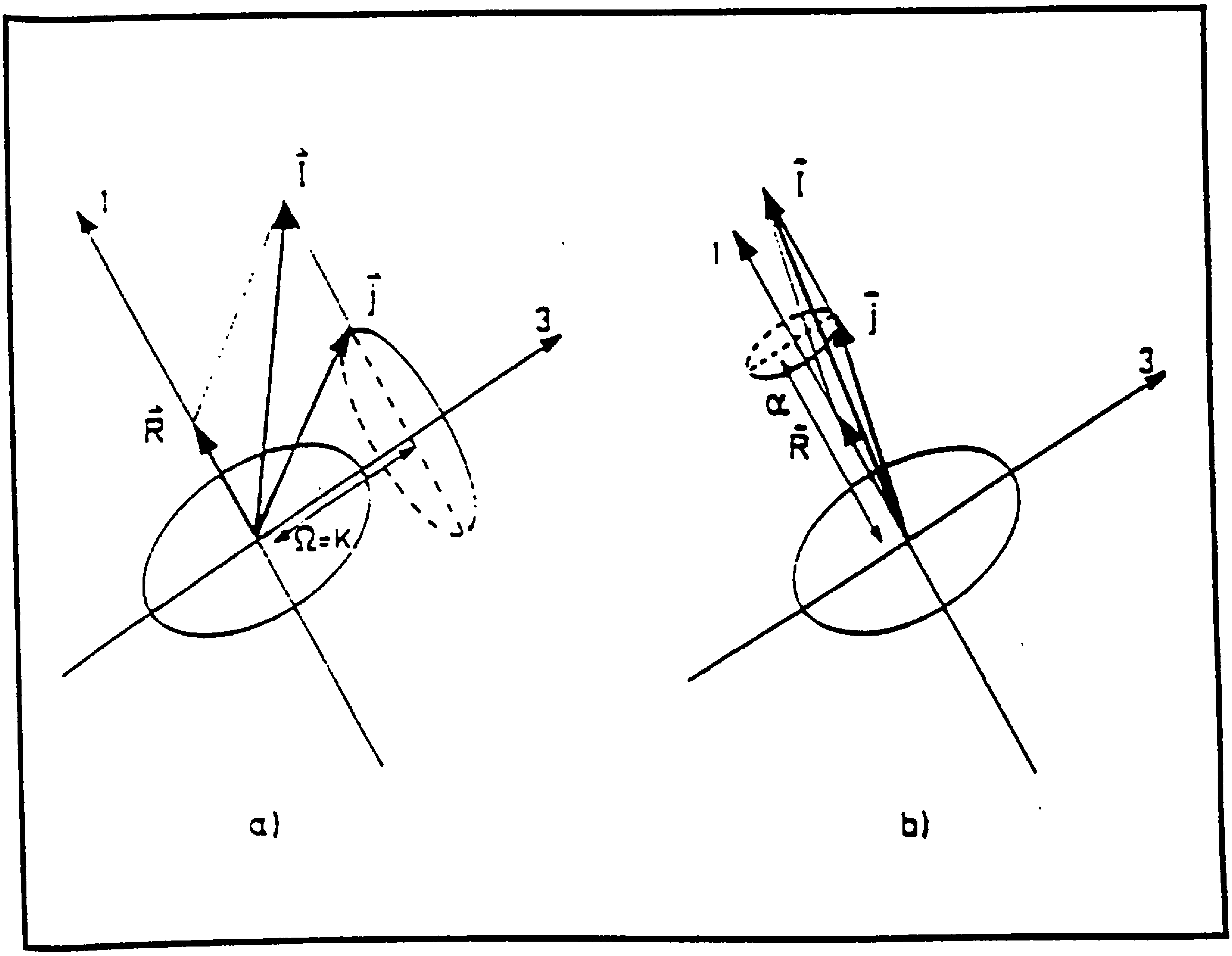

Figure 3.11: *A schematic plot to illustrate the two extreme angular momentum coupling schemes. (a) The intrinsic angular momentum 'j' is aligned along the symmetry axis. This represents the strong coupling or the deformation alignment (DAL). (b) The intrinsic angular momentum 'j' is aligned along the axis of rotation. This represents the Rotational alignment (RAL). The figure is from [PP 80].*

is the pure rotational operator of the rotor. Here, the operators I_1, I_2 and I_3 are the projections of I onto the body-fixed axes and $\Im_1$, $\Im_2$ and $\Im_3$ are the respective moments of inertia. The term

$$H_{rec} = (\sum_{i=0}^{3} \frac{j_i^2}{2\Im_1})\hbar^2 \tag{3.51}$$

is called the recoil term. It represents the recoil energy of the rotor. This term is usually neglected since it acts on the valence particles, the single particle energies being adjusted to fit the experimental data. Finally, the Coriolis interaction

$$H_{cor} = -(\sum_{i=1}^{3} \frac{I_i j_i}{\Im_i})\hbar^2 \tag{3.52}$$

couples the valence particles to the core. The PRM has is a powerful tool for explaining the experimental spectra of odd A nuclei, where the model couples only one valence particle to a collective core. However, the model has also been employed to good effect when considering multiple valence particles coupled to the core. In such cases, at low rotational frequencies, pairs of valence nucleons are constrained to occupy time-reversed orbits due to the pairing interaction, the Coriolis term being small compared to the intrinsic term for large deformations and for low values of I. In such cases the intrinsic angular momentum of the valence particles is strongly coupled to the motion of the collective core and corresponds to the deformation alignment (DAL) of the valence particles (figure 3.11 (a)). As the rotational frequency increases then it no longer remains possible to neglect the Coriolis term. In section 3.1 it was seen how the Coriolis force tends to break a pair of nucleons in time-reversed orbits and align their spins parallel to the rotational axis of the system (known as rotational alignment - RAL, see figure 3.11 (b)). The Coriolis force is general proportional to j and so the high-j intruder orbitals such as the $i_{13/2}$ neutron orbital in rare-earth nuclei, feel the strongest aligning force.

3.8 Superdeformation

The large gaps at closed shells of the energy level spectrum of the spherical nuclei are related to the magic numbers. These large gaps can also be seen in the single particle energy levels of the deformed harmonic oscillator where they correspond to the highly deformed (superdeformed) shapes having integer axis ratios, e.g., 2:1, 3:2 etc (figure 3.12). These gaps even exist (although with different magic numbers) when the more realistic Nilsson or deformed Woods-Saxon potential are employed. Modification of the overall liquid drop energy with such shell corrections demands the inclusion of an extra energy term to generate the appreciable minimum in the potential energy surface, which stabilises these highly deformed shapes. The highly deformed or superdeformed shapes are known from the observation of fission isomers in the mass A=240 region where they were first observed in ^{242}Am [Po 62] and were explained by a theory [St 68] indicating shell structure favourable for superdeformation. In the case of fission isomers the superdeformed shape is stabilised by the Coulomb force due to the larger proton separation in the elongated shape. In the case of lighter nuclei, as in the rare earth region the shell structure is expected to be washed out by the large fission barrier predicted [Ab 88] from the LDM. In this case the superdeformed shapes can be stabilised by the shell structure and an energy term due to the rotation of the nucleus. Figure 3.13 shows the tilting of the fission barrier towards higher deformations for a spin of I=40$\hbar$ compared with I=0$\hbar$ in ^{152}Dy and a second minimum appears for the high spin curve similar to that observed for ^{236}U (e.g. in the actinide region).

3.8.1 The A≈150 Superdeformed Region

From calculation performed for most nuclei, it was predicted [Ra 78, Ra 80, Be 81, DN 85] that nuclei in the mass A=150 region were good candidates for superdeformation. Figure 3.14 shows the shell correction energy plotted as a function of neutron number and deformation (the corresponding diagram

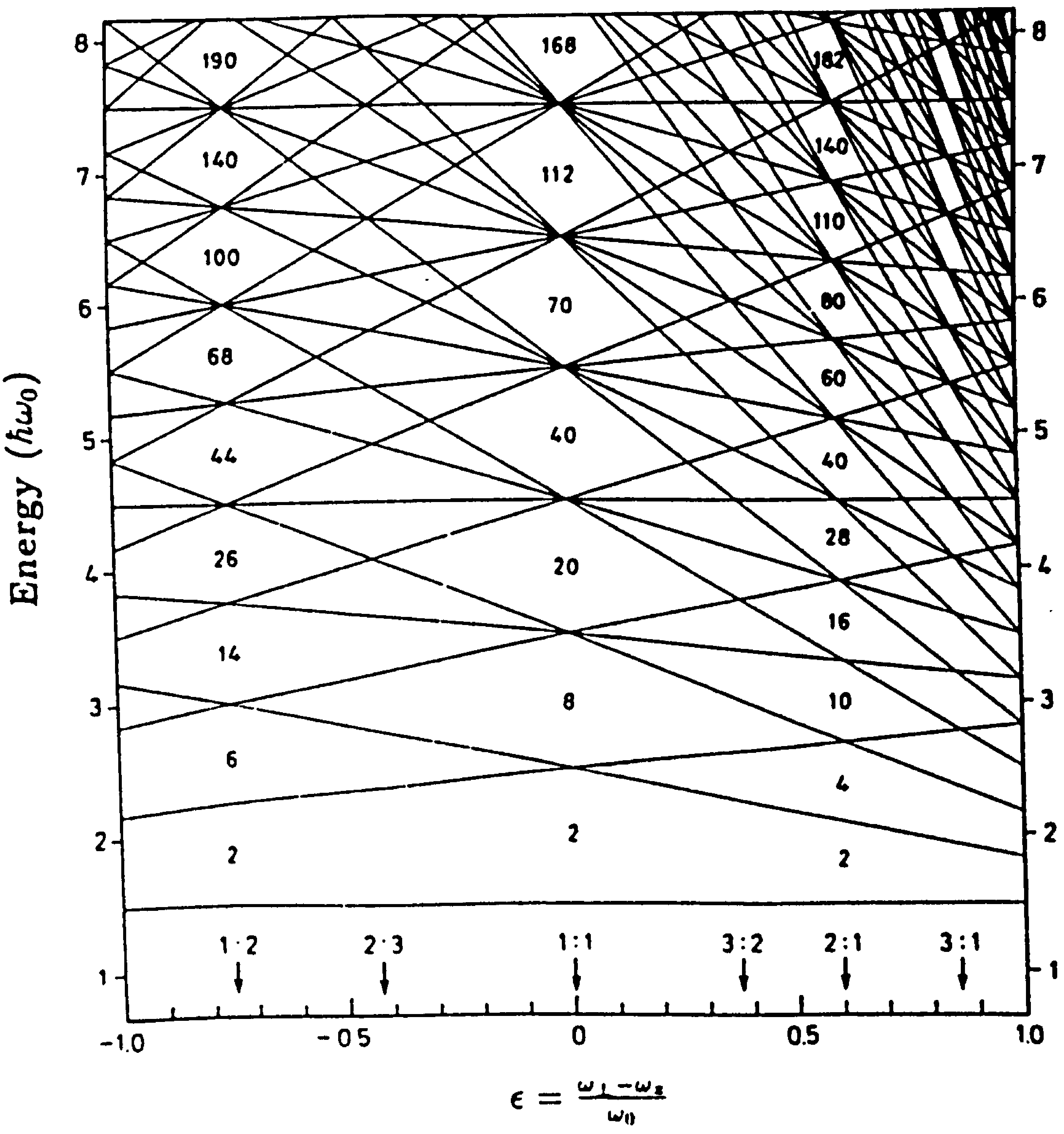

Figure 3.12: *Single particle spectrum as a function of quadrupole deformation for an axially symmetric harmonic oscillator potential illustrating the occurence of shell closures for integer ratios of axes, from [Sh 72].*

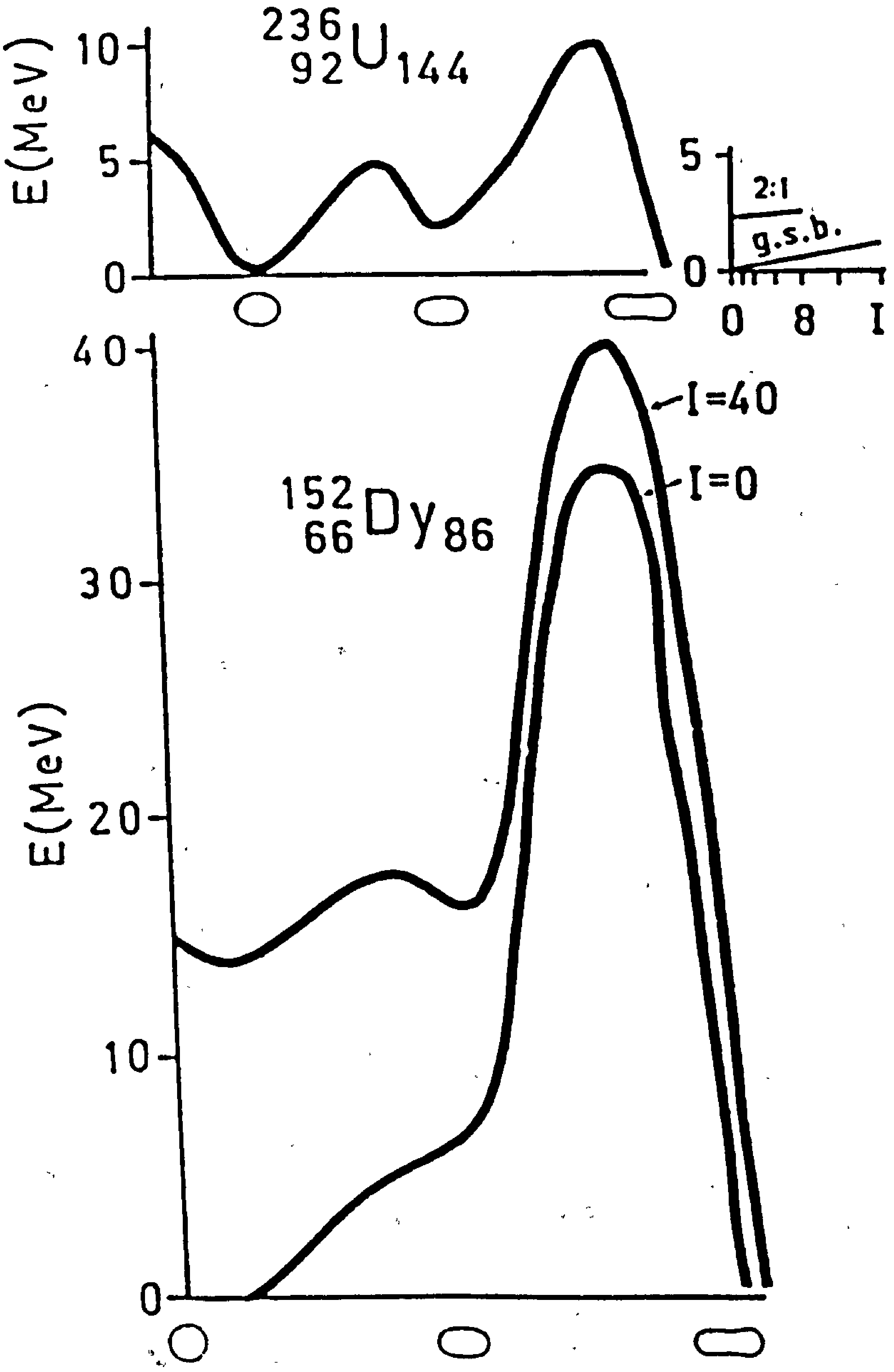

Figure 3.13: *Schematic fission barriers for ^{236}U and ^{152}Dy. When a rotation is imposed on ^{152}Dy (I=40 curve) a secondary minimum develops similar to the ^{236}U. The figure is from [Ab 88].*

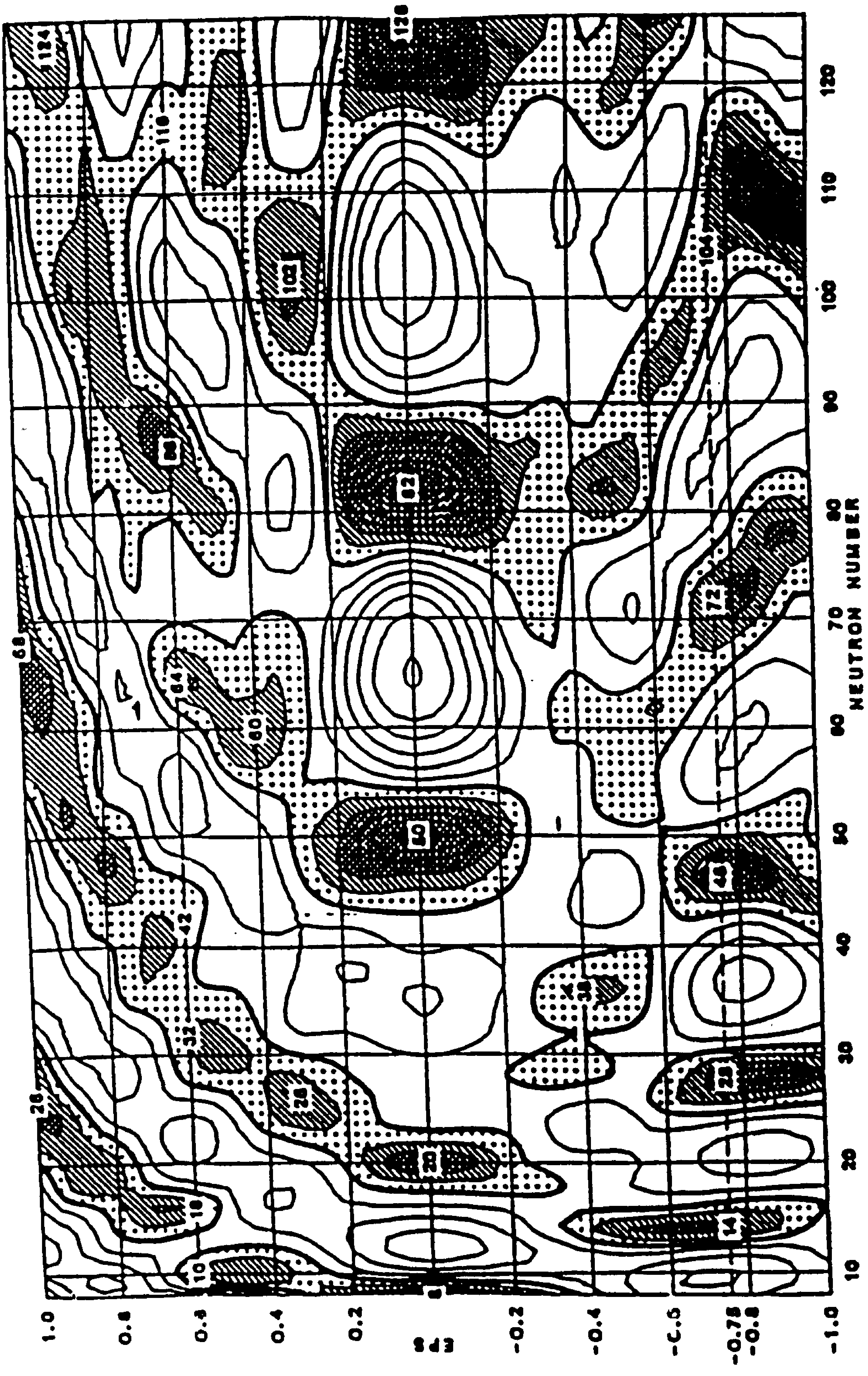

Figure 3.14: *The shell correction energy plottd as a function of deformation, ϵ_2, and neutron number, N. Shaded areas correspond to negative values of the shell energy. The figure is from [Ra 78].*

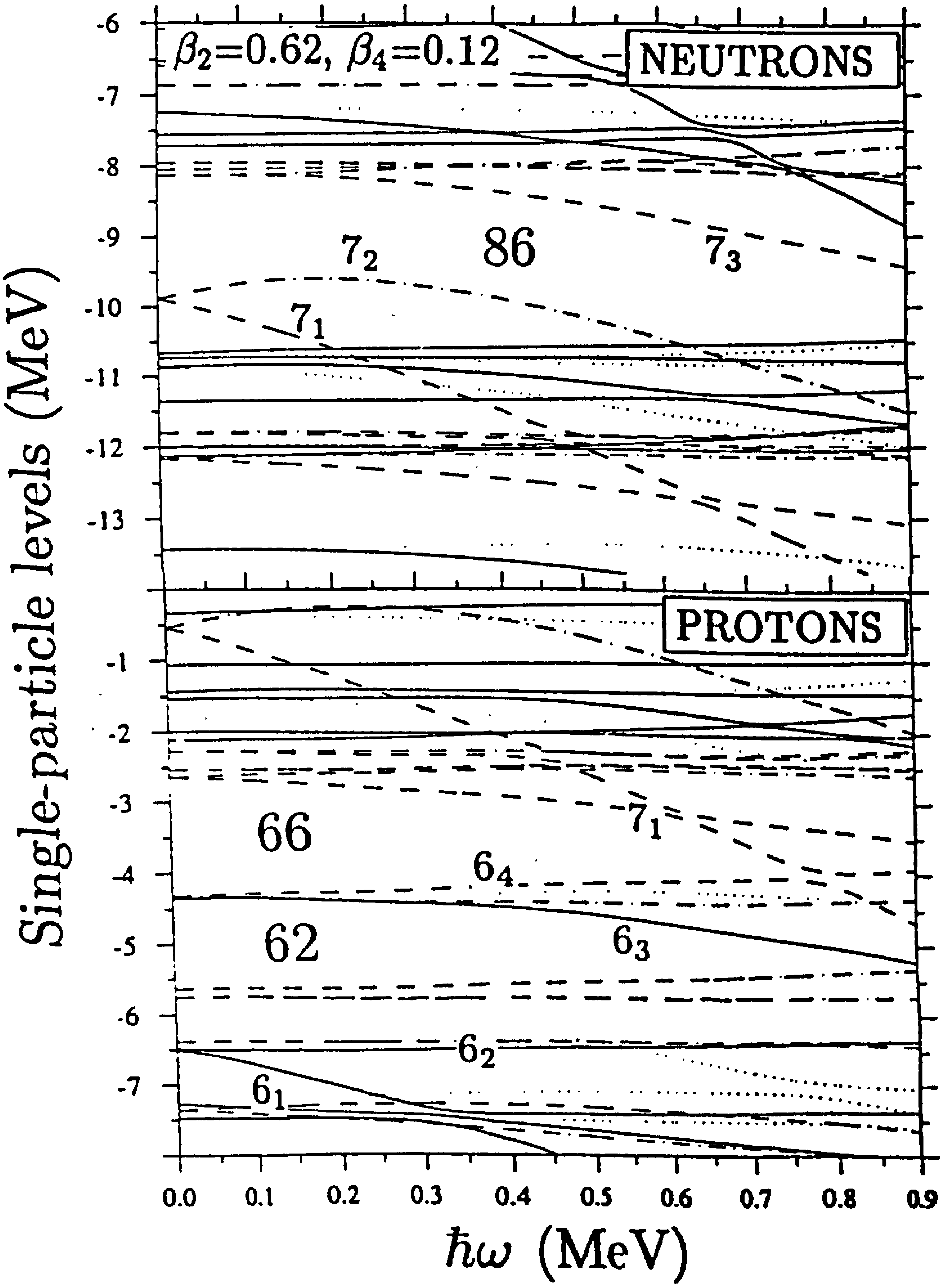

Figure 3.15: *Single particle Woods-Saxon Routhian diagrams for neutrons and protons as a function of $\hbar\omega$ in the superdeformed minimum for ^{152}Dy. The parity and signature are indicated by solid (π = +, α = 1/2), dotted (π = +, α = -1/2), dot-dashed (π = -, α = 1/2) and long dashed (π = -, α = -1/2) orbitals. The figure is from [NWJ 89].*

for protons is similar). For a value of the Nilsson quadrupole deformation parameter of ϵ_2=0.6 (axis ratio 2:1) minima are observed for close to both Z=66 and N=86. It is important that the modifying shell effects should survive and, therefore, influence the nuclear structure at high spin. This is indeed indicated from calculations [DN 85] using the deformed Woods-Saxon potential in CNS type calculations and is illustrated in figure 3.15.

The lowest lying high-N orbitals at zero deformation are above the Fermi surface but at the 2:1 axis ratio are moved down to within the vicinity of the Fermi surface to create the new shell closures. The large shell gaps occuring at the same deformation for Z=66 and N=86 lead to ^{152}Dy being considered to be a doubly magic nucleus. It can be seen from the figure 3.15 that there are four protons in the N=6 ($i_{13/2}$) and two neutrons in the N=7 ($j_{15/2}$) shells, the configurations being frequently written as $\pi 6^4 \nu 7^2$. The contribution to the dynamic moment of inertia for a particular orbital, ν, is given by the curvature of the orbital (derived from equation 3.41):

$$\Im_\nu^{(2)} = \hbar \frac{di_\nu}{d\omega} \tag{3.53}$$

Summing over all proton and neutron orbitals gives the total dynamic moment of inertia.

Chapter 4

The Compound Nucleus

4.1 Heavy Ion Compound Nucleus Reaction

Heavy ion fusion-evaporation reactions [MG 63], [SLD 65] are the most effective and commonly used mechanism to populate nuclear states with high angular momentum. The idea that a target and projectile fuse to form a compound nucleus and, at a given excitation energy and angular momentum, the subsequent decay of the system is independent of its formation was introduced by Niels Bohr [Bo 36]. Fusion evaporation reactions are generally used to populate the highest spins, $60\hbar$-$70\hbar$.

The necessary condition for fusion to occur is that the energy of an incident projectile must exceed the Coulomb barrier height, E_{cb}. An empirical estimate [Ho 78] gives:

$$E_{cb}(MeV) = \frac{Z_1 Z_2 e^2}{R} = \frac{1.44 Z_1 Z_2}{R_{cb}(fm)} \tag{4.1}$$

where

$$R_{cb} = 1.16(A_1^{1/3} + A_2^{1/3} + 2.07)(fm) \tag{4.2}$$

where Z_1, A_1, Z_2, A_2 are the atomic and mass numbers of the projectile and target nuclei respectively, and R_{cb} is a distance parameter related to the radii of the two nuclei. The maximum angular momentum brought into the compound system through heavy ion reactions can be classically estimated since the heavy ion wavelengths are smaller than the size of the nucleus. If the colliding nuclei are considered to be charged black spheres, the reaction cross section, σ_r, is given as:

$$\sigma_r = \pi(R_1 + R_2)^2(1 - E_{cb}/E_{cm}) = \pi\lambda^2 l_{max}(l_{max} + 1) \qquad (4.3)$$

where R_1 and R_2 are the target and projectile radii, E_{cb} is defined by equation 4.1 and E_{cm} is the centre of mass bombarding energy, λ is the de Broglie wavelength in the centre-of-mass system and l_{max} the classical angular momentum. The value of l_{max} is obtained from equation 4.3 as

$$l_{max} = 0.219 R_{cb}[\mu(E_{cm} - E_{cb})]^{1/2} \qquad (4.4)$$

where R_{cb} is given by equation 4.2, E_{cm} and E_{cb} are in MeV and μ, the reduced mass, is given as:

$$\mu = \frac{A_1 A_2}{A_1 + A_2} \qquad (4.5)$$

and E$_{cm}$ is given as:

$$E_{cm} = \frac{A_2}{A_1 + A_2} E_{lab} \qquad (4.6)$$

The maximum excitation energy of the system expressed in the center-of-mass is the sum of the initial energy of the system and the Q value of the reaction:

$$E_{EX}^{max} = E_{cm} + Q \qquad (4.7)$$

4.1.1 The Decay of the Compound Nucleus

The compound system is formed at high excitation energy and with a range of angular momenta up to the highest possible values. In this region the level density is extremely high and a statistical approach [BW 52, GG 67] is used to describe the decay of the compound nucleus. This assumption is further supported by the Bohr's original hypothesis (section 4.1) that the decay is independent of the formation process. The compound nucleus must find the most efficient way of losing energy (cooling). This it will do via the modes or channels of de-excitation open to it, namely fission, particle emission (neutrons, protons and α - particles) or γ-ray decay. The de-excitation of a compound nucleus is characterised by four stages:

(a) Particle evaporation, typically neutron evaporation

(b) Emission of statistical γ-rays

(c) Continuum γ-ray emission (usually E2 γ-rays)

(d) Discrete dipole and quadrupole γ-ray emission which arise for yrast or near yrast states.

Figure 4.1 illustrates the population of the residual nuclei formed by a typical heavy-ion reaction, the ^{124}Sn($^{40}Ar, xn$) $^{164-xn}$Er reaction while figure 4.2 illustrates the different phases of de-excitation of the compound nucleus.

In this example the compound system ^{164}Er is formed at an excitation energy of 53.8 MeV for a bombarding energy of 147 MeV. The first de-excitation of such a compound system is dominated by particle emission, since the intrinsic width of the particle decay is several orders of magnitude larger than that for electromagnetic decay (It may be noted here that for approximately one cascade in 10^3 a very high energy gamma ray is observed to compete with particle emission [Ne 81]. Such transitions are interpreted as the de-excitation of the giant resonances based on the highly excited states of the compound system or one of the daughter nuclei). For the rare earth region (A $\sim$ 170), the particle emission threshold (the sum of the binding energy and the particle kinetic energy) strongly favours neutron emission, since there is no Coulomb barrier to overcome in the case of neutrons. After the emission of the first neutron, the excitation energy of the system is reduced by the neutron binding energy and kinetic energy of the emitted neutron. The spread in the neutron kinetic energy gives a distribution to the excitation energy associated with ^{163}Er, the 1n reaction product. However, only one or two units of angular momentum is carried away by the emitted neutron. The angular momentum distribution of the 1n reaction product is therefore slightly reduced from that of the compound system, (figure 4.1). The angular momentum and excitation energy associated with 2n and 3n reaction channels are also shown in figure 4.1. After the emission of three neutrons, the population is sufficiently near to the

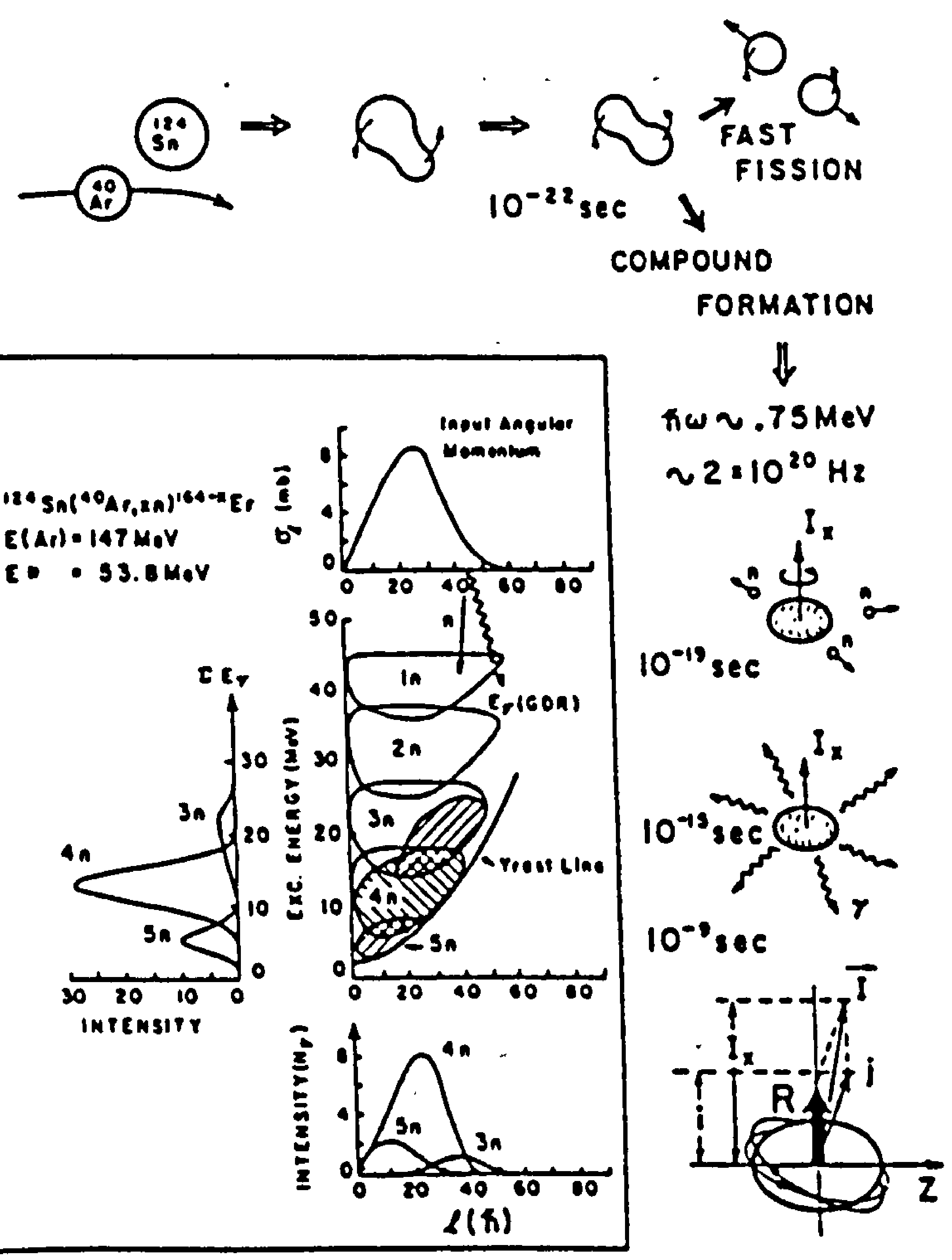

Figure 4.1: *Schematic figure depicting the excitation energy and angular momentum distribution for the formation and decay of the* ^{164}Er *system formed by the reaction of 147 MeV* ^{40}Ar *ions with* ^{124}Sn. *The formation and decay of the system are illustrated as a function of time. The initial population of the system formed at an excitation energy of 53.8 MeV is shown as a function of angular momentum at the top of the insert. Populations, calculated in the statistical model, are given as a function of excitation energy and angular momentum for the system after the emission of 1–5 neutrons. The shaded parts of the 3n–5n population cloud indicate the region of gamma-ray competition. The entry populations for the 3n–5n evaporation residues are shown as a function of angular momentum and excitation energy at the bottom and to the left. The figure is taken from [Be 84].*

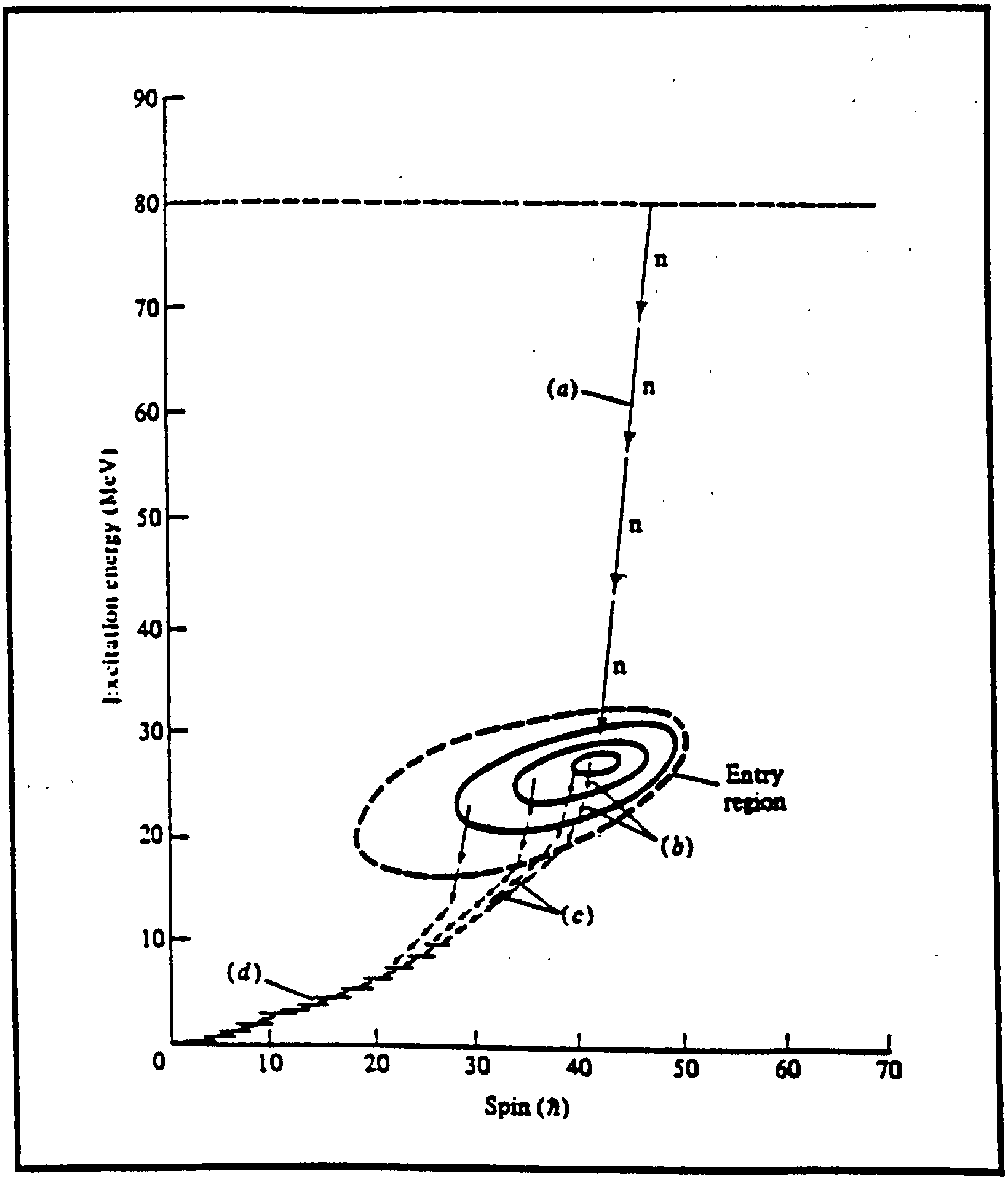

Figure 4.2: *Schematic figure illustrating the different stages of a decaying nucleus: (a) Particle emission; (b) Statistical γ-rays; (c) continuum γ-rays; (d) yrast (dipole and quadrupole transitions) γ-rays. The figure is taken from [No 86].*

yrast line[1] at large angular momenta that further particle emission is excluded. Large values of angular momentum, however, remain in the system until this stage. The remaining de-excitation is therefore via γ-ray cascades in the 3n channel, ^{161}Er. At lower angular momentum, the particle emission is again favoured, since the yrast line decreases with decreasing angular momentum. The emission of the fourth, or even fifth, neutron is therefore possible. The evaporation residues for such fusion-evaporation reactions are thus distributed over a number of nuclei. Larger angular momenta and higher excitation energies are associated with the residues having fewer emitted neutrons. Thus it is possible to select different products by selecting different angular momenta and excitation energies of the residual nuclei. Three types of γ-ray transitions can decay from the deformed residual nuclei:

- Statistical γ-rays which remove excitation energy but very little angular momentum.
- Stretched ($E2$, $\Delta I = 2$) collective cascades which remove most of the angular momentum but little excitation energy. The large number of these transitions from the many states with approximately constant moment of inertia produce a continuum 'bump' in the γ ray spectra. These γ-rays contain information about the particular nuclear structure, for example, the constant moment of inertia ([Si 77, De 78, Fo 81] and [Tr 79, Tr 82]) indicates they arise from fairly well defined rotational structures. In this way it is possible to infer whether these decays arise from collective or non-collective effects.
- As the evaporation residue cools the level density falls and less γ-rays are emitted. This corresponds to a change from a continuum to a discrete γ-ray regime. This γ-ray decay is illustrated in figure 4.2.

---

[1] A yrast state is the state with the highest angular momentum for a given energy. The locus of such states forms the yrast line.

4.2 Gamma Ray Directional Correlation Measurements.

Different γ-ray multipolarities correspond to different distributions of the emission probability in space. This can be employed to gain information about the multipolarity of the detected radiation. Consider a transition $I_i \rightarrow I_f$ (see figure 4.3 (a)), where I_i and I_f are the spins of the initial and final states having π_i and π_f as initial and final parities.

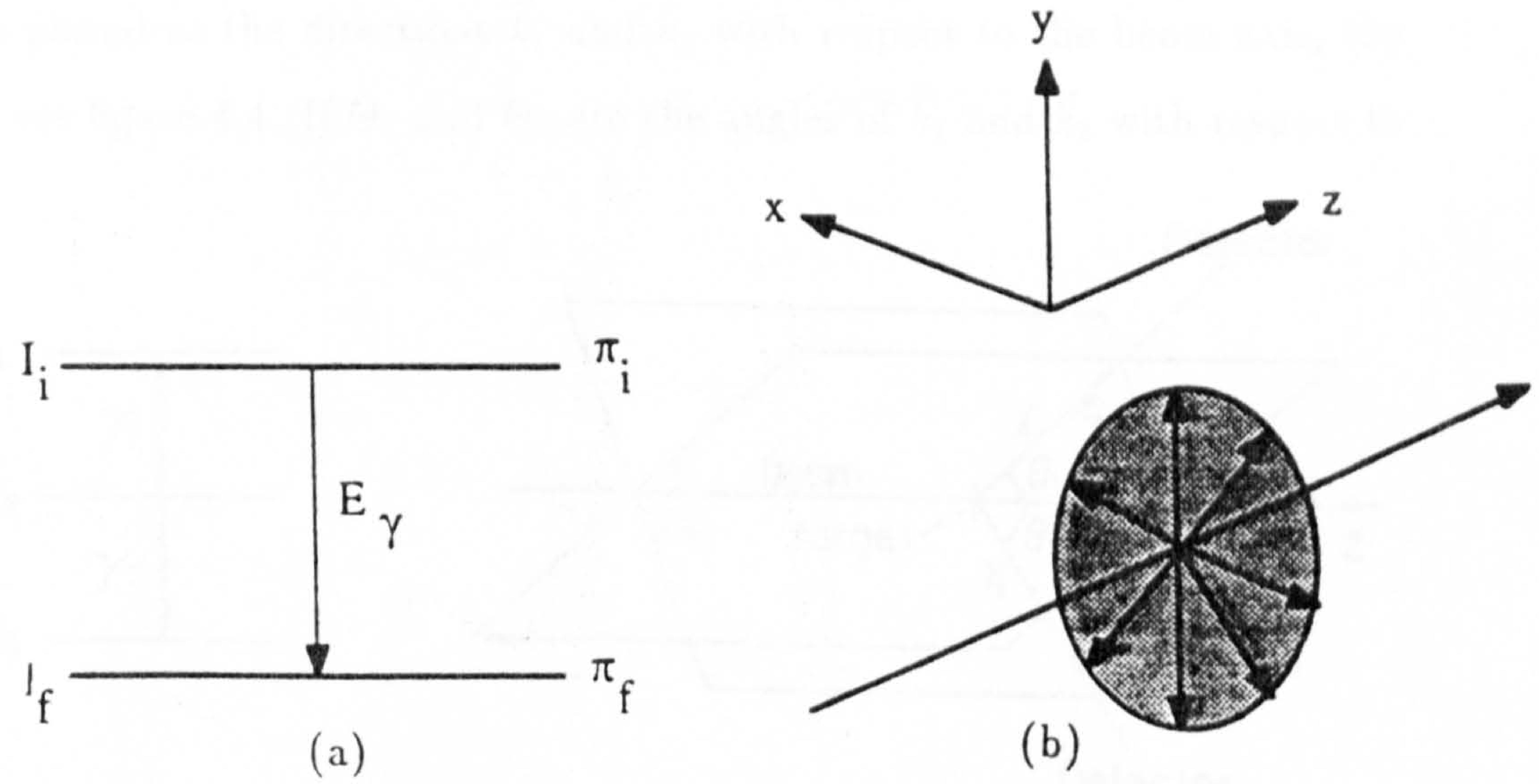

Figure 4.3: *(a) A gamma ray transition $I_i \rightarrow I_f$, where I_i and I_f are the spins of the initial and final spin states having π_i and π_f as initial and final parities, respectively and (b) The angular momentum ($\vec{I}$) is shown perpendicular to the beam axis (z-axis).*

The selection rules for γ-ray decay are then

$$|I_i - I_f| \leq \lambda \leq I_i + I_f \tag{4.8}$$

(where λ is the multipolarity of the transition)

and

$$\pi_i \pi_f = +1 \; for \; M1, E2, M3 \; etc \tag{4.9}$$

$$\pi_i \pi_f = -1 \; for \; E1, M2, E3 \; etc \tag{4.10}$$

with usually only the lowest multipoles having to be considered and with electric transitions dominating over magnetic transitions of the same multipolarity

(E1, M1, E2, M2, etc...) emitted from the same state. For an ensemble of nuclei with randomly oriented spin directions, the observed γ-ray intensity is isotropic (that is, the same in all directions). The spins of the compound nuclei populated in fusion-evaporation reactions are aligned. The spin directions are perpendicular to the beam axis thus displaying cylindrical symmetry along the beam direction (see figure 4.3 (b)).

Assume γ_1 and γ_2 are two successive γ-rays which are emitted during the de-excitation of the residual compound system and are detected by two detectors placed at the directions $\vec{k}_1$ and $\vec{k}_2$ with respect to the beam axis, the z-axis, see figure 4.4. If Θ_1 and Θ_2 are the angles of $\vec{k}_1$ and $\vec{k}_2$ with respect to

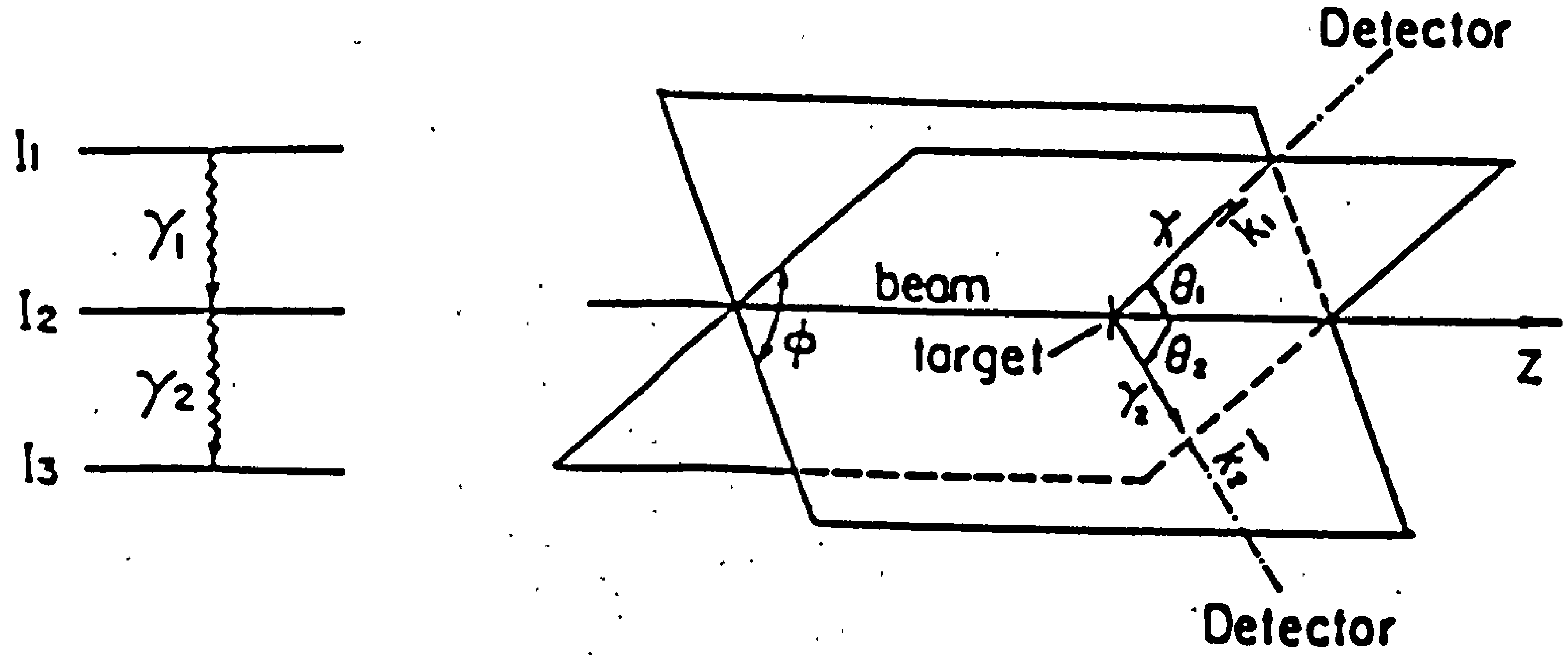

Figure 4.4: *Illustration of the geometry employed to define the relative probability* $W_{\Theta_{1,2}}(\Phi)$ *of* γ_2 *being emitted at an angle* Φ *with respect to* γ_1. *The beam axis is chosen as z axis.*

the beam axis, and Φ is the angle between the two planes defined by $\vec{k}_1, \vec{z}$ and $\vec{k}_2, \vec{z}$, respectively, the relative probability $W_{\Theta_{1,2}}(\Phi)$ of γ_2 emitted at an angle Φ with respect to γ_1 is given by [Kr 73]

$$W_{\Theta_{1,2}}(\Phi) = \sum_{\lambda_{1,2}\lambda} B_{\lambda_1}(I_1) A_{\lambda}^{\lambda_{1,2}}(\gamma_1) A_{\lambda_2}(\gamma_2) H_{\lambda_{1,2}\lambda}^{\Theta_1,\Theta_2}(\Phi) \qquad (4.11)$$

The parameters in this relation are well defined as explained in [Kr 73]. By comparing the angular correlation function $W_{\Theta_{1,2}}(\Phi)$ with the experimentally measured intensity $I_{\Theta_{1,2}}^{\gamma}$, information about the γ-ray multipolarity of γ_2 can be extracted from the data. The method is referred to as the DCO (Directional

Correlation of Oriented states) technique, since it detects the **Directional Correlations** of γ-rays of oriented states, see figure 4.5. Due to the particular nature of this work, mainly stretched quadrupole (Δ I=2) and stretched dipole (Δ I=1) γ-ray are of interest and the results are discussed in chapter 6.

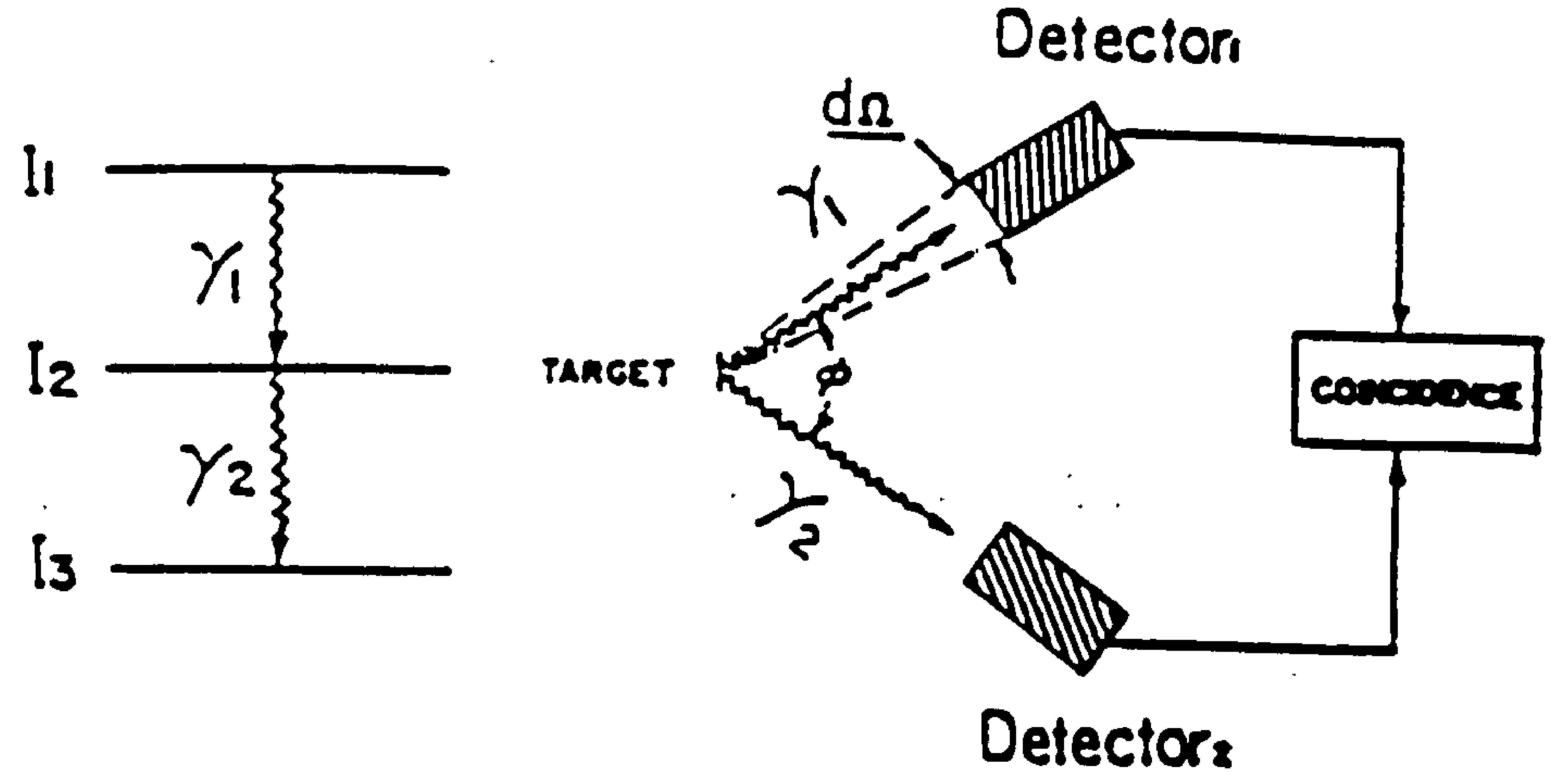

Figure 4.5: *The experimental set up for a DCO measurement.*

Chapter 5

Experimental Details and Analytical Techniques

5.1 Heavy Ion Beam and Target Considerations

In section 4.1 it was seen that for a fusion reaction to take place HI beams need to be accelerated to energies of the order of the Coulomb barrier and above. The heavy ion beams for the experiments performed in this work were provided by the Nuclear Structure Facility (NSF) at Daresbury (see figure 5.1) using a tandem Van de Graaff accelerator capable of reaching a terminal voltage of 20 MV. The negative ions (usually produced with a cesium sputter source) are attracted towards the positively charged centre terminal, at which point electrons are stripped from the atom resulting in a net positive charge. The beam is repelled away from the terminal and accelerated to high energy. It is then diverted to the relevant beam line via an analysing magnet and focused onto the target with a series of quadrupole magnets.

The targets are chosen to satisfy certain requirements which usually involve some compromise between the obvious necessity for high statistics and good resolution. In high spin gamma-ray spectroscopy two types of targets are used.

Figure 5.1: *The Nuclear Structure Facility (NSF) at Daresbury Laboratory. The 70 m high tower contains a vertical 20 MV tandem accelerator. Ion sources and injector equipment are housed at the top of the tower. The heavy ion beams of the accelerator are employed in the experimental areas inside the hall at the bottom of the building.*

- Thick targets
- Thin targets

Thick targets, although they increase the event rate (number of interactions between the beam and the target particles), degrade the recoil (and beam) energy by scattering events, within the target. In addition, Doppler broadening in the γ-ray energies may result as a consequence of the variation in the recoil velocity as the compound nuclei slow down within the target material. However, thick targets are important for lifetime measurements using the Doppler Shift Attenuation Methods [NS 79], where the recoil nucleus stops in the backing material (usually gold).

To overcome the problem a compromise is made. Several thin targets with a thickness of around 400 μgcm^{-2} stacked together and separated with a sufficient gap between them, ensure that most of the compound nuclei will decay whilst recoiling in vacuum, with the full recoil velocity. This results in a small variation in the velocity of the recoils and therefore, all γ-rays exhibit approximately the same Doppler energy shifts.

5.2 The Experimental Detection of γ-rays

A large number of discrete γ-rays within the energy range of a few tens of keV to just above 2 MeV are contained in the near yrast de-excitation of a residual nucleus formed by the fusion evaporation reaction. To resolve these γ-rays, it is necessary to employ high energy resolution γ-ray detectors. Two types of detectors are usually employed in γ-ray measurements: the semiconductor and the scintillation detector.

Semiconductor detectors have good energy resolution, but low γ-ray detection efficiency, conversely the scintillation detectors have high detection efficiency but poor energy resolution. In high spin spectroscopy, semiconductor detectors are preferred in order to resolve the large number of γ-rays emitted from experiments.

Coincidence analysis techniques are essential in establishing decay schemes, since these decay schemes usually consist of several decay sequences and each sequence can contain several tens of transitions. To obtain coincidence data, at least two detectors are needed to make possible the recording of two events in coincidence. A multi-detector array will enhance the probability of detecting the higher fold event thus enhancing the number of measured coincidence pairs in the same amount of time. The number of pairs of coincident γ-rays recorded is proportional to the number of detector, N

$$Number\ of\ coincident\ pairs = \frac{N(N-1)}{2!} \tag{5.1}$$

A multi-detector array with large number of detectors can therefore considerably reduce the running time of the experiment. Likewise, high-fold coincidences can resolve accidental degeneracies in the γ-ray energy in a decay sequence.

In many cases the selection of a reaction channel is important for high spin studies in which a large numbers of γ-rays are produced and which are associated with several different evaporation residues. The existence of multiple reaction channels complicates the energy spectra with a large number of undesired lines, many of which may have energies overlapping those of the transitions in the channel of interest. The elimination of such contaminants is especially important for resolving weak transitions. One commonly used instrument for channel selection in high spin spectroscopy is an array of a large number of lower resolution but high efficiency detectors subtending a solid angle approaching 4π. This device measures the total cascade energy and γ-ray multiplicity of an event. By setting restrictions on these two quantities, it is possible to select the events having the total cascade energy and multiplicity (the number of γ-rays emitted by the cascade) of the reaction channel of interest.

5.3 γ-ray Interaction Mechanism

Three kinds of interactions between γ-rays and matter are the basis for the detection of γ-rays.

- Photo-electric absorption
- Compton scattering
- Pair production

These three mechanisms are discussed below:

Photo-electric Absorption

In the photo-electric absorption process, the incident γ-ray undergoes an interaction with an absorber atom in which the photon completely disappears. In its place, an energetic photo-electron is ejected by the atom from one of its bound shells. The interaction is with the atom as a whole and cannot take place with free electrons. For gamma rays of sufficient energy, the K shell of the atom is the most probable origin of the photo-electron. The photo-electron appears with an energy given by

$$E_{e^-} = h\nu - E_b \tag{5.2}$$

where E_b represents the binding energy of the photo-electron in its original shell. For γ-ray energies of more than a few hundred keV, the photo-electron carries off the majority of the original photon energy. In addition to the photo-electron, the interaction also creates an ionized absorber atom with a vacancy in one of its bound shells. Such an electron vacancy in the inner shell of an atom results in the emission of characteristic X-rays or Auger electron. The X-rays are generally absorbed in a secondary photo-electric event and the total γ-ray energy is absorbed within the detector. As a result a photo-electric event produces a number of electron-hole pairs corresponding to the total γ-ray energy.

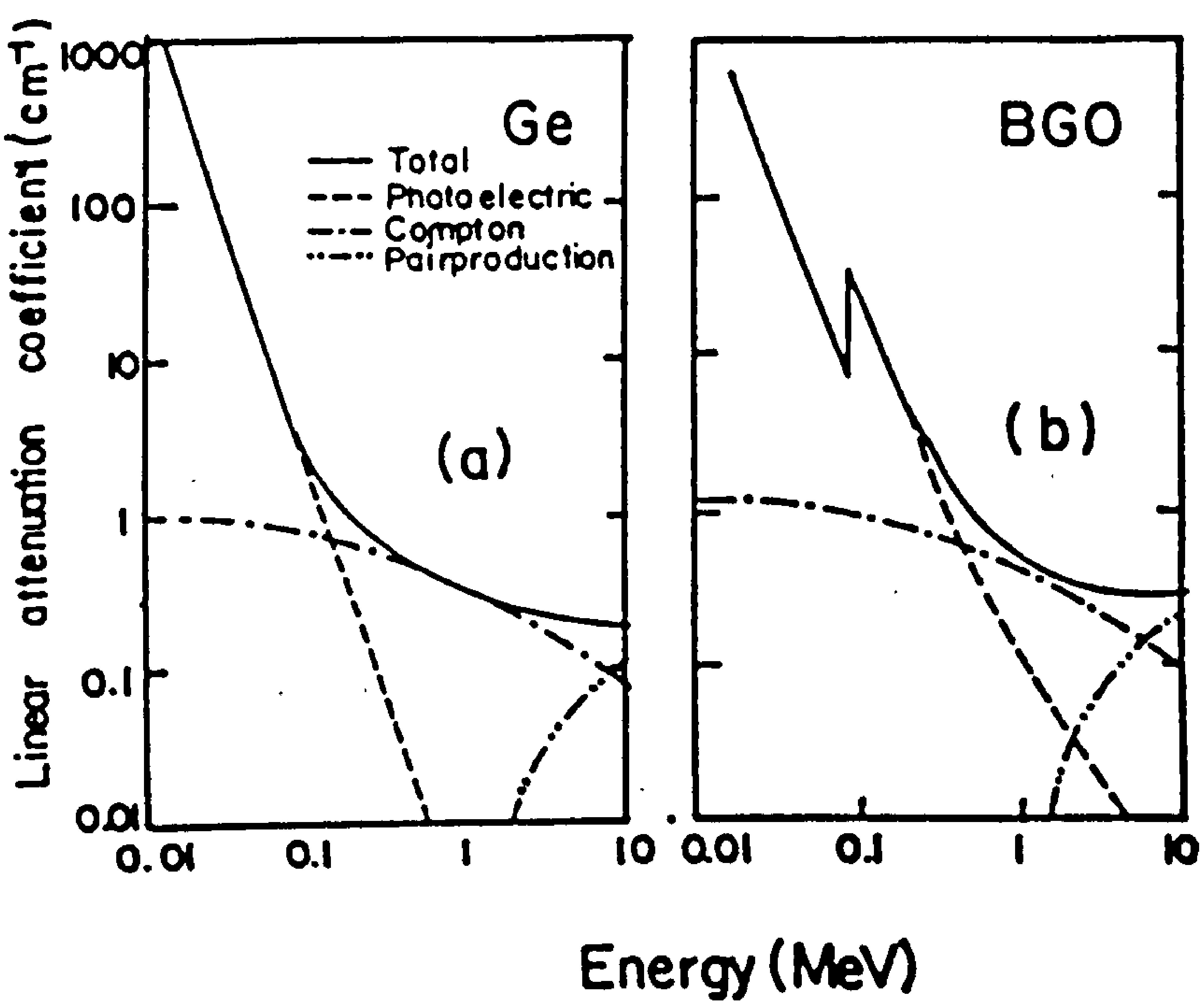

Figure 5.2: *Linear attenuation co-efficients as a function of γ-ray energy for (a) Germanium (b) BGO. The figure is taken from [SS 88].*

Compton Scattering

In a Compton scattering process the incoming γ-ray is scattered by the electrons of the atoms and lose only part of its energy. The energy of the photon (E'_γ) scattered through an angle θ is given as:

$$E'_\gamma = \frac{E_\gamma}{1 + \frac{E_\gamma}{m_oc^2}(1 - \cos\theta)} \tag{5.3}$$

where E_γ is the incident γ-ray energy measured in units of MeV and m_oc^2 is the electron rest mass energy (0.511 MeV). The kinetic energy of the recoil electron is therefore given as:

$$E_{e^-} = E_\gamma - E'_\gamma = E_\gamma(\frac{(E_\gamma/m_oc^2)(1 - \cos\theta)}{(1 + h\nu/m_oc^2)(1 - \cos\theta)} \tag{5.4}$$

Two extreme cases can be identified:

- When $\theta = 0$. In this case from equations 5.3 and 5.4 it can be predicted that $E_{e^-} \approx 0$. So the recoil electron has a very small energy and $E_\gamma \approx E'_\gamma$.

- When $\theta = \pi$. In this case the energy of the γ-ray is scattered back in its direction of origin and the electron recoils along the direction of incidence such that it has a maximum energy which can be transferred to it during any Compton interaction.

Pair Production

If the incident photon has an energy larger than $2m_oc^2 = 1.02$ MeV, pair production is possible. In this process, a positron electron pair is created. The energy above $2m_oc^2$ is transferred into kinetic energy of the positrons and electrons. The positron can then annihilate with an electron by the emission of two photons moving in opposite direction with equal energies of 0.511 MeV. If one or both of these photons escape from the detector without further interactions, energy peaks at E_γ-0.511 and E_γ-1.022 MeV respectively will be produced. Such energy peaks are called single or double escape peaks.

Attenuation Co-efficients

The intensity I_0 of a monoenergetic beam of γ-rays entering a detector of thickness d is reduced to the transmitted intensity I due to the interactions between photons and matter. The relation between I and I_0 is given by:

$$I(E) = I_0(E)e^{-\mu(E)d} \tag{5.5}$$

where the total linear attenuation coefficient $\mu(E)$ is the sum of the three interaction cross sections. Figure 5.2 shows the linear attenuation coefficients for the above three types of processes in germanium and BGO crystals as a function of incident γ-ray energy.

5.4 Germanium Detectors

In modern γ-ray spectroscopy the semi-conductor radiation detectors are widely used due to their advantages over the scintillation detectors. Two types of semi-conducting materials are generally used, namely silicon and germanium. Germanium is preferred over silicon in γ-ray spectroscopy due to its higher Z (photo-electric effect being $\propto Z^5$). A γ-ray entering the crystal may produce electron-hole pairs during the absorption process described in section 5.3. For germanium the average energy, ϵ, required to produce such a pair is small and constant at low temperature (for germanium, $\epsilon \sim 3$eV at T$\approx$ 77K, i.e., liquid nitrogen temperature). When an electric bias is applied to a germanium crystal electron-hole pairs will be collected. This collection produces an electronic current pulse, which is proportional to the number of pairs and consequently to the incident γ-ray energy. In order to minimise the leakage current at the high operating voltages a very high resistance is required and to reduce the electronic noise and the randomness in the electron-hole production process (which gives fluctuations in the pulse height for the photons of the same energy), the germanium detectors are operated in a reverse biased mode at liquid nitrogen temperature. The main advantage of a germanium detector compared with a scintillation detector lies in its higher intrinsic resolution which is a very important factor in the study of discrete line γ-rays. The detector energy resolution is defined as the full width at half maximum height and is about 2.0–2.5 keV for 1.33 MeV γ-ray emitted from a ^{60}Co source. The corresponding resolution of a NaI(Tl) typical scintillation detector for the same mono-energetic γ-ray is around 100 keV and is $\sim$ 180 keV for a BGO scintillator. The resolutions for the NaI(Tl) and BGO detectors are worse because of the larger energy required to create an electron–hole pair and the low efficiency of the photomultiplier tube. Crystal growth techniques have improved in the recent years and it is now possible to grow hyper-pure n-type germanium crystals with impurity concentrations $<10^{10}$ per cm^3. Hyper-pure Germanium detectors have several advantages compared with earlier lithium drifted germanium detector [Ge(Li)] detectors. For example, neutron damage in the n-type hyper-germanium detector is not as rapid as in Ge(Li). A neutron may damage a germanium crystal by creating charge trapping centres.

Hyper pure Ge detectors also have ion implanted outer contacts, giving a much smaller dead layer (around 3 orders of magnitude smaller).

5.5 Scintillation Detectors

Scintillation phosphors convert the energy lost by ionising radiation into pulses of light which are detected by a sensitive photocathode attached to a photomultiplier tube. The signal from the photomultiplier tube is then a measure of the energy deposited in the phosphor. Typically, the energy resolutions are poor when compared with those from semiconductor detectors as the scintillation counters have larger statistical fluctuations in the number of charge carriers produced per interacting photon as compared with the semiconductors. Statistical fluctuations in light production, reflection and internal absorption all result in varying numbers of photons reaching the photocathode. Additionally the response of the photomultiplier to the incident photons may introduce further variations in the final signal. These disadvantages are offset by the high gamma stopping powers (due to the relatively higher densities) and the short decay times, leading to good timing characteristics for many inorganic scintillators.

5.5.1 BGO Scintillation Detector

One shortcoming of semiconductor detectors is their low γ-ray detection efficiency. The relative detection efficiency of a detector is defined as the ratio of the absolute peak efficiency to the peak efficiency of a 3-inch by 3-inch NaI(Tl) scintillation detector for the 1.33 MeV γ-ray from a ^{60}Co source at a distance of 25 cm. The average relative efficiency of a typical Ge detector is only about 20 - 30%. Due to this reason scintillation detectors are used for various purposes taking advantage of their high efficiency when energy-resolution is not playing a crucial role.

Because of the high atomic number of bismuth $Z = 83$, bismuth-germanate

($Bi_4Ge_3O_{12}$) scintillation detectors have been widely used for various purposes in γ-ray spectroscopy. The compound has a high density $\sim$ 3 gm cm^{-3} and hence a large γ-ray stopping power. The volume of such a detector can be made 16 times smaller than a NaI(Tl) detector which used to be commonly in use. When a γ-ray enters the detector, it causes ionization as described in previous section 5.3. A photomultiplier tube collects the photons from the detector and produces a signal which is proportional to the number of electrons and consequently the incident energy of the gamma ray. This signal is then further processed by the different types of electronics depending on the requirement.

5.6 Compton Suppression

Because of Compton cross section, a large number of Compton scattered photons will escape from the Ge crystal, producing a continuous background in the energy spectrum. A germanium counter with a peak to total ratio of around 20%, would give rise to a photopeak-photopeak detection probability of around $\sim$ 4% when used in in a coincidence experiment. The remainder appear as Compton-Compton and Compton-photopeak coincidences resulting in low quality spectra.

The very low peak to total ratio for a solitary germanium counter can be improved by surrounding the germanium detector with a scintillation material. The scintillation shield is coupled electronically (in anti-coincidence) to the germanium, rejecting those signals (mainly Compton scatter events) which do not correspond to total γ-ray absorption in the germanium. This "composite" detector is called an escape suppressed spectrometer (ESS) and typically improves the peak to total ratio from about 20% to around 50% (see figure 5.4), resulting in a γ-γ coincidence peak to total of $\sim$25%.

In practice it is nice to use n-type hyper pure germanium (HpGe) counters, as the lack of dead layer increases the peak to total ratio. Also, due to the increased density of BGO over NaI, it is advantageous to use BGO as the

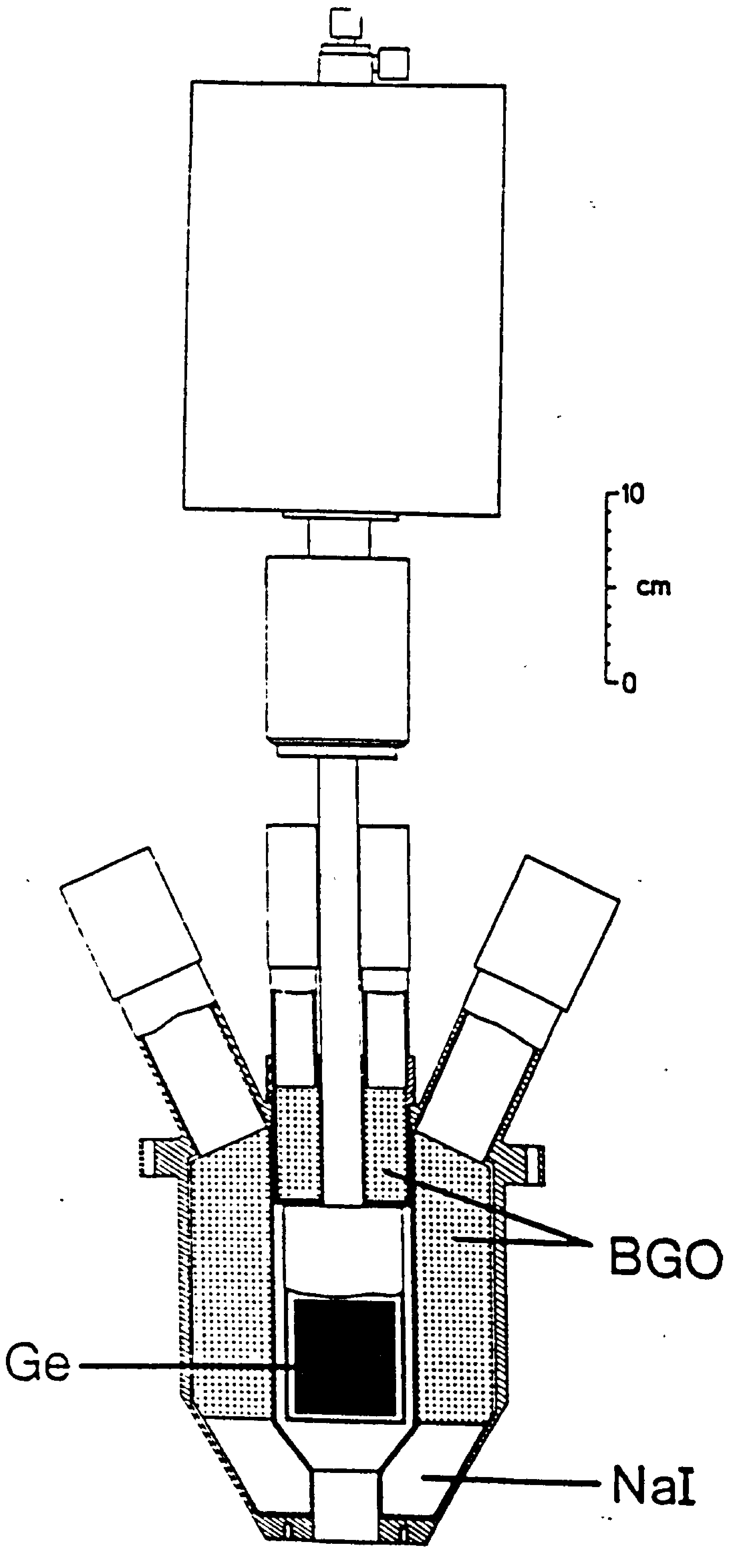

Figure 5.3: *An escape suppressed spectrometer (ESS) of the duet type. The front of the shield is composed of NaI(Tl) scintillator. The sides have BGO scintillator and the rear may have a BGO 'catcher' shield, (see text). The figure is from [No 85].*

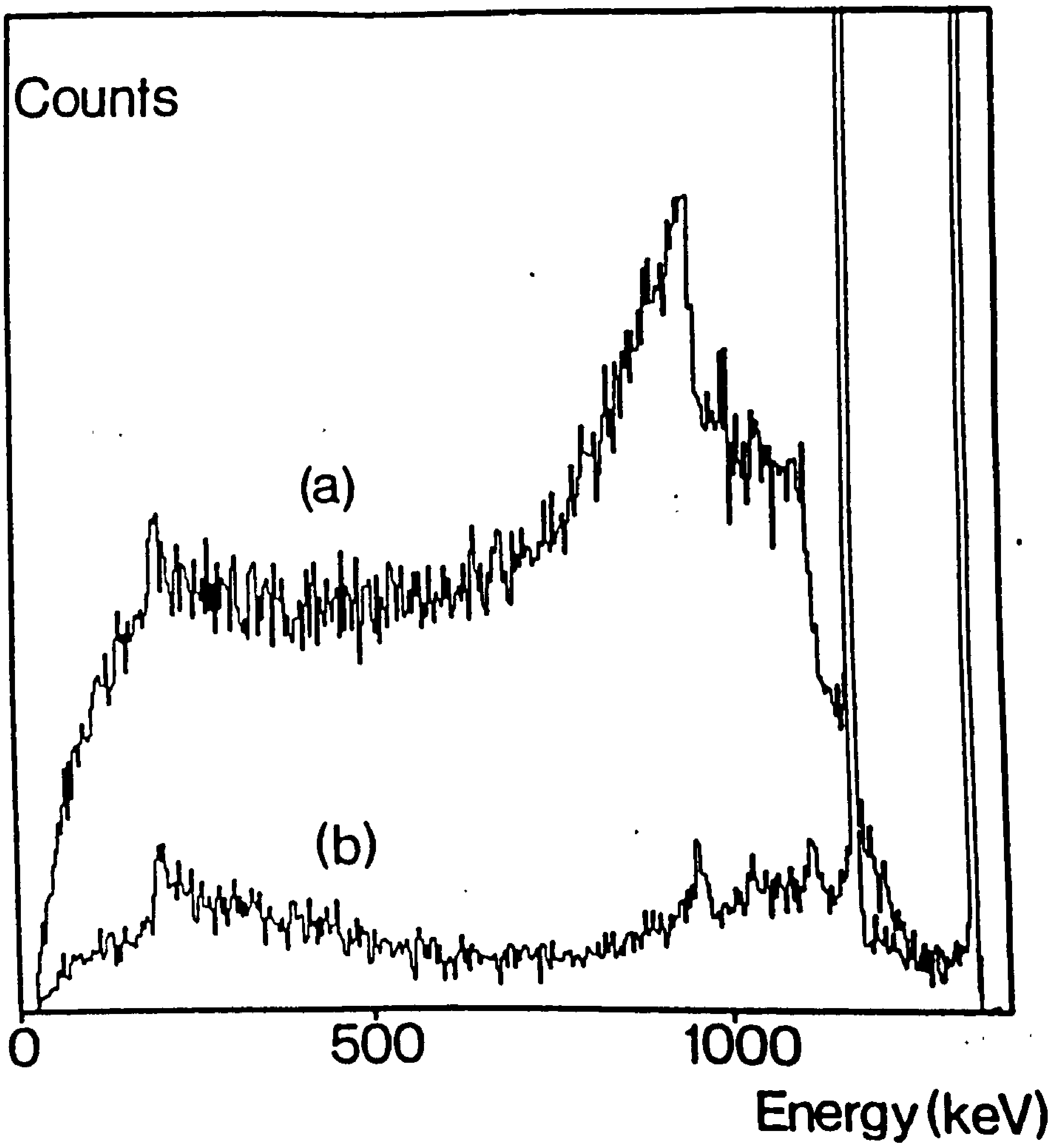

Figure 5.4 *Comparison of γ-ray spectra of a ^{60}Co source detected by (a) Unsuppressed and (b) Suppressed germanium detectors. The spectra (a) and (b) are normalised such that the peaks contain equal counts.*

shield material allowing a more compact design and up to 30 ESS's may then be placed around the target in close geometry. An ESS [No 85] is shown schematically in figure 5.3. Backward scattered gammas ($E_\gamma \leq 300$ keV) are detected by NaI situated at the front of the shield, taking advantage of the increased light output from NaI for the low gamma energies involved. The NaI is a single crystal optically coupled to the BGO. The BGO comprises of 8 optically separate elements, each having their own photomultiplier, angled as shown to allow the inclusion of a 'catcher'. This annular BGO catcher is in 4 independent pieces and detects γ-rays scattered in the forward direction. Its use is restricted to the 'Duet' type of germanium counter.

The germanium crystal is operated at liquid nitrogen temperature and is thus enclosed in a cryostat while the scintillation requires a surface protection and light excluder. These coverings are designed to minimise the interaction with scattered photons.

5.7 Detector Arrays

The formation of a compound nucleus at high spin and excitation energy is followed by the emission of large numbers of γ-rays. The study of the gamma decay demands an instrument of sufficient selectivity and resolution by which weak γ-rays (eg. ~1% of the channel cross section), de-exciting these high spin states, may be detected. Many reaction channels and a large continuum background make such measurements extremely difficult. Multidetector 4π (ESS) arrays are used to overcome these problems. One such array is "The Total Energy Suppression Shield Array" (TESSA) [Tw 83], situated on the tandem Van de Graaff accelerator at Daresbury, combining escape suppressed spectrometers with a compact inner BGO ball.

5.7.1 The TESSA3 Spectrometer Array

The present version of TESSA (TESSA3) at the Daresbury Laboratory is an array consisting of 16 ESS's in two rings of six detectors at angles of ±19° in the vertical plane and one ring of four detectors in the horizontal plane of the beam along with a 50 element BGO inner ball [NT 88], see figure 5.5. Each ring of 6 ESS's has detectors at ±35°, ±90°, ±145° to the beam direction in the horizontal plane whereas other four ESS's make a ring of four detectors at ±60° and ±120° in the horizontal plane. The resultant detector to beam angles are, therefore, 2×(±35°, ±90°, ±145°), ±60° and ±120°.

The germanium crystals are positioned ~ 23 cm from the target and view the target through 'heavy metal' collimators giving each detector a subtended solid angle of around 0.26% of 4π sr. The 120 different detector combinations with which to record E_γ-E_γ coincidence events, in conjunction with the added

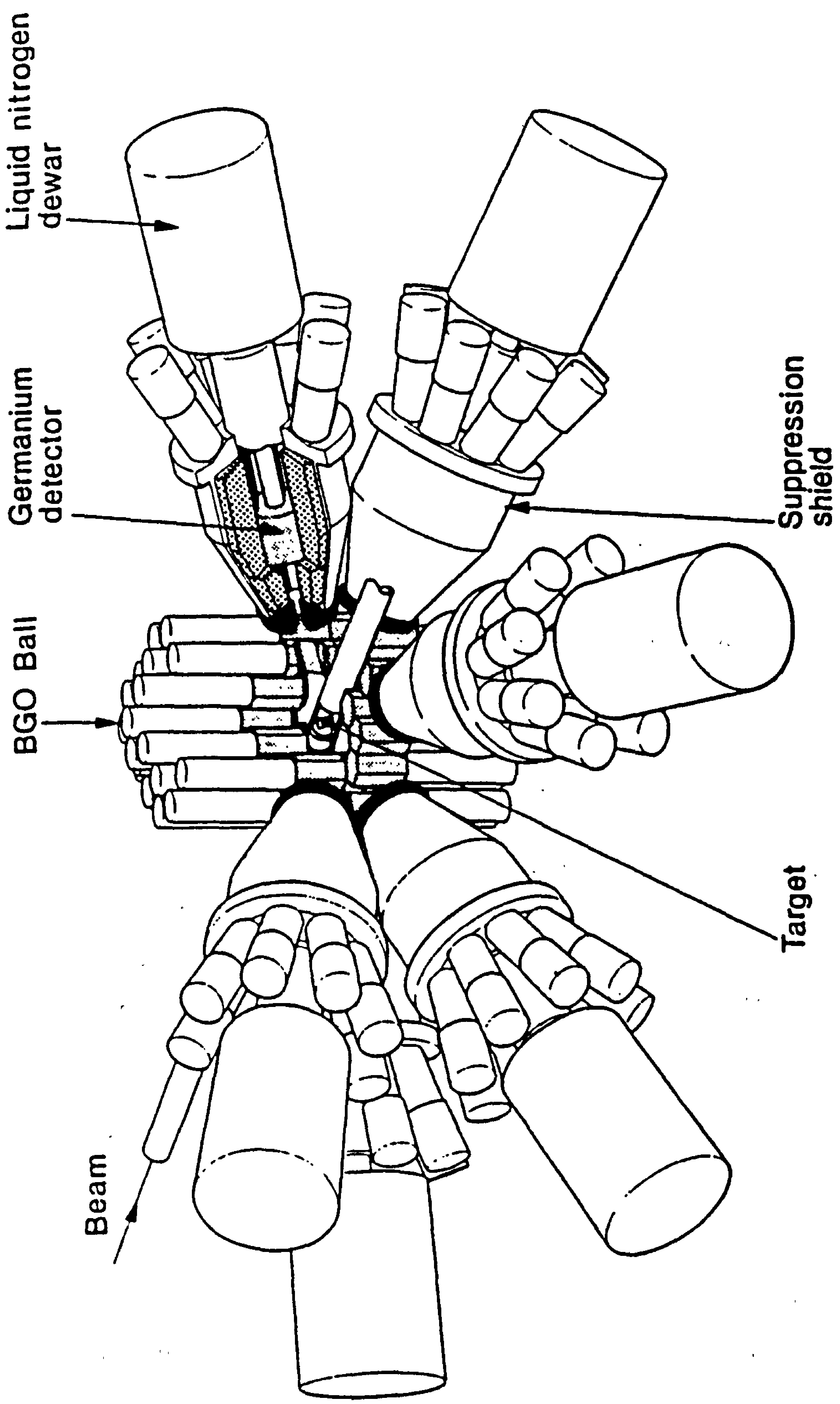

Figure 5.5: *A schematic diagram of some of the 16 ESS's of 'The Escape Suppressed Spectrometer Array TESSA3' and the '50 element inner ball BGO calorimeter'. The BGO ball acts as a channel selection device and can be seen in the centre of the picture surrounding the target chamber. The Germanium semiconductor crystals and the corresponding BGO suppression shields are located in the Aluminium housing. The photomultiplier-tubes of the suppression shields and the liquid nitrogen dewars of the Germanium detectors are also shown.*

peak to total ratio gained in using ESS's allow for sufficient detection efficiency and high resolution (the ability to resolve low intensity peaks above the background). The inner "ball" of BGO detectors is surrounded by the ESS's and forms a gamma ray multiplicity and total energy device.

5.7.2 The Electronics and Logic System

The function of the electronics is to provide a method for extracting the useful data from the total number of events. Coincidence experiments require at least two γ-rays to be detected within the resolving time of the electronic system ($\sim$100ns).

The electronic setup for the TESSA3 spectrometer array can be divided into two major sections, the first being concerned with channel selection and the second with high resolution γ-ray energy measurements. The block diagram for the electronics of the TESSA3 setup is shown in figure 5.6.

5.7.3 The BGO Ball Channel Selection

The inner BGO ball is a 50 element filter/calorimeter device and is located between the target and rings of ESS's. Each BGO crystal has a hexagonal shape with dimensions of 3.8 cm face to face and a length of 5.0 cm to 7.0 cm. These BGO detectors are arranged in a honeycomb pattern and all have approximately the same detection efficiency. Holes have been cut through some of the elements of the ball to allow the target to be viewed by the ESS's. The information that is recorded from the ball is the number of gamma rays detected in the ball (defined as the fold) and the total γ-ray energy (sum energy) obtained by summing the pulse heights of signals from each BGO detector. The pattern and number of the detectors that register (termed as multiplicity or fold) can also be obtained. The BGO ball is designed to operate at a rate of around $350 \times 10^3\ s^{-1}$. The measured fold is generally less than the actual gamma multiplicity (fold $\sim$25 corresponds to multiplicities $\sim$30) which

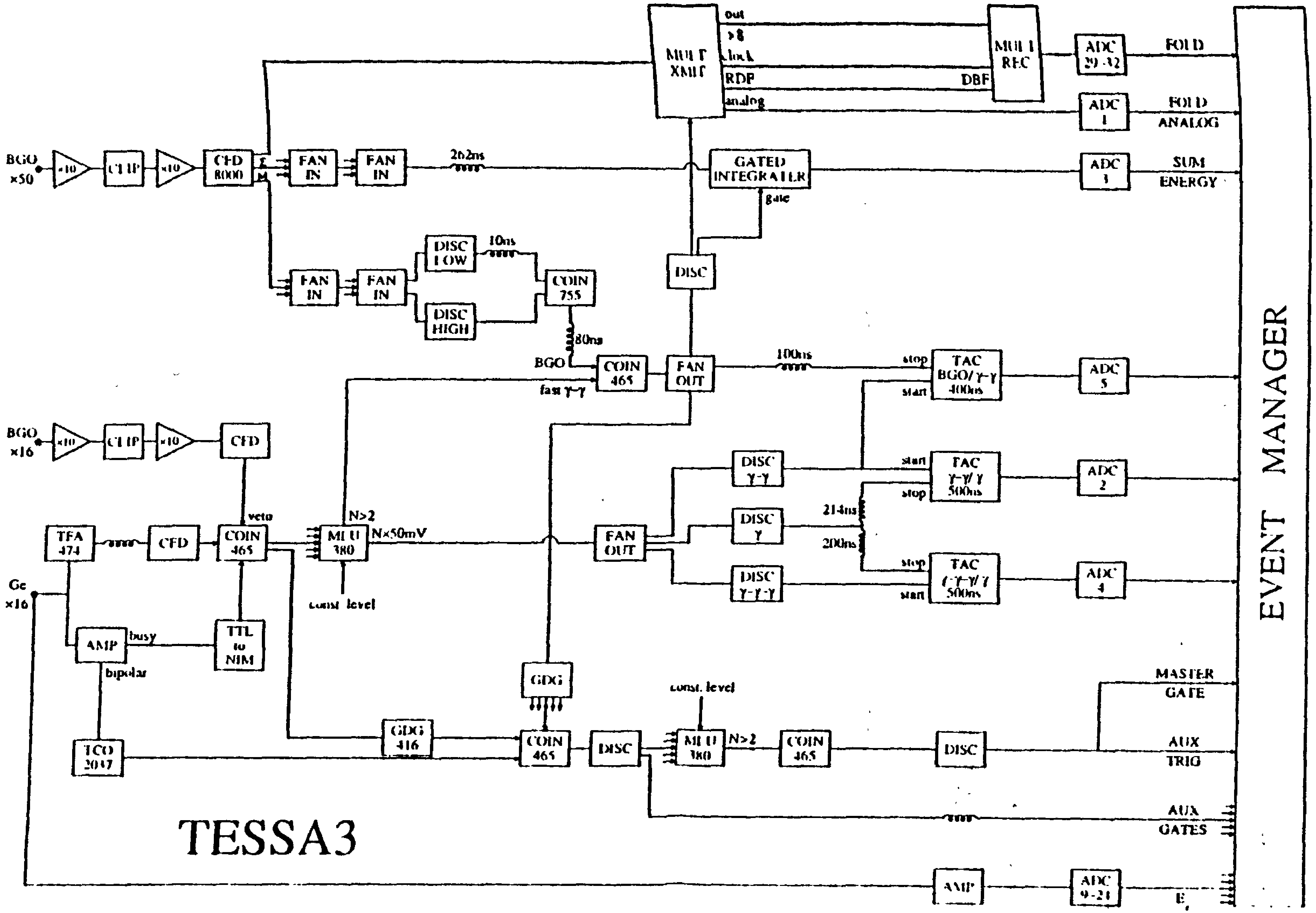

Figure 5.6: *Block diagram of the electronic setup for TESSA3 Array.*

is related to the average spin $< I >$ removed in the cascade.

$$< I >= 2(< M > -\delta) \tag{5.6}$$

where <M> is the average multiplicity and δ is the number of statistical transitions (ie. those that on average remove no angular momentum). It is assumed that the majority of the remaining gammas are stretched E2's. It is also possible to use the ball as a detector for decays from isomeric states, allowing an isomer tagging technique to be employed, and also as a high energy γ-ray detector. However, the principal mode of operation for the ball is as a channel selection device. By selecting germanium signals in coincidence with appropriate filters on the fold and sum energy signals, it is possible to enhance the required exit channel over all other exit channels.

5.7.4 Germanium High Resolution Energy Measurements

Two identical analogue output signals are provided by each Ge detector, one of which is used as a logic signal for the timing (fast∼ ns timing) applications and the other in γ-ray energy measurements (slow ∼μs timing). The energy signal is amplified with a pulse shaping time of ∼ 2-3μs. From the shaping amplifier a unipolar signal is produced which is fed into an analogue to digital convertor (ADC). This ADC is gated by an external trigger and its digital output enters the event manager. The event manager interfaces the electronics to the data acquisition system and requires a gate or an external trigger to inform it which events to collect. These gates are produced from the Ge detector timing and BGO ball signals and are called the auxiliary and the master gates. The gate signals arise from the γ-γ events which are escaped suppressed, pile-up rejected, pulse shape discriminated and are in coincidence with a well defined BGO ball event.

The fast timing signal contains only those events which are escaped suppressed and have been produced from a germanium detector which did not register a busy signal. The shield signal is coupled in anti-coincidence with the germanium logic signal to veto any events which correspond to gamma-rays scattering from Ge to BGO shield and detector. A signal from the (slow) germanium spectroscopic amplifier is required to indicate the 'not busy' condition, thereby rejecting any 'piled up' events. These fast escaped suppressed and 'not busy' signals are then fed into a multiplicity logic unit which has a filter condition N>2. The coincidence between the output signal from the multiplicity logic unit and a fast BGO ball signal that acts as the gate for the rest of the electronics.

The slow timing signals are derived from pulse shape discriminating logic circuits with the application of the cross-over pick-off technique. Each slow Ge timing signal and the suppressed, busy rejected, fast Ge timing signals are coupled together with a coincidence box, after the fast signals have been delayed by a gate and delay generator. These signals are then gated with a delayed BGO-γ-γ from the fast timing circuit and produce the 'auxiliary gate'. A second multiplicity logic unit combines the 16 auxiliary pulses to produce a slow γ-γ-BGO logic pulse which is termed as the 'master gate'.

A γ-γ time to amplitude conversion (TAC) spectrum may also be generated to distinguish between n-γ and γ-γ events. The start signal is provided by a good γ-γ coincidence and the stop by a good delayed γ-γ-BGO event. The output of this TAC is a time spectrum having a sharp peak if the events detected are all γ-rays. However, the measured TAC spectrum has a tail coming from those events for which the signal from Ge detector corresponds to a neutron instead of γ-ray, as the velocity of a neutron is less than that of photon (which is the velocity of light). Therefore the time interval between a neutron detected in a Ge detector and a γ-ray detected in a BGO ball is less than that of γ-γ event.

5.7.5 Data Acquisition

The event manager collects the information from the ADC's and formats the event prior to writing to tape. An ADC is read only if the germanium ADC signal, an auxiliary trigger and a master gate signal are in coincidence. The event manager is controlled by a GEC4070 computer.

5.8 General Methods of Data Analysis

5.8.1 Two Dimensional $E_\gamma - E_\gamma$ Correlation Matrix

The essential data analysis technique in high spin spectroscopy is the $\gamma - \gamma$ coincidence technique. A common approach for establishing the coincidence relationship between the γ-rays is to construct a two dimensional $E_\gamma - E_\gamma$ spectrum. The experimental two or greater fold coincidence data are stored event by event onto magnetic tape during the experiment. Each event contains the γ-ray energies (channel number) detected simultaneously by two or more Ge detectors, and the identification for these detectors. Other information such as the total cascade energy, the γ-ray multiplicity and the time information, TAC, can also be stored depending on the equipment employed. If an event contains two γ-rays with energies $E_{\gamma 1}$ and $E_{\gamma 2}$ information is stored by incrementing the two dimensional $E_\gamma - E_\gamma$ spectrum at the positions $(E_{\gamma 1}, E_{\gamma 2})$ and $(E_{\gamma 2}, E_{\gamma 1})$. If an event contains three γ-rays, $E_{\gamma 1}$, $E_{\gamma 2}$ and $E_{\gamma 3}$, three $\gamma - \gamma$ coincidences are recognised, i.e., $(E_{\gamma 1}, E_{\gamma 2})$,$(E_{\gamma 1}, E_{\gamma 3})$ and $(E_{\gamma 2}, E_{\gamma 3})$. Each coincidence pair increments the matrix at the two corresponding positions. By this procedure a symmetrised 2 dimensional matrix is obtained with x- and y-axes being γ-ray energies and containing the number of counts. Nuclear level schemes are then constructed by analysing the spectrum in coincidence with a particular gamma-ray of interest by projecting the spectrum onto the y-axis corresponding to the peak limits ("gate") imposed on the x-axis and vice versa. Coincidences due to the background radiation under the peak of interest are subtracted. The major part of the background in spectrum results from the Compton scattered events that are not completely removed by the suppression shields of the Ge detectors and from random coincidence events that are not completely removed by setting a gate on the TAC spectrum.

In a complicated total projection spectrum that often has intense peaks appearing close in energy one after another, it is difficult to select specific background windows for the background subtraction for the gated spectra. To a good approximation the total projection can be used as a background spectrum for all the gated projections. Other methods of background subtraction shall be discussed in the following chapters.

5.8.2 γ-ray Energy, Efficiency and Intensity Calibrations

The energy and efficiency calibrations are made by collecting 'singles' (the collection of those events which have a fold condition equal to one) from a ^{152}Eu radioactive source before and after the experiment. The determination of the γ-ray energies and relative intensities require an integration of the peaks of interest in the relevant spectra. To integrate an energy peak, a least square fitting technique is used to fit the spectrum, assuming a linear background and a Gaussian peak shape. The peak centroid and intensity together with their associated errors are then computed after subtracting the fitted background. Figure 5.7 shows an example of the peak fitting. In the case where the γ-ray peaks are close together, a multi Gaussian peak fitting can be performed by the programme. The intensity of a particular γ-ray is usually quoted relative to the intensity of the strongest γ-ray of the particular reaction channel. For an even-even rotational nuclei this is generally the $2^+ \rightarrow 0^+$ γ-ray transition

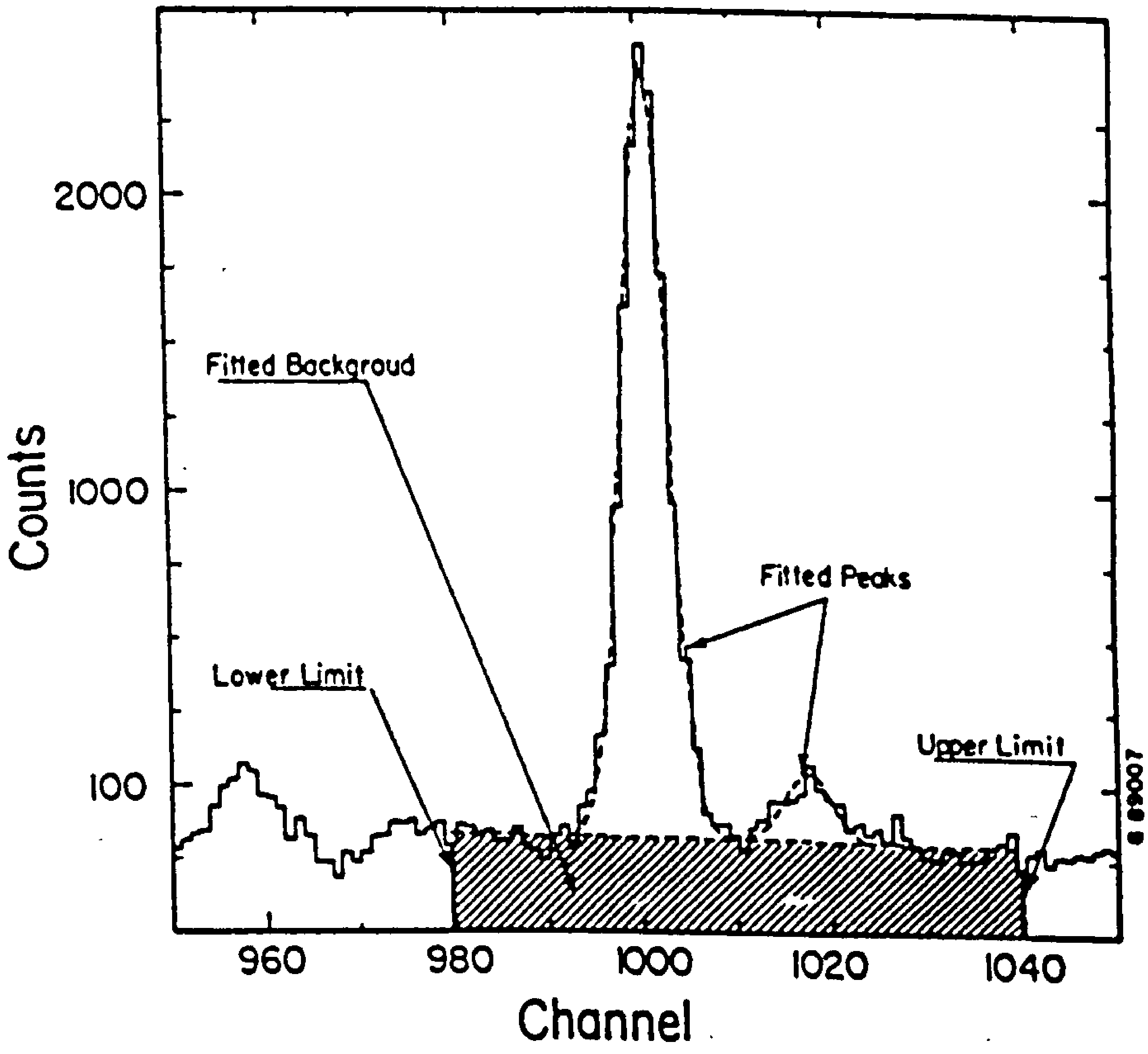

Figure 5.7: *Example of fitted peaks for a gamma ray spectrum.*

ground state rotational band. However, since these peaks are measured with different energies they have to be corrected for the efficiency of the detector system. An efficiency curve (e.g., see figure 5.8) is obtained from a comparison of the γ-ray intensities in the singles ^{152}Eu source spectra to the tabulated values, [LS 78]. Other methods used to extract the γ-ray intensities in this work are described in section 6.1 and section 6.3.

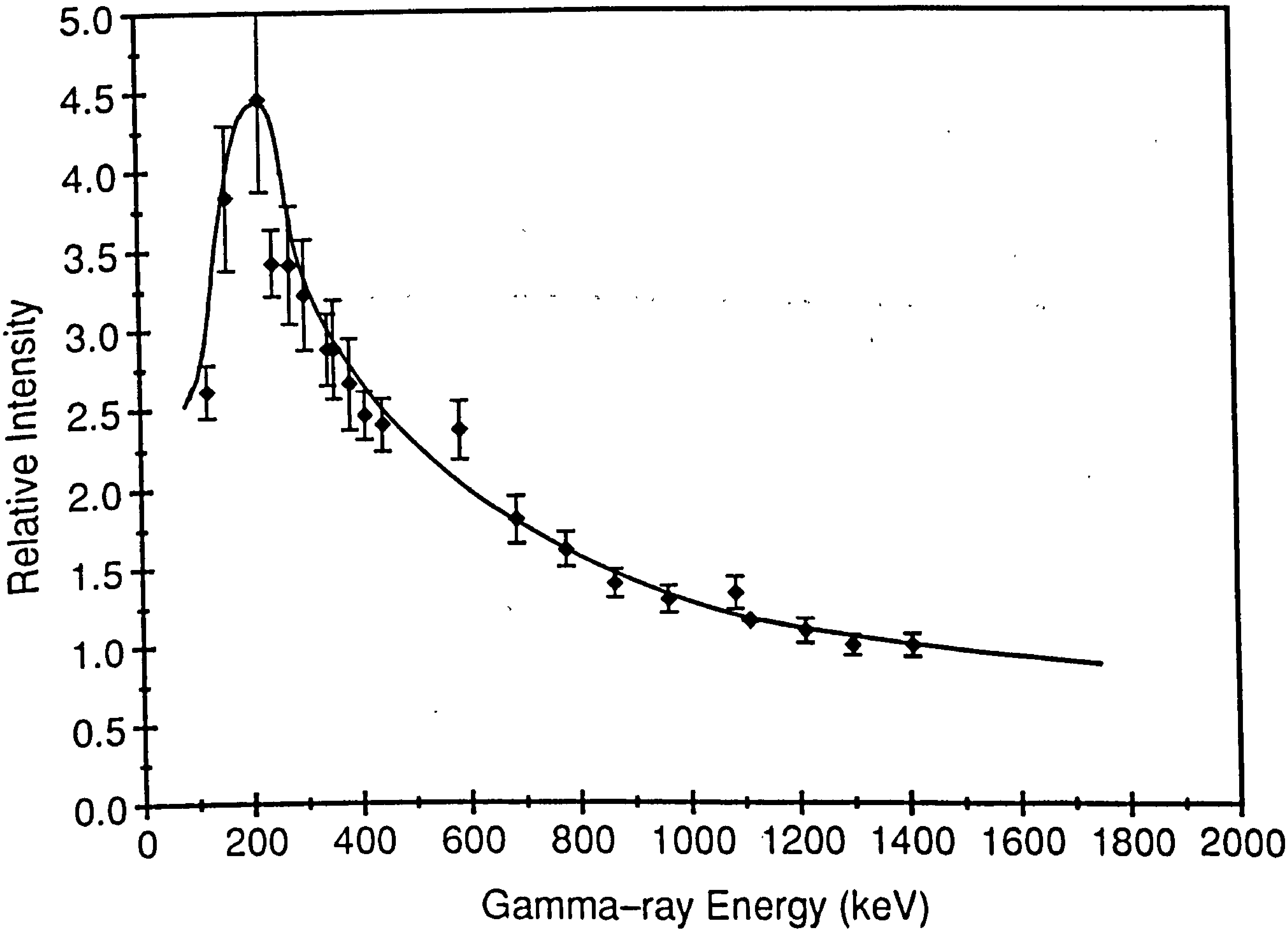

Figure 5.8: *An efficiency curve for the TESSA3 detector array.*

5.9 The Experiments

In order to study the behaviour of ^{150}Gd, ^{151}Tb and ^{152}Dy in the first and second potential well, HI fusion reaction experiments were performed at the Nuclear Structure Facility at the Daresbury Laboratory. The gamma rays emitting from these reactions were detected by the TESSA3 spectrometer array described in the preceding sections. The experimental information for the experiments is summarised in table 5.1.

Table 5.1

Reaction	E_{beam} $^{a)}$ (MeV)	E_x $^{b)}$ (MeV)	l_{max} $^{c)}$	Target Thickness	Backing
^{130}Te(^{26}Mg,6n)^{150}Gd	145	90	79	2×400 μgm/cm^2	none
^{130}Te(^{27}Al,6n)^{151}Tb	150	90	79	2×400 μgm/cm^2	none
^{108}Pd(^{48}Ca,4n)^{152}Dy	197	73	78	2×400 μgm/cm^2	none

Table 5.1: Table summarising the data analysed and presented in this thesis.

$^{a)}$ Energy of the beam at the center of the target.

$^{b)}$ Average excitation energy in the compound nucleus.

$^{c)}$ Classical maximum angular momentum.

5.9.1 The ^{150}Gd and ^{151}Tb Experiments

The high spin states in ^{150}Gd and ^{151}Tb were populated by the reactions $^{130}Te(^{26}Mg,6n)^{150}Gd$ and $^{130}Te(^{27}Al,6n)^{151}Tb$ at beam energies of 145 MeV and 150 MeV respectively. The beam energies were chosen to give the required energy and l_{max} in the final system (Program Qval) based on the Bass model and were provided by the tandem van de Graff accelerator at Daresbury. In both the experiments the tellurium targets were in the form of 2x400 μgcm^{-2} self supporting foils and the compound systems were formed at an excitation energy of 90 MeV and a maximum classical angular momentum (l_{max})

of around $79\hbar$. For each experiment over 230×10^6 $\gamma - \gamma$ coincidences were recorded. To reduce the amount of unwanted data written to tapes a high fold condition was introduced into the master gate: at least 10 elements of the BGO inner ball were required to fire. The fragile nature of self-supporting ^{130}Te targets set a limit to the beam current for the experiment, a current of around 2-3 pnA was maintained and gated event rates of around 800 s^{-1} were achieved.

5.9.2 The ^{152}Dy Experiment

High spin states in ^{152}Dy were populated by using the reaction $^{108}Pd(^{48}Ca, 4n)^{152}Dy$ at a beam energy of 197 MeV and a maximum angular momentum (l_{max}) of $78\hbar$. The target was in the form of two $\sim$ 95% isotopically enriched self supporting foils of ^{108}Pd. The logic circuit was essentially the same as in the case of ^{150}Gd and ^{151}Tb experiments with the exception that an isomer detector consisting of eight BGO elements surrounding a gold stopper foil placed down stream of the target and out of focus of the ESS's and BGO ball was used, detecting decays from the 10 and 60 ns isomers at 21^- and 17^+ single particle levels in ^{152}Dy. An isomer TAC (shown in figure 5.9) circuit was used in the logic system which was started by a Ge-Ge-BGO ball signal and stopped by a signal from the isomer detector when two or more elements are registered. The isomer signal was also required to be in delayed coincidence with a prompt γ-γ event. In order to maximize the amount of useful data recorded onto magnetic tape the BGO ball elements had thresholds of $\sim$ 500 keV set before they would fire (usually the threshold for the BGO ball is set at 120 keV), which artificially lowered the detected fold distributions, and the mastergate had a fold requirement built into it of fold ≥ 8. A total of 136 $\times$ 10^6 events were recorded. It shall be seen in the next chapter that due to the isomer TAC and fold filters, this experiment yielded excellent quality data and that the ^{152}Dy exit channel could be selected with almost total exclusion of all other exit channels.

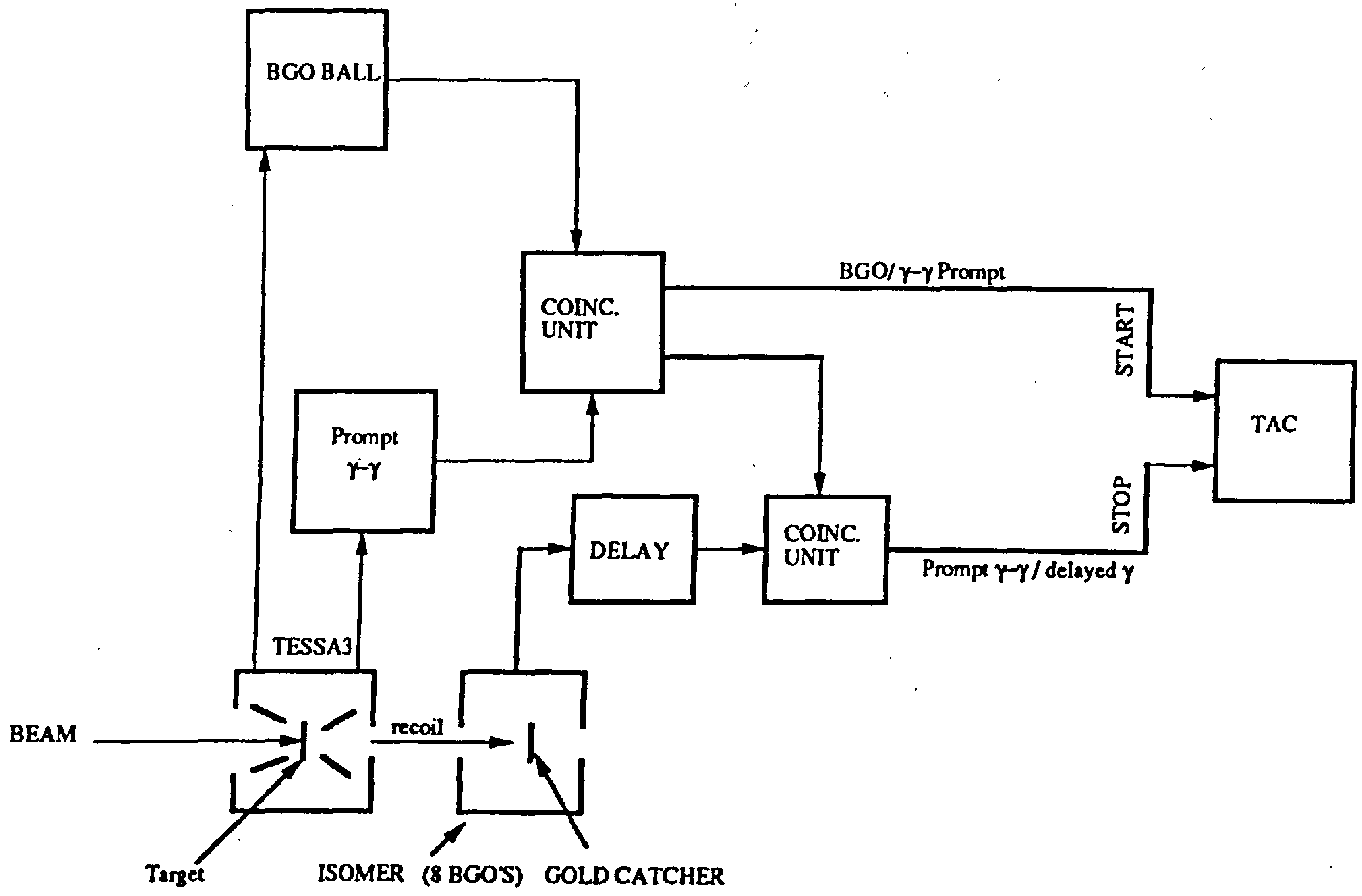

Figure 5.9: *An isomer TAC logic circuit used in the ^{152}Dy experiment. The start signal for the TAC was a Ge-Ge-BGO ball signal while a signal from the isomer detector when two or more elements were fired was used as the stop signal.*

Chapter 6

Analysis and Results: Single Particle Experimental Level Schemes of ^{150}Gd and ^{152}Dy

This chapter is divided into two parts. Part I contains the analysis and results from the ^{130}Te(^{26}Mg,6n)^{150}Gd experiment, and the single particle experimental level scheme of ^{150}Gd is presented. Part II contains the analysis and results from the ^{108}Pd(^{48}Ca,4n)^{152}Dy experiment, and the single particle level scheme of ^{152}Dy is discussed.

It shall be mentioned here that the data from all the experiments was sorted into 2-dimensional E_γ-E_γ correlation matrices using the method described in the previous chapter.

Part I

Level Scheme of ^{150}Gd

6.1 Level Scheme of ^{150}Gd

6.1.1 Introduction

Previously the level scheme of ^{150}Gd has been studied by many authors such as Haenni *et al.* [Ha 77], Kleinheinz *et al.* [Kl 79] and A. W. Sunyar [Su 81]. In figure 6.1 the previously published level scheme of ^{150}Gd by A. W. Sunyar [Su 81] is shown. In this work the level scheme of ^{150}Gd is extended up to higher spins than previously observed. The following sections show the level scheme extended up to spin 39^+.

6.1.2 Methods

The states in ^{150}Gd were populated using the reaction described in section 5.9. For the analysis two matrices were made: One with fold condition between 8 and 17 and another with the fold condition greater than 17. The matrix with a fold condition between 8 and 17 will be termed the lowfold matrix and the one with a fold condition greater than 17 will be termed the highfold matrix. Approximately, 54% of the events in the highfold matrix belonged to the 6n (^{150}Gd), 44% to the 5n (^{151}Gd) and about 2–3% to the 7n (^{149}Gd) reaction channels while 75% of the events in the lowfold matrix belonged to the 6n (^{150}Gd), 22% to the 5n (^{151}Gd) and 3% to the 7n (^{149}Gd) reaction channels. The highfold and lowfold $\gamma-\gamma$ matrices for ^{150}Gd contained 56×10^6 and 132×10^6 events respectively. Results from both matrices were taken for comparison and were found consistent for the two matrices. It can be seen from the relative intensities of the 306 keV (which belongs to ^{151}Gd) and the 395 keV (which belongs to ^{150}Gd) transitions in the two projections that the contamination of ^{151}Gd is greater in the highfold matrix and is smaller in the lowfold matrix (figure 6.2). As further evidence one can observe that the 155 keV and 521 keV transitions belonging to ^{151}Gd are stronger in the highfold matrix and weaker in the lowfold matrix.

In order to deduce the ordering of transitions within the level scheme of

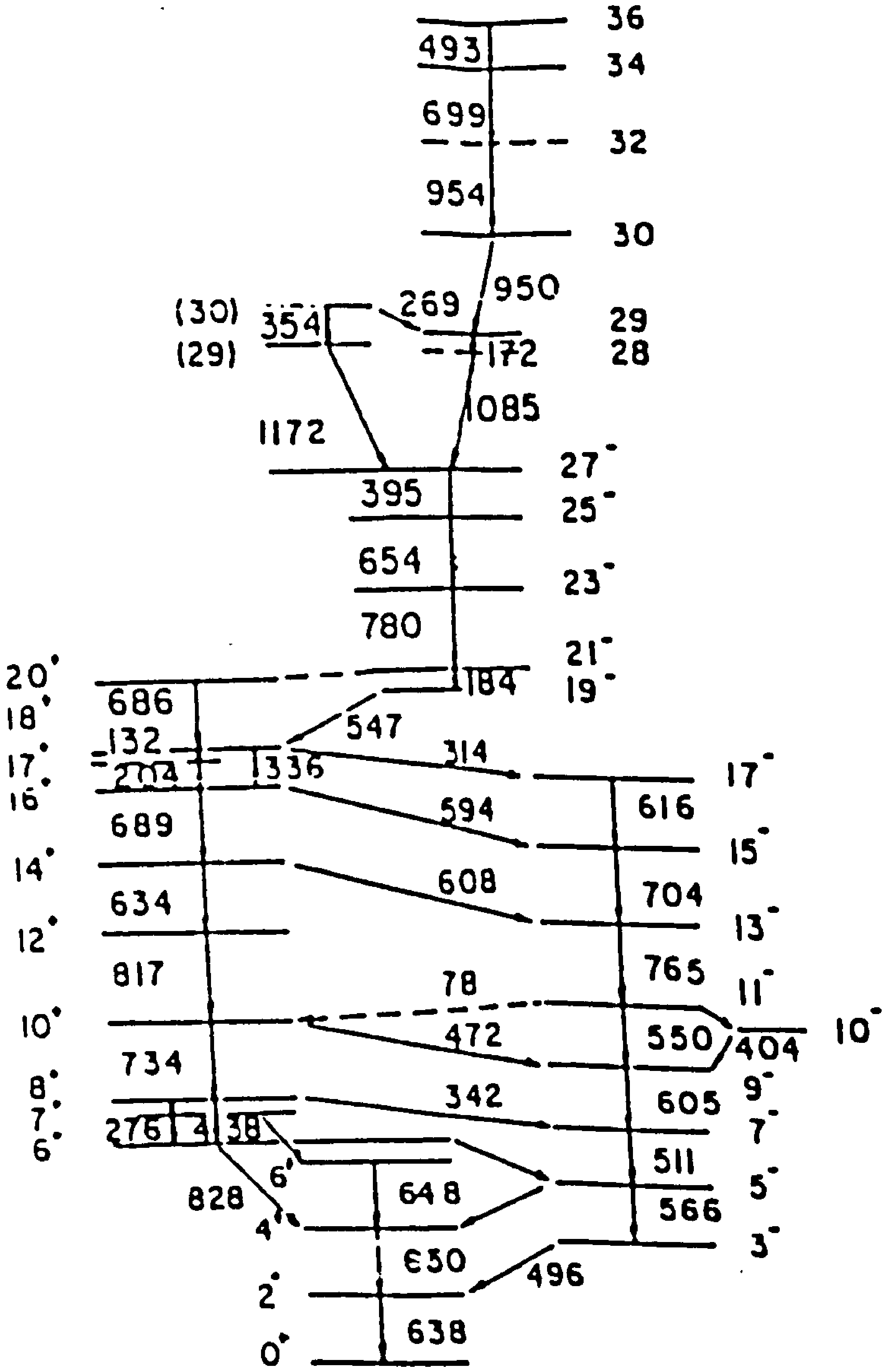

Figure 6.1: *The level scheme of ^{150}Gd as published by A. Sunyar [Su 81].*

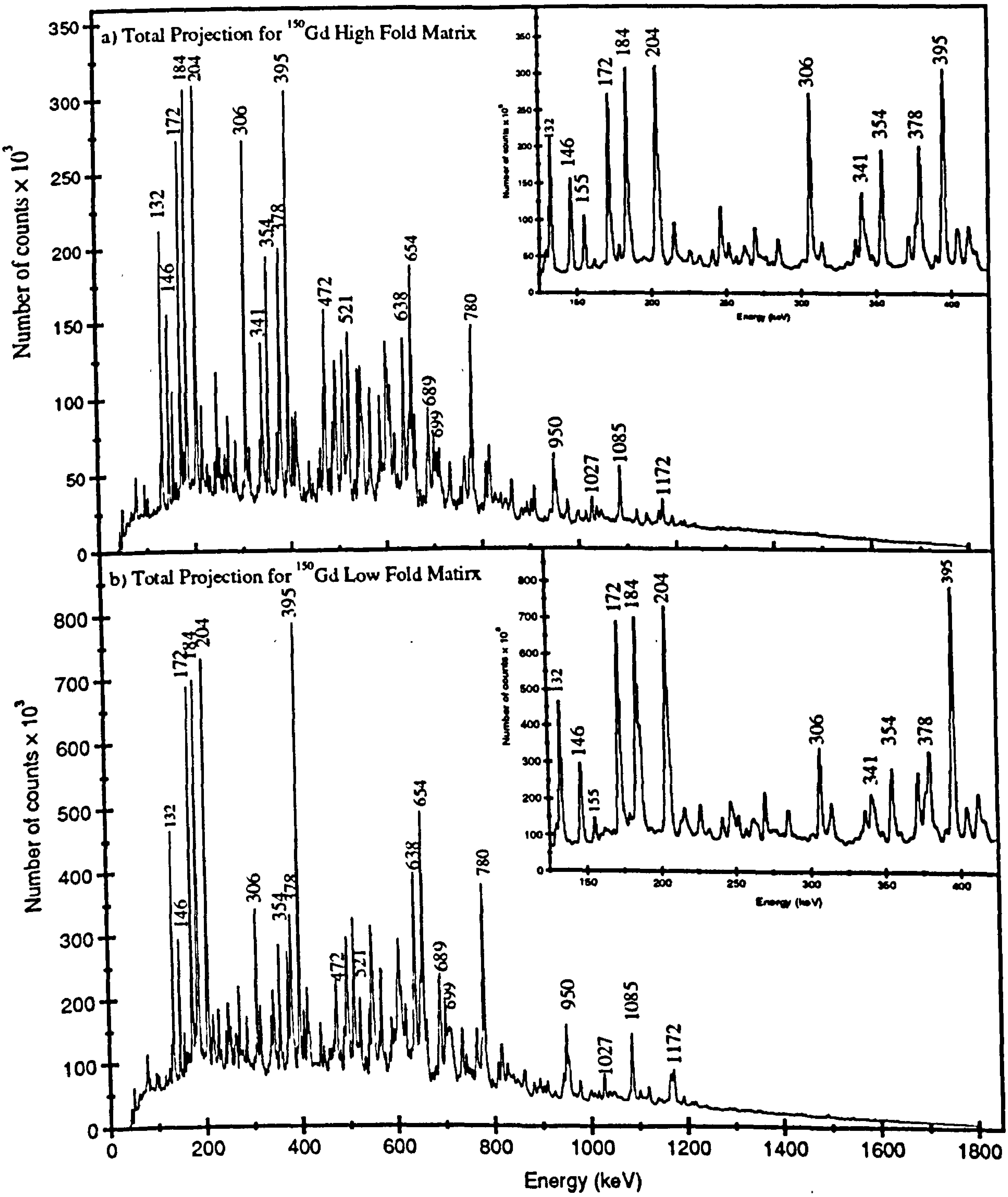

Figure 6.2: *Total projections for (a) lowfold and (b) highfold matrices for* $^{150}_{64}Gd_{86}$*. It can be seen that the 155 keV and 306 keV gamma-rays which belong to* ^{151}Gd *are stronger in the highfold matrix and weaker in the lowfold matrix. This clearly means that the highfold is more contaminated than the lowfold matrix. The insets show the low energy portion of the total projection.*

^{150}Gd it was important to look at both the coincidence relationships of individual γ-rays and their relative intensity to one another. To find the intensities of transitions relative to the 780 keV transition in ^{150}Gd, coincidence spectra for the 395 keV and 654 keV transitions were combined and the intensities were measured for the transitions of interest. It shall be mentioned here that for gammma ray transitions having low energies, the intensities of the gamma rays were corrected for the effects due to internal conversion. The total gamma ray intensity was then given by [Kr 87]:

$$I_t = I_\gamma(1 + \alpha_{tot}) \tag{6.1}$$

where I_t is the total gamma ray intensity, "I_γ" the experimentally observed intensity of the gamma ray and α_{tot} [RFP 78] is the total internal conversion co-efficient.

6.2 Results

The total projections for the highfold and the lowfold matrices are shown in figure 6.2. The new level scheme is in agreement with the previously published level scheme by A. W. Sunyar [Su 81] up to spin 27^- but differs above 27^-, where several transitions have been re-ordered and 20 more found. The energies of the new gamma-ray transitions are 129 keV, 174 keV, 178 keV, 206 keV, 251 keV, 261 keV, 262 keV, 336 keV, 372 keV, 393 keV, 416 keV, 816 keV, 862 keV, 977 keV, 1027 keV, 1078 keV, 1119 keV, 1164 keV, 1191 keV and 1216 keV. The new level scheme is shown in figure 6.3 and a section above $I = 21^-$ is shown in figure 6.4. In figure 6.4 the thickness of the arrow is related to the intensity of the gamma-ray. The measured relative intensities are given in table 6.1.

6.2.1 Yrast cascade from spin $39^{(+)}$ to $29^{(-)}$

From figures 6.3 and 6.4, it is seen that the transitions around spin $33^{(+)}$, having energies 493 keV, 699 keV, 950 keV and 954 keV have been re-ordered compared with figure 6.1. Figure 6.5 shows that the 1164 keV and 336 keV transitions are in coincidence with the 699 keV and 950 keV transitions but not in coincidence with the 954 keV transition. The transitions having energies 372 keV ($35^{(+)}$)and 174 keV ($36^{(+)}$) are in coincidence with each other and with all the transitions below $33^{(+)}$ and above $36^{(+)}$, but are not in coincidence with the 336 keV, 1164 keV, 393 keV, 977 keV and 862 keV gamma rays. This is illustrated in figure 6.6. The 1027 keV and 1216 keV transitions are in coincidence with all the gamma rays in the level scheme. They have been placed in the level scheme in accordance with their relative intensity to each other and their coincidence relationship with the remaining transitions.

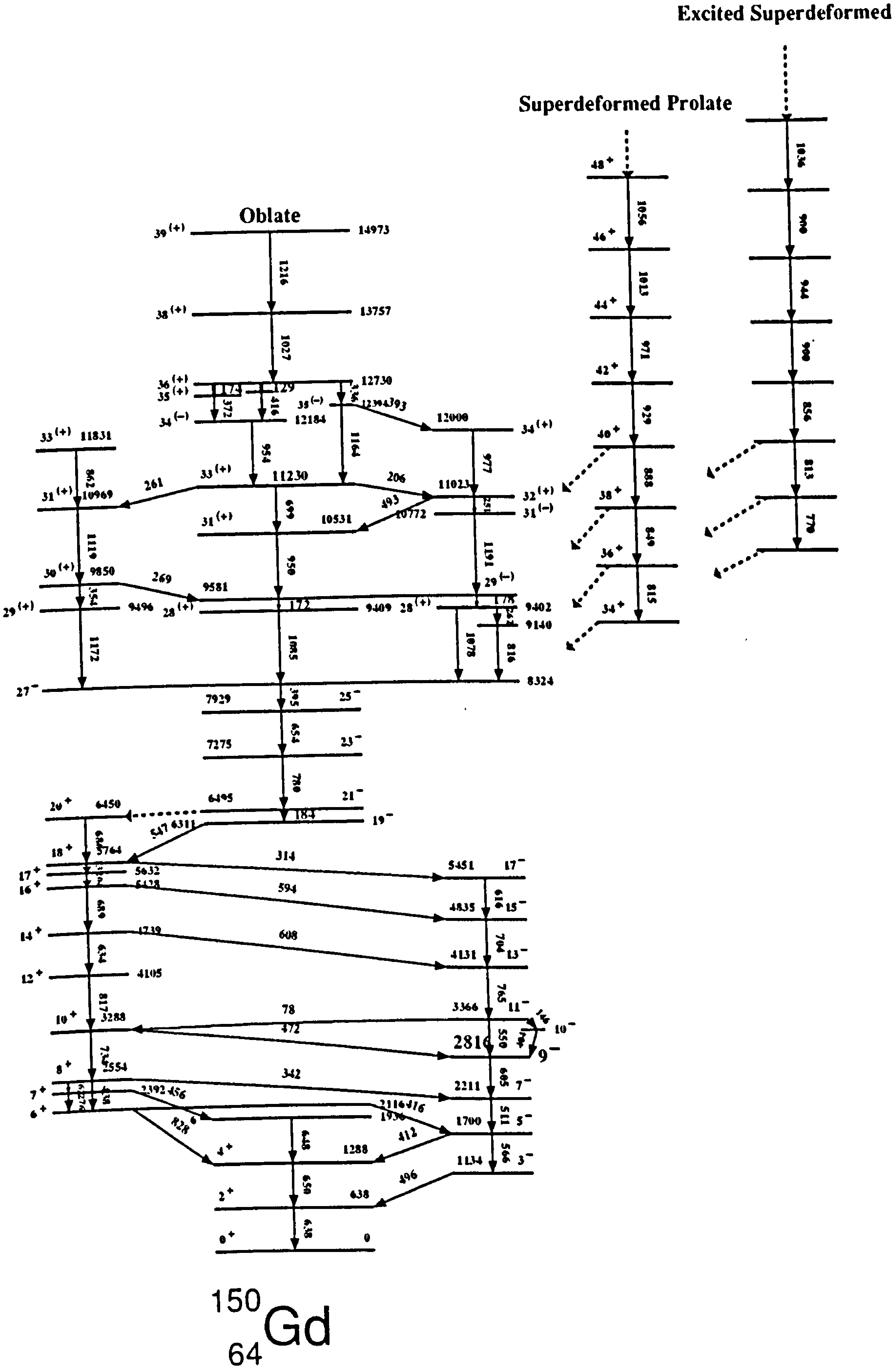

Figure 6.3: *The level scheme of ^{150}Gd deduced in this work.*

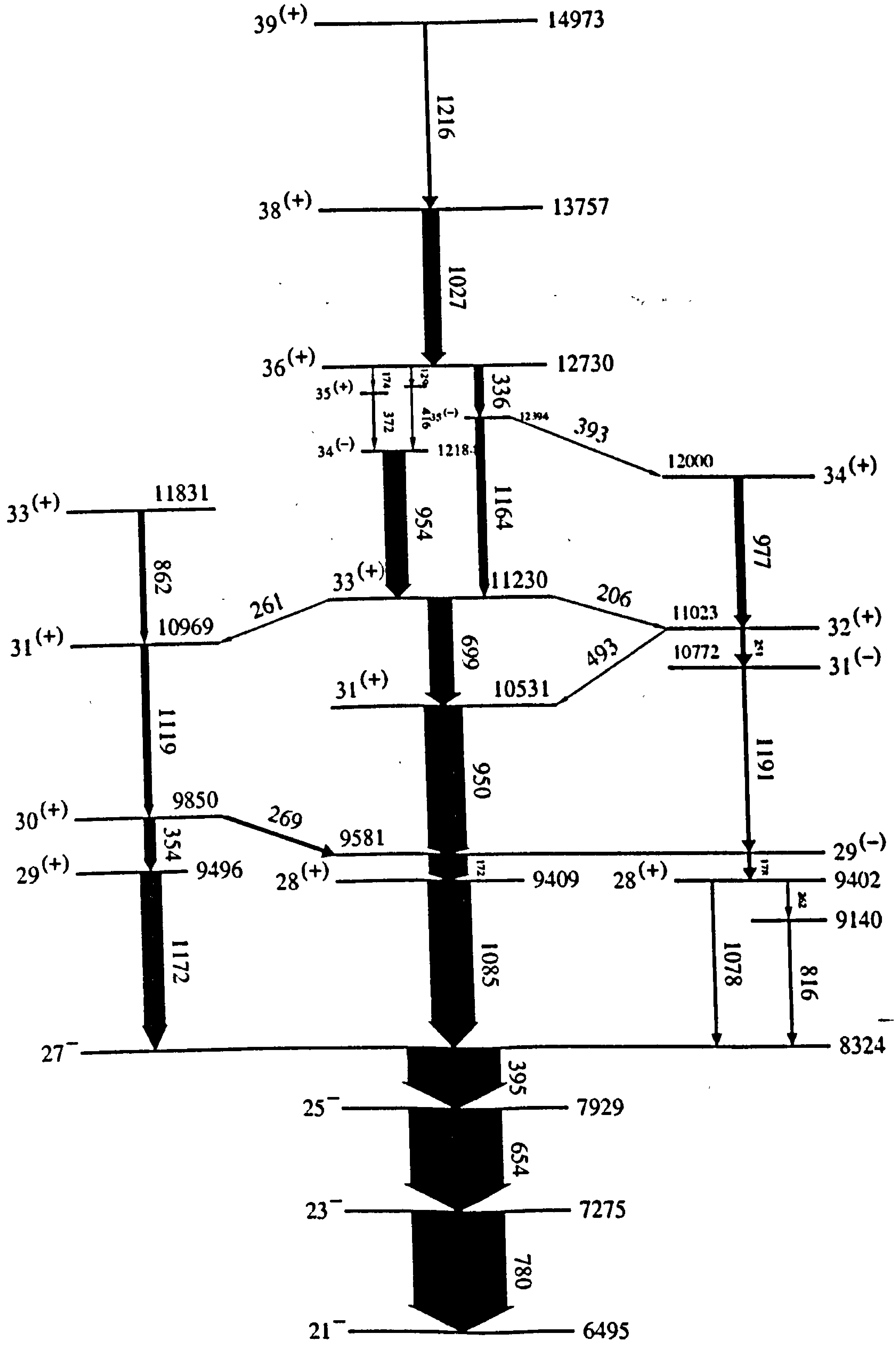

Figure 6.4: *Partial level scheme of* ^{150}*Gd above spin 21*$^-$*. Relative* γ*-ray intensities are shown by the thickness of the arrows.*

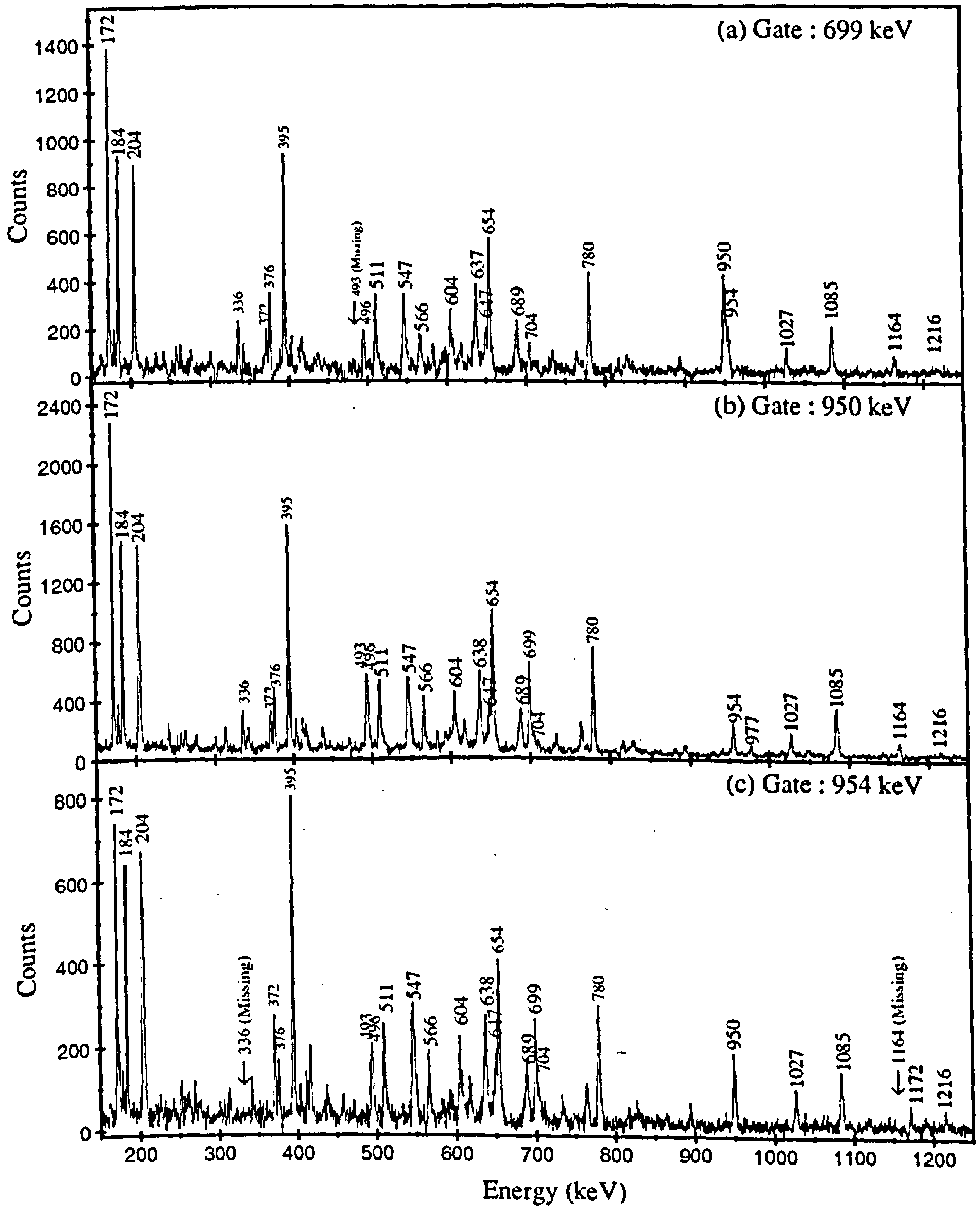

Figure 6.5: *Gates on (a) 699 keV, (b) 950 keV, and (c) 954 keV gamma-rays. The spectra are background subtracted. It can be seen that the 493 keV gamma-ray is present in both the 950 keV and 954 keV gated spectra while it is missing in the 699 keV gated spectrum. This shows that the 493 keV transition is not in coincidence with the 699 keV transition, while it is in coincidence with the 950 keV and 954 keV transitions. It can also be seen that the 336 keV and 1164 keV transitions are present in both the 950 keV and 699 keV gates but is not present in the 954 keV gate. This shows that the 336 keV and 1164 keV transitions are in coincidence with the 950 keV and 954 keV transitions but are not in coincidence with the 954 keV transition.*

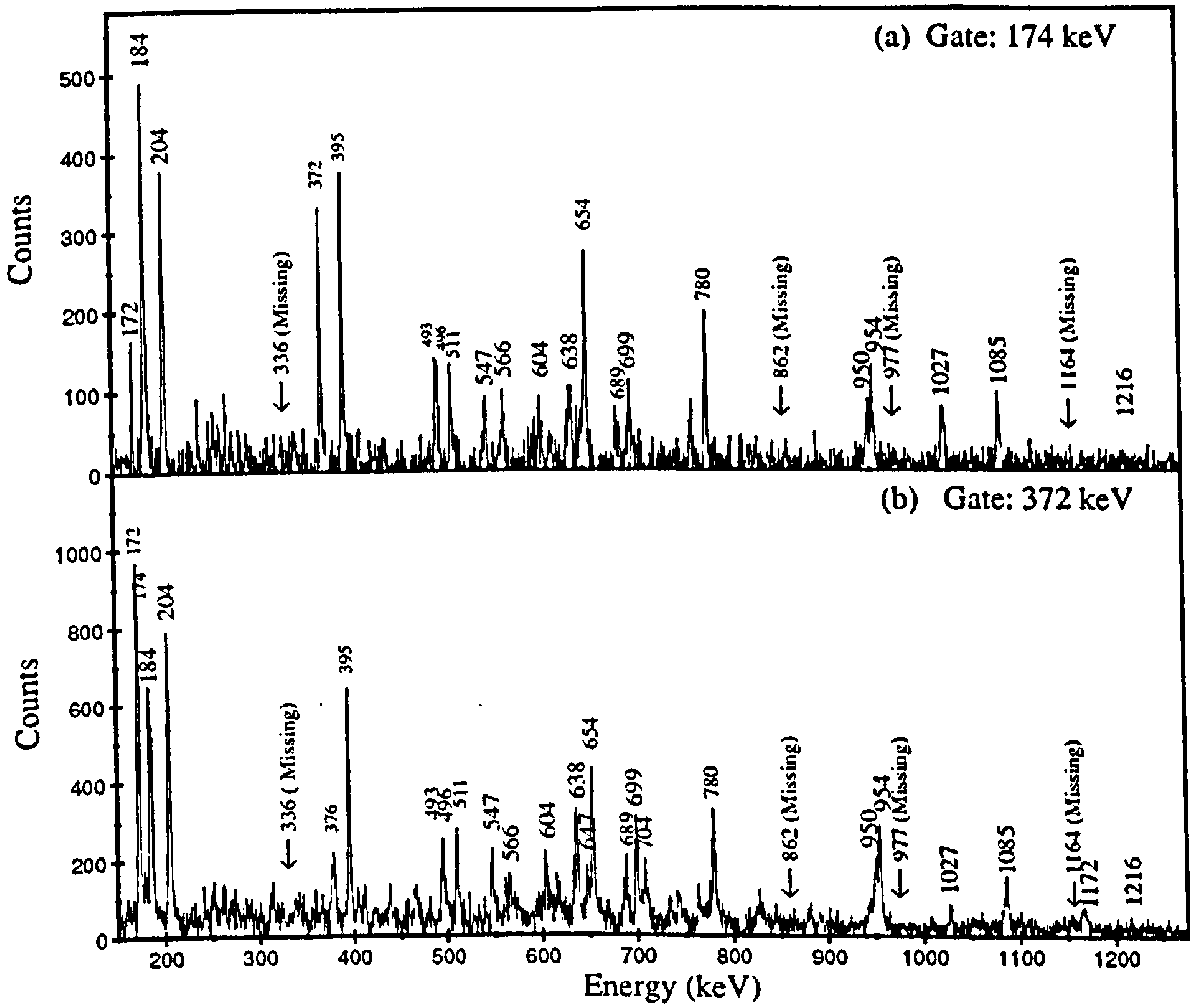

Figure 6.6: *Gates on (a) 174 keV and (b) 372 keV gamma rays. Both these gamma rays are in coincidence with each other and with the 950 keV and 954 keV gamma ray. But it can be seen that the 174 keV and 372 keV gamma ray transitions are not in coincidence with the 336 keV, 1164 keV, 393 keV, 977 keV and 862 keV gamma rays.*

6.2.2 Cascade from spin $35^{(-)}$ to 27^-

Eight transitions have been found in this cascade. These transitions have energies 393 keV, 977 keV, 251 keV, 1191 keV, 178 keV, 262 keV, 816 keV, 1078 keV and are shown on the right of figure 6.4. The 816 keV and 262 keV gamma rays are not in coincidence with 172 keV, 1085 keV, 1078 keV, 1172 keV, 354 keV, 493 keV, 699 keV and 950 keV gamma rays while they are in coincidence with rest of the transitions in the level scheme. The 206 keV gamma ray which feeds the $32^{(+)}$ level is not in coincidence with the 977 keV gamma ray in the cascade while the 393 keV gamma ray which feeds the 34^+ level is in coincidence with all the gamma rays of the cascade. The 493 keV gamma ray which feeds from the $32^{(+)}$ level to 31^+ does not coincide with transitions below the $32^{(+)}$ level in the cascade.

6.2.3 Cascade from spin $33^{(+)}$ to 27^-

This cascade of gamma rays consists of four transitions having energies 862 keV, 1119 keV, 354 keV and 1172 keV. The 354 keV and 1172 keV are already known transitions in this cascade. The 261 keV gamma ray feeds from $33^{(+)}$ to $31^{(+)}$ level into the cascade while the 269 keV gamma ray feeds out from $30^{(+)}$ level of the cascade into the 29^+ level. This cascade is in coincidence with all the transitions below 27^-.

6.2.4 Directional Correlation Results

In order to study the directional correlation of the gamma rays in ^{150}Gd and hence to find their spin values the total 230×10^6 events were re-sorted. Twelve out of the sixteen detectors of TESSA3 were used to measure the angular distributions.

Two correlation matrices were constructed with the following coincidence conditions respectively:

- Coincidences between two transitions detected in any 35° (or equivalent 145°) detectors (so called symmetrised (35° - 35°) matrix)
- Coincidences between 90° and 35° (145°) detectors (so called non - symmetrised (90° - 35° matrix).

Figure 6.7 (a) shows a spectrum which is a sum of the three spectra which were obtained after placing the gates on the 395 keV, 654 keV and 780 keV gamma ray transitions in the (35° - 35°) matrix. Before the generation of the "sum of gates" spectrum the individual gated spectra were background subtracted. Figure 6.7 (b) shows the "sum of gates" spectrum for the same gamma rays and with the same peak and background limits as in (a) but obtained from the (90° - 35°) matrix by gating on the 35° axis. It can be seen from the figure 6.7 that the known stretched quadrupole transitions are bigger in the (35° - 35°) matrix as compared with the (90° - 35°) matrix while the known stretched dipole transitions are bigger in the (90° - 35°) matrix as compared with the (35° - 35°) matrix.

From these spectra, the ratio $\mathcal{R} = (\frac{I(35^\circ - 35^\circ)}{I(90^\circ - 35^\circ)})$ for the intensities of the gamma-rays was extracted, where I(35° - 35°) is the intensity of γ_2 detected in a 35° detector while gated on γ_1 in another 35° detector, and I(90° - 35°) is the intensity of γ_2 detected in a 90° detector while gated on γ_1 in a 35° detector.

The ratios of the intensities, $\mathcal{R} = \frac{I(35^\circ - 35^\circ)}{I(90^\circ - 35^\circ)}$ were then normalised to the average value of the ratios of the intensities $\frac{I(35^\circ - 35^\circ)}{I(90^\circ - 35^\circ)}$ of the known stretched ($\Delta I = 2$) quadrupole γ rays in ^{150}Gd and are given in table 6.1. Hence,

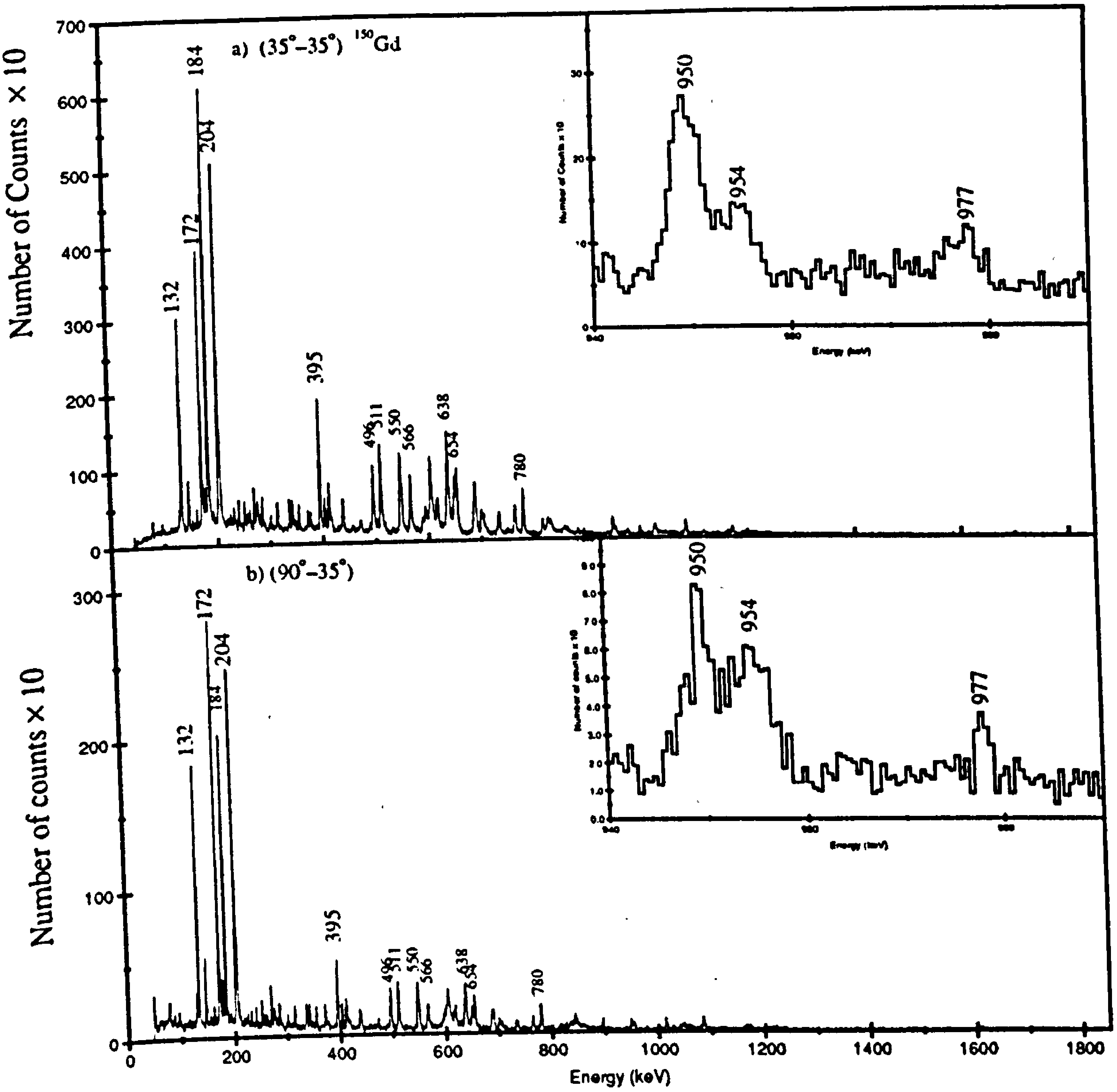

Figure 6.7: *(a) A "sum of gates" spectrum obtained by adding individual background subtracted spectra of the 395 keV, 654 keV and 780 keV gamma rays (known stretched quadrupoles) gates in the (35° - 35°) matrix. (b) A "sum of gates" spectrum with the same gamma rays and with the same peak and background limits as in (a) but for the (90° - 35°) matrix. It can be seen that the 184 keV, 395 keV, 654 keV, 780 keV and 699 keV etc... transitions which are known stretched quadrupole transitions are seen bigger in the (35° - 35°) matrix as compared with the (90° - 35°) matrix while the 132 keV, 172 keV, 354 keV etc transitions which are known stretched dipoles are stronger in the (90° - 35°) matrix as compared with the (35° - 35°) matrix. The insets show the 950 keV, 954 keV and 977 keV gamma ray transitions. The 950 keV transition is considered to be a stretched quadrupole while the 954 keV transition is considered to be a stretched dipole transition. The 977 keV transition is considered to be a stretched quadrupole transition.*

stretched quadrupole transitions were found to have values $\mathcal{R}\approx 1$ and stretched dipole ($\Delta I = 1$) transitions were found to have values $\mathcal{R}\approx 0.6$.

Fig. 6.8 and table 6.1 give the summary of the results from the DCO analysis. It can be seen from the figure 6.8 that the ratio '$\mathcal{R}$' for the newly observed γ-rays is consistent with those from known yrast stretched dipole (ΔI=1) and quadrupole (ΔI=2) transitions. The newly observed γ-ray transitions having energies 129 keV, 178 keV, 206 keV, 251 keV, 262 keV, 336 keV, 372 keV, 1078 keV and 1119 keV are therefore considered as stretched dipole (ΔI=1) transitions while 977 keV, 1027 keV, 1164 keV, 1191 keV are considered to be the stretched quadrupole (ΔI=2) transitions. The 1216 keV ($39^{(+)}$) is clearly seen in the ($90^\circ - 35^\circ$) matrix but is very weak in ($35^\circ - 35^\circ$) matrix, so it is difficult to find exact intensity ratio ($\mathcal{R}$) for this gamma ray transition, but due to its consistency with other stretched dipole transitions which are bigger in the ($90^\circ - 35^\circ$) matrix, and weaker in the ($35^\circ - 35^\circ$) matrix, it is considered to be a stretched dipole transition. The 862 keV ($33^{(+)}$) gamma ray transition is very weak in the ($90^\circ - 35^\circ$) matrix but it is much stronger in the ($35^\circ - 35^\circ$) matrix and hence the 862 keV transition has been considered to be a stretched quadrupole (ΔI=2) transition in the present work. The transitions having energies 950 keV ($31^{(+)}$) and 954 keV ($34^{(-)}$) which have been considered to be a stretched dipole and stretched quadrupole respectively in the previous work, are now considered to be a stretched quadrupole and stretched dipole respectively, in this work. The new spin assignments for the levels decaying via these transitions are quite consistent with the data for the present work. Finally, the 372 keV ($35^{(+)}$) transition is considered as an ambiguous transition because it has the value of $\mathcal{R} \approx 0.8$. This ambiguity may arise from the uncertainties in the mixing ratio (the ratio of the transition matrix elements for the higher to the lower multipole). Since the ratio $\mathcal{R}$ for this transition is close to the ratio $\mathcal{R}$ of the other stretched E1 transitions, it is considered to be a stretched dipole (E1) transition. The 174 keV transition is considered to be an M1 trasition, because M1 ratios appear "low" because of mixing ratio.

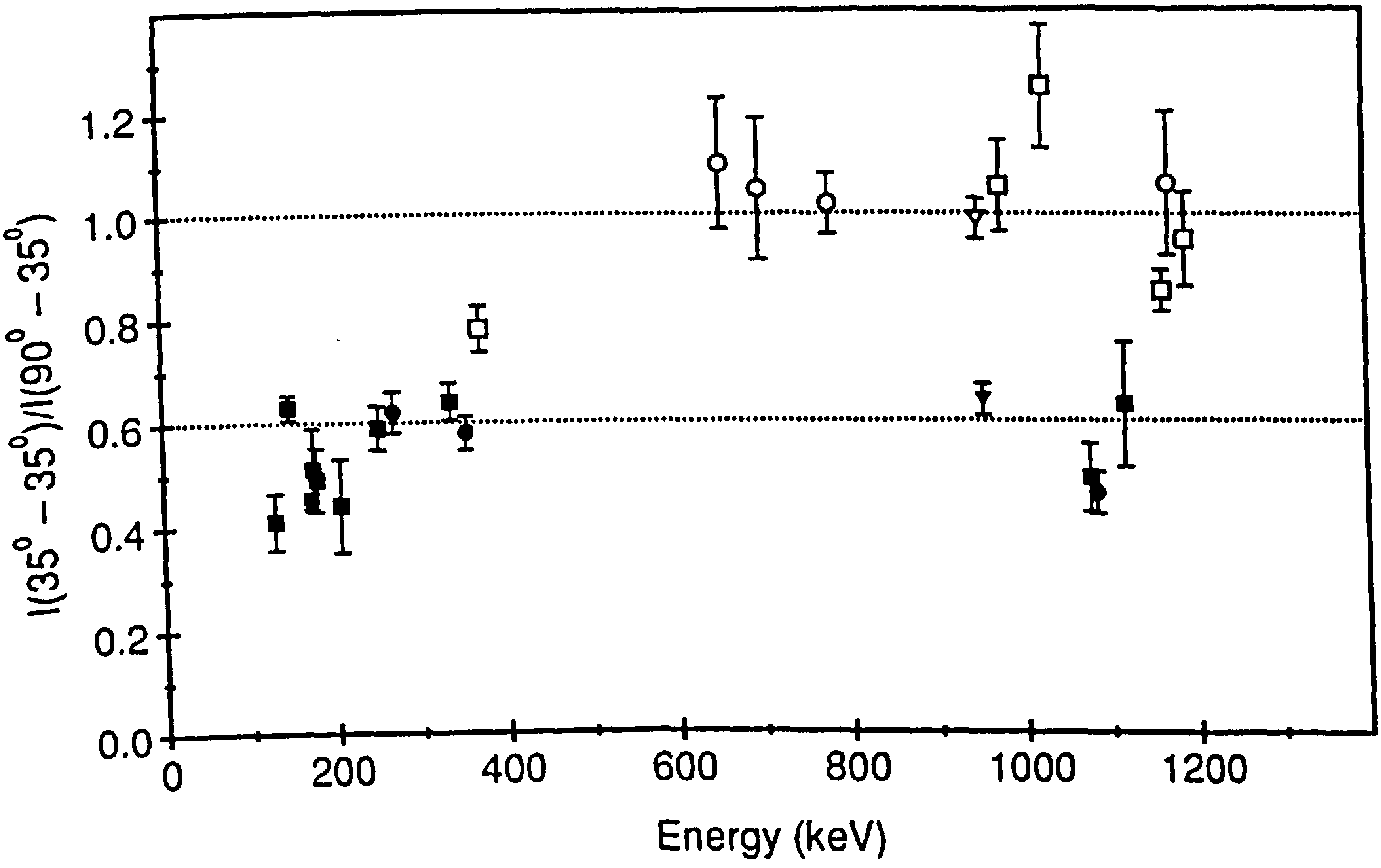

Figure 6.8: *Results from the DCO analysis for the ratio* $\mathcal{R} = \frac{I(35^\circ-35^\circ)}{I(90^\circ-35^\circ)}$ *for the stretched dipole and stretched quadrupole* γ*-ray transitions in the* ^{150}*Gd nucleus above spin* 27^-*. The dotted lines indicates the value of* $\mathcal{R}$ *at* ≈ 0.6 *and* $\mathcal{R}$ *at* ≈ 1*. The open circles reperesent the ratio "*$\mathcal{R}$*" for the known stretched quadrupole transitions while the open squares represent the ratio for the stretched quadrupole transitions which have been observed in this work. Similarly the closed circles and closed squares represent the ratio for the known and newly observed stretched dipole transitions in this work, respectively. The open and closed triangles represent the transitions whose previously observed spins have been changed due to this work.*

Table 6.1

$E_x$$^{a)}$ (keV)	$E_\gamma$$^{b)}$ (keV)	$I_\gamma$$^{c)}$ (%)	$\mathcal{R}^d = \frac{I(35^\circ-35^\circ)}{I(90^\circ-35^\circ)}$	$^{e)}I_i^\pi \rightarrow {}^{f)}I_f^\pi$
6495	780	100.0±2.1	1.02±0.12	$23^- \rightarrow 21^-$
7275	654	99.0±4.0	1.10±0.13	$25^- \rightarrow 23^-$
7929	395	99.0±3.0	1.05±0.11	$27^- \rightarrow 25^-$
8324	1085	46.3±0.5	0.46±0.04	$28^{(+)} \rightarrow 27^-$
8324	1172	24.3±0.3	1.06±0.14	$29^{(+)} \rightarrow 27^-$
8324	1078	2.7±0.3	0.35±0.09	$28^{(+)} \rightarrow 27^-$
9409	172	42.0±0.3	0.46±0.04	$29^{(-)} \rightarrow 28^{(+)}$
9402	178	6.0±0.2	0.51±0.04	$29^{(-)} \rightarrow 28^{(+)}$
9496	354	8.0±0.3	0.51±0.04	$30^{(+)} \rightarrow 29^{(+)}$
9581	950	44.0±1.2	0.94±0.06	$31^{(+)} \rightarrow 29^{(-)}$
9850	1119	4.0±0.5	0.53±0.18	$31^{(+)} \rightarrow 30^{(+)}$
9581	1191	4.0±0.2	0.90±0.11	$32^{(+)} \rightarrow 30^{(+)}$
10531	493	Doublet	——	$32^{(+)} \rightarrow 31^{(+)}$
10531	699	28.3±0.9	0.98±0.13	$33^{(+)} \rightarrow 31^{(+)}$
10772	251	6.0±0.3	0.54±0.04	$32^{(+)} \rightarrow 31^{(-)}$
11023	206	2.0±0.2	0.45±0.09	$33^{(+)} \rightarrow 32^{(+)}$
11023	977	9.0±0.3	0.94±0.27	$34^{(+)} \rightarrow 32^{(+)}$
11230	954	25.0±1.0	0.70±0.05	$34^{(-)} \rightarrow 33^{(+)}$
11230	1164	10.0±0.5	1.11±0.1	$35^{(-)} \rightarrow 33^{(+)}$
12000	393	Doublet	————	$35^{(-)} \rightarrow 34^{(+)}$
12184	372	9.0±0.4	0.74±0.02	$35^{(+)} \rightarrow 34^{(-)}$

continued ....

$E_x{}^{a)}$ (keV)	$E_\gamma{}^{b)}$ (keV)	$I_\gamma{}^{c)}$ (%)	$\mathcal{R}^d = \frac{I(35^\circ-35^\circ)}{I(90^\circ-35^\circ)}$	${}^{e)}I_i^\pi \rightarrow {}^{f)}I_f^\pi$
12184	416	Doublet	0.51±0.06	$(36)^{(+)} \rightarrow 35^{(-)}$
12394	336	10.1±0.74	0.70±0.05	$36^{(+)} \rightarrow 35^{(-)}$
12556	174	4.3±0.5	0.49±0.05	$36^{(+)} \rightarrow 35^{(+)}$
12600	129	2.7±0.3	0.40±0.03	$36^{(+)} \rightarrow 35^{(+)}$
12730	1027	18.0±0.5	1.04±0.09	$38^{(+)} \rightarrow 36^{(+)}$
13757	1216	4.0±0.2	0.51±0.03	$39^{(+)} \rightarrow 38^{(+)}$

Table 6.1: The properties of the transitions in ^{150}Gd above spin 21^- as measured in the present work.

$^{a)}$ Excitation energy E_x of the decaying level.

$^{b)}$ The transition energy E_γ.

$^{c)}$ The intensities I_γ of the gamma-rays.

$^{d)}$ Ratio of the intensity of the gamma-ray transition detected in a 35° detector while gated on another 35° detector to the intensity of gamma-ray transition detected in a 90° detector while gated on a 35° detector.

$^{e)}$ Initial spin and parity of the energy state.

$^{f)}$ Final spin and parity of the energy state.

Part II

Level Scheme of ^{152}Dy

6.3 Level Scheme of ^{152}Dy

6.3.1 Introduction

The level scheme of ^{152}Dy has been studied by many groups since 1974. Jansen *et al.*, [Ja 74a, Ja 79] established the sequence up to about 8 MeV excitation energy and included the discovery of two isomeric states with lifetimes of $\tau = 60$ ns and $\tau = 13$ ns. The transition energy from the decay of the longer lived state was unobserved but was later measured by Nagai *et al.*, [Na 80] to be $E_\gamma = 53.3$ keV. Groups at the Argonne National Laboratory, (Khoo *et al.*, [Kh 78]) and at Chalk River, (Haas *et al.*, [Ha 79, Ha 81]) along with groups at Strasbourg, (Merdinger *et al.*, [Me 79]) extended the scheme up to spin $38\hbar$ using many experimental techniques. These include measurements of prompt and delayed gamma rays, prompt and delayed $\gamma-\gamma$ coincidences, $\gamma-\gamma$ angular correlations of delayed gamma rays, excitation functions, angular distributions, n-γ coincidences, gamma ray linear polarizations and Doppler shift recoil distance measurements. The lifetime, spin and parity of the isomers were found to be

- $\tau = 60\pm$ 4 ns, $I^\pi = 17^+$
- $\tau = 9.5\pm$ 0.7 ns, $I^\pi = 21^-$
- $\tau = 1.6\pm$ 0.3 ns, $I^\pi = 27^-$.
- The lifetime (in the range of ps), spin and parity of the other isomeric states can be found in [Vo 83].

The discovery of a low deformation prolate band (B.M. Nyako *et al.*, [Ny 86]) and superdeformed prolate band (P.J. Twin *et al.*, [Tw 86]) made ^{152}Dy a classic nucleus for the study of high spin states.

6.3.2 Methods

In order to study various properties of the nucleus at very high spin, an experiment (see section 5.9.2) was performed at Daresbury Laboratory using the reaction $^{108}Pd(^{48}Ca,4n)^{152}Dy$ at a beam energy of 197 MeV. A two dimensional E_γ-E_γ correlation matrix was created having a fold condition 8<fold<16 with an isomer TAC filter selecting "delayed" events. It should be remembered that the fold data recorded in the BGO ball was artificially low in this experiment due to the elements of the ball having a threshold of $\sim$ 500 keV. A form of background subtraction on the isomer matrix was performed during data sorting by subtracting events filtered by an isomer TAC gate associated primarily with random events.

A portion of the total γ-ray yield from the 197 MeV thin target γ-γ experiment with only the highfold (fold $\geq$ 8) condition in the mastergate is shown in figure 6.9 (a) while figure 6.9 (b) is the total projection of the final isomer matrix containing $\sim$ 17.5$\times$ 10^6 events. Figure 6.9(b) indicates the excellent quality of the data from this experiment as a consequence of the high statistics involved. The selection power of the TESSA3 array is clearly illustrated in figure 6.9 with the isomer matrix consisting of approximately 95% ^{152}Dy and 4% ^{151}Dy with almost no ^{153}Dy.

The previous decay scheme of ^{152}Dy is shown in figure 6.10 and illustrates the information gained from many of the spectroscopic methods and provides a good starting point for a continued study into the very high spin states of this nucleus.

6.4 Results

Gamma ray spectra were generated by gating on all the visible peaks in the total projection spectrum and making projections from the total $E_\gamma - E_\gamma$ matrix. The total projection for ^{152}Dy is shown in figure 6.9. New transitions were added to the level scheme and the order of several transitions has been

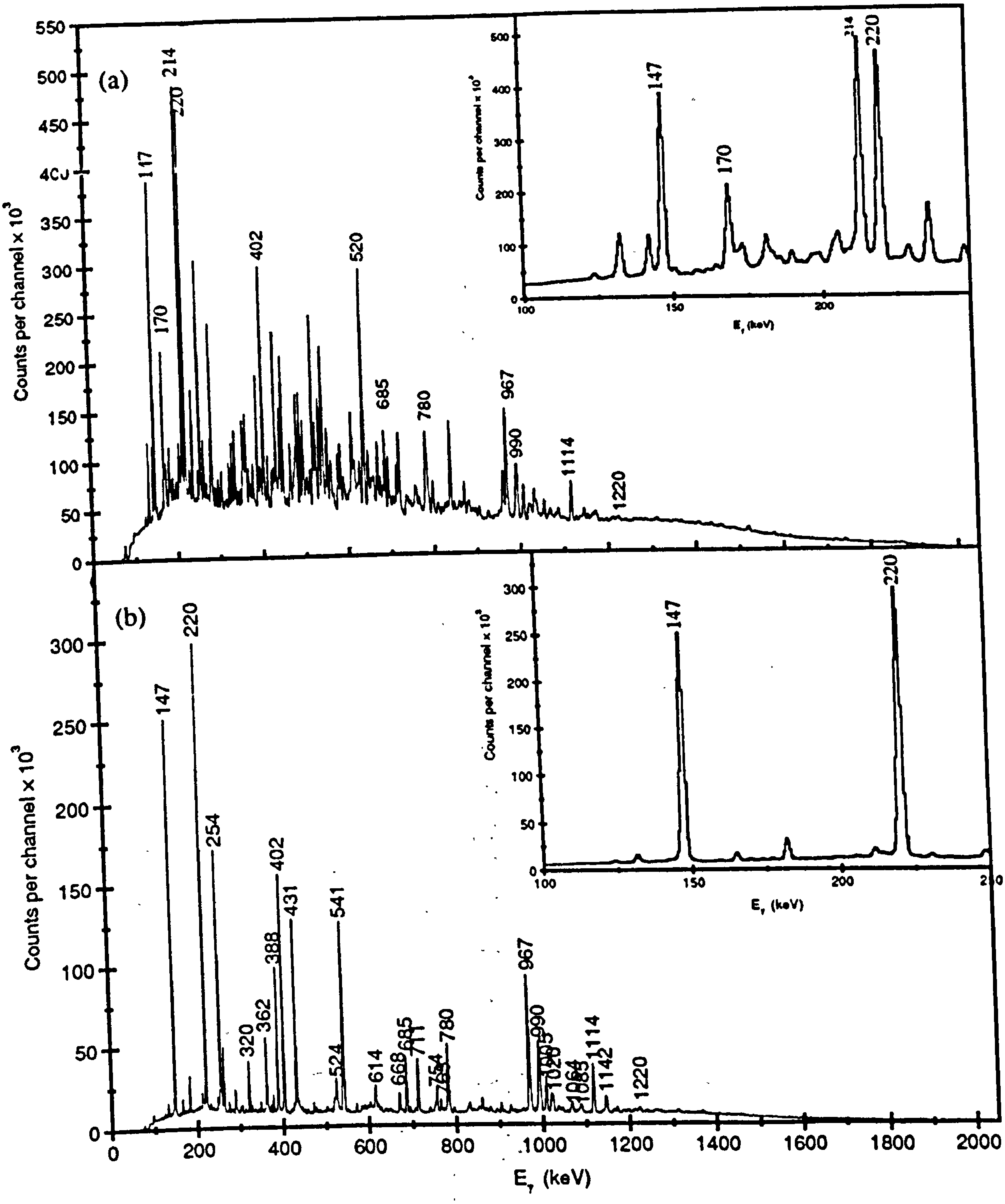

Figure 6.9: *(a) Total gamma-ray spectrum for the 197 MeV thin target experiment and (b) the same data satisfying two or more Compton-suppressed germanium detectors firing simultaneously with a fold condition of 8<fold<16 after appropriate filtering on the isomer TAC signal. The 170 and 214 keV gamma ray transitions which belong to ^{153}Dy can be seen in the inset of (a) and are almost negligible in the inset of (b).*

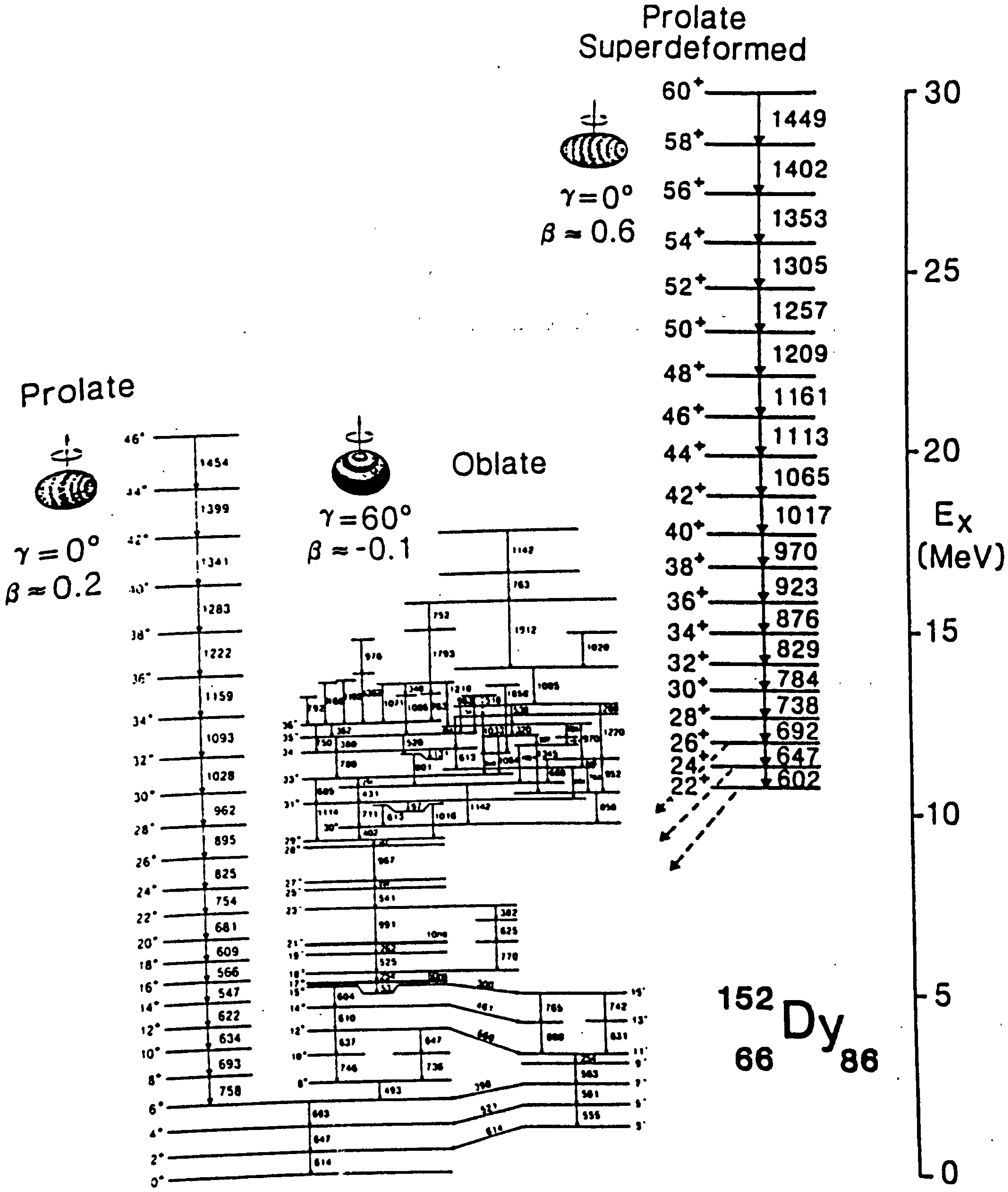

Figure 6.10: *The level scheme of* ^{152}*Dy incorporating the previously observed information by many groups. The low deformation prolate rotational band (left), the oblate single particle states (middle) and the superdeformed prolate rotational band (right) can be seen clearly.*

changed. Figure 6.11 shows the level scheme of ^{152}Dy which has been extended above spin 27$^-$ in this work. Figure 6.12 shows the level scheme expanded to include I$\geq$27$^-$ only.

6.4.1 Decays Feeding the 36$^-$ Level

Directly above I=36$^-$ the level scheme becomes extremely fragmented which is probably due to the breaking of the ^{146}Gd core. Several new transitions have been observed to feed the 36$^-$ level. In order to find these new trasitions gates were placed on the 362 keV (36$^-$) and 388 keV (35$^-$) γ-ray transitions. Figure 6.13 shows the spectrum obtained by adding the background subtracted gates of the 388 keV and 362 keV gamma-rays. Six new transitions have been observed which feed into this level. These new transitions which feed into the 36$^-$ level have energies 477 keV, 724 keV, 1037 keV, 1042 keV, 1078 keV and 1235 keV and are shown in figure 6.14 along with the previously observed transitions. The intensities of all the previously observed and newly observed transitions feeding the 36$^-$ level are obtained relative to the intensity of the 362 keV gamma ray in 388 keV gamma ray gate and are presented in table 6.2. It can be seen from the table 6.2 that the intensities of the transitions feeding into the 36$^-$ level equals that decaying via the 36$^-$ level. From the measurement of the intensities of the the gamma-ray transitions which feed out of the 36$^-$ level and which feed into the 36$^-$ level it is evident (within the experimental errors) that no more transition can be observed which feed into the 36$^-$ level.

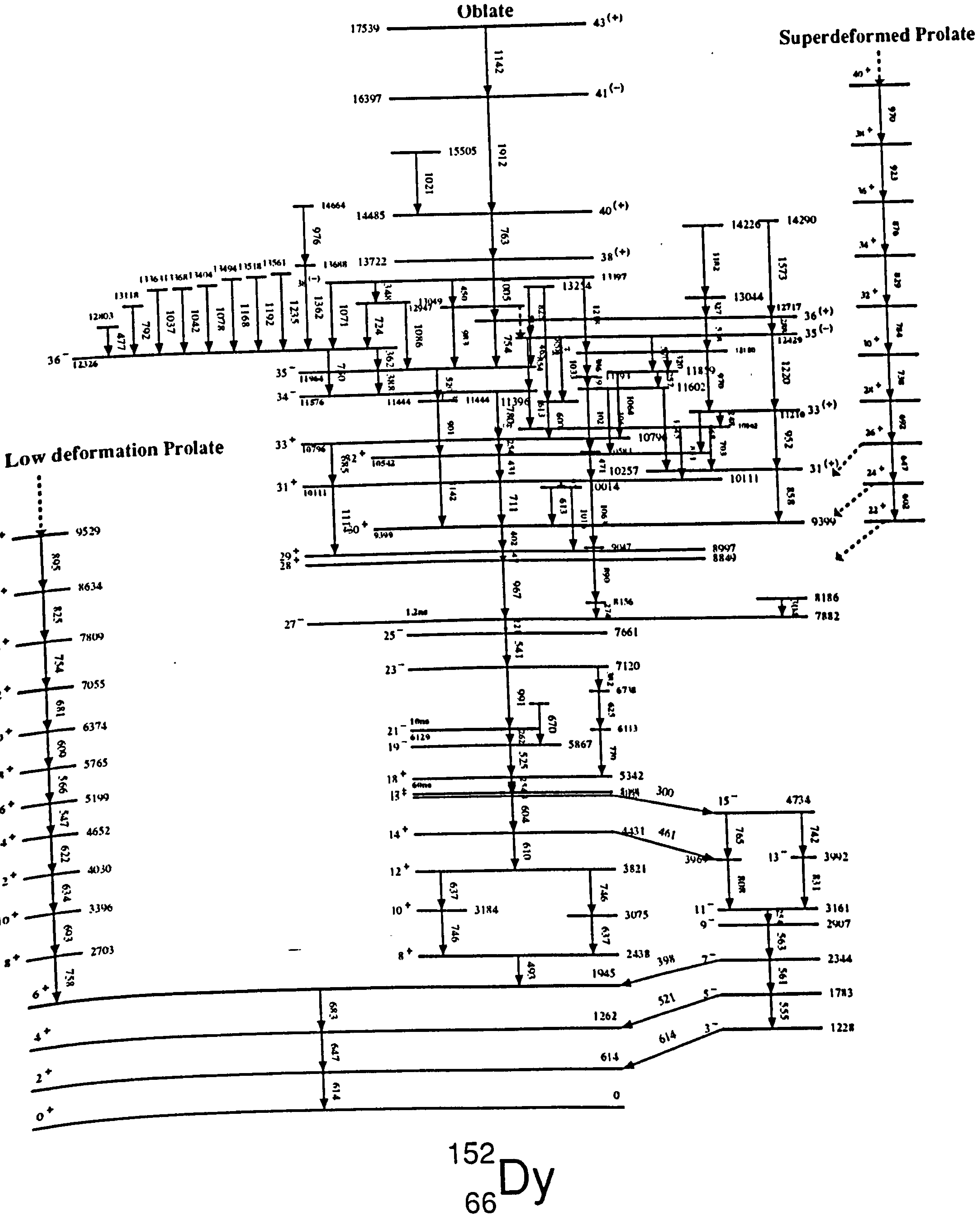

Figure 6.11: *The new level scheme of* ^{152}*Dy. Above spin* 27^- *the difference between the new and old level schemes for the oblate single particle states has been discussed in detail in the text.*

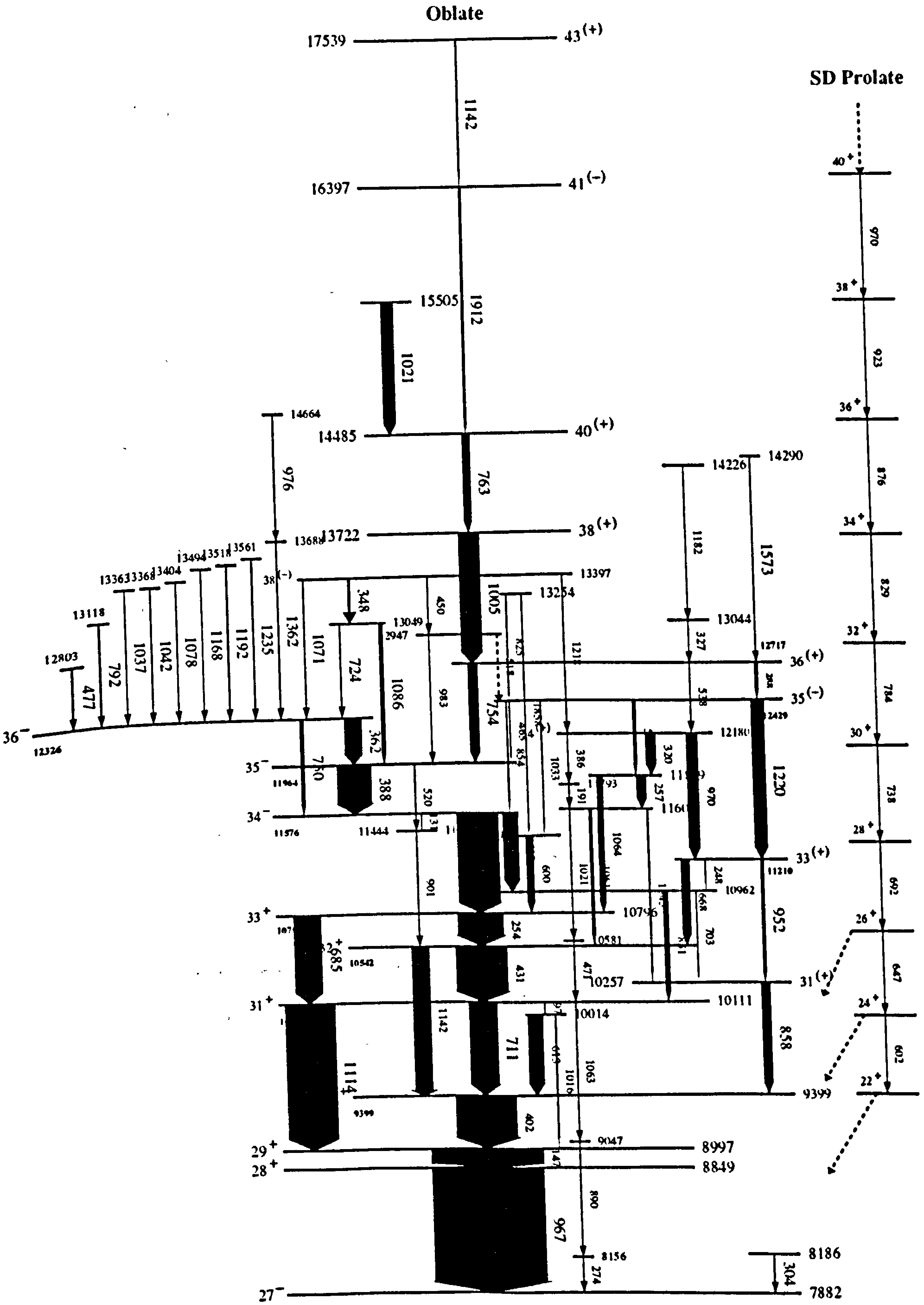

Figure 6.12: *Partial level scheme of ^{152}Dy above spin 27^-. Relative γ-ray intensities are represented by the thickness of the arrow.*

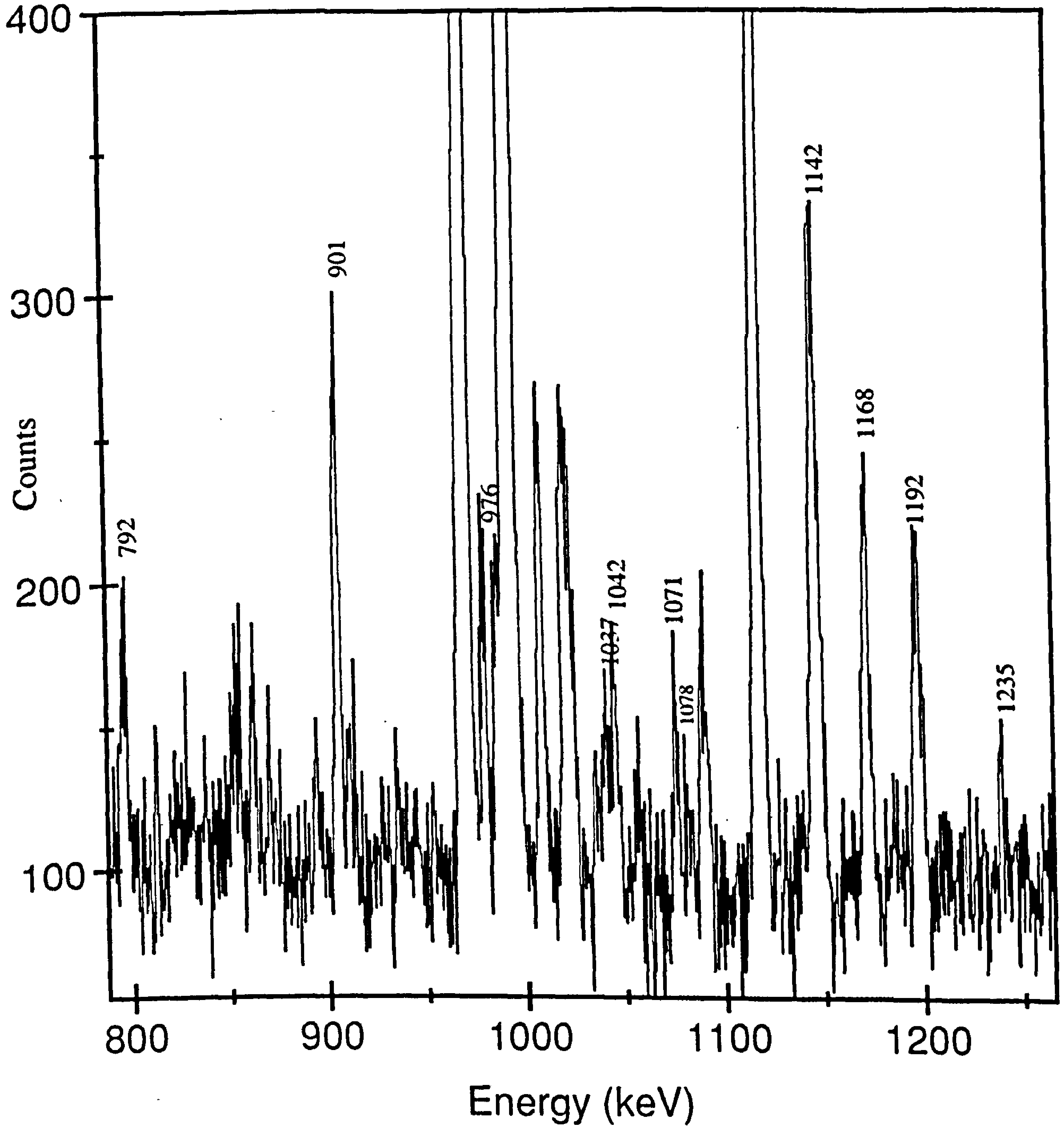

Figure 6.13: *Spectrum obtained by combining the gates on 362 keV and 388 keV γ - rays. The spectrum shows the energies of the gamma-rays between 750 keV to 1300 keV only.*

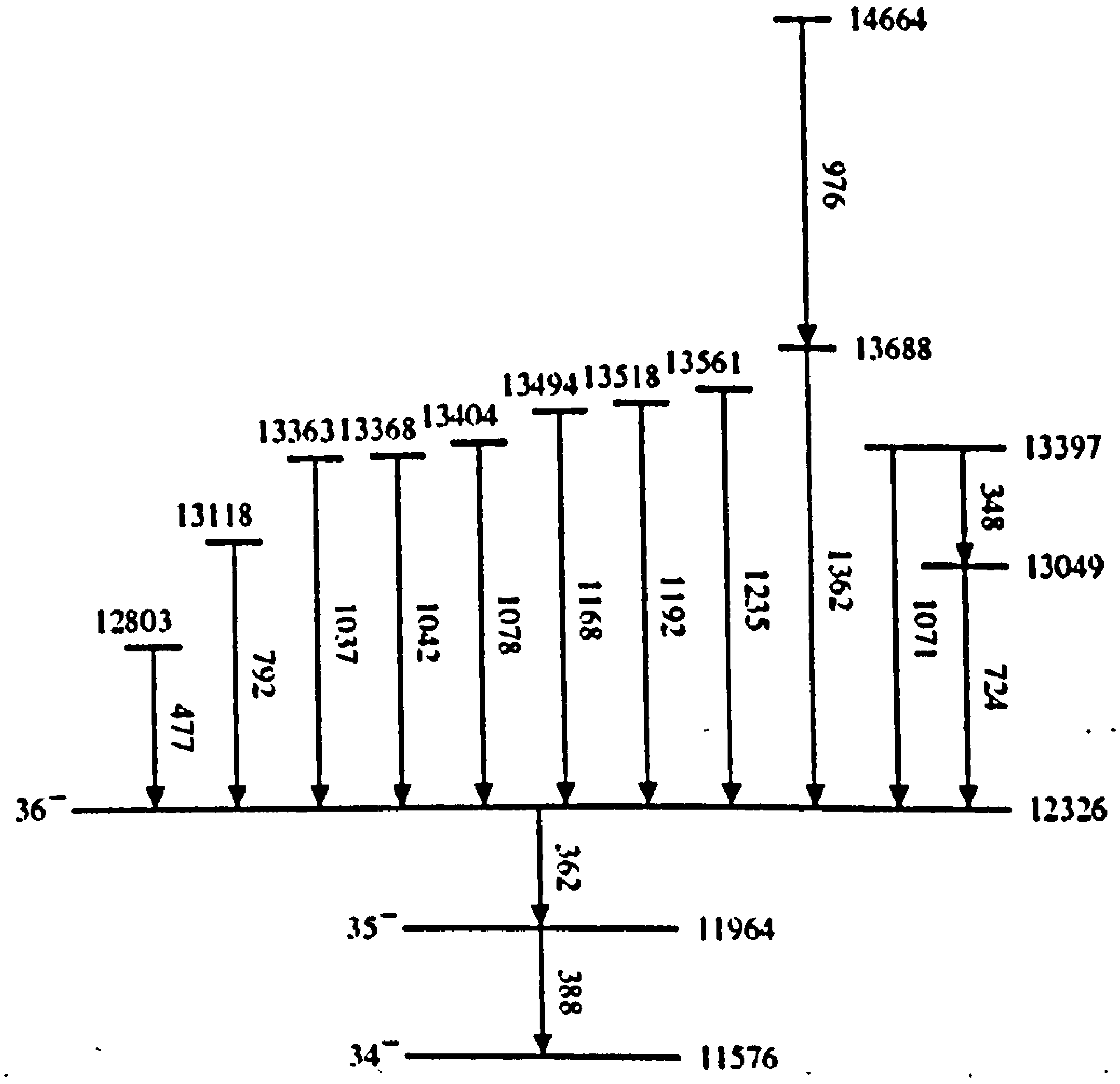

Figure 6.14: *Partial level scheme of* ^{152}Dy *showing the part of the level scheme above spin* 34^-.

Table 6.2

E_γ [a] (keV)	I_γ^{rel} [b]	I% [c]
362	3914±148	100±3.78

E_γ(keV)	I_γ^{rel}	I%	Cumulative of I%
348	335±20	8.55±0.51	
477*	116±13	2.96±0.33	11.51±0.84
724*	51±8	1.30±0.20	12.80±1.04
792	137±8	3.50±0.21	16.30±1.25
976	333±21	8.51±0.53	24.81±1.78
1037*	177±15	4.52±0.38	28.33±2.16
1042*	336±20	8.58±0.51	36.91±2.66
1071	161±21	4.11±0.53	41.02±3.19
1078*	294±22	7.51±0.56	48.53±3.75
1168	490±27	12.51±0.69	61.04±4.44
1192	677±37	17.31±0.95	78.35±5.39
1235*	105±22	2.69±0.56	81.04±6.85
1362	835±40	21.34±1.02	102.38±7.28

Table 6.2: *The intensity of the γ-rays feeding the 36^- level.*

[a] *The energy of the γ-ray transition emitted during the heavy ion fusion evaporation reaction.*

[b] *The intensity of the γ-ray relative to the intensity of 362 keV gamma- ray in 388 keV gamma ray gate.*

[c] *Percentage of I_γ^{rel}.*

[*] *Energy of the newly observed gamma-ray transition.*

6.4.2 Decay of States Around Spin 27^-

The states around spin 27^- are of interest because this is the region into which the superdeformed band decays. Figure 6.15 shows the partial level scheme of ^{152}Dy around spin 27^-. In this work several new transitions have been identified in this spin region of which one, the 304 keV transition feeding the 27^- state, is in coincidence with the superdeformed band. It has also be seen from the spectrum obtained by placing a gate on the 304 keV gamma-ray transition that the intensity of the superdeformed peaks is very low so that it is difficult to find the linking transition(s) between the normal deformed and the superdeformed decays. However, it may be possible with high statistics to find the linking transition(s). The remaining new transitions (274 keV, 890 keV, 1063 keV, 471 keV, 1021 keV) in this spin region form a cascade feeding the 27^- state. The 274 keV, 890 keV, 1063 keV gamma ray transitions are in coincidence with all the transitions above 31^+ and below 27^- level but are not in coincidence with transitions in between the $31^+ \rightarrow 27^-$ levels. The 471 keV gamma ray transition is not in coincidence with the 431 keV and other yrast transitions above spin 31^+ but is in coincidence with all the transitions below 31^+. The 1021 keV gamma ray transition which is a doublet (the transition having near identical energy to another transition in the level scheme) has been shown feeding the 471 keV gamma ray. The other transitions (191 keV, 386 keV, 1218 keV) in the cascade were known prior to this work. Since the intensities of the transitions in this cascade are very weak, it is difficult to find the exact spins of these transitions from this data.

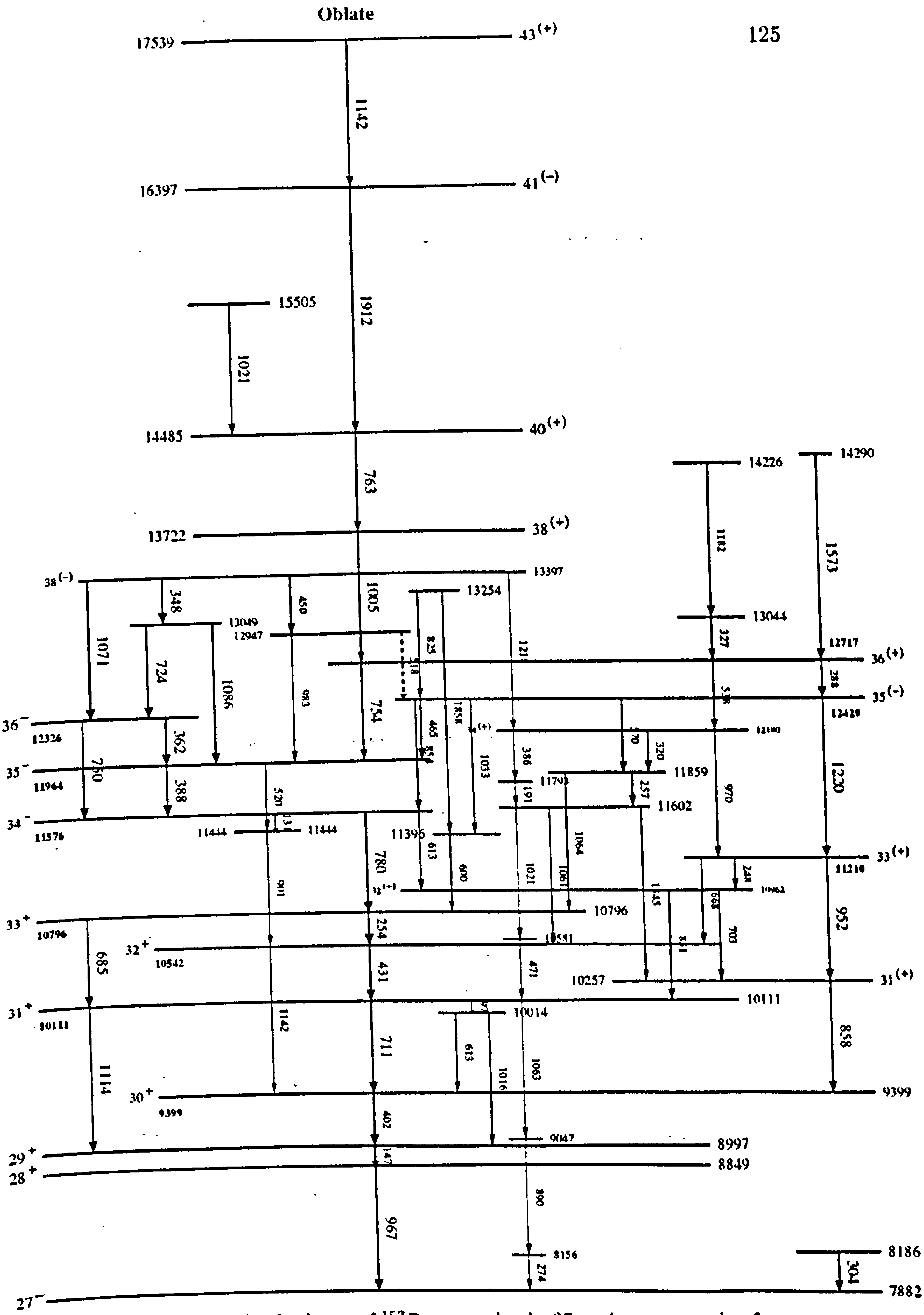

Figure 6.15: *Partial level scheme of ^{152}Dy around spin 27^{-}. A new cascade of γ-rays feeding the 27^{-} state is clearly seen.*

6.4.3 Decays By Passing the 36^- Level

A cascade of gamma ray transitions has already been found from spin $43^+ \rightarrow 35^-$ in this region of the level scheme (figure 6.15). Most of the gamma ray transitions in this region have been assigned as positive parity. None of the gamma ray transitions in the cascade (from 43^+ to 35^-) are in coincidence with the 36^- energy state. The ordering and positioning of the known and newly found transitions in this region is discussed below:

- The 763 keV ($40^{(+)}$) and 1912 keV ($41^{(-)}$) gamma rays have been reordered according to their intensities, measured in the gates of the 288 keV and 1005 keV gamma rays. In these gates we observe that the 1912 keV gamma ray is much weaker than the 763 keV gamma ray. The relative intensities of 763 keV and 1912 keV gamma rays as measured in the 288 keV and 1005 keV gamma ray are shown in tables 6.3 and 6.4, respectively.
- The new transitions (327 keV, 450 keV, 465 keV, 570 keV, 1182 keV and 1573 keV) have been placed in accordance with their coincidence relationships with the known transitions. These γ-rays are very weak and it is difficult to find their relative intensities and spins.
- The 327 keV and 1182 keV transitions feeding into the $36^{(+)}$ level are in coincidence with each other and are not in coincidence with the 362 keV transition (which feeds out from the 36^- level) and all the gamma rays above this level. The 1573 keV gamma ray transition feeding into the $36^{(+)}$ is not in coincidence with the 327 keV and 1182 keV (which also feed into the $36^{(+)}$ level) and the 362 keV gamma ray transition, and all the transitions above the 36^- level. The 327 keV, 1182 keV and 1573 keV gamma rays are also not in coincidence with other transitions which feed the 36^+ level.
- The 450 keV gamma ray transition is in coincidence with the known 983 keV and 388 keV transitions but it is not in coincidence with the 362

keV transition and all the other transitions feeding the 35^- level.

- The 465 keV transition links the 35^- non yrast level to the 35^- yrast level. This gamma ray is in coincidence with all the transitions above and below the 35^- non yrast level and 35^- yrast level respectively, but is not in coincidence with all the transitions which feed directly into the 35^- yrast level or which are above the 36^- level.

- The 570 keV gamma ray transition is in coincidence with the 288 keV and 257 keV gamma rays and with all the gamma rays which feed the $(33)^{(+)}$ level. But this gamma ray is not in coincidence with the 320 keV, 386 keV, 538 keV gamma rays in this region. So this gamma ray is shown feeding from the 35^- level to the $(33)^{(+)}$ level.

Table 6.3

E_γ (keV)	I_γ
763	288±28
1912	99±35

Table 6.3: Gate on 288 keV gamma ray transition. In the table E_γ represents the energy of the γ-ray while I_γ represents the intensity of the gamma ray.

Table 6.4

E_γ (keV)	I_γ
763	710±50
1912	415±85

Table 6.4: Gate on 1005 keV gamma ray transition. In the table E_γ represents the energy of the γ-ray while I_γ represents the intensity of the gamma ray.

6.4.4 Directional Correlation Results

The directional correlation measurements for ^{152}Dy were carried out in a similar way as described in section 6.2.4. Two correlation matrices were constructed with the same coincidence condition as given in section 6.2.4 i.e.,

- Coincidences between two transitions detected in any 35°(or equivalent 145°) detectors (so called symmetrised (35° - 35°) matrix)
- Coincidences between a 90° and 35°(145°) detectors (so called non - symmetrised (90° - 35°) matrix).

A background subtracted spectrum, obtained by placing a gate on the 991 keV γ-ray (which is a known stretched (Δ I=2) quadrupole transition in the level scheme) in (35° - 35°) matrix, is shown in figure 6.16 (a), while figure 6.16 (b) shows the spectrum obtained from the (90° - 35°) matrix for the same gate with the same peak and background limits as in (a). Figure 6.17 (a) shows a similar spectrum which has been obtained by placing a gate on the known stretched dipole (Δ I=1) transition in the (35° - 35°) matrix while figure 6.17 (b) shows the spectrum from the same gate as in (a) but from the (90° - 35°) matrix. It can be seen we get similar results for the ratio $\mathcal{R}$, whether the spectrum used for the calculation of $\mathcal{R}$ is obtained from a gate on a stretched quadrupole or stretched dipole radiation.

From such spectra, the ratio $\mathcal{R} = (\frac{I(35^\circ-35^\circ)}{I(90^\circ-35^\circ)})$ for the intensities of the gamma-rays was extracted in a similar way as in section 6.2.4, where I(35° - 35°) is the intensity of γ_2 detected in a 35° detector while gated on another 35° detector, and I(90° - 35°) is the intensity of γ_2 detected in a 90° detector while gated on a 35° detector.

The ratios of the intensities, $\mathcal{R} = \frac{I(35^\circ-35^\circ)}{I(90^\circ-35^\circ)}$ were normalised to the average value of the ratios of the intensities $\frac{I(35^\circ-35^\circ)}{I(90^\circ-35^\circ)}$ of the known stretched quadrupole (Δ I=2) γ rays in ^{152}Dy. Hence, stretched quadrupole (Δ I=2)radiations were found to have $\mathcal{R} \approx 1$ and stretched dipole (Δ I=1) radiations were found to have $\mathcal{R} \approx 0.5$.

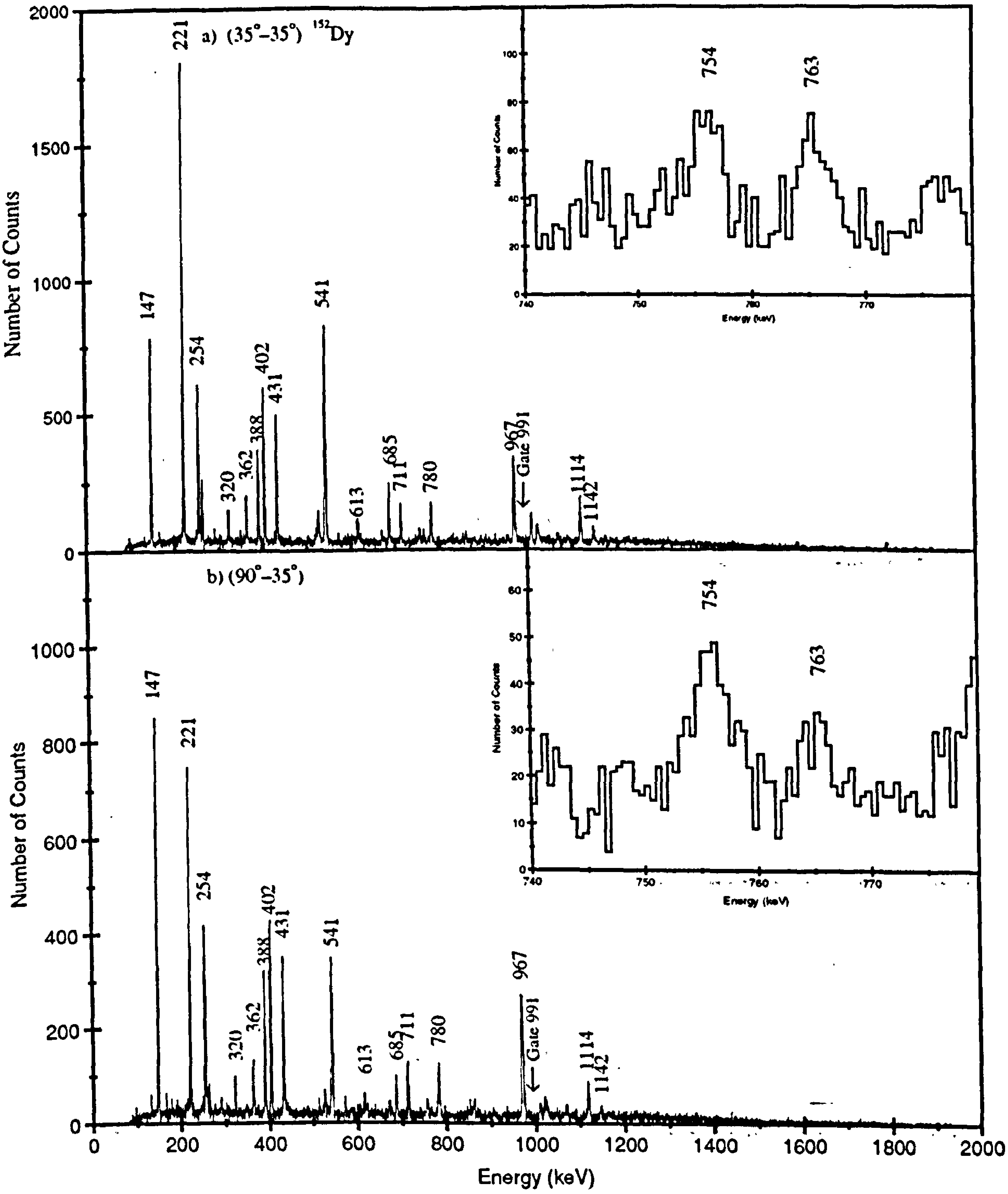

Figure 6.16: *(a) A spectrum gated on the 991 keV gamma ray (stretched dipole) after background subtraction, obtained from the (35° - 35°) matrix. (b) A spectrum with the same peak and background limits as for (a) but for the (90° - 35°) matrix. Insets show the 754 keV and 763 keV transitions which have been considered as the stretched dipole and stretched quadrupole transitions respectively, in the present work.*

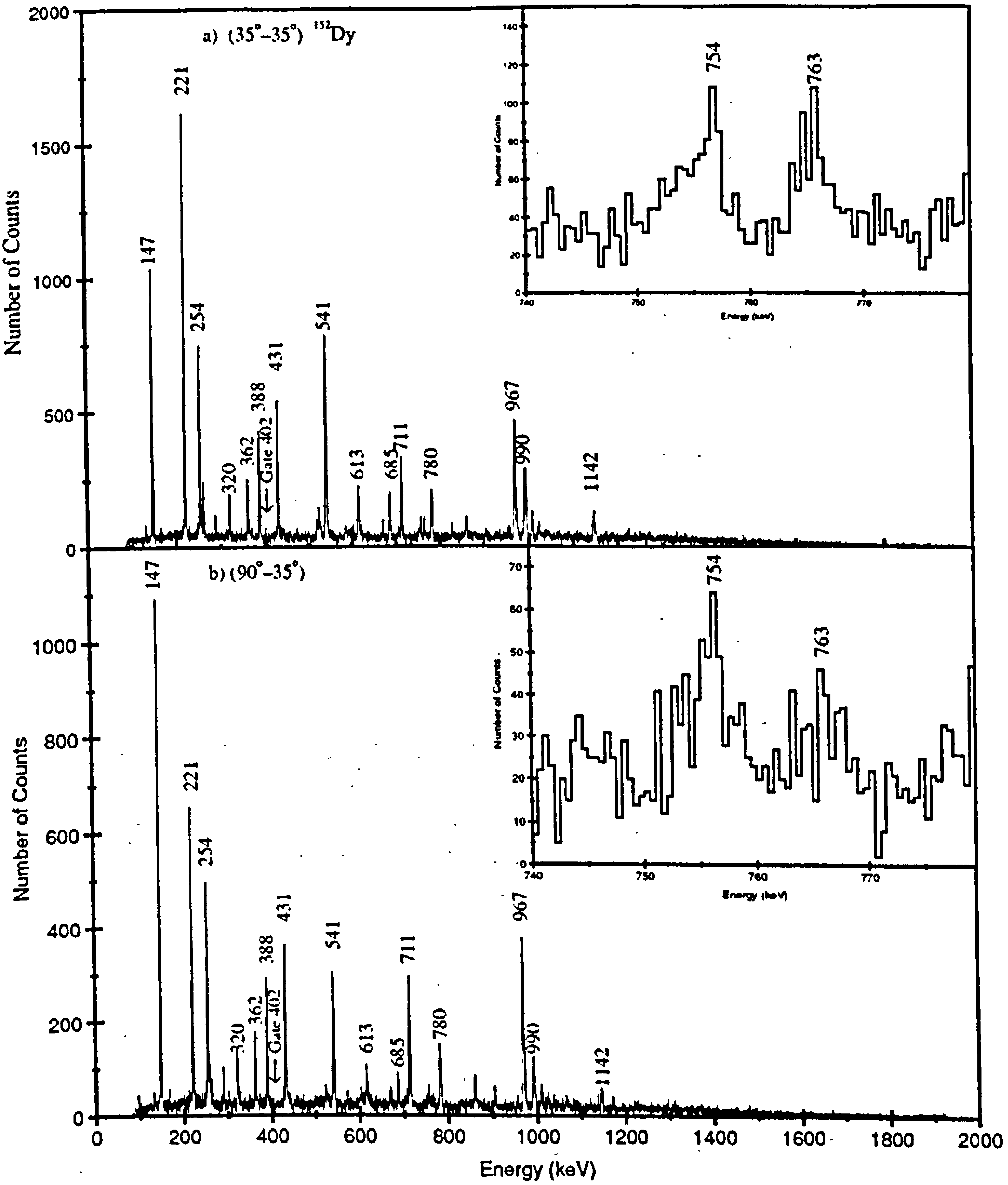

Figure 6.17: *(a) A spectrum gated on the 402 keV gamma ray (stretched quadrupole) after background subtraction, obtained from the (35° - 35°) matrix. (b) A spectrum with the same peak and background limits as for (a) but for the (90° - 35°) matrix. The insets show the 754 keV and 763 keV gamma ray transitions which have been considered as the stretched dipole and stretched quadrupole transitions respectively, in the present work.*

Figure 6.18 and table 6.5 summarises the results from the DCO analysis. It can be seen from the figure that the ratio '$\mathcal{R}$' for the newly observed as well as the previously observed non-yrast gamma rays is consistent with those from known yrast stretched dipole (Δ I=1) and stretched quadrupole (Δ I=2) radiations.

The gamma-rays having low energies are seen to possess slightly low values of '$\mathcal{R}$', this may be due to the uncertainties in the mixing ratios (the ratio of the transition matrix elements for the higher to the lower multipoles). The 1912 keV gamma ray for which the $\mathcal{R}$ value is consistent with the other stretched dipole transitions has been considered to be a stretched dipole transitions in the present work. The 851 keV and 1020 keV transitions which look ambiguous in the figure 6.18 have been considered to be stretched quadrupole transitions due to them being more consistent with other stretched quadrupole transitions.

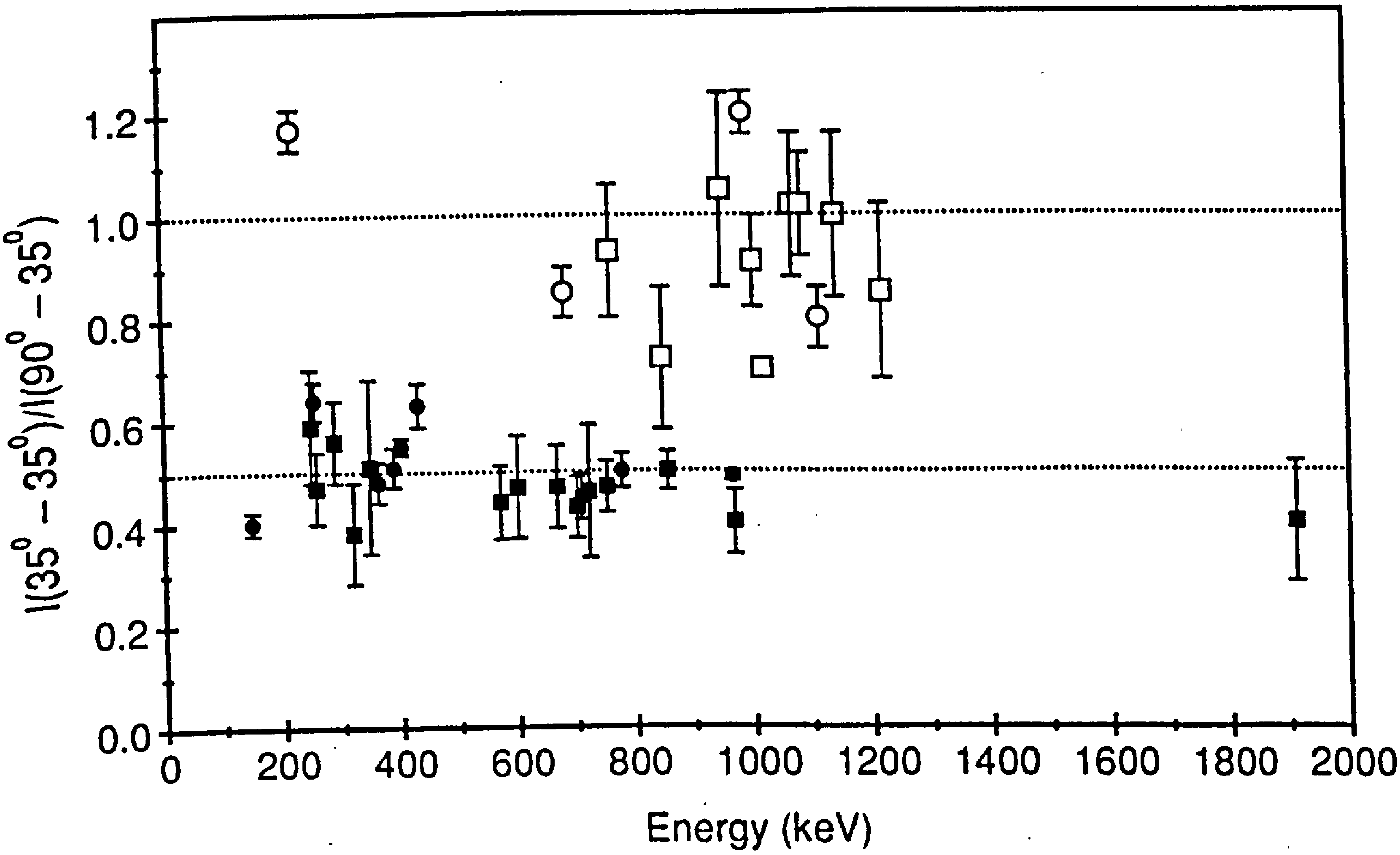

Figure 6.18: *Results from the DCO analysis for the ratio* $\frac{I(35^\circ-35^\circ)}{I(90^\circ-35^\circ)}$ *for stretched dipole and stretched quadrupole* γ*-ray transitions in the* ^{152}Dy*. The lines indicate the value of* $\mathcal{R}$ *at* $\approx$ *0.5 and* $\mathcal{R}$ *at* $\approx$ *1. The open circles reperesent the ratio "*$\mathcal{R}$*" for the known stretched quadrupole transitions while the open squares represent the ratio for the stretched quadrupole transitions observed in the present work. Similarly the closed circles represent the ratio for the known stretched dipole and closed squares represnt the ratio for stretched dipole transitions whose experimental spins have been observed in the present work.*

Table 6.5

$E_x{}^{a)}$ (keV)	$E_\gamma{}^{b)}$ (keV)	$I_\gamma{}^{c)}$ (%)	$\mathcal{R}^{d)} = \frac{I(35°-35°)}{I(90°-35°)}$	$^{e)}I_i^\pi \rightarrow {}^{f)}I_f^\pi$
7882	967	100.0±1.0	0.49± 0.01	$28^+ \rightarrow 27^-$
7882	274	1.2±0.1	———	———
8849	147	99.0±2.0	0.40±0.02	$29^+ \rightarrow 28^+$
8997	402	54.3±0.5	0.55±0.06	$30^+ \rightarrow 29^+$
8997	1114	45.0±0.6	1.05±0.07	$31^+ \rightarrow 29^+$
9399	711	24.4±0.4	0.45±0.04	$31^+ \rightarrow 30^+$
9399	858	9.8±0.2	0.50±0.03	$31^{(+)} \rightarrow 30^+$
10111	431	47.0±0.5	0.63±0.04	$32^+ \rightarrow 31^+$
10111	851	5.0±0.1	0.72±0.14	$32^{(+)} \rightarrow 31^+$
10257	952	2.2±0.2	1.05±0.19	$33^{(+)} \rightarrow 31^{(+)}$
10257	703	2.5±0.1	0.43±0.06	$32^{(+)} \rightarrow 31^{(+)}$
10542	254	41.5±0.9	0.60±0.03	$33^+ \rightarrow 32^+$
10796	780	37.0±0.7	0.50±0.03	$34^- \rightarrow 33^+$
10962	248	2.6±0.1	0.59±0.1	$33^{(+)} \rightarrow 32^{(+)}$
11210	1220	4.6±0.1	0.83±0.17	$35^{(-)} \rightarrow 33^{(+)}$
11576	388	31.0±0.4	0.50±0.03	$35^- \rightarrow 34^-$
11964	362	16.0±0.7	0.48±0.04	$36^- \rightarrow 35^-$
12180	970	9.1±0.7	0.40±0.06	$34^{(+)} \rightarrow 33^{(+)}$
12429	288	3.5±0.1	0.56±0.08	$36^{(+)} \rightarrow 35^{(+)}$
12717	1005	18.9±0.4	0.91±0.09	$38^{(+)} \rightarrow 36^{(+)}$
13049	724	———	0.46±0.13	$37^{(+)} \rightarrow 36^-$

continued ....

E_x a) (keV)	E_γ b) (keV)	I_γ c) (%)	$\mathcal{R}$ d) = $\frac{I(35^\circ-35^\circ)}{I(90^\circ-35^\circ)}$	e) I_i^π → f) I_f^π
13049	1086	3.8±0.2	1.02±0.10	$37^{(+)} \rightarrow 35^-$
13397	348	2.2±0.2	0.51±0.17	$38^{(-)} \rightarrow 37^{(+)}$
13397	1071	1.7±0.3	1.02±0.14	$38^{(-)} \rightarrow 36^-$
13722	763	7.1±0.2	0.93±0.13	$40^{(+)} \rightarrow 38^{(+)}$
14485	1912	2.3±0.2	0.40±0.12	$41^{(-)} \rightarrow 40^{(+)}$
16397	1142	Doublet	1.00±0.16	$43^{(+)} \rightarrow 41^{(-)}$

Table 6.5: The properties of the transitions in ^{152}Dy above spin 27^- as measured in the present work.

a) Excitation energy E_x of the decaying level.

b) The transition energy.

c) The intensity of the gamma-ray.

d) Ratio of the intensity of the gamma ray transition detected in a 35° detector while gated on another 35° detector to the intensity of the gamma ray transition detected in a 90° detector while gated on a 35° detector.

e) Initial spin and parity of the energy state.

f) Final spin and parity of the energy state.

Chapter 7

Discussion and Interpretation of the Single Particle Level Schemes

7.1 Introduction

The experimentally deduced level schemes of ^{150}Gd and ^{152}Dy were presented in chapter 6. This chapter is in two parts. In parts I and II the spectrum of nuclear energy states of ^{150}Gd and ^{152}Dy are interpreted in terms of single particle shell model configurations.

In particular, similarities in these level schemes compared with those of their Z+1 isotones are investigated.

Part I

Interpretation of the Level Schemes of the ^{150}Gd and ^{152}Dy

7.2 Interpretation of the Level Schemes of ^{150}Gd and ^{152}Dy

The nuclei ^{150}Gd and ^{152}Dy are even-even nuclei. The ground state spin of both nuclei will therefore be 0^+. Figure 7.1 shows the experimentally deduced level schemes for ^{150}Gd and ^{152}Dy. The spectrum of energy states in these level schemes can be explained in terms of single particle shell model configurations. As mentioned in section 3.5, the level spacing in the case of a rotation around the symmetry axis has a statistical character, and consequently one expects yrast traps (high spin isomeric states). They are defined as the yrast states which cannot undergo a rapid gamma-transition and have been predicted by Bohr and Mottelson [BM 74]. Filling the levels in the rotating nuclear potential we eventually obtain, with increasing angular velocity, jumps in the angular momentum by several units. Figure 7.2 shows a plot of excitation energy E_x versus the spin I. The experimental data for ^{151}Tb and ^{153}Ho have been taken from references [Cu 88] and [Ha 88] respectively. The calculated values are shown with an offset of 5 MeV. The plots show small parabolas and it is expected that at the start of each point of a parabola we have an yrast trap. These yrast traps are referred to as fully aligned states. It may be mentioned here that all the points at the start of a parabola may not necessarily be an isomeric state (yrast trap) but one may expect that this state has the maximum possibility of being an isomeric state. The production of angular momentum due to the single particle motion of the nucleons around the symmetry axis can also be presented in a plot of the eigenvalues (e_i), in the non-rotating oblate deformed single particle well, as a function of the components (Ω) of the angular momentum along the symmetry axis. The eigenvalues (e_i) for levels in the same j-shell lie on approximate inverted parabolas (see section 3.5). At oblate deformations (β<0) the highest m_j-values, that is, the most aligned states have the deepest energy, because their oblate density distribution in the equatorial plane has the maximal overlap with the oblate

Figure 7.1: *Comparison of the experimental level schemes of the (a) ^{150}Gd and (b) ^{152}Dy. It can be seen that states from spin 0^+ to 19^- show almost the similar level spacing, thus illustrating almost similar mode of excitation which in this case is neutrons. Similarly, the states from spin 19^- to 27^- have similar level spacing, again showing that the angular momentum has been generated in a similar way in both the cases. The yrast states from spin 28^+ to 33^+ also show similar behaviour. The 954 keV transition at $34^{(-)}$ in the ^{150}Gd level scheme is similar to the yrast transition having energy 780 keV at state 34^- in ^{152}Dy. Most of the non-yrast states in ^{152}Dy have been assigned positive parities as predicted by the calculations. The transition having energy 1027.5 keV and spin $38^{(+)}$ in ^{150}Gd is similar to the 1005 keV transition having spin 38^+ in ^{152}Dy.*

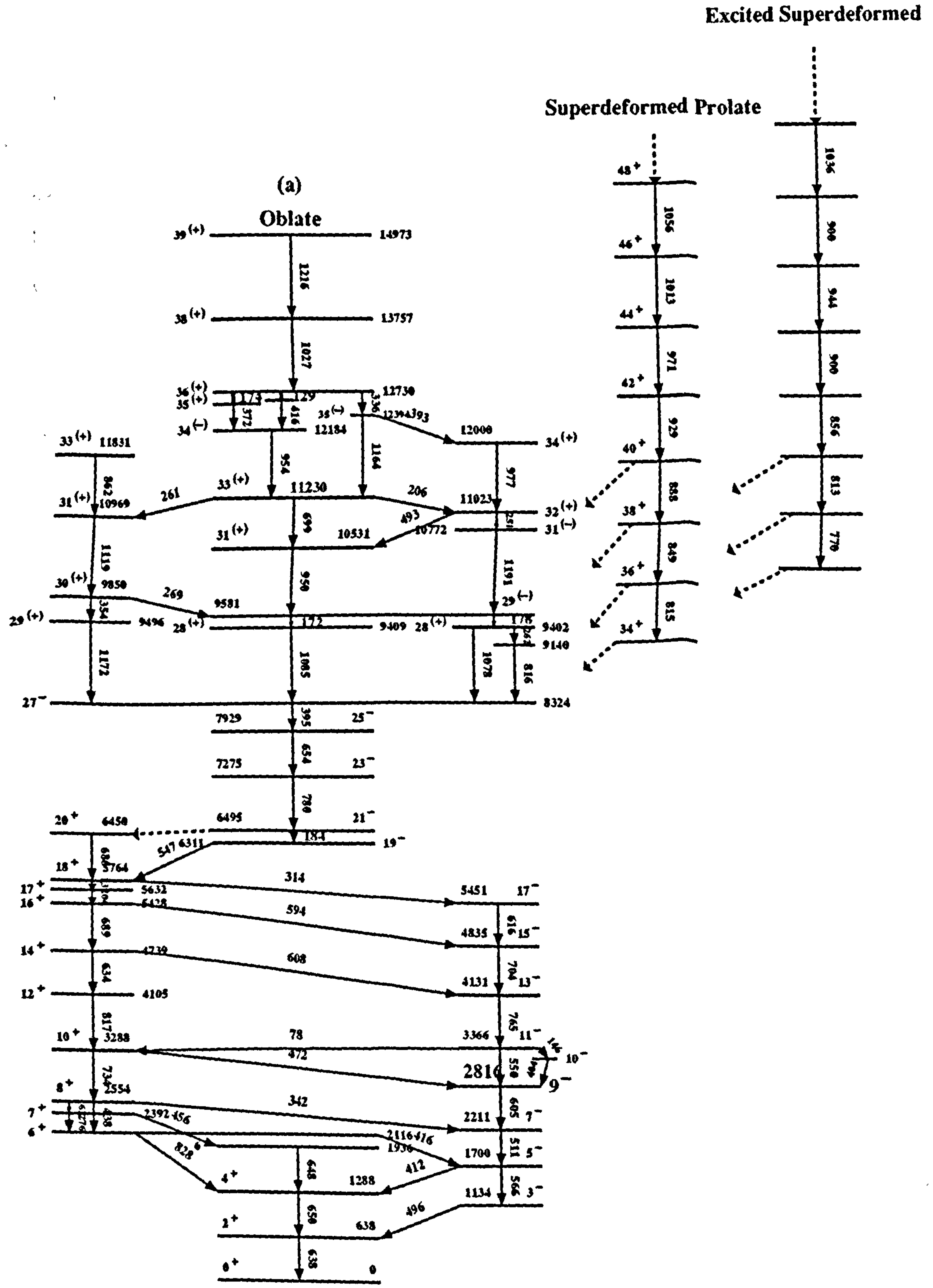

$^{150}_{64}$Gd

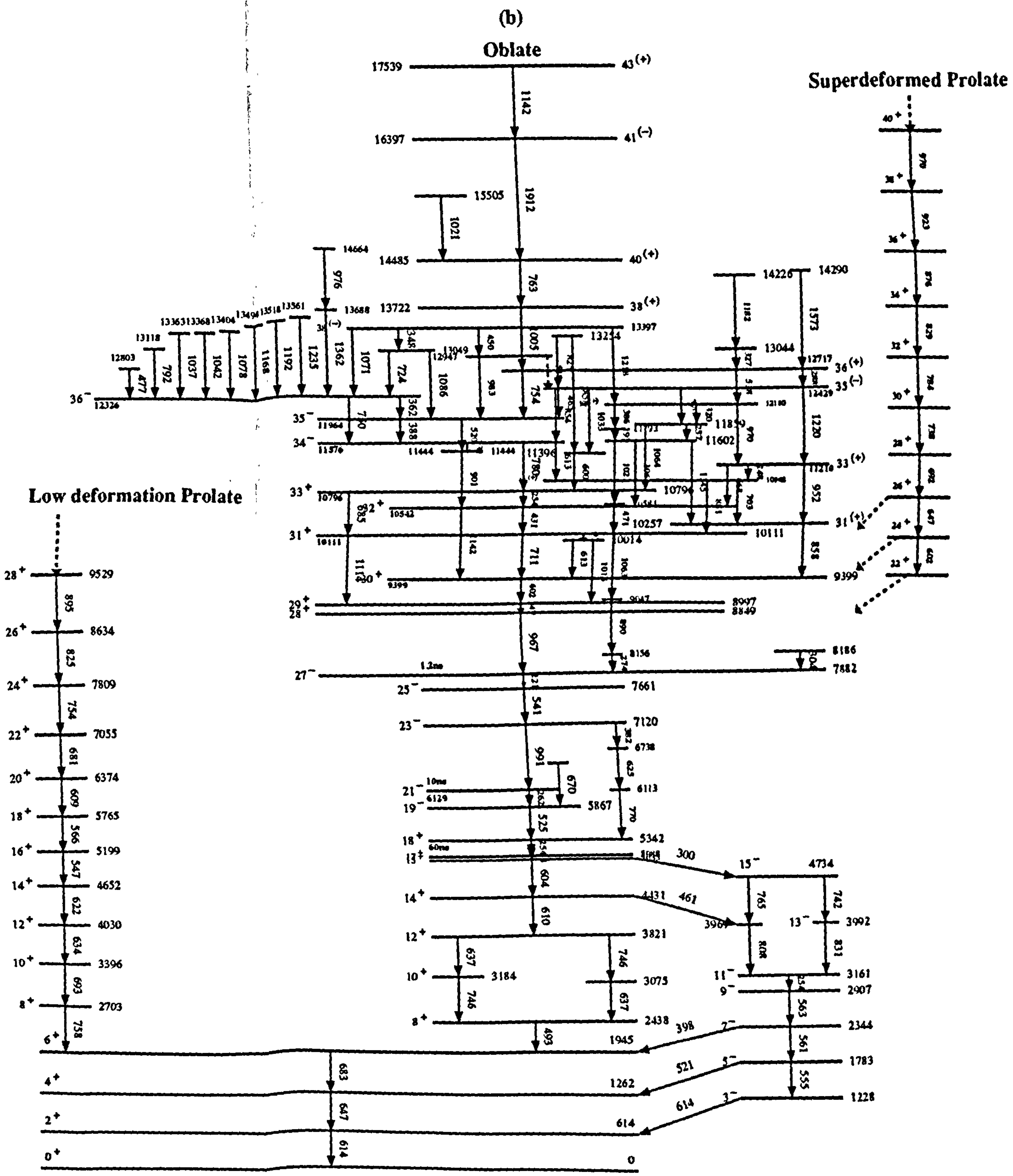

$^{152}_{66}$Dy

density of the core.

At zero rotation frequency (ω=o), the Fermi surface is a horizontal line and all levels below it are occupied. At finite ω-values (section 3.5), the Fermi level can be represented by a tilted line. As the value of ω increases, levels with negative m_j values are vacated and those with positive m_j values become occupied. Figure 7.3 shows this with the aid of so called "umbrella" plots for ^{150}Gd. Figure 7.4 shows the same plot for ^{152}Dy. In these figures the Fermi surfaces are represented where a jump of 11 units of angular momentum and 20 units of angular momentum occurs in the case of neutrons, while in the case of protons a jump of 10 units of angular momentum and 20 units of angular momentum occurs with respect to the ground state spin. Other spin-values on the yrast line are obtained by constructing proton-hole configurations with respect to the rotated energy surface. This is usually connected with an increase in energy.

Since both nuclei have the same number of neutrons i.e., N=86, the spectra of states observed in both nuclei show a similar behaviour up to spin 20^+. Above spin 20^+, the states are based on excitations/re-arrangements of the protons in the $d_{5/2}$ and $h_{11/2}$ orbits. The level schemes of these nuclei can be understood by their single particle behaviour using calculations based on the deformed Woods-Saxon potential. Commonly used versions of this potential can be found for example in [Ro 67, Ch 67, Da 69]. Dudek and Werner [DW 78] readjusted the parameters of the Woods-Saxon potential to fit the nuclear energy levels of the odd-A nuclei in the deformed regions of the heavy nuclei. Another modification in the single particle orbitals was suggested by [Do 80, Do 81]. At certain proton and neutron numbers, orbitals which are active in the light neutron-deficient rare earth nuclei are selected (1 $h_{11/2}$, $3s_{1/2}$, $2d_{3/2}$, $2f_{7/2}$, $1h_{9/2}$ and $1i_{13/2}$ for neutrons, and $1g_{7/2}$, $2d_{5/2}$, $1h_{11/2}$, $3s_{1/2}$, and $2d_{3/2}$ for protons). Using the Woods-Saxon potential, the positions of some of the energy levels are modified in the spherical case so as to best fit the experimental data.

The calculations used in the present work employ a deformed Woods-Saxon single particle Hamiltonian [Du 82]. The total angular momentum is taken to be the sum of the single particle angular momenta along the symmetry axis. The parameters are nearly identical for neutrons and protons and are close to the parameter values obtained by optimising the potential to high spin spectra in the vicinity of ^{208}Pb [Du 81].

As mentioned earlier, the experimental level schemes of ^{150}Gd and ^{152}Dy are very similar. Indeed the single particle configurations for the yrast states of these nuclei are also very similar. A summary of the calculations of the single particle configuration, above spin 11^- is presented in table 7.1 for ^{150}Gd and in table 7.2 for ^{152}Dy. The experimentally deduced level schemes of ^{150}Gd and ^{152}Dy along with their configurations, from spin 17^+ to 34^-, are shown in figure 7.6 (a) and (b) and from spin 34^- to above in figure 7.7 (a) and (b), respectively.

It can also be seen from figures 7.3 and 7.4 that both the nuclei have spin zero at their ground state as the neutrons and protons are fully paired. It can be seen that the maximum obtainable spin by aligning all the four valence neutrons is $I=20\hbar$. The angular momentum up to spin 9^- is obtined by re-arranging the neutrons in the $\nu f_{7/2}$ and $\nu h_{9/2}$ orbitals. Spin 11^- is obtained by promoting one neutron from $\nu \mathrm{h}_{9/2}$ to $\nu \mathrm{i}_{13/2}$ and two neutrons in the $\nu \mathrm{f}_{7/2}$ orbit re-arrange themselves to give spin from 11^- to 17^-. Up to this stage there is no contribution to the spin from the protons for both the nuclei. Figure 7.5 shows the experimentally deduced energy states from spin 11^- to spin 17^- along with their configurations.

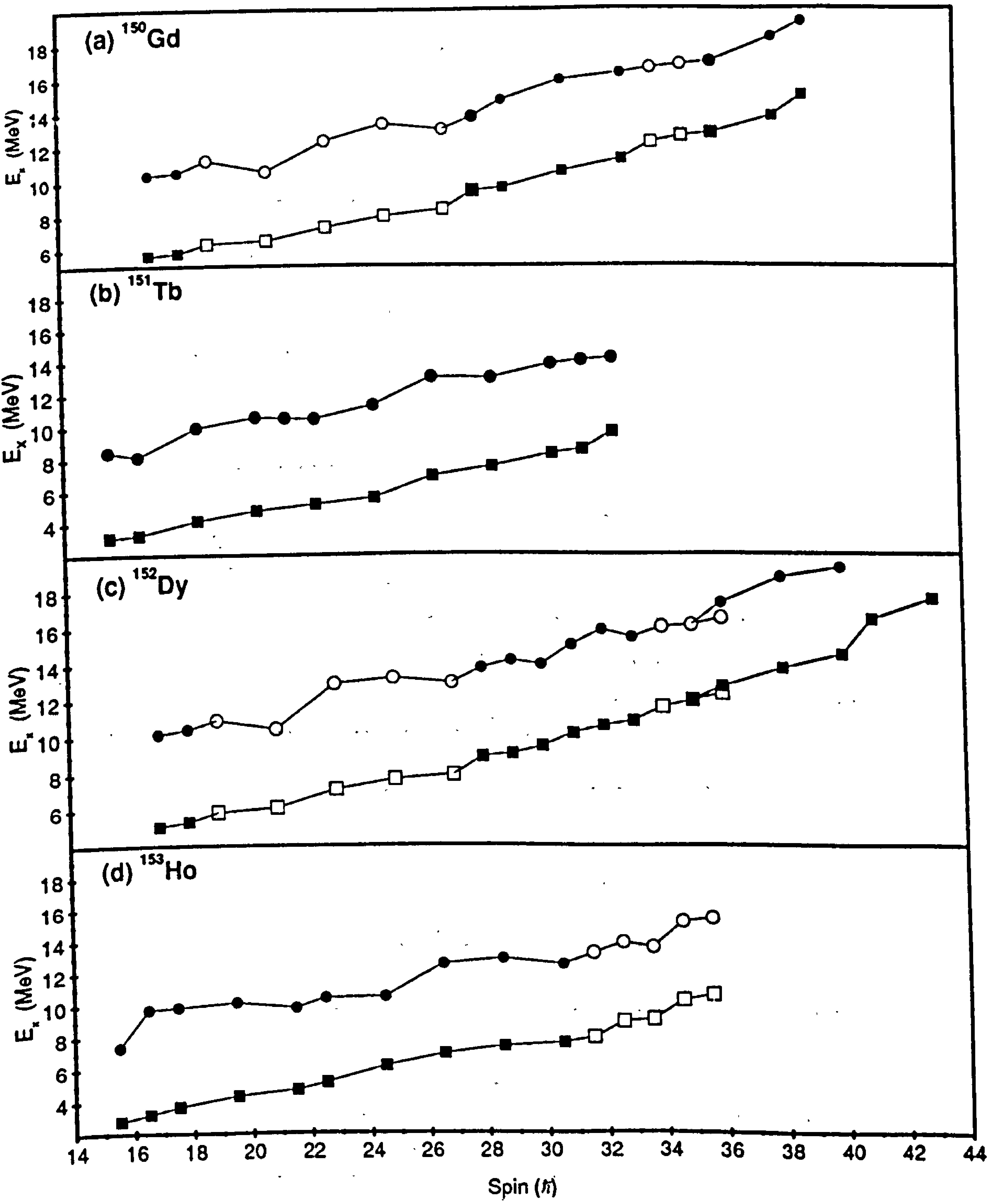

Figure 7.2: *A plot of excitation energy vs spin for (a)* ^{150}*Gd, (b)* ^{151}*Tb, (c)* ^{152}*Dy and (d)* ^{153}*Ho. The experimental curves for* ^{151}*Tb and* ^{153}*Ho are based on the data taken from references [Cu 88] and [Ha 83] respectively. For all figures the experimental values are shown by squares and calculated values by circles (note that the calculated values are offset by 5 MeV). In addition filled symbols refer to +ve parity while open symbols refer to -ve parity.*

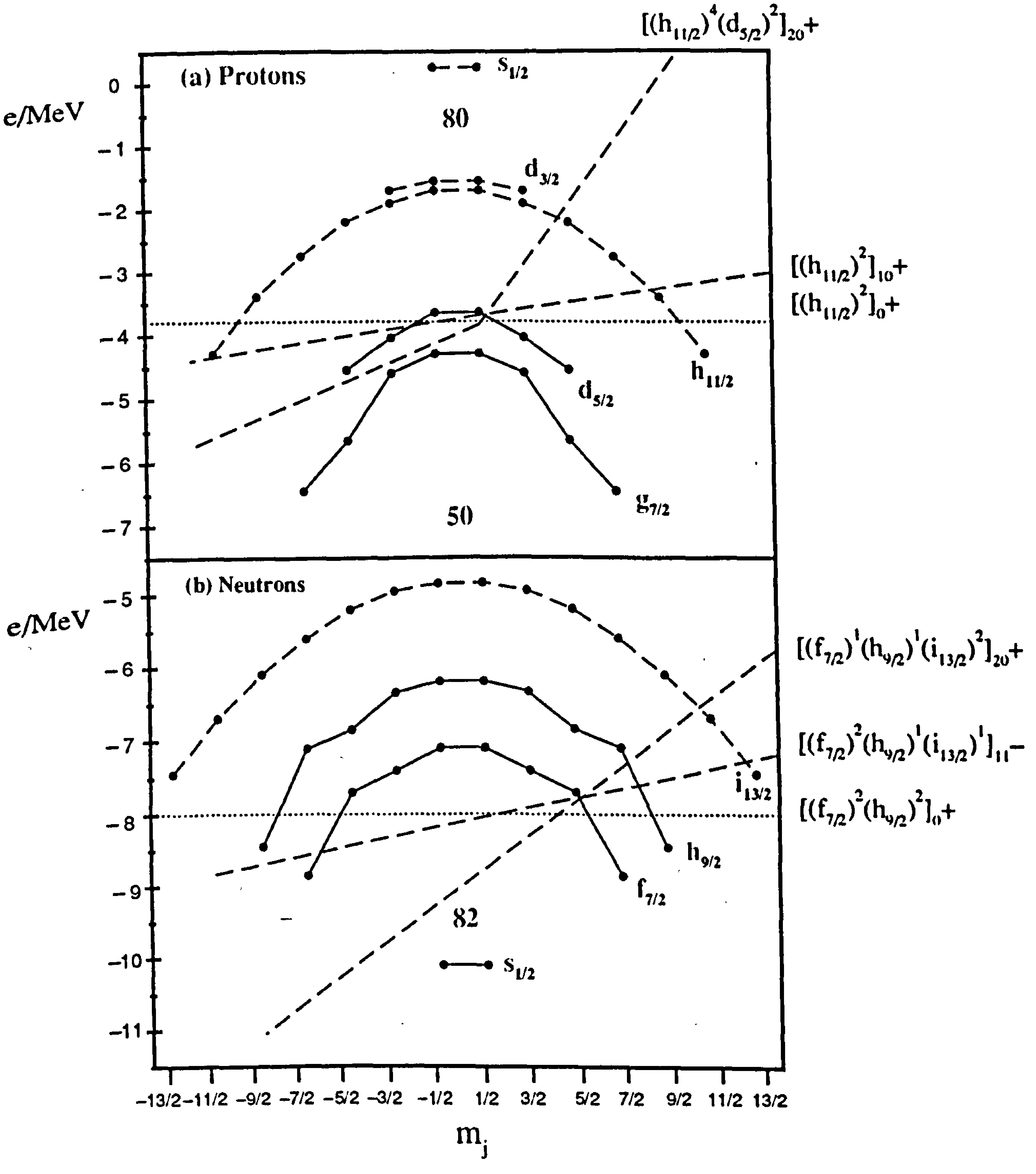

Figure 7.3: *Schematic representation of the single particle orbital energies versus angular momentum component (the eigen-value of j_r) at deformation $\beta_2=0.14$ for ${}^{150}_{86}Gd_{64}$. The dotted line shows the Fermi surface at $\omega=0$ and all levels below it are occupied. The dashed lines show tilted Fermi surfaces. Tilted Fermi surfaces correspond to the different optimal configurations and are shown at I = 10^+, 20^+ for protons and at I = 11^- and 20^+ for neutrons.*

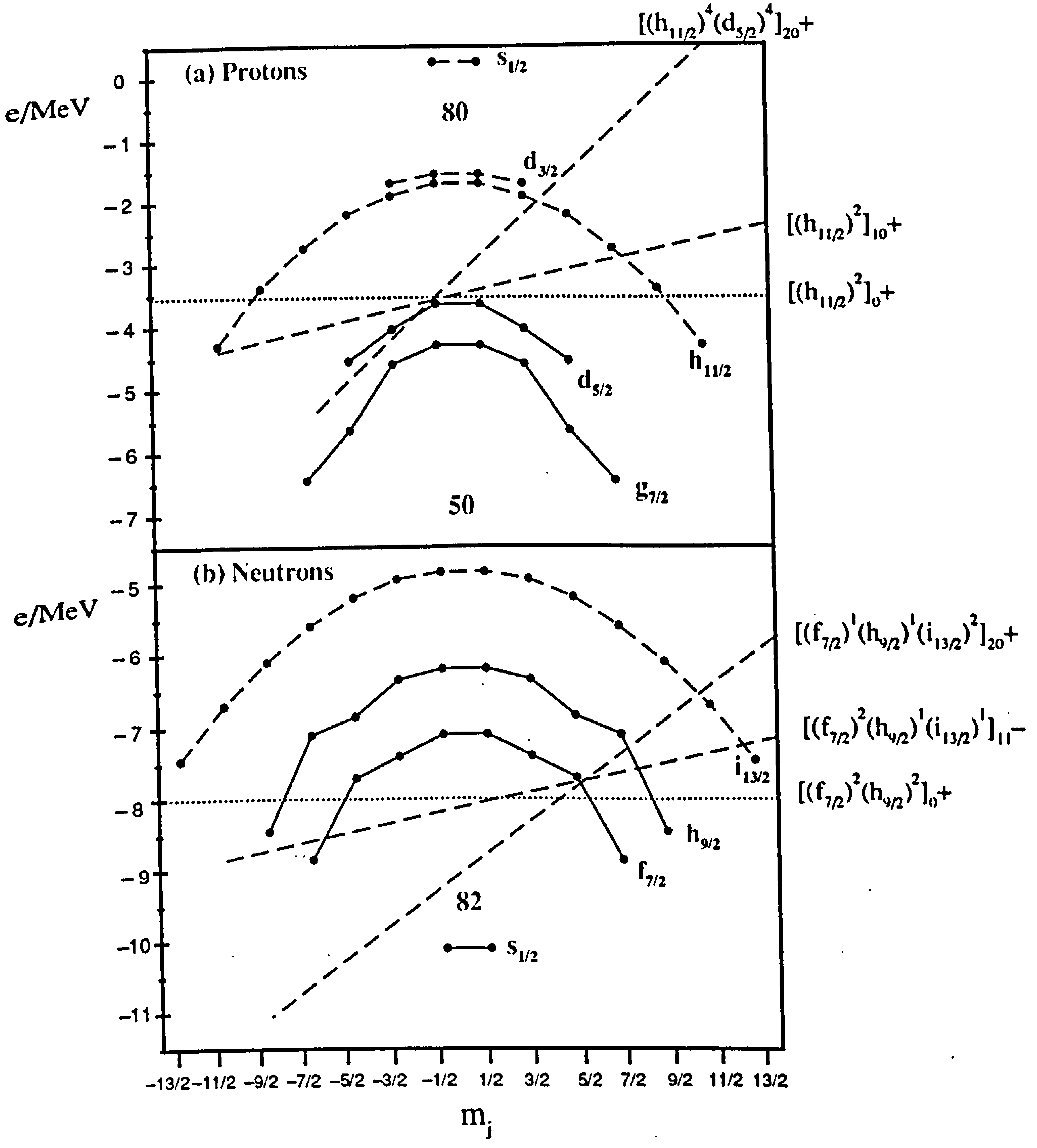

Figure 7.4: *Schematic representation of the single particle orbital energies versus angular momentum component at deformation β_2=0.14 for $^{152}_{86}Dy_{66}$. The dotted line shows the Fermi surface at ω=0 and all levels below it are occupied. The dashed lines show tilted Fermi surfaces. Tilted Fermi surfaces correspond to the different optimal configurations and are shown at $I = 10^+$, 20^+ for protons and at $I = 11^-$ and 20^+ for neutrons.*

Table 7.1

I^{π}	*Neutron Configuration*	*Proton Configuration*
11^-	$\nu(h_{9/2},i_{13/2})_{11}^{-}$	$\pi(h^{2}_{11/2})_{0}^{+}$
$11^- \rightarrow 17^-$	$\nu(h_{9/2},i_{13/2})_{11}^{-}\otimes\nu(f_{7/2})_{(0^+\rightarrow 6^+)}$	$\pi(h^{2}_{11/2})_{0}^{+}$
17^+	$\nu(h_{9/2},i_{13/2})_{11}^{-}$	$\pi(h^{3}_{11/2})_{9/2}^{-}\otimes\pi(d^{3}_{5/2})_{3/2}^{+}$
18^+	$\nu(h_{9/2},i_{13/2})_{11}^{-}$	$\pi(h^{3}_{11/2})_{9/2}^{-}\otimes\pi(d^{3}_{5/2})_{5/2}^{+}$
19^-	$\nu(h_{9/2},i_{13/2})_{11}^{-}$	$\pi(h^{2}_{11/2})_{8+}\otimes\pi(d^{4}_{5/2})_{0}^{+}$
21^-	$\nu(h_{9/2},i_{13/2})_{11}^{-}$	$\pi(h^{2}_{11/2})_{10}^{+}$
$21^- \rightarrow 27^-$	$\nu(h_{9/2},i_{13/2})_{11}^{-}\otimes\ \nu(f_{7/2})_{(0^+\rightarrow 6^+)}$	$\pi(h^{2}_{11/2})_{10}^{+}$
28^+	$\nu(i^{2}_{13/2})_{12}^{+}(f_{7/2},h_{9/2})_{8}^{+}$	$\pi(h^{2}_{11/2})_{8}^{+}$
$28^+ \rightarrow 30^+$	$\nu(i^{2}_{13/2})_{12}^{+}(f_{7/2},h_{9/2})_{8}^{+}$	$\pi(h^{2}_{11/2})_{8^+\rightarrow 10^+}$
$31^+ \rightarrow 33^+$	$\nu(i^{2}_{13/2})_{12}^{+}(f_{7/2},h_{9/2})_{8}^{+}$	$\pi(h^{2}_{11/2})_{10}^{+}\otimes\pi(d^{4}_{5/2})_{1^+\rightarrow 3^+}$
34^-	$\nu(i^{2}_{13/2})_{12}^{+}(f_{7/2},h_{9/2})_{8}^{+}$	$\pi(h^{3}_{11/2})_{25/2}^{-}\otimes\pi(d^{3}_{5/2})_{3/2}^{+}$
35^-	$\nu(i^{2}_{13/2})_{12}^{+}(f_{7/2},h_{9/2})_{8}^{+}$	$\pi(h^{3}_{11/2})_{27/2}^{-}\otimes\pi(d^{3}_{5/2})_{3/2}^{+}$
36^-	$\nu(i^{2}_{13/2})_{12}^{+}(f_{7/2},h_{9/2})_{8}^{+}$	$\pi(h^{3}_{11/2})_{27/2}^{-}\otimes\pi(d^{3}_{5/2})_{9/2}^{+}$
34^+	$\nu(h^{2}_{9/2})_{8}^{+}\otimes(f_{7/2},i_{13/2})_{10}^{-}$	$\pi(h^{3}_{11/2})_{27/2}^{-}\otimes\ \pi(d^{3}_{5/2})_{5/2}^{+}$
35^+	$\nu(f^{2}_{7/2})_{6}^{+}\otimes(h_{9/2},i_{13/2})_{11}^{-}$	$\pi(h^{3}_{11/2})_{27/2}^{-}\otimes\ \pi(d^{3}_{5/2})_{9/2}^{+}$
36^+	$\nu(h^{2}_{9/2})_{8}^{+}\otimes(f_{7/2},i_{13/2})_{10}^{-}$	$\pi(h^{3}_{11/2})_{27/2}^{-}\otimes\ \pi(d^{3}_{5/2})_{9/2}^{+}$
38^-	$\nu(i^{2}_{13/2})_{12}^{+}\otimes(f_{7/2},h_{9/2})_{8}^{+}$	$\pi(h^{3}_{11/2})_{27/2}^{-}\otimes\ \pi(d^{3}_{5/2})_{9/2}^{+}$
38^+	$[\nu(d^{3}_{3/2})_{1/2}^{-},(f^{2}_{7/2})_{6}^{+},\ (h^{1}_{9/2},i^{2}_{13/2})_{12}^{-}]_{23}^{-}$	$\pi(h^{3}_{11/2})_{27/2}^{-}\otimes\ \pi(d^{3}_{5/2})_{3/2}^{+}$
39^+	$\nu(i^{2}_{13/2})_{12}^{+}(f_{7/2},h_{9/2})_{8}^{+}$	$\pi(h^{4}_{11/2})_{15}^{+}\otimes\pi(d^{2}_{5/2})_{4}^{+}$

Table 7.1: Single Particle Configuration for the nucleus ^{150}Gd. I^{π} represents the spin and parity of the nuclear energy state.

Table 7.2

I^{π}	*Neutron Configuration*	*Proton Configuration*
11^-	$\nu(h_{9/2},i_{13/2})_{11}{}^-$	$\pi(h^2_{11/2})_0{}^+$
$11^- \rightarrow 17^-$	$\nu(h_{9/2},i_{13/2})_{11}{}^-\otimes\nu(f^2_{7/2})_{(0^+\rightarrow 6^+)}$	$(\pi h^2_{11/2})_0{}^+$
17^+	$\nu(h_{9/2},i_{13/2})_{11}-$	$\pi(h^3_{11/2})_{9/2}{}^-\otimes\pi(d^5_{5/2})_{3/2}{}^+$
18^+	$\nu(h_{9/2},i_{13/2})_{11}{}^-$	$\pi(h^3_{11/2})_{9/2}{}^-\otimes\pi(d^5_{5/2})_{5/2}{}^+$
19^-	$\nu(h_{9/2},i_{13/2})_{11}{}^-$	$\pi(h^2_{11/2})_8{}^+\otimes\pi(d^6_{5/2})_0{}^+$
21^-	$\nu(h_{9/2},i_{13/2})_{11}{}^-$	$\pi(h^2_{11/2})_{10}{}^+$
$21^- \rightarrow 27^-$	$\nu(h_{9/2},i_{13/2})_{11}{}^-\otimes\ \nu(f_{7/2})_{(0^+\rightarrow 6^+)}$	$\pi(h^2_{11/2})_{10}{}^+$
28^+	$\nu(i^2_{13/2})_{12}{}^+(f_{7/2},h_{9/2})_8{}^+$	$\pi(h^2_{11/2})_8{}^+$
$28^+ \rightarrow 30^+$	$\nu(i^2_{13/2})_{12}{}^+(f_{7/2},h_{9/2})_8{}^+$	$\pi(h^2_{11/2})_{8^+\rightarrow 10^+}$
$31^+ \rightarrow 33^+$	$\nu(i^2_{13/2})_{12}{}^+(f_{7/2},h_{9/2})_8{}^+$	$\pi(h^4_{11/2})_{8^+\rightarrow 9^+}\otimes\pi(d^4_{5/2})_{3^+\rightarrow 4^+}$
34^-	$\nu(i^2_{13/2})_{12}{}^+(f_{7/2},h_{9/2})_8{}^+$	$\pi(h^3_{11/2})_{27/2}{}^-\otimes\pi(d^5_{5/2})_{1/2}{}^+$
35^-	$\nu(i^2_{13/2})_{12}{}^+(f_{7/2},h_{9/2})_8{}^+$	$\pi(h^3_{11/2})_{27/2}{}^-\otimes\pi(d^5_{5/2})_{3/2}{}^+$
36^-	$\nu(i^2_{13/2})_{12}{}^+(f_{7/2},h_{9/2})_8{}^+$	$\pi(h^3_{11/2})_{27/2}{}^-\otimes\pi(d^5_{5/2})_{5/2}{}^+$
34^+	$\nu(h^2_{9/2})_8{}^+\otimes(f_{7/2},i_{13/2})_{10}{}^-$	$\pi(h^3_{11/2})_{27/2}{}^-\otimes\ \pi(d^5_{5/2})_{5/2}{}^+$
35^+	———	———
$36^+ \rightarrow 40^+$	$\nu(i^2_{13/2})_{12}{}^+(f_{7/2},h_{9/2})_8{}^+$	$\pi(h^4_{11/2})_{16}{}^+\otimes\pi(d^4_{5/2})_{0^+\rightarrow 4^+}$

Table 7.2: Single particle configuration for the nucleus ^{152}Dy. I^{π} represents the spin and parity of the nuclear energy state.

The maximum spin obtainable from the two protons which lie outside the Z=64 core, when they are fully aligned, is $10\hbar$. When these two fully aligned protons which lie in the $\pi h^2_{11/2}$ orbit are coupled with the $\nu(h^1_{9/2}, i^1_{13/2})_{11^-}$, we obtain spin 21^- (an optimal state).

Similarly the spins from 21^- to 27^- are obtained by re-arranging the neutrons in the $(f^2_{7/2})_{(0^+\rightarrow 6^+)}$ orbit and coupling them with $\pi(h^2_{11/2})_{10^+}$.

Spin 28^+ is obtained by maximally aligning four neutrons outside N=82 core to give spin $20\hbar$ i.e.,$\nu(i^2_{13/2})_{12^+}\otimes$ $(f^2_{7/2}, h^1_{9/2})_{8^+}$ and then these neutrons are coupled with the two protons, which lie outside the Z=64 core, in the $\pi(h^2_{11/2})$ orbit, so that we get a contribution of $8\hbar$ of angular momentum.

The spins from $28^+ \rightarrow 29^+ \rightarrow 30^+$ are obtained by coupling the maximally aligned neutron spin i.e., $20\hbar$, to the proton spins. The proton spins are made by re-arrangning the two protons in the $\pi h^2_{11/2}$ to get spins from 8 to $10\hbar$, i.e., $\pi(h^2_{11/2})_{8^+\rightarrow 10^+}$.

In order to generate higher angular momentum the Z=64 core must either be broken or the protons be re-arranged in the same orbit, as desired by the situation. For example, in the case of ^{152}Dy the core must be broken while in the case of ^{150}Gd the protons are re-arranged within the orbit while they are also promoted to higher orbits to produce spins higher than 33^+.

Configurations for spins greater than 30^+ in the case of ^{150}Gd

If we refer to table 7.1 and figure 7.3, we can see that the four protons in the $d_{5/2}$ orbit re-arrange themselves to give a contribution of 1 to 3 units to the total spin and coupled to the maximally aligned two protons in the $\pi(h_{11/2})$ orbit. These protons then couple with the maximally aligned neutrons ($I=21^-$) to give spins from 31^+ to 33^+.

In order to produce spin 34^- the one proton from the $d_{5/2}$ orbit ($m_j = -3/2$ orbital of $d_{5/2}$ orbit) can be promoted to the $\pi(h_{11/2})$ orbit to make spin $25/2^-$. When the protons in the $\pi h_{11/2}$ orbit are coupled to the protons of the $d_{5/2}$ orbit, they give a total spin of 14^-. This proton configuration

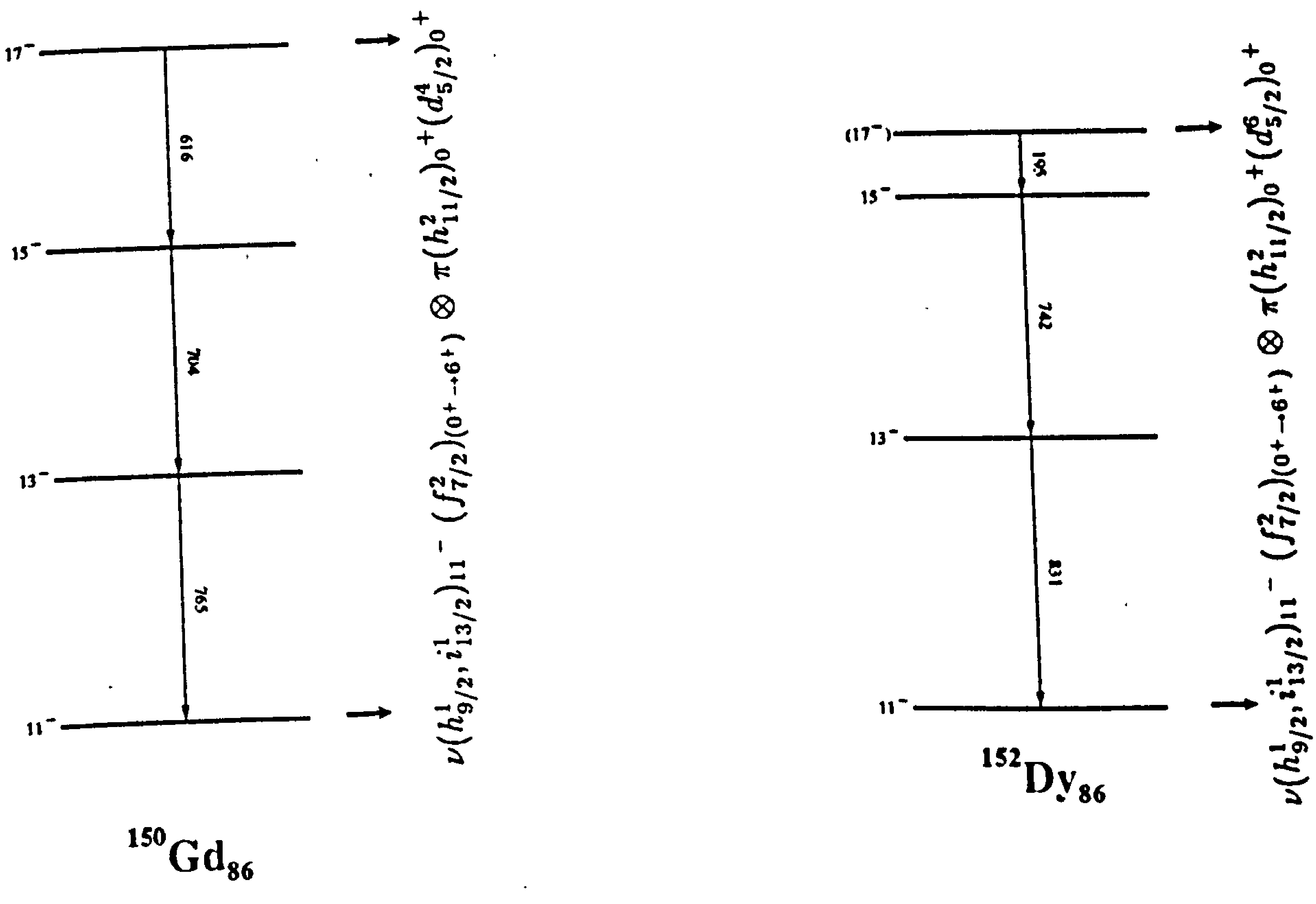

Figure 7.5: *Comparison of the experimentally deduced energy states of ^{150}Gd with experimentally deduced energy states of ^{152}Dy from spin 11⁻ to 17⁻ together with the assigned configurations. It can be seen that these states are based on the excitation/re-arrangement of neutrons in the* $\nu(h^1_{9/2}, i^1_{13/2})_{11^-}(f^2_{7/2})_{0^+\to6^+}$ *orbitals, which lie outside N=82 core and there is no contribution to the angular momentum from the protons.*

Figure 7.6: *Comparison of the experimental level scheme of (a) ^{150}Gd along with its configuration with the (b) experimental level scheme of ^{152}Dy along with its configurations, from spin 17^+ to 33^+. It can be seen that not only the experimental level schemes of both the nuclei are similar but also their configurations are similar. The different behaviour of the protons is due to the different number of protons in these nuclei.*

Figure 7.7: *Comparison of the experimentally deduced level schemes of (a) ^{150}Gd (from spin 33^+ to 39^+) along with its configuration (above spin 34^-) with the (b) experimental level scheme of ^{152}Dy (from spin 33^+ to 40^+) along with its configuration (above spin 34^-). It can be seen that the neutron configuration "$\nu(i^2_{13/2})_{12^+}(f_{7/2},h_{9/2})_{8^+}$" is present in all the states.*

$\pi(h^3_{11/2})_{25/2}{}^{-}\otimes\pi(d^3_{5/2})_{3/2}{}^{+}$ is then coupled with the maximally aligned neutron's configuration $\nu(i^2_{13/2})_{12}{}^{+}(f_{7/2},h_{9/2})_8{}^{+}$ to give spin 34^-. Similarly the states from 34^- to 36^- are based on the re-arrangement of the protons in the $\pi d_{5/2}$ and $\pi h_{11/2}$ orbits.

Configuration of the non-yrast states ($34^{(+)}$ to $39^{(+)}$) in ^{150}Gd

The non-yrast states are a little more complicated to describe, since the number of possible configurations for a given spin become much larger than for yrast the states.

The $34^{(+)}$ state may be produced by
$\nu(f^1_{7/2},h^2_{9/2},i^1_{13/2})_{18}{}^{-}\otimes[\pi(h^3_{11/2})_{27/2}{}^{-}\pi(d^3_{5/2})_{5/2}{}^{+}]_{16}{}^{-}$.

Similarly the $35^{(+)}$ state can be produced by
$\nu(f^2_{7/2},h^1_{9/2},i^1_{13/2})_{17}-\otimes[\pi(h^3_{11/2})_{27/2}{}^{-}\pi(d^3_{5/2})_{9/2}{}^{+}]_{18}{}^{-}$.

The 36^+ state may be considered to arise from
$\nu(f^1_{7/2},h^2_{9/2},i^1_{13/2})_{18}{}^{-}\otimes[\pi(h^3_{11/2})_{27/2}-\pi(d^3_{5/2})_{9/2}{}^{+}]_{18}{}^{-}$.

It is difficult to assign a parity to the state having a spin 38. However, due to experimental similarity of this state to the 38^+ state of the nucleus ^{152}Dy, it may be assigned a positive parity. If this state has a positive parity, then according to the calculations a neutron from the $d_{3/2}$ orbit may be promoted to the $i_{13/2}$ orbit. This would give the neutron configuration as $[\nu((d^3_{3/2})_{1/2}-,(f^2_{7/2})_6{}^{+},(h^1_{9/2},i^2_{13/2})_{12}{}^{-}]_{23}{}^{-}$ which is coupled to the proton configuration $[\pi(h^3_{11/2})_{27/2}{}^{-}\otimes\pi(d^3_{5/2})_{3/2}{}^{+}]_{15}{}^{-}$. But if we assign it negative parity, then the configuration may be described as $\nu(f^1_{7/2},h^1_{9/2},i^2_{13/2})_{20}{}^{+}$ coupled to $[\pi(h^3_{11/2})_{27/2}{}^{-}\otimes\pi(d^3_{5/2})_{9/2}{}^{+}]_{18}{}^{-}$. The large energy gap between the state $36^{(+)}$ and state having spin 38, is consistent with promoting 1 neutron from the $d_{3/2}$ orbit to the $i_{13/2}$ orbit. It is therefore concluded that the parity of the energy state 38 is more likely to be positive, hence this state is written as $38^{(+)}$.

The configuration of the $39^{(+)}$ state is assigned as $\nu(f^1_{7/2},h^1_{9/2},i^2_{13/2})_{20}{}^{+}\otimes[\pi(h^4_{11/2})_{15}{}^{+}\pi(d^2_{5/2})_4{}^{+}]_{19}{}^{+}$.

The Configurations of the spins having values greater than 30^+ in the case of ^{152}Dy

Referring to the figures 7.3 and 7.4 along with the tables 7.1 and 7.2, it can be seen that the states up to spin 30^+ have a very similar configuration to that of ^{150}Gd. However, due to a different number of protons in the $\pi d_{5/2}$ orbit, the theoretical configuration changes above spin $30\hbar$ although the experimental states look similar in both the nuclei even at such higher spins. The configurations for states above spin 30^+ are shown in table 7.2 and can be explained in a similar way as in the case of ^{150}Gd. For example, the yrast states from spins 31^+ to 33^+ have the same neutron configuration while the protons re-arrange themselves in the $d_{5/2}$ and $h_{11/2}$ orbitals as shown in the table 7.2. Similarly the yrast states from spins 34^- to 36^- have the same neutron configurations $[\nu(i^2_{13/2})_{12}{}^+(f_{7/2},h_{9/2})_8{}^+]_{20}{}^+$ which are coupled to various proton configurations as shown in table 7.2. It can be seen that above 36^- level, the population is severely fragmented. There are no states produced by the calculations which have spin $35^{(+)}$. Hence the non-yrast trasition having energy 1220 keV is assigned a negative parity and is written as $35^{(-)}$. The cascade from spin $36^{(+)}$ to $40^{(+)}$ has the same neutron configuration $[\nu(i^2_{13/2})_{12}{}^+(f_{7/2},h_{9/2})_8{}^+]_{20}{}^+$ coupled to different proton configurations $\pi(h^3_{11/2})_{27/2}{}^-\otimes\pi(d^5_{5/2})_{1/2^+\rightarrow 5/2^+}$. It can be seen from the calculations that a proton from the $\pi d_{5/2}$ orbit is promoted to the $\pi h_{11/2}$ orbit to make spin $38^{(+)}$ in ^{152}Dy. Spin $40^{(+)}$ is made from a re-arrangement of the protons in the $\pi d_{5/2}$ orbit, which should not 'cost' too much energy (i.e., $\leq$ 1MeV). In order to produce the spin $41^{(-)}$, a neutron from the $\nu(s_{1/2})$ orbit, is promoted to the $h_{9/2}$ orbit, which costs $\approx$ 2MeV energy. A big energy gap of 1912 keV from spin $40^{(+)}$ to $41^{(-)}$ in the experimental level scheme of ^{152}Dy is indicative of this fact.

A comparison between the experimental and the theoretical partial level schemes of ^{150}Gd and ^{152}Dy along with their configurations is shown in figures 7.8 and 7.9 respectively. The similarities between the theoretical and experimental level schemes of both ^{150}Gd and ^{152}Dy are very striking up to spin 34^-. Above spin 34^-, although very similar energy gaps are observed in the experimental level schemes of ^{150}Gd and ^{152}Dy, the configurations for the energy states are not similar. This difference in configurations is mainly due to the different re-arrangement (due to different number of protons) of protons in the $d_{5/2}$ and $h_{11/2}$ orbits at very high spins; the neutron contribution generally remaining the same even for higher spins.

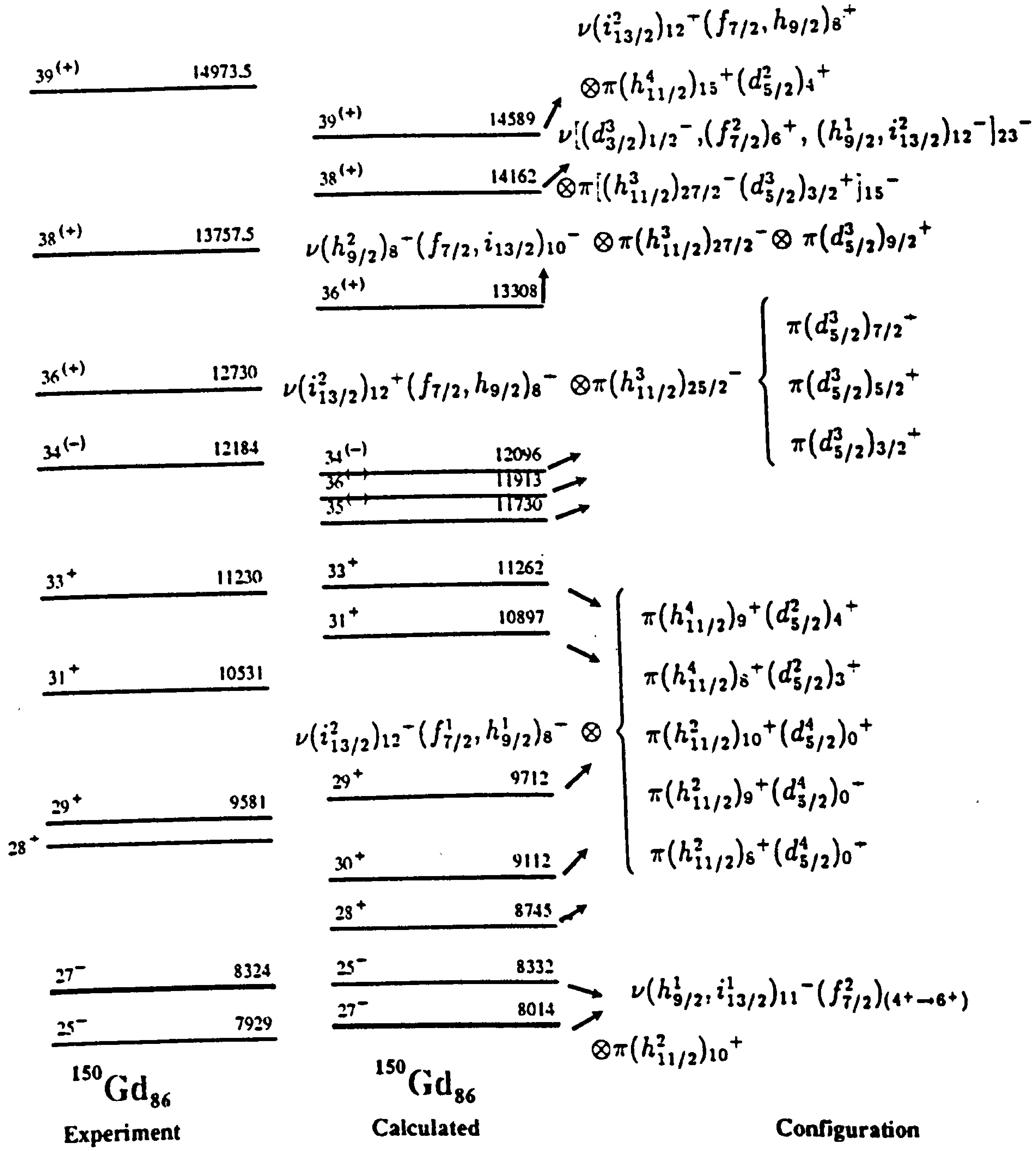

Figure 7.8: *Experimental and calculated spectrum of states for* ^{150}*Gd along with the configuration for each nuclear energy state above spin* 25^-.

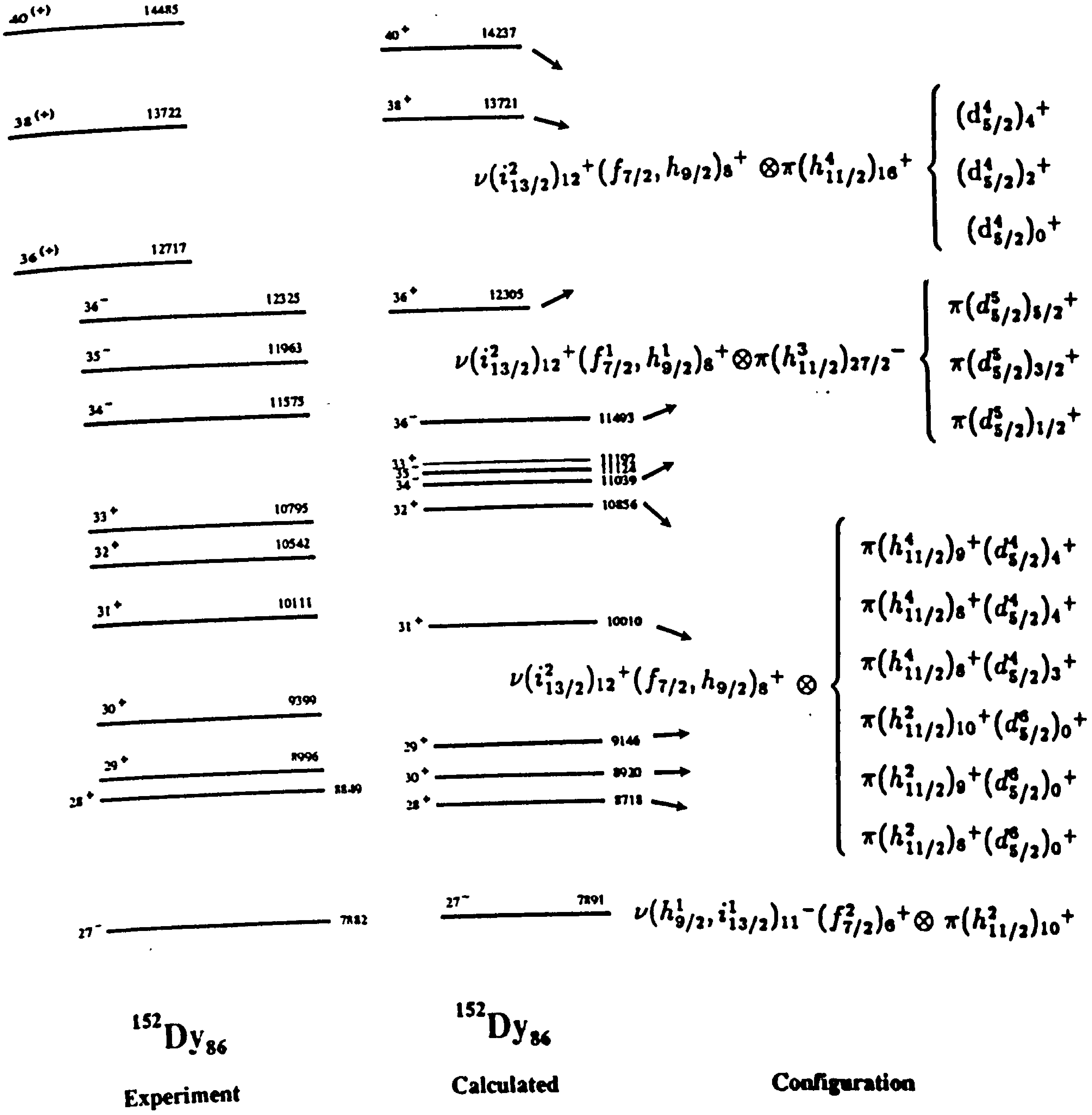

Figure 7.9: *Experimental and calculated spectrum of states for ^{152}Dy along with the configuration for each nuclear energy state above spin 27^-.*

Part II

Comparison of the Level Schemes of the ^{150}Gd and ^{152}Dy with their Z+1 N=86 Neighbours

7.3 Comparison of the Level Schemes of ^{150}Gd and ^{152}Dy with Z+1 N=86 Neighbours

When the level schemes of ^{150}Gd and ^{152}Dy are compared with their Z+1 neighbours i.e., ^{151}Tb and ^{153}Ho, we observe some remarkable similarities in the spectra of energy states of these nuclei. The similarities in the spectra of energy states of these nuclei can be explained in terms of the single particle shell model. Figures 7.10 and 7.11 show "umbrella" plots for ^{151}Tb and ^{153}Ho while tables 7.3 and 7.4 show the single particle configurations.

It turns out that a few single particle configurations play a very special role and they generally correspond to the maximum-aligned configurations. For example, the neutron configuration $(h_{9/2}, i_{13/2})_{11}{}^{-}$ is present in the wave functions of all strongly populated high-spin states lying between 11^- to 27^- in case of ^{150}Gd and ^{152}Dy and also those lying between $33/2^+$ to $57/2^+$, and $31/2^+$ to $61/2^+$ in the case of ^{151}Tb and ^{153}Ho, respectively.

A comparison of the level schemes of ^{150}Gd and ^{151}Tb above spins 21^- and $49/2^+$, respectively, is made in figure 7.12. A close examination of the figure 7.12 shows that not only are the experimental energy levels of ^{150}Gd and ^{151}Tb very similar but their single particle configurations are similar as well. For example, the neutron configuration $\nu(h_{9/2}, i_{13/2})_{11}{}^{-}$ is present in the wave functions of all the states having spins from $25^- \rightarrow 23^-$ and $23^- \rightarrow 21^-$ in ^{150}Gd and the same neutron configuration is also present in the wave functions of the energy states of ^{151}Tb with spins $57/2^+ \rightarrow 53/2^+$ and $53/2^+ \rightarrow 49/2^+$. The proton configuration for states in both nuclei looks different as they have different numbers of protons. Similarly, the neutron configuration $\nu(i^2_{13/2})_{12}{}^{+}(f_{7/2}, h_{9/2})_{8}{}^{+}$ is present in all the states having spins 28^+ to 34^- in ^{150}Gd while the same neutron configuration is also present in the wave functions of states having spins from $65/2^+$ to $77/2^{(-)}$. A compaison of the level schemes of ^{152}Dy and ^{153}Ho can be seen in figure 7.13. Similarities in the experimental level schemes for these nuclei can also be explained in terms of single particle shell model configurations. For example, the neutron configuration $\nu(h_{9/2}, i_{13/2})_{11}-$ is present in the wave-function of all states having spins from 21^- to 27^- in ^{152}Dy and in those states having spins from $49/2^+$ to $61/2^+$ in Ho^{153}. Similarly, the neutron configuration $\nu(i^2_{13/2})_{12}{}^+(f_{7/2}, h_{9/2})_8{}^+$ is present in the wave function of the states having spins from 34^- to 36^- in ^{152}Dy and also in those of the states having spins from $73/2^{(+)}$ to $77/2^{(+)}$ in ^{153}Ho.

However, the states having spins 33^+ and $71/2^-$ in ^{152}Dy and ^{153}Ho respectively, have different neutron as well as proton configurations. A big gap between the states $33^+ \rightarrow 34^-$ in ^{152}Dy and between the $71/2^- \rightarrow 73/2^{(+)}$ in ^{153}Ho is indicative of the promotion of the nucleon(s) from lower to higher orbits and for this energy has to be supplied. The energy cost for promotion of one proton from $\pi d_{5/2}$ to $\pi h_{11/2}$ for both the ^{152}Dy and ^{153}Ho is $\approx$ 1MeV. The small energy gaps between the states $34^- \rightarrow 35^- \rightarrow 36^-$ in the experimental level scheme of ^{152}Dy indicate that no promotion of any nucleon from lower to the higher orbit has taken place; indeed the nucleons (protons) re-arrange themselve in the $\pi d_{5/2}$ orbit and in doing so cost only a few hundred keV energy. In the case of ^{152}Dy, the 36^- level is severely fragmented which is probably due to breaking up of the ^{146}Gd core.

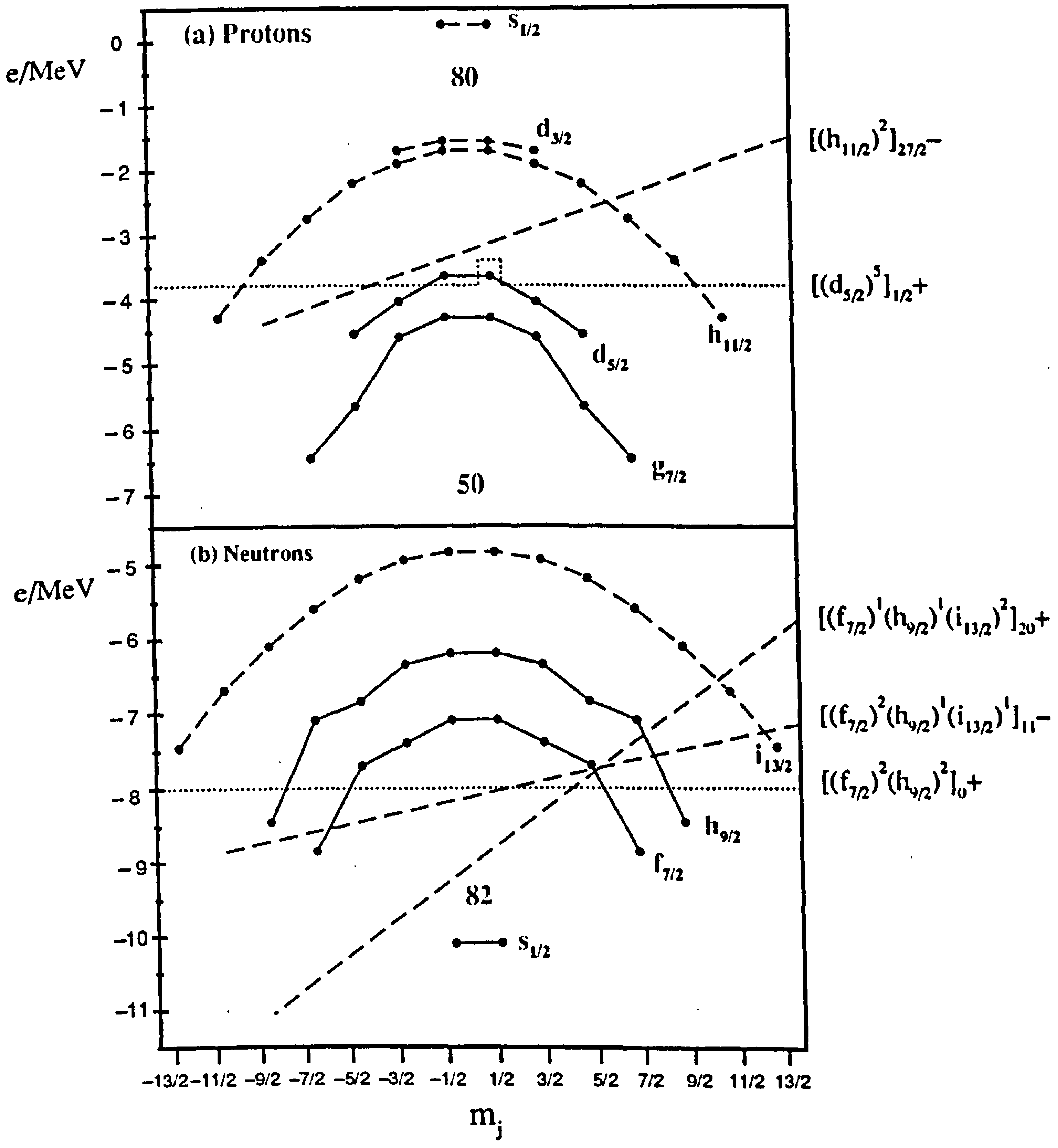

Figure 7.10: *Single particle orbital energies versus angular momentum component at deformation* $\beta_2=0.14$ *for* $^{151}_{86}\mathrm{Tb}_{65}$. *The dotted line shows the Fermi surface at* $\omega=0$ *and all levels below it are occupied. The dashed lines show tilted Fermi surfaces. Tilted Fermi surfaces correspond to different optimal configurations.*

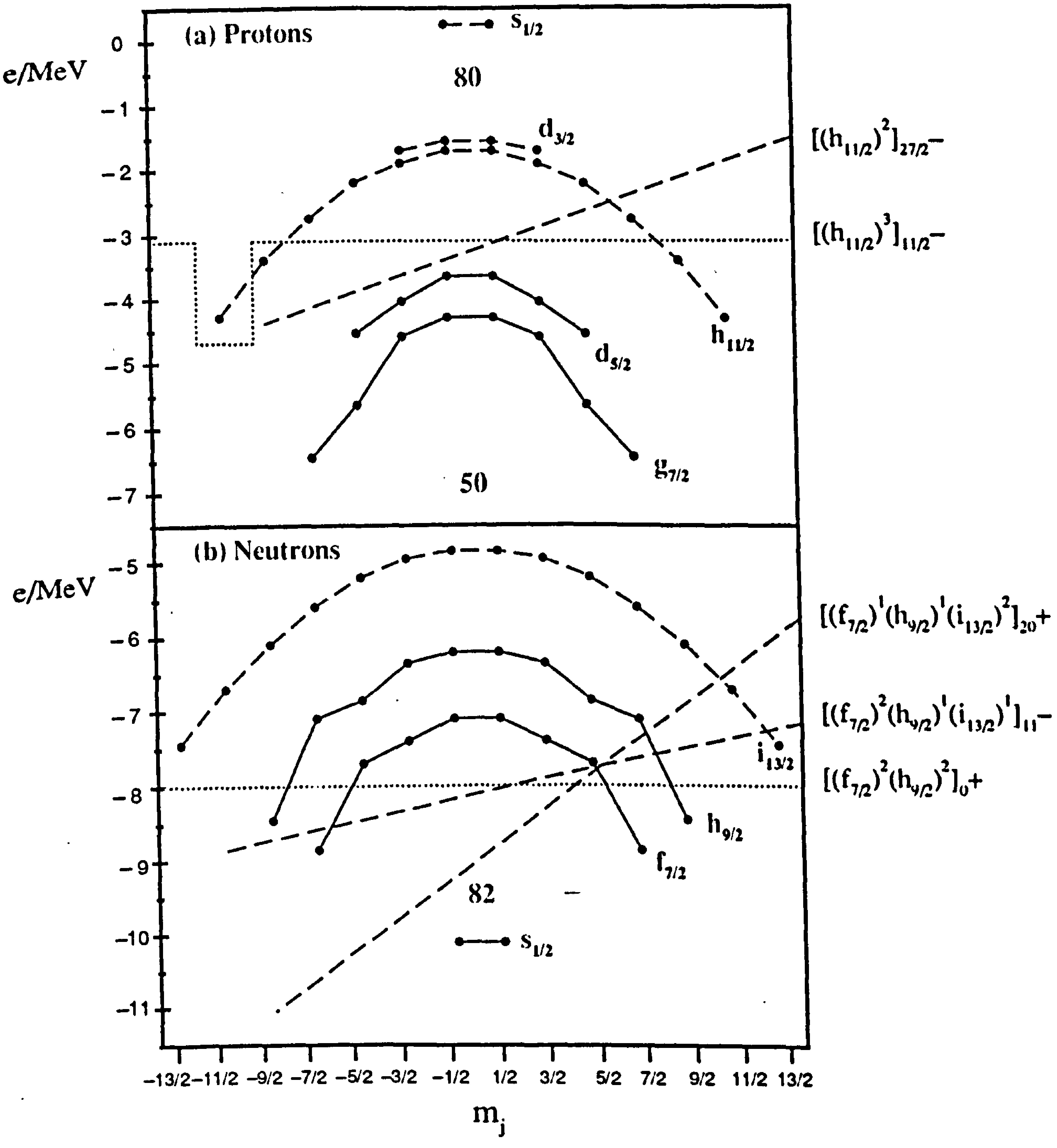

Figure 7.11: *Single particle orbital energies versus angular momentum component at deformation $\beta_2=0.14$ for $^{153}_{86}Ho_{67}$. The dotted line shows the Fermi surface at $\omega=0$ and all levels below it are occupied. The dashed lines show tilted Fermi surfaces. Tilted Fermi surfaces correspond to different optimal configurations.*

Table 7.3

I^{π}	*Neutron Configuration*	*Proton Configuration*
$33/2^{+}$	$\nu(h_{9/2}, i_{13/2})_{11}{}^{-}$	$\pi(h^{1}_{11/2})_{11/2}{}^{-}$
$33/2^{+} \rightarrow 45/2^{+}$	$\nu(h_{9/2}, i_{13/2})_{11}{}^{-} \otimes \nu(f_{7/2})_{(0^{+} \rightarrow 6^{+})}$	$\pi(h^{1}_{11/2})_{11/2}{}^{-}$
$49/2^{+}$	$\nu(h_{9/2}, i_{13/2})_{11}{}^{-}$	$\pi(h^{3}_{11/2})_{27/2}{}^{-} \otimes \pi(d^{4}_{5/2})_{0}{}^{+}$
$53/2^{+}$	$\nu(h_{9/2}, i_{13/2})_{11}{}^{-}$	$\pi(h^{3}_{11/2})_{27/2}{}^{-} \otimes \pi(d^{4}_{5/2})_{2}{}^{+}$
$57/2^{+}$	$\nu(h_{9/2}, i_{13/2})_{11}{}^{-}$	$\pi(h^{3}_{11/2})_{27/2}{}^{-} \otimes \pi(d^{4}_{5/2})_{4}{}^{+}$
$61/2^{+}$	$\nu(i^{2}_{13/2})_{12}{}^{+}(f_{7/2}, h_{9/2})_{8}{}^{+}$	$\pi(h^{2}_{11/2})_{20/2}{}^{-} \otimes \pi(d^{5}_{5/2})_{1/2}{}^{-}$
$65/2^{+}$	$\nu(i^{2}_{13/2})_{12}{}^{+}(f_{7/2}, h_{9/2})_{8}{}^{+}$	$\pi(h^{2}_{11/2})_{20/2} - \otimes \pi(d^{5}_{5/2})_{5/2}{}^{+}$
$67/2^{(-)}$	$\nu(i^{2}_{13/2})_{12}{}^{+}(f_{7/2}, h_{9/2})_{8}{}^{+}$	$\pi(h^{3}_{11/2})_{27/2}{}^{-} \otimes \pi(d^{4}_{5/2})_{0}{}^{+}$
$71/2^{(-)}$	$\nu(i^{2}_{13/2})_{12}{}^{+}(f_{7/2}, h_{9/2})_{8}{}^{+}$	$\pi(h^{3}_{11/2})_{27/2}{}^{-} \otimes \pi(d^{4}_{5/2})_{2}{}^{+}$
$75/2^{(-)}$	$\nu(i^{2}_{13/2})_{12}{}^{+}(f_{7/2}, h_{9/2})_{8}{}^{+}$	$\pi(h^{3}_{11/2})_{27/2}{}^{-} \otimes \pi(d^{4}_{5/2})_{4}{}^{+}$
$77/2^{(+)}$	$\nu(i^{2}_{13/2})_{12}{}^{+}(f_{7/2}, h_{9/2})_{8}{}^{+}$	$\pi(h^{4}_{11/2})_{32/2}{}^{-} \otimes \pi(d^{3}_{5/2})_{5/2}{}^{+}$

Table 7.3: Single particle configuration for the nucleus ^{151}Tb. I^{π} represents the spin and parity of the nuclear energy state.

Table 7.4

I^π	*Neutron Configuration*	*Proton Configuration*
$31/2^+$	$\nu(h_{9/2}, i_{13/2})_{11}{}^-$	$\pi(h^3_{11/2})_{9/2}{}^-$
$31/2^+ \rightarrow 43/2^+$	$\nu(h_{9/2}, i_{13/2})_{11}{}^- \otimes \nu(f_{7/2})_{(0^+ \rightarrow 6^+)}$	$(\pi h^3_{11/2})_{9/2}{}^-$
$49/2^+$	$\nu(h_{9/2}, i_{13/2})_{11}{}^-$	$\pi(h^3_{11/2})_{27/2}{}^-$
$49/2^+ \rightarrow 61/2^+$	$\nu(h_{9/2}, i_{13/2})_{11}{}^- \otimes \nu(f_{7/2})_{(0^+ \rightarrow 6^+)}$	$\pi(h^3_{11/2})_{27/2}{}^-$
$63/2^+$	$\nu(f_{7/2}, i_{13/2})_{10}{}^- \otimes \nu\ (h^2_{9/2})_8{}^+$	$\pi(h^3_{11/2})_{27/2}{}^-$
$67/2^-$	$\nu(i^2_{13/2})_{12}{}^+(f_{7/2}, h_{9/2})_8{}^+$	$\pi(h^3_{11/2})_{27/2}{}^-$
$71/2^-$	$\nu(h^1_{9/2}, i^1_{13/2})_{11}{}^-(f^2_{7/2})_6{}^+$	$\pi(h^4_{11/2}, d^5_{5/2})_{37/2}{}^-$
$73/2^{(+)}$	$\nu(i^2_{13/2})_{12}{}^+(f_{7/2}, h_{9/2})_8{}^+$	$\pi(h^4_{11/2}, d^5_{5/2})_{33/2}{}^-$
$75/2^{(+)}$	$\nu(i^2_{13/2})_{12}{}^+(f_{7/2}, h_{9/2})_8{}^+$	$\pi(h^4_{11/2}, d^5_{5/2})_{35/2}{}^-$
$77/2^{(+)}$	$\nu(i^2_{13/2})_{12}{}^+(f_{7/2}, h_{9/2})_8{}^+$	$\pi(h^4_{11/2}, d^5_{5/2})_{37/2}{}^-$

Table 7.4: Single particle configurations for the nucleus ^{153}Ho. I^π represents the spin and parity of the nuclear energy state.

The respective yrast energy levels for ^{150}Gd, ^{151}Tb, ^{152}Dy and ^{153}Ho above spins 11^- to 17^-, $33/2^+$ to $45/2^+$, 11^- to 17^- and $31/2^+$ to $43/2^+$ are shown in figure 7.14. It can be seen that not only is the configuration $\nu(h_{9/2}, i_{13/2})_{11^-}$ present in the wave function of all states in ^{150}Gd, ^{151}Tb, ^{152}Dy and ^{153}Ho shown in figure 7.14, but the contribution from the configuration $\nu(f^2_{7/2})_{0^+\to 6^+}$ is also present in the wave function. The contribution to the wave functions of ^{151}Tb and ^{153}Ho from the odd proton is quite obvious, both the ^{151}Tb and ^{153}Ho nuclei having one more proton compared with Z-1 neighbours i.e., ^{150}Gd and ^{152}Dy.

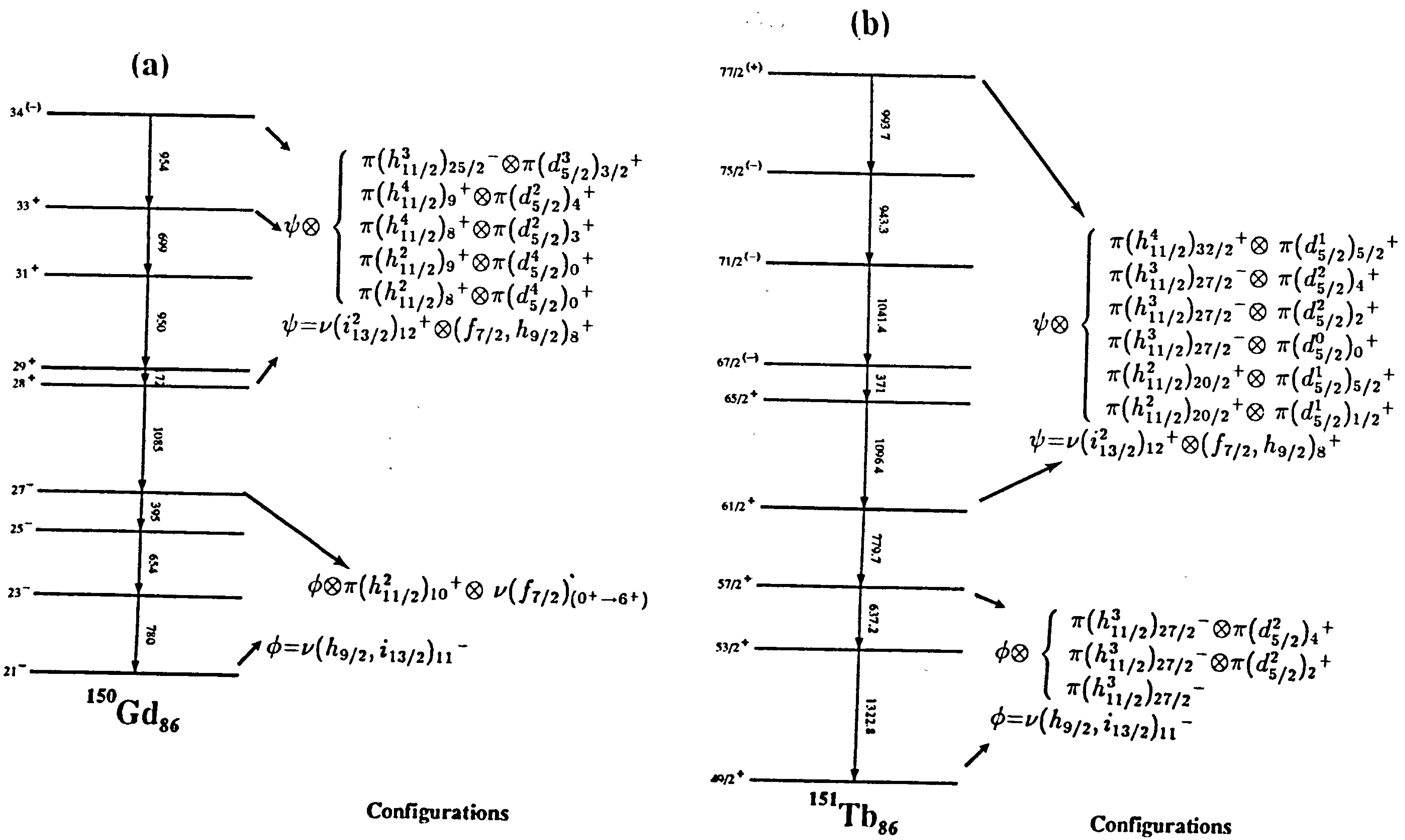

Figure 7.12: *Partial decay schemes of two N=86 isotones: (a) $^{15''}$Gd (b) ^{151}Tb along with their configurations. The experimental data for ^{151}Tb is from [Cu 88].*

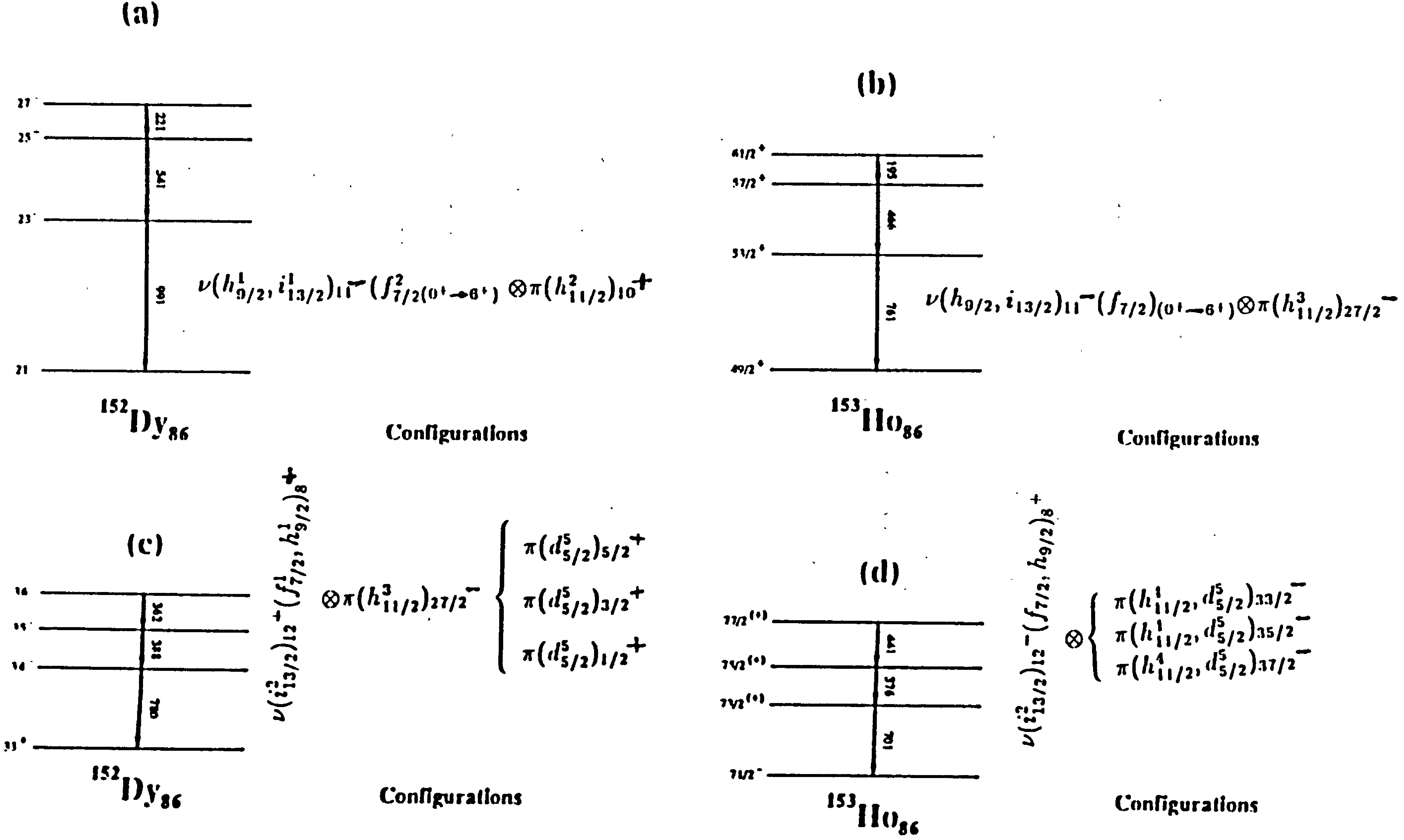

Figure 7.13: *Partial level schemes of two N = 86 isotones along with their configurations: (a), (c) ^{152}Dy and (b), (d) ^{153}Ho. The experimental data for ^{153}Ho is from [Ha 83].*

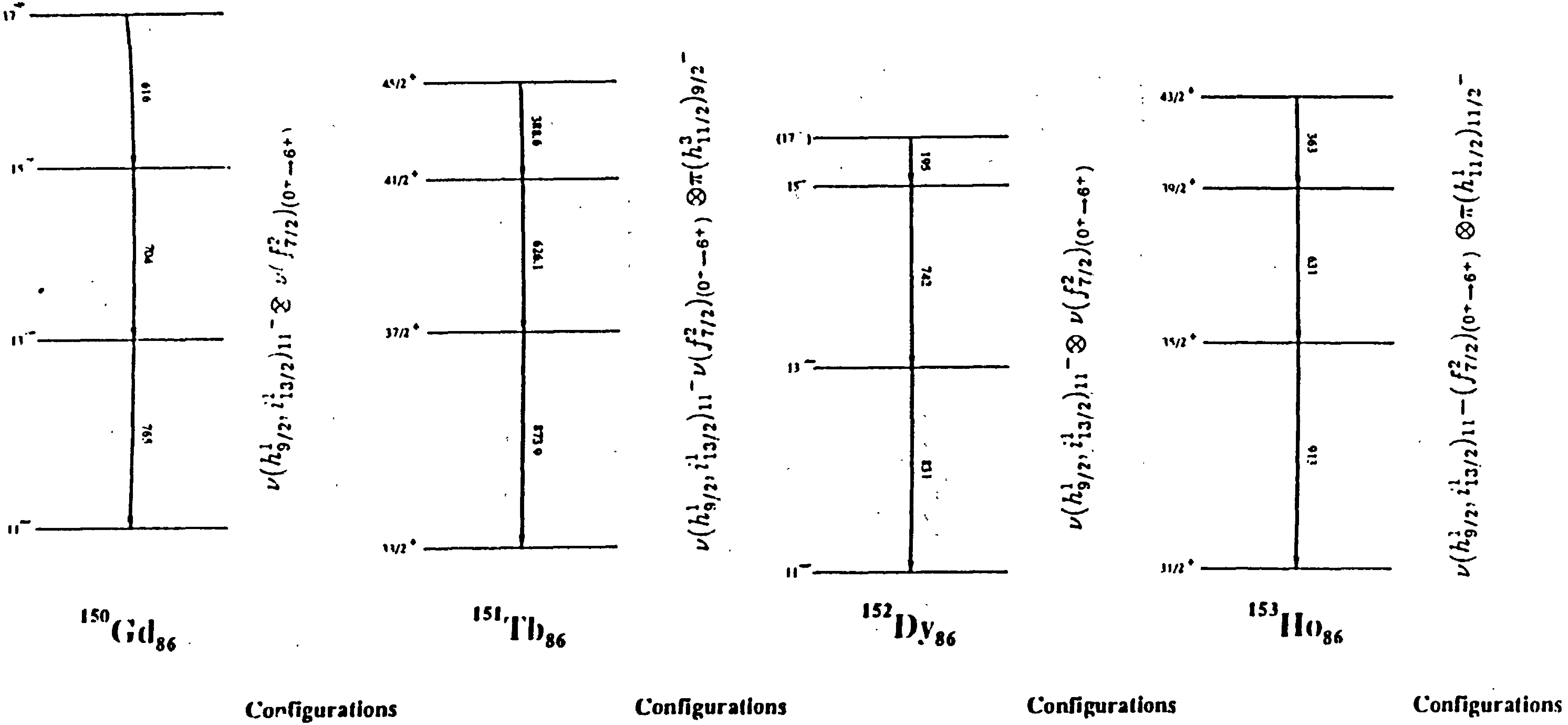

Figure 7.14: *The yrast energy levels for ^{150}Gd, ^{151}Tb, ^{152}Dy and ^{153}Ho from spin 11^- to 17^-, $33/2^+$ to $15/2^+$, 11^- to 17^- and $31/2^+$ to $13/2^+$, respectively. The experimental data for ^{151}Tb and ^{153}Ho is taken from [Cu 88] and [Ha 83], respectively.*

Chapter 8

Results and Discussion on Superdeformed Bands

This chapter is in two parts. Part I is about the results from the ^{130}Te(^{26}Mg,6n)^{150}Gd and ^{130}Te(^{27}Al,6n)^{151}Tb experiments and the observation of the identical superdeformed bands in the ^{150}Gd and ^{151}Tb. In part II the excited superdeformed bands in ^{150}Gd and ^{151}Tb are discussed and interpreted in terms of single particle shell model configurations.

Part I

Excited Superdeformed Bands in ^{150}Gd and ^{151}Tb

8.1 Introduction

It has already been mentioned that the first discrete line superdeformed states in the mass A=150 region were reported by Twin *et al.* [Tw 86]. The occurrence of exotic nuclear shapes with large prolate deformations ($\beta_2 \approx 0.6$) stabilised by microscopic shell effects confirmed the many calculations [St 67, NPS 76, Be 81, DN 85]. With the discovery of several other examples of superdeformation in neighbouring nuclei [Ha 88, Ra 88, De 88, Fa 89, De 89, Jo 89, BAR 88] it soon became apparent that some properties of these bands differed considerably. In particular the dynamic moments of inertia $\Im^{(2)}$ and the de-excitation frequencies were seen to vary from one example to the next. Bengtsson *et al.* [Be 88] proposed that the properties of the superdeformed bands would be influenced by the occupation of high-N intruders. Indeed they calculated the contribution to the total $\Im^{(2)}$ from the intruder orbitals and found that over the frequency range of interest each intruder orbital contributed almost uniquely to $\Im^{(2)}$. Furthermore, TRS (Total Routhian Surface) calculations [NWJ 89] have confirmed these results.

Thus from the slopes of the $\Im^{(2)}$ (ω) curves it is possible to assign configurations to the superdeformed bands in terms of the high-N intruder occupation scheme. It is expected that excited superdeformed bands would be built on particle-hole excitations and it is not clear how these particle excitations should affect the properties of the superdeformed bands.

8.2 Excited Superdeformed Bands in ^{150}Gd and ^{151}Tb

The yrast superdeformed bands in ^{150}Gd and ^{151}Tb were reported by Fallon *et al.*, [Fa 89]. More recently, a second superdeformed band in ^{151}Tb was observed. Following this observation work was carried out to identify a second superdeformed band in ^{150}Gd. The excited superdeformed band in ^{150}Gd was found in the same data set (see section 5.9) which were used to develop the level scheme of ^{150}Gd presented in this work.

Figures 8.1 and 8.2 show background subtracted spectra for these new superdeformed bands in ^{150}Gd and ^{151}Tb. Background subtraction was performed by generating a spectrum in coincidence with a wide gate from 600 to 1450 keV (covering the entire energy range of the band) but not in coincidence with any superdeformed or intense oblate single particle transitions within this range.

8.2.1 The Intensities of the Excited Superdeformed Bands

The energetically favoured superdeformed bands (yrast superdeformed) in ^{150}Gd and ^{151}Tb [Fa 89] are found to each carry around 1% of the reaction channel intensity.

The new superdeformed bands are very weak and are found to be a factor of three weaker than the yrast bands [By 90]. Assuming that yrast states are usually fed more intensively than excited states, for rotational band structures, it is concluded that the new bands are energetically unfavoured and are referred to as excited superdeformed bands. The intensities of the excited superdeformed band peaks in ^{150}Gd and ^{151}Tb (relative to the maximum intensities of the yrast bands in ^{150}Gd and ^{151}Tb respectively) are plotted in figure 8.3 for ^{150}Gd and in figure 8.4 for ^{151}Tb.

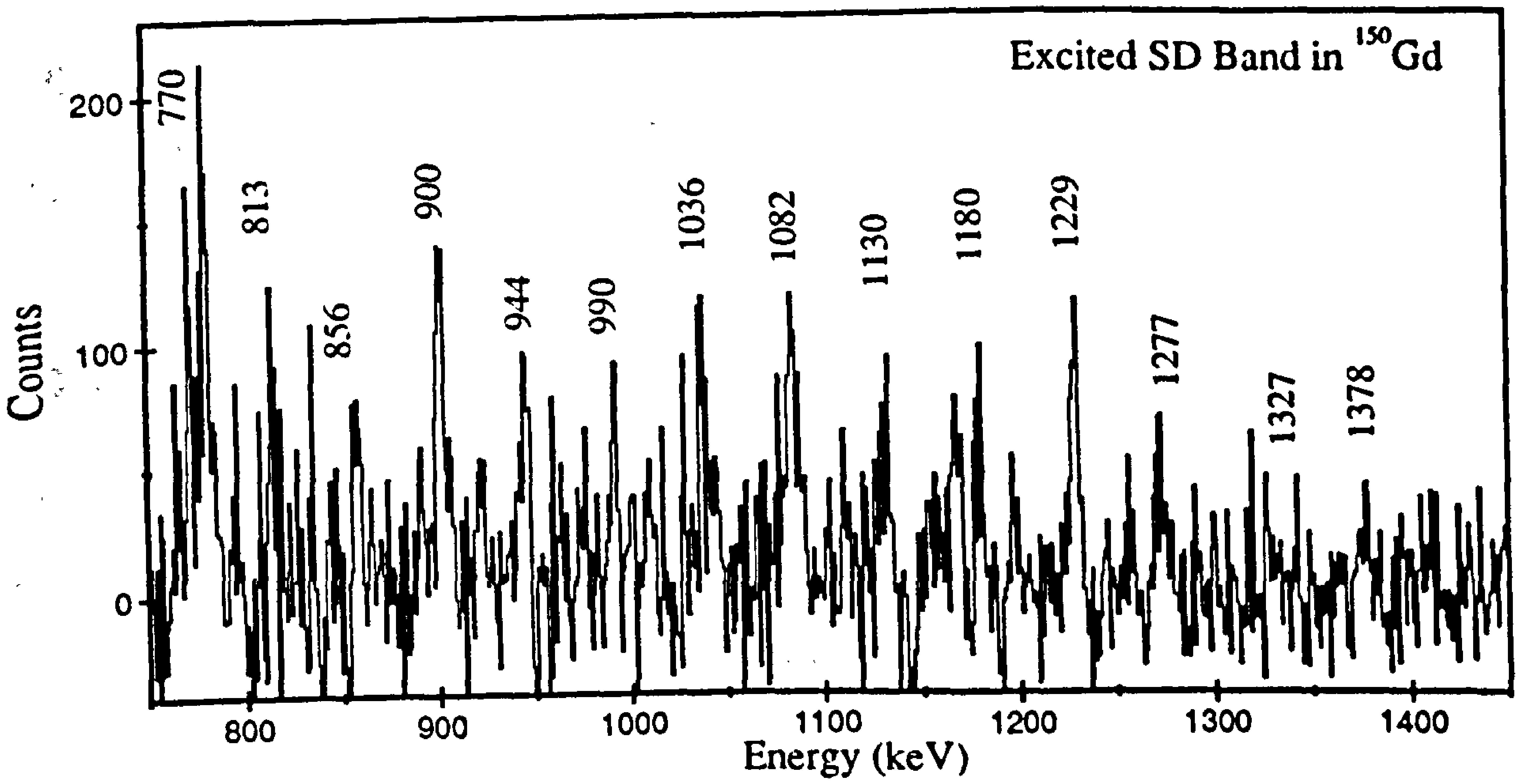

Figure 8.1: *Sum of individual spectra in coincidence with transitions in the excited superdeformed band in ^{150}Gd. The spectrum is background subtracted after normalising to transitions not in coincidence with the band. The energies of the γ rays in the excited superdeformed band are also shown.*

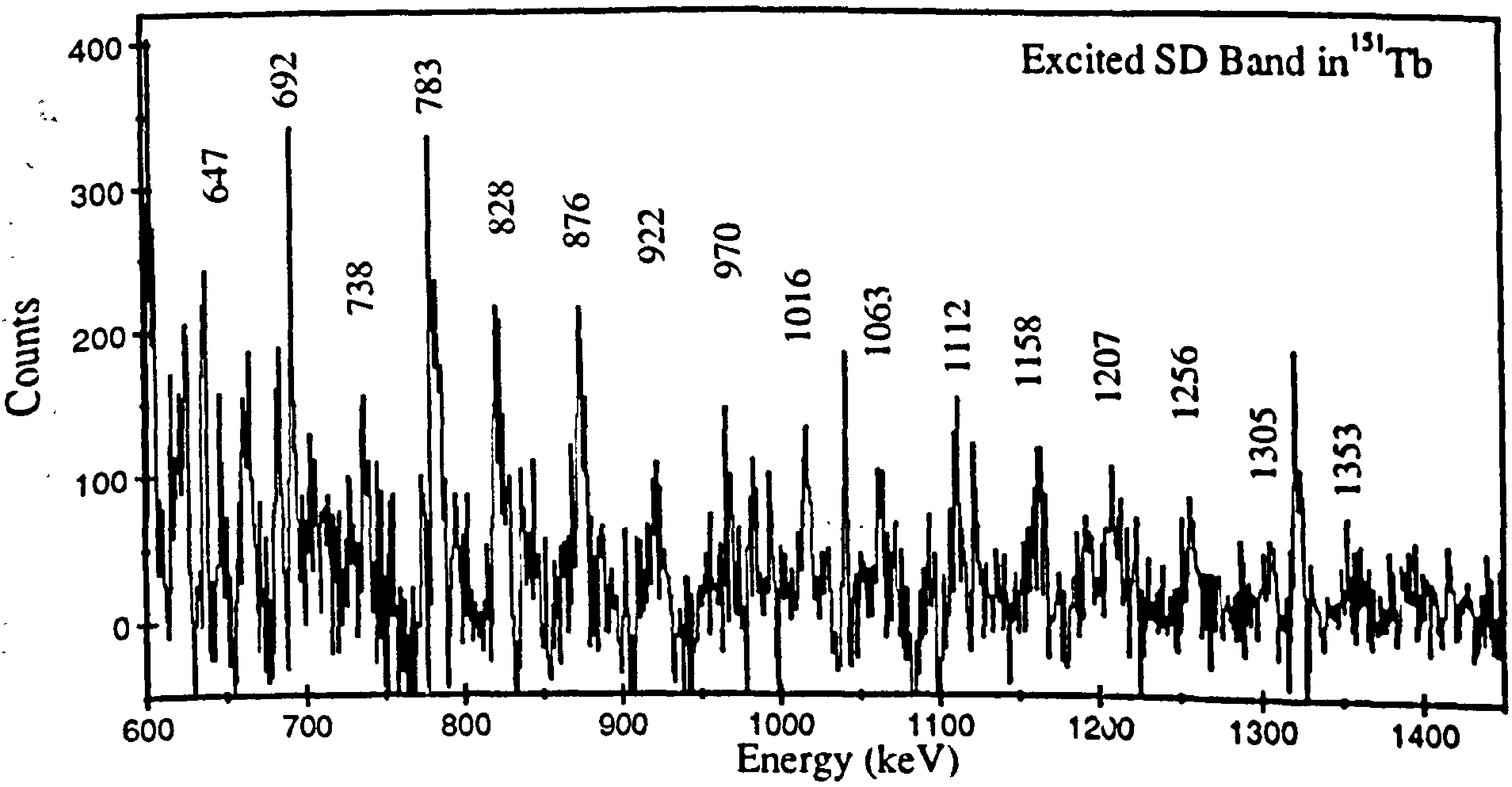

Figure 8.2: *Sum of individual spectra in coincidence with transitions in the excited superdeformed band in ^{151}Tb. The spectrum is background subtracted after normalising to transitions not in coincidence with the band. The energies of the γ rays in the excited superdeformed band are also shown.*

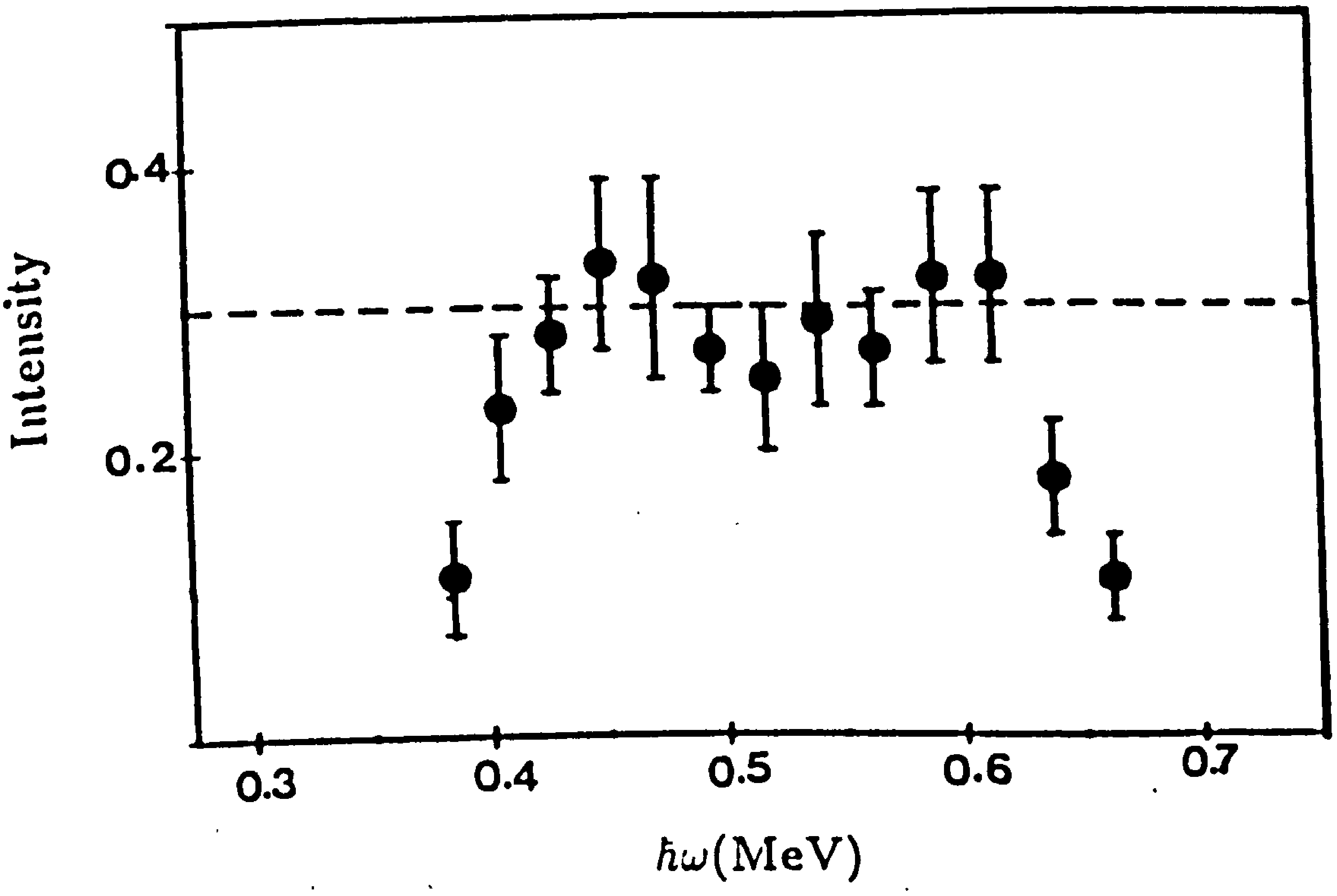

Figure 8.3: *The excited superdeformed band intensities for the ^{150}Gd relative to the maximum intensity of the yrast superdeformed band in ^{150}Gd.*

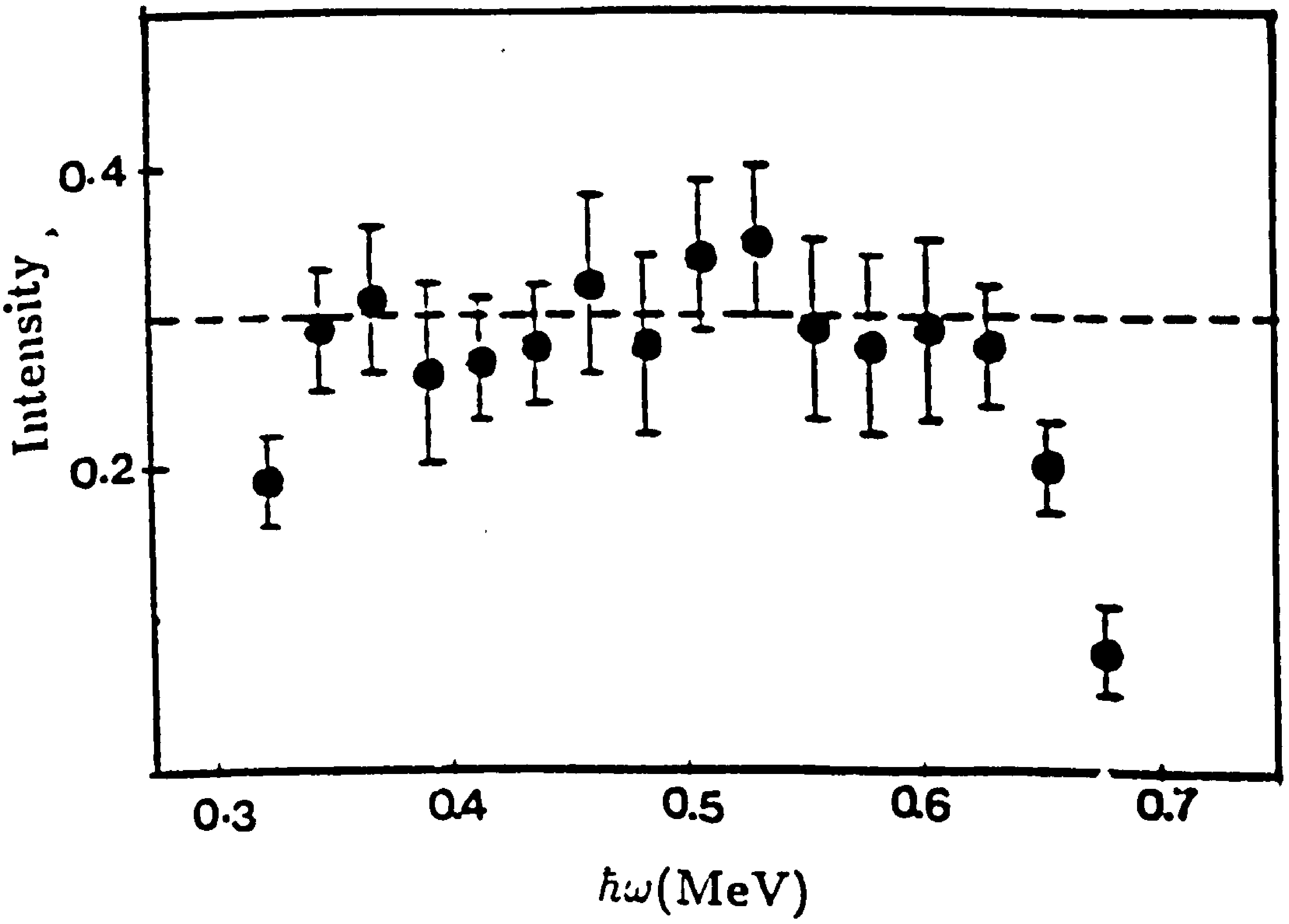

Figure 8.4: *The excited superdeformed band intensities for the ^{151}Tb relative to the maximum intensity of the yrast superdeformed band in ^{151}Tb.*

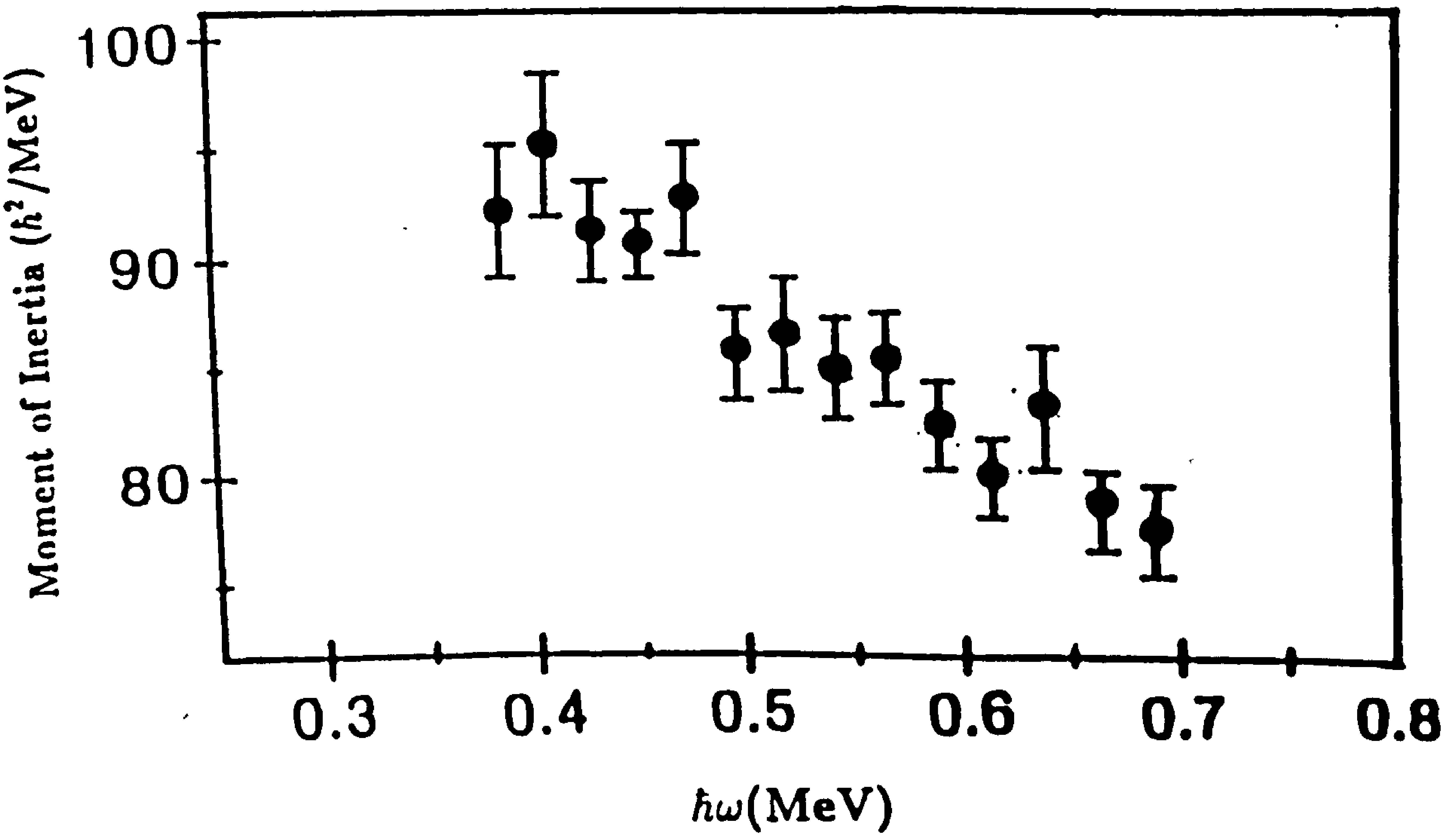

Figure 8.5: *The dynamic moment of inertia* $\Im^{(2)}$ *as a function of rotational frequency for excited SD in* ^{150}*Gd.*

8.2.2 The Dynamic Moments of Inertia of the Excited Superdeformed Bands

The entry point of the superdeformed band into the yrast states could not be clearly identified and hence no definite spin assignments to the superdeformed levels could be made. The dynamic $\Im^{(2)}$ moments of inertia for excited SD bands in ^{150}Gd and ^{151}Tb were determined as described in section 3.6.1 (equation 3.45). They are shown as a function of rotational frequency (figures 8.5 and 8.6).

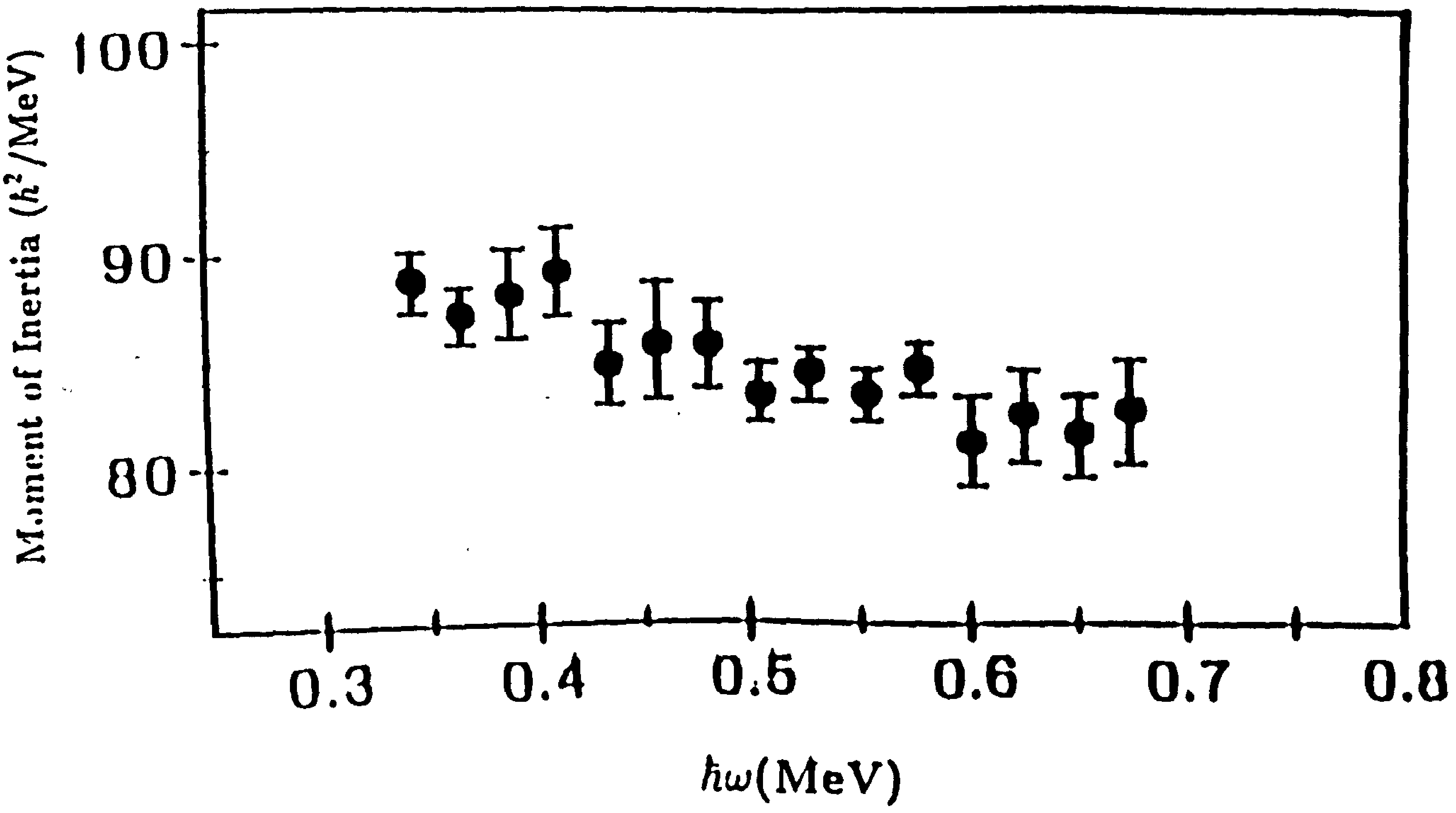

Figure 8.6: *The dynamic moment of inertia $\Im^{(2)}$ as a function of rotational frequency for the excited SD in ^{151}Tb.*

8.2.3 Comparison of the Excited SD Bands with Z+1 N=86 Isotones

These new bands are essentially identical to the yrast superdeformed bands in their Z+1 N=86 isotones i.e., the excited superdeformed band in ^{150}Gd is similar to the yrast superdeformed band in ^{151}Tb and the excited SD band in ^{151}Tb is similar to the yrast superdeformed band in ^{152}Dy .

Figure 8.7 shows (a) the "sum of gate" spectrum in coincidence with transitions in the yrast superdeformed band in ^{151}Tb and (b) the "sum-of-gate" spectra in the excited superdeformed band in ^{150}Gd. Figure 8.8 shows (a) the "sum of gate" spectra in coincidence with transitions in the yrast superdeformed band in ^{152}Dy and (b) the "sum-of-gate" spectra in the excited superdeformed band in ^{151}Tb.

The excited superdeformed bands in ^{150}Gd and ^{151}Tb are seen to be in coincidence with known γ-rays in ^{150}Gd and ^{151}Tb , respectively. The excited superdeformed bands in ^{150}Gd and ^{151}Tb are seen to have similar properties to the previously observed yrast superdeformed bands in their Z+1 isotones. In particular the transition energies are almost identical. However one may rule out the possibility of these identical (twin) bands being one and the same as the Z+1 isotones cannot be produced in the reactions used.

The remarkable similarities between the excited superdeformed bands and the previously observed yrast superdeformed bands in the Z+1 isotones are further illustrated when direct comparisons of the γ-ray energies are made. Figure 8.9 a) and b) shows the differences between the γ-ray energies observed in the identical bands in the pairs of nuclei ^{151}Tb - ^{152}Dy and ^{150}Gd - ^{151}Tb respectively. It can be seen that on average the deviation is less than 1 keV for the ^{151}Tb - ^{152}Dy pair and slightly larger for the ^{150}Gd - ^{151}Tb pair. Since the γ-ray energy for a given spin (angular momentum) is dependent on the kinematic moment of inertia $\Im^{(1)}$, a 1 part in 1000 difference in the γ-ray energies corresponds to a difference in $\Im^{(1)}$ of the same order. This very small difference is extremely surprising since a simple $A^{\frac{5}{3}}$ scaling ($\Im \propto MR^2$) would

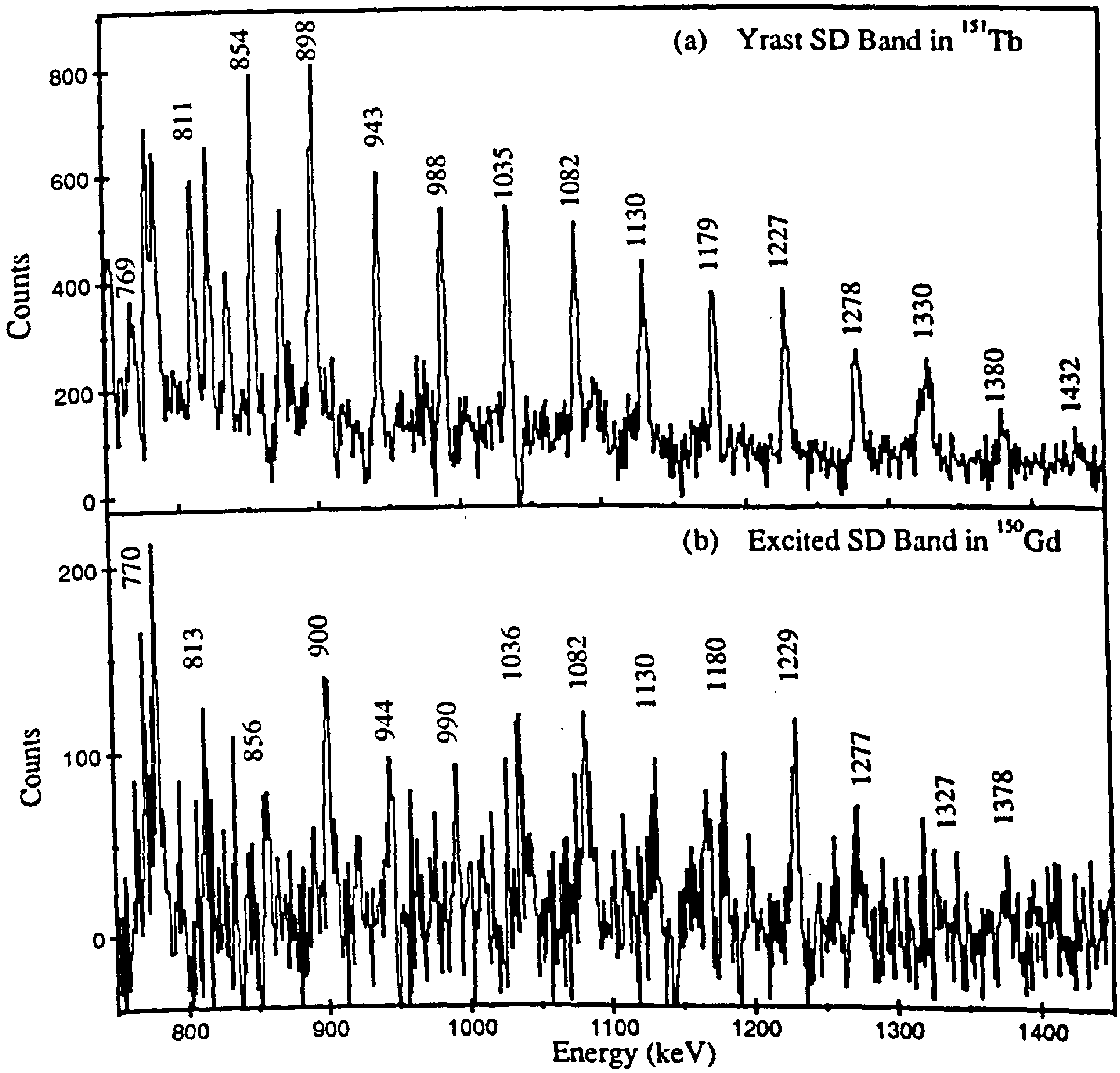

Figure 8.7: *(a) Sum of spectra in coincidence with transitions in the yrast superdeformed band in ^{151}Tb (upper) and (b) sum of spectra in the non yrast superdeformed band in ^{150}Gd (lower). Other γ-rays are associated with normal deformation yrast decays following the de-excitation of the bands.*

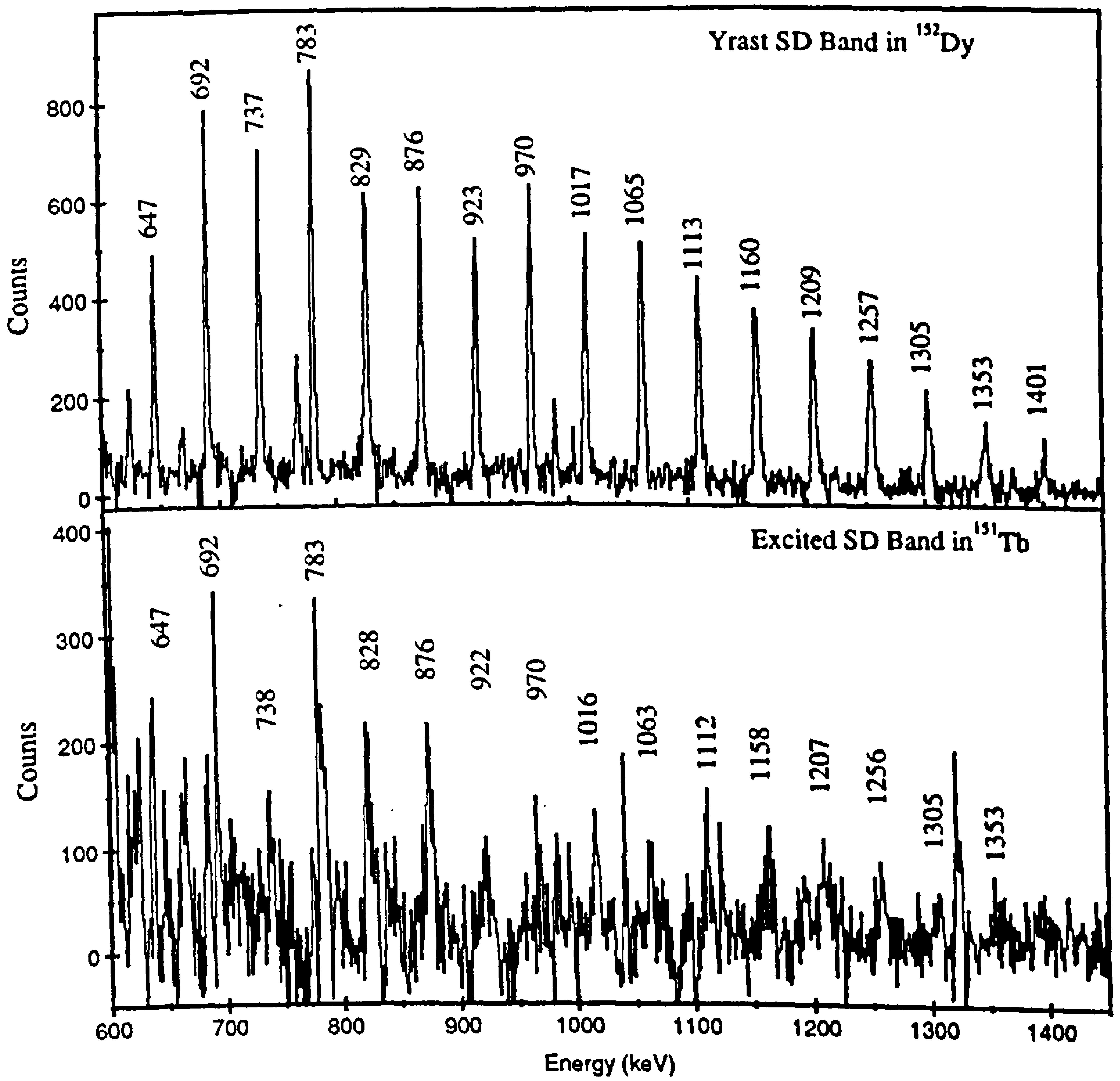

Figure 8.8: *Sum of spectra in coincidence with transitions in yrast superdeformed band in^{152}Dy (upper) and sum of spectra in the non yrast superdeformed band in ^{151}Tb (lower). Other γ-rays are associated with normal deformation yrast decays following the de-excitation of the bands.*

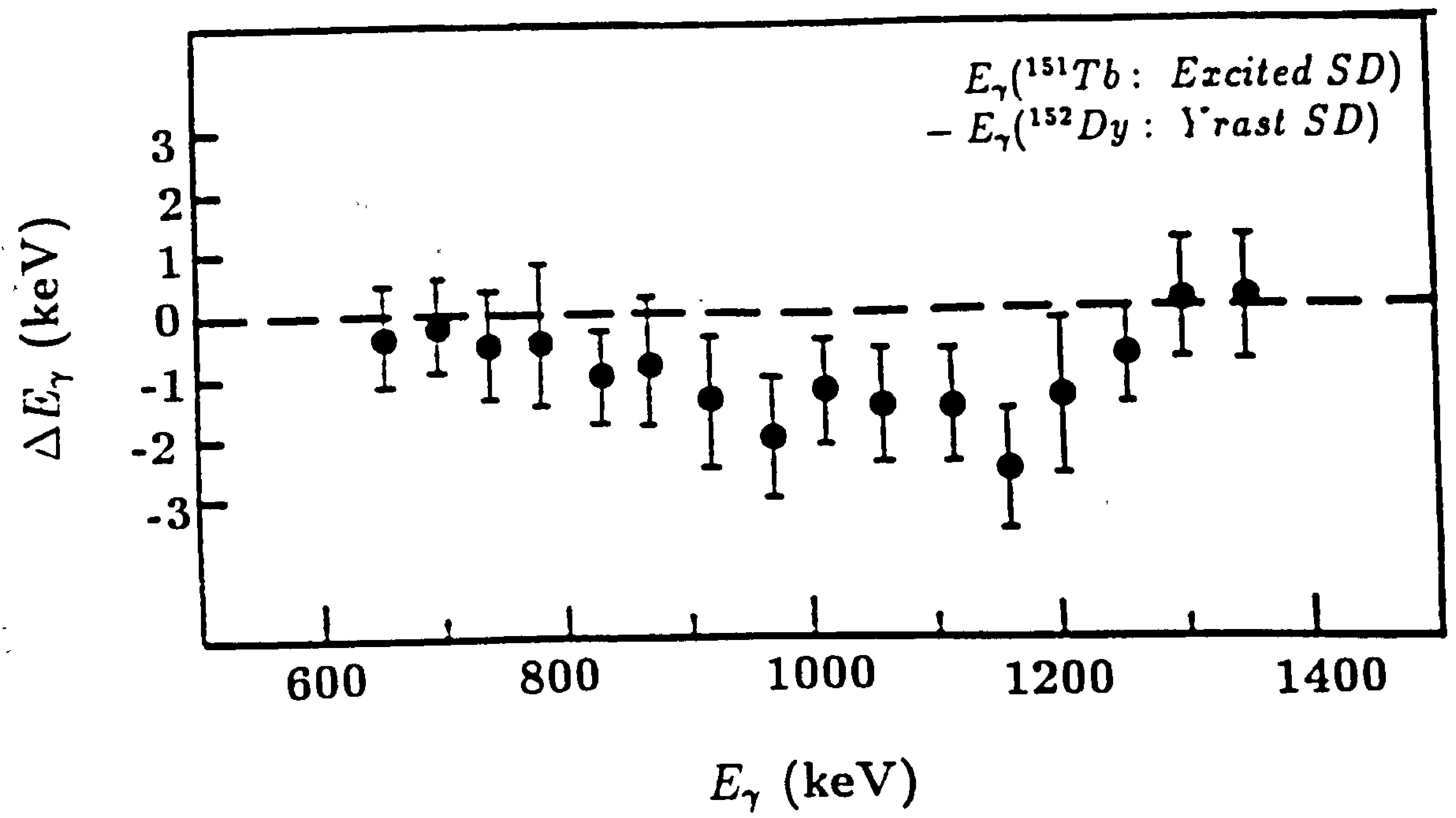

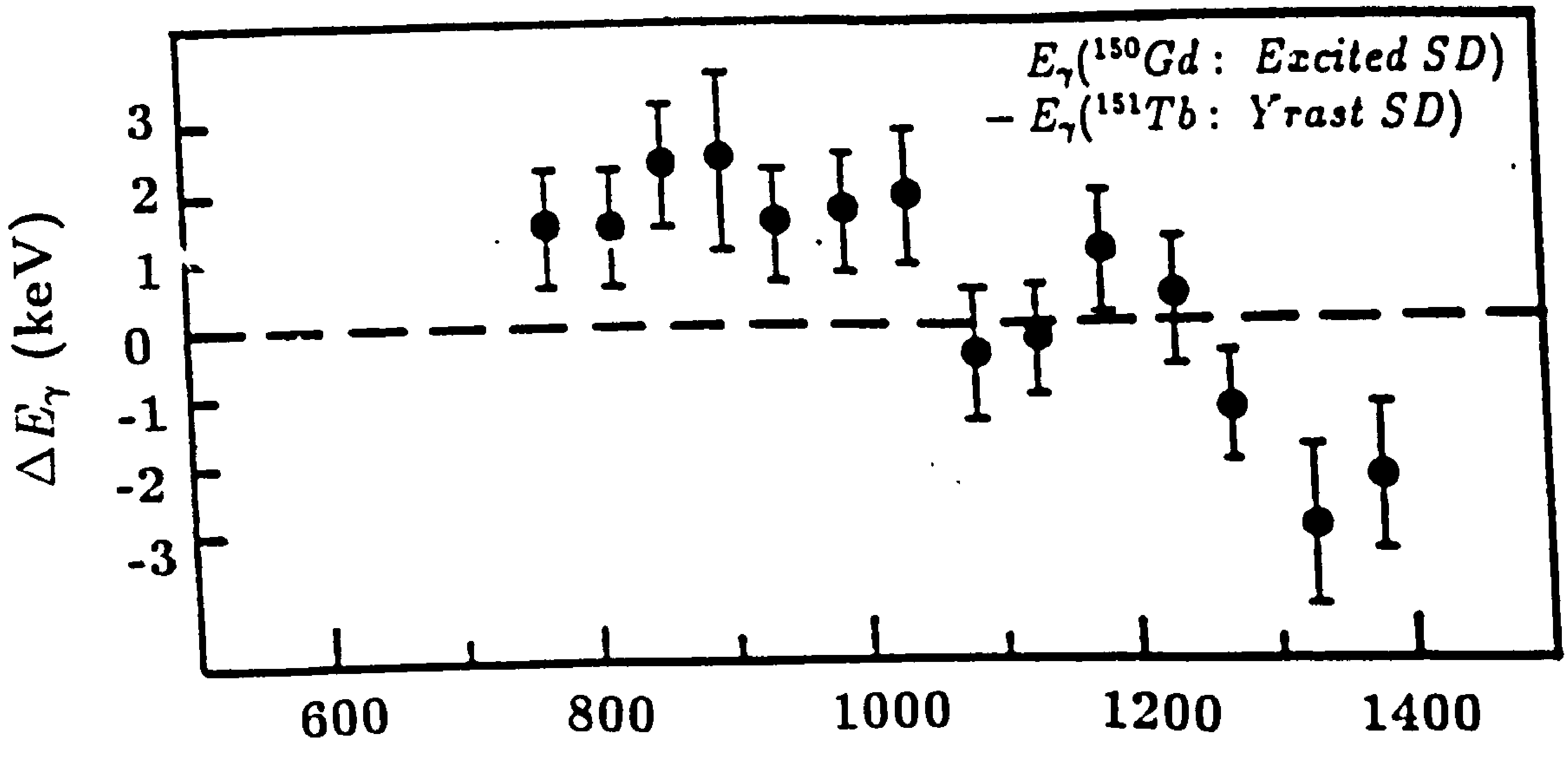

Figure 8.9: *The difference between γ-ray energies observed in the identical bands in the pairs of nuclei (top)* $^{151}Tb - ^{152}Dy$ *and (bottom)* $^{150}Gd - ^{151}Tb$.

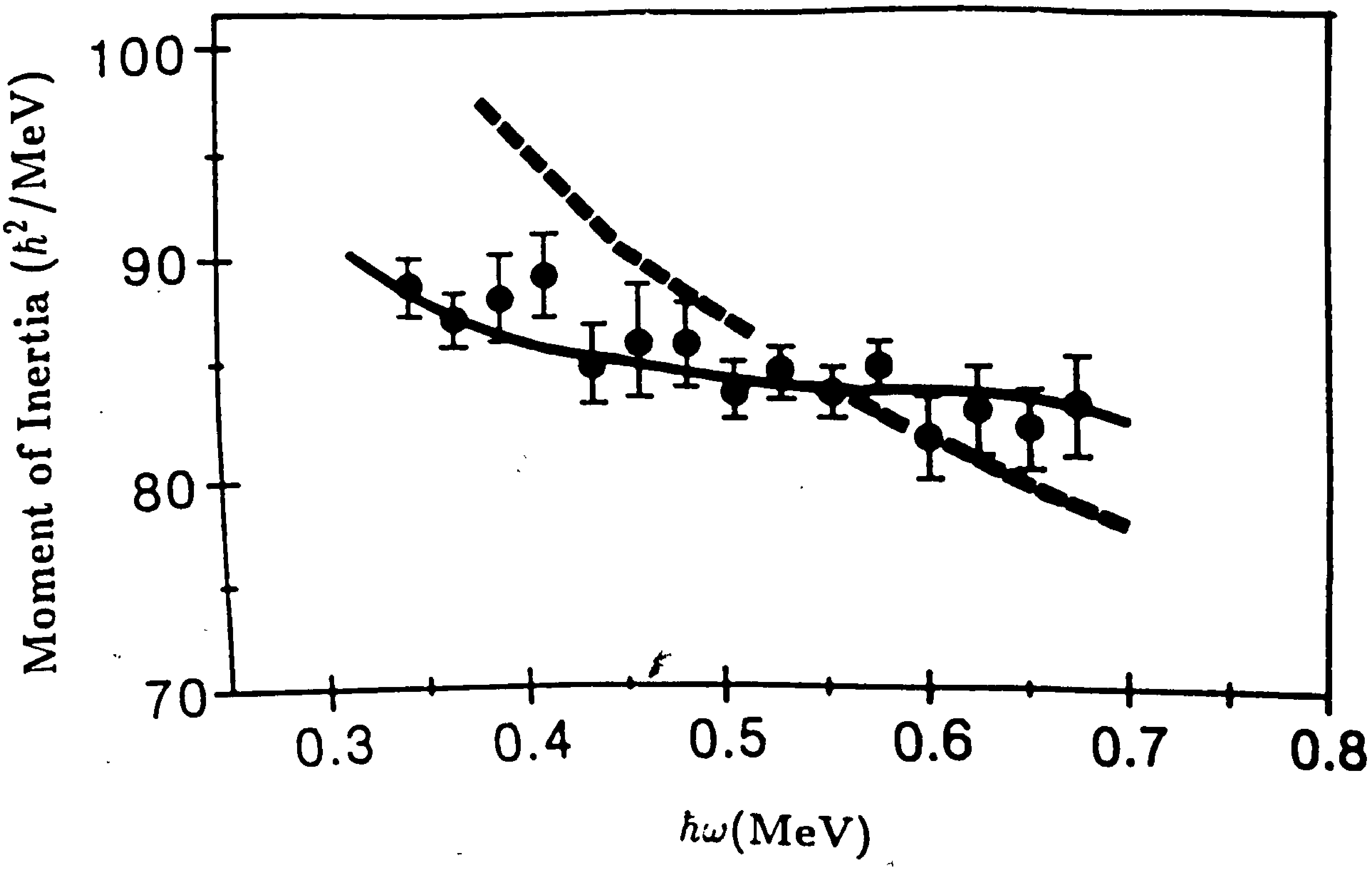

Figure 8.10: *The dynamic moment of inertia $\Im^{(2)}$ as a function of rotational frequency for the excited superdeformed band in ^{151}Tb (circles) together with the $\Im^{(2)}$ curves for the yrast superdeformed band in ^{151}Tb (dashed line) and the yrast superdeformed band in ^{152}Dy (solid line). Clearly the $\Im^{(2)}$ values for the excited superdeformed bands are very similar to the yrast superdeformed bands in their Z+1 N=86 isotone. This implies similar high-N intruder configurations.*

imply differences in γ-ray energies of the order of $\Delta E \approx 10$ keV for $E_\gamma \approx 1$ MeV. A plot of $\Im^{(2)}$ (ω) for the excited superdeformed band in ^{151}Tb figure 8.10 gives a curve that is practically constant and which closely follows the $\Im^{(2)}$ curve traced out by the yrast superdeformed band in ^{152}Dy (solid line) but which is very different from the yrast superdeformed band in ^{151}Tb (dashed line). Similarly the ^{150}Gd excited superdeformed band (figure 8.11) has $\Im^{(2)}$ values which resemble those observed in the ^{151}Tb yrast superdeformed band. (solid line).

It is noticed from these comparisons that the excited superdeformed bands in ^{151}Tb and ^{150}Gd have the same high-N orbitals occupied as the yrast superdeformed bands observed in ^{152}Dy and ^{151}Tb respectively.

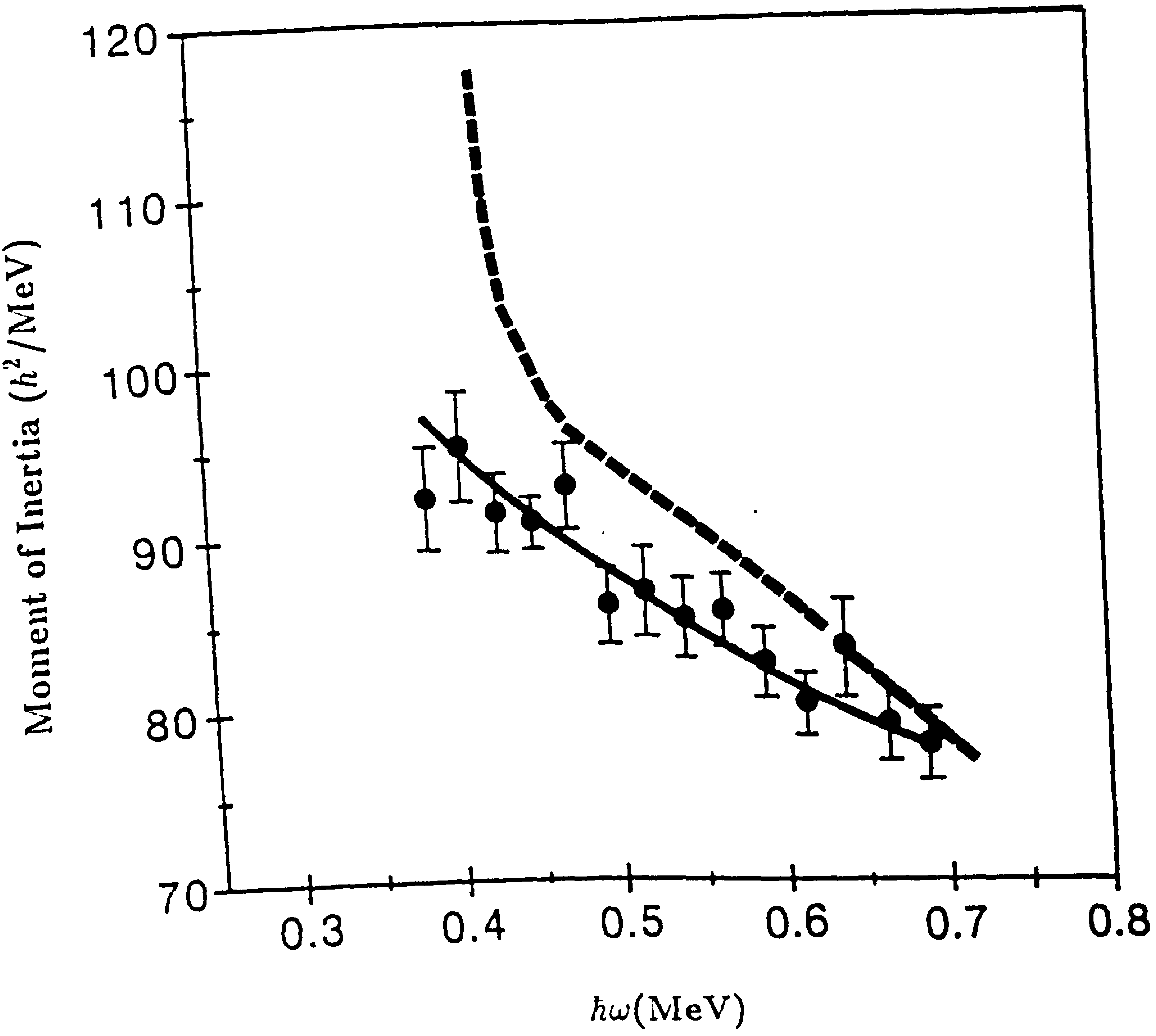

Figure 8.11: *The dynamic moment of inertia $\Im^{(2)}$ as a function of rotational frequency for the excited band in ^{150}Gd (circles) and the yrast bands in ^{150}Gd and ^{151}Tb (dashed and solid lines respectively). Clearly the $\Im^{(2)}$ values for the excited superdeformed bands are very similar to the yrast superdeformed bands in their Z+1 N=86 isotone. This implies similar high-N intruder configurations.*

Part II

Interpretation of the Excited Superdeformed Bands in ^{150}Gd and ^{151}Tb

8.3 Interpretation of the Excited Superdeformed Bands in ^{150}Gd and ^{151}Tb

In the previous chapters the non-collective rotational spectra of energy states of ^{150}Gd and ^{152}Dy and a comparison with their Z+1 neighbours was described in terms of single particle shell model configurations.

It shall be re-called that in the presence of a stable deformation and for axially symmetric shapes ($\gamma=0°$; Lund convention [An 76]) angular momentum can also be generated due to collective rotation of the nucleus as a whole. The rotation in this case shall be about the axis which is perpendicular to the symmetry axis (z-axis) of the nucleus, since for axially symmetric shapes the rotations around the symmetry axis are quantum mechanically indistinguishable from each other.

In this section the excited superdeformed bands (which are produced due to the collective motion of the nucleus) in ^{150}Gd and ^{151}Tb are intrepreted in terms of the shell model single particle configurations. It has been mentioned that the excited superdeformed bands have almost identical gamma-ray energies to the yrast superdeformed bands of their Z+1 neighbours i.e., ^{151}Tb and ^{152}Dy respectively. Hence, the excited superdeformed bands were observed to have almost the same dynamic moments of inertia of their Z+1 neighbours.

The calculated configuration for the superdeformed shapes can be written in terms of the high N intruder orbitals, N being the principal oscillator quantum number. In the case of ^{150}Gd, ^{151}Tb and ^{152}Dy the intruder orbitals are N=6 proton states (originating from the $1i_{13/2}$ subshells) and the N=7 neutron states (originating from the $1j_{15/2}$ subshells) [NWJ 89], the configurations frequently written as $\pi(i_{13/2})^n\nu(j_{15/2})^m$ with n and m being the number of proton and neutron intruder states occupied.

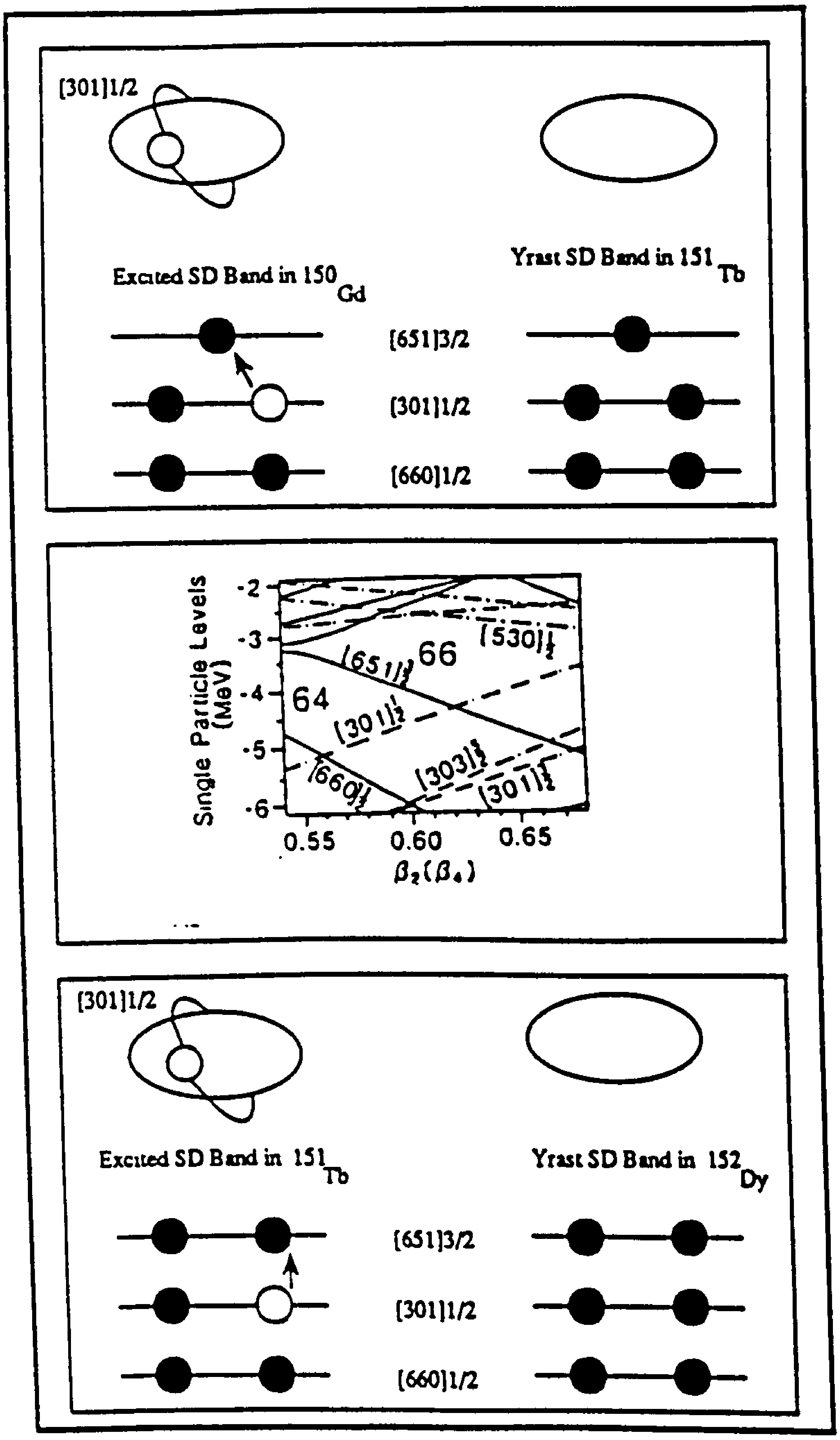

Figure 8.12: *The top and bottom portions of the figure are a schematic representation of the configuration of the excited band in ^{150}Gd and ^{151}Tb, respectively. The excited band in ^{150}Gd is shown as a hole (in the [301]1/2 orbital) in the ^{151}Tb superdeformed core and the excited band in ^{151}Tb is shown as a hole (in the [301]1/2 orbital) in the ^{152}Dy superdeformed core (top and bottom portions of the figure). In the middle of the figure a section of the proton single particle levels as a function of deformation $\beta_2(\beta_4)$ is shown. At $\beta_2\approx0.6$ the oblate driving [301]1/2 orbital and the prolate driving [651]3/2 intruder orbital cross each other, hence a proton excitation from the [301]1/2 to the [651]3/2 level is energetically favourable.*

Table 8.1

Band	*Proton Configuration*	*Neutron Configuration*
Yrast SD in ^{151}Tb	$\pi(i_{13/2})^3$	$\nu(j_{15/2})^2$
Excited SD in ^{150}Gd	$\pi(i_{13/2})^3([301]1/2)^{-1}$	$\nu(j_{15/2})^2$
Yrast SD in ^{152}Dy	$\pi(i_{13/2})^4$	$\nu(j_{15/2})^2$
Excited SD in ^{151}Tb	$\pi(i_{13/2})^4([301]1/2)^{-1}$	$\nu(j_{15/2})^2$

Table 8.1: Single particle shell model configurations for the yrast and excited superdeformed bands in ^{151}Tb,^{152}Dy and ^{150}Gd, ^{151}Tb, respectively.

In the case of ^{150}Gd, ^{151}Tb and ^{152}Dy there are two, three and four protons, respectively in the N=6 ($i_{13/2}$) and two neutrons in the N=7 ($j_{15/2}$) shells (as explained in figure 3.15 from [NWJ 89]): the single particle shell model configurations for ^{150}Gd, ^{151}Tb and ^{152}Dy can be written as $\pi(i_{13/2})^2\nu(j_{15/2})^2$, $\pi(i_{13/2})^3\nu(j_{15/2})^2$ and $\pi(i_{13/2})^4\nu(j_{15/2})^2$ respectively. The contribution to the dynamic moment of inertia for a particular orbit, ν, is given by the curvature of the orbital (derived from equation 3.41):

$$\Im_\nu^{(2)} = \frac{di_\nu}{d\omega} \tag{8.1}$$

The total dynamic moment of inertia "$\Im^{(2)}$" is then obtained by summing over all proton and neutron orbitals.

Figure 8.12 presents the calculated [NWJ 89] single particle levels for protons as a function of deformation β_2 while table 8.1 presents the single particle shell model configurations for the yrast and excited superdeformed bands in ^{151}Tb, ^{152}Dy and ^{150}Gd, ^{151}Tb, respectively. A close examination of figure 8.12 shows that at $\beta_2 \approx 0.6$ a strongly prolate deformation driving intruder orbital originating from the N=6 ($1i_{13/2}$ subshells) oscillator shell is crossed by the equally deformation sensitive but oblate driving orbital labelled [301]1/2. The slope of the [301]1/2 orbital is unaffected by the rotation and hence this orbital does not contribute to the moment of inertia $\Im^{(2)}$.

It is therefore possible to excite a proton from the [301]1/2 orbital into the [651]3/2 intruder orbital and hence the excited superdeformed band in ^{150}Gd can be associated with the configuration $\pi(i_{13/2})^3([301]1/2)^{-1} \otimes\nu(j_{15/2})^2$ (i.e., the same proton and neutron intruder configurations as the yrast SD band in ^{151}Tb) and the excited band in ^{151}Tb can be associated with the configuration $\pi(i_{13/2})^4([301]1/2)^{-1}\otimes\nu(j_{15/2})^2$ (i.e., the same proton and neutron intruder configuration as the yrast SD band in ^{152}Dy). These configurations have been presented in table 8.1.

Chapter 9

Summary

9.1 Non Collective Rotations

The experimental level schemes of ^{150}Gd and ^{152}Dy, describing the normal deformed single particle excitations in the first potential energy well, have been extended up to spin$\sim 40\hbar$ and calculations have been performed to interpret these level schemes.

The yrast nuclear energy states of ^{150}Gd and ^{152}Dy look very similar up to spin 34^- whereas there are differences in the energy levels above spin 34^-. The differences in the nuclear energy states in latter cases are due to the breaking up of the N=82 and Z=64 cores and subsequent excitations/re-arrangements of the protons and neutrons. Since both nuclei have different numbers of protons, their different behaviour at very high spins may be due to the excitations/re-arrangemengts of protons in the $d_{5/2}$ and $h_{11/2}$ orbits.

The feeding of the yrast energy level at 36^- in ^{152}Dy is severely fragmented in contrast to the 36^+ non-yrast level. This fragmentation may be due to breaking up of the N=82 and Z=64 core with a resultant increase in the level density.

By comparing the experimental level schemes of ^{150}Gd and ^{152}Dy with the respective calculations, it appears that up to spin 34^- it is not only the experimental level schemes of ^{150}Gd and ^{152}Dy that are similar but their single particle configurations up to spin 34^- are also very similar. These configurations are based mainly on the excitation/re-arrangements of neutrons in the $\nu h^2_{9/2}\nu f^2_{7/2}$ orbitals and protons in the $\pi h_{11/2}$ and $d_{5/2}$ orbitals. The configurations above 34^- are predicted to be different due to the different re-arrangement of neutrons and protons in these nuclei at very high spins.

Furthermore, a comparison of ^{150}Gd and ^{152}Dy with their Z+1 neighbours (i.e., ^{151}Tb and ^{153}Ho, respectively) reveals some remarkable similarities amongst these nuclei. From the single particle configurations of ^{150}Gd, ^{151}Tb, ^{152}Dy and ^{153}Ho it appears that a few configurations play a very special role and they generally correspond to the maximum-aligned configurations. These maximum aligned configurations are generally associated with yrast traps (isomeric states). For example the configuration such as
$[\nu(h_{9/2}, i_{13/2})_{11}-\otimes\pi(h^3_{11/2})_{9/2}{}^-\pi(d^5_{5/2})_{3/2}{}^+]_{17}{}^+$,
$[\nu(h_{9/2}, i_{13/2})_{11}{}^-\otimes\pi(h^2_{11/2})_{10}{}^+]_{21}{}^-$ and
$[\nu(h_{9/2}, i_{13/2})_{11}{}^-\nu(f^2_{7/2})_6{}^+\otimes\pi(h^2_{11/2})_{10}{}^+]_{27}{}^-$
in the case of ^{150}Gd and ^{152}Dy,
and $[\nu(h_{9/2}, i_{13/2})_{11}{}^-\otimes\ \pi(h^1_{11/2})_{11/2}{}^-]_{33/2}{}^+$,
$[\nu(h_{9/2}, i_{13/2})_{11}{}^-\otimes\pi(h^3_{11/2})_{27/2}{}^-\pi(d^4_{5/2})_0{}^+]_{49/2}{}^+$
in the case of ^{151}Tb,
and $[\nu(h_{9/2}, i_{13/2})_{11}{}^-\otimes\pi(h^3_{11/2})_{9/2}{}^-]_{31/2}{}^+$,
$[\nu(h_{9/2}, i_{13/2})_{11}{}^-\nu(f_{7/2})_6{}^+\otimes\pi(h^3_{11/2})_{27/2}{}^-]_{61/2}{}^+$
in the case of ^{153}Ho.

9.2 Collective Rotations

A particle-hole excitation in the second potential energy well of ^{150}Gd and ^{151}Tb has been identified. The single particle shell model configuration for the excited SD bands in ^{150}Gd and ^{151}Tb are similar to the yrast SD bands of their Z+1 neighbours. This means that the excited SD bands in ^{150}Gd and ^{151}Tb have the same intruder orbitals occupied as the yrast superdeformed bands in their respective Z+1 neighbours, ^{151}Tb and ^{152}Dy. Hence the contribution to the $\Im^{(2)}$ from the excited superdeformed bands in ^{150}Gd and ^{151}Tb is the same as from the yrast superdeformed bands in the Z+1 isotones.

By comparing the experimental γ-ray energies for the pair of bands with the same intruder configurations it can be seen that the γ-ray energies are almost identical; hence the bands have same moments of inertia. Why they are so identical is still a matter of debate.

9.3 Future Developments

At present no linking transitions have been observed between the superdeformed to normal deformed states. This work may further be extended and one may expect that this problem will be solved with the help of the new generation of arrays such as Eurogam, Euroball and Gamma-sphere.

Furthermore, an experiment is proposed in order to find the experimental parities of the high spin states of ^{150}Gd and ^{152}Dy. The single particle shell model configurations for both the ^{150}Gd and ^{152}Dy nuclei are mainly based on the excitation of protons and neutrons in the $\pi(d_{5/2})\pi(h_{11/2})$ and $\nu(f_{7/2})^2\nu(h_{9/2})^2$ orbitals respectively. It is expected that the experimental parities at higher spins would be very similar for both the ^{150}Gd and ^{152}Dy nuclei and we could make a more solid comparison between the predicted and the experimental level schemes of ^{150}Gd and ^{152}Dy.

Appedix A

List of Publications

1. *"Observation of Identical Bands in N=86 Nuclei"*
   T. Byrski, F. A. Beck, D. Curien, P. Fallon, A. Alderson, I. Ali, M. A. Bentley, A. M. Bruce, P. D. Forsyth, D. Howe, J. W. Roberts, J. F. Sharpey-Schafer, G. Smith, P. J. Twin.
   Physical Review Letters 64 (1990) 1650 - 1653

2. *"The Collectivety and De-excitation of the Yrast Superdeformed Band in ^{150}Gd"*
   P. Fallon, A. Alderson, I. Ali, D. M. Cullen, M. A. Bentley, A. M. Bruce, P. D. Forsyth, M. A. Riley, J. W. Roberts, J. F. Sharpey-Schafer, P. J. Twin.
   Physics Letters B 257 (1991) 269 - 272

3. *"The Spectroscopy of $^{161,162}Er$ at Spins upto $50\hbar$ in the Unpaired Regime"*
   M. A. Riley, J. W. Roberts, J. simpson, A. Alderson, I. Ali, M. A. Bentley, A. M. Bruce, R. Chapman, D. M. Cullen, P. Fallon, P. D. Forsyth, J. C. Lisle, J. N. Mo and J. F. Sharpey-Schafer.
   J. Phys. G: Nuclear Physics 16 (1990) L67 - L73

4. *"Multiple superdeformed Bands in ^{194}Hg and their Dynamical Moments of Inertia"*
   M. A. Riley, D. M. Cullen, A. Alderson, I. Ali, P. Fallon, P. D. Forsyth, F. Hanna, S. M. Mullins, J. W. Roberts, J. F. Sharpey-Schafer, P. J. Twin, R. Poynter, R. Wadsworth, M. A. Bentley, A. M. Bruce, J. Simpson, G. Sleten, W. Nazarewicz, T. Bengtsson and R. Wyss.
   Nuclear Physics A512 (1990) 178 - 188

5. *"Landau-Zener Crossing in Superdeformed* ^{193}*Hg: Evidence for Octupole Correlations in Superdeformed nuclei"*
   D. M. Cullen, M. A. Riley, A. Alderson, I. Ali, P. Fallon, P. D. Forsyth, F. Hanna, S. M. Mullins, J. W. Roberts, J. F. Sharpey-Schafer, P. J. Twin, R. Poynter, R. Wadsworth, M. A. Bentley, A. M. Bruce, J. Simpson, G. Sleten, W. Nazarewicz, T. Bengtsson and R. Wyss.
   Physical Review Letters 65 (1990) 1547 - 1550

6. *"Evidence for Octupole Softness of the Superdeformed Shape from Band Interactions in* ^{193,194}*Hg"*
   D. M. Cullen, M. A. Riley, A. Alderson, I. Ali, P. Fallon, P. D. Forsyth, F. Hanna, S. M. Mullins, J. W. Roberts, J. F. Sharpey-Schafer, P. J. Twin, R. Poynter, R. Wadsworth, M. A. Bentley, A. M. Bruce, J. Simpson, G. Sleten, W. Nazarewicz, T. Bengtsson and R. Wyss.
   Nuclear Physics A520 (1990) 105c - 113c

7. *"The unpaired spectroscopy of* ^{161,162}*Er at spins upto* $50\hbar$*"*
   M. A. Riley, J. W. Roberts, J. Simpson, A. Alderson, I. Ali, D. M. Cullen, P. Fallon, P. D. Forsyth, J. F. Sharpey-Schafer, M. A. Bentley, A. M. Bruce, R. Chapman, J. C. Lisle and J. N. Mo.
   Nuclear Physics A520 (1990) 279c - 286c

8. *"Gamma-ray spectroscopy of A=56 Nuclei"*
   M.A. Bentley, A. M. Bruce, H.J. Price, J. Simpson, I. Ali, P. Fallon, A.N. James, S.M. Mullins, M.A. Riley, B.R. Fulton and G. Lobianco.
   Daresbury Annual Report (1990)

9. *"The collectivety of the superdeformed band in* ^{152}*Dy at the point of de-excitation"*

A. Alderson, I. Ali, D. M. Cullen, P. Fallon, P. D. Forsyth, M. A. Riley, J. W. Roberts, J. F. Sharpey-Schafer, P. J. Twin, M. A. Bentley and A. M. Bruce.

Daresbury Annual Report (1990)

10. *"New superdeformed behaviour in* ^{193}Hg*"*

    D. M. Cullen, M. A. Riley, W. Nazarwicz, A. Alderson, I. Ali, P. Fallon, P. D. Forsyth, F. Hanna, S. M. Mullins, J. W. Roberts, J. F. Sharpey-Schafer, P. J. Twin, R. J. Poynter, P. Reagan, R. Wadsworth, M. A. Bentley, A. M. Bruce, J. Simpson, G. Sleten, T. Bengtsson, W. Satula and R. Wyss.

    Daresbury annual Report(1990)

11. *"The quadrupole moment of the K=25 isomer in* ^{182}Os*"*

    C. Broude, M. Hass, G. Golgring, A. Alderson, I. Ali, D. M. Cullen, P. Fallon, F. Hanna, J. W. Roberts and J. F. Sharpey-Schafer.

    Physics Letters B264 (1991) 17-20

12. *"First Observation of a Collective Dipole Rotational Band in a Spherical Nucleus"*

    R.M. Clark, R. Wadsworth, E.S.Paul, C.W. Beausang, I. Ali, A.Astier, D.M.Cullen, P.J.Dagnall, P.Fallon, M.J.Joyce, M.Meyer, N.Redon, P.H.Reagan.

    Submitted to Physics Letters B (1991)

13. *"Shape Co-existence in* ^{119}I *at High Spin"*

    E.S.paul, J. Simpson, H. Timmers, I. Ali, M.A. Bentley, A.M.Bruce, D.M.Cullen, P. Fallon, F.Hanna

J. Physics G. 18 (1992)

14. *"Entrance-Channel Effects in the Population of Superdeformed Bands"*
G. smith, B. Haas, A. Alderson, I. Ali, C.W. Beausang, M. A. Bentley, P. Dagnall, P. Fallon, G. de France, P. D. Forsyth, U. Huttmeier, P. Romain, D. Santos, P. J. Twin and J. P. Vivien.
Physical Review Letters 68 (1992) 158

15. *"First observation of a collective dipole rotational band in the A∼200 mass region"*
R.M. Clark, R. Wadsworth, E.S.Paul, C.W. Beausang, I. Ali, A.Astier, D.M.Cullen, P.J.Dagnall, P.Fallon, M.J.Joyce, M.Meyer, N.Redon, P.H.Reagan, J.F. Sharpey-Schafer and W.Nazarwicz, R.Wyss
Physics Letters B275 (1992) 247-251

16. *"Collective dipole rotational bands in ^{197}Pb"*
R.M. Clark, R. Wadsworth, E.S.Paul, C.W. Beausang, I. Ali, A.Astier, D.M.Cullen, P.J.Dagnall, P.Fallon, M.J.Joyce, M.Meyer, N.Redon, P.H.Reagan, J.F. Sharpey-Schafer and W.Nazarwicz, R.Wyss.
Z. Phys. January (1992)

17. *"Collective dipole bands in ^{198}Pb"*
R.M. Clark, R. Wadsworth, E.S. Paul, C.W. Beausang, I. Ali, A. Astier, D.M. Cullen, P.J. Dagnall, P. Fallon, M.J. Joyce, M. Meyer, N. Redon, P.H. Regan, J.F. Sharpey-Schafer, W. Nazarewicz and R. Wyss.
submitted to Nucl. Phys. A (1992).

Appendix B

Conference Contributions

1. *"A Study of the N=86 Isotones Around A=150"*

   I. Ali *et al.*

   Spring Meeting of Nuclear Physics Sections

   March (1990) Strasbourg, France

2. *"A study of the single particle excitations in the $N = 86$ nuclei ^{150}Gd and ^{152}Dy"*

   I. Ali, P. J. Twin, P. Fallon, C. W. Beausong, A. Alderson, P. D. Forsyth, J. W. Roberts, J. F. Sharpey-Schafer, M. A. Bentley, A. M. Bruce, G. Smith, T. Byrski, F. A. Beck, D. Curien, C. Schuck and W. Nazarwicz.

   Conference on Nuclear and Particle Physics

   April (1991) Liverpool, U.K.

Bibliography

[Ab 87] S. Åberg, *et al.*, *Proc. International Winter Meeting on Nuclear Physics, Bormio, Italy* (1987)

[Ab 88] S. Åberg, *et al.*, *Proc. International Winter Meeting on Nuclear Physics, Bormio, Italy* (1988)

[AK 77] C.G. Anderson and J. Krumlinde, Nucl. Phys. **A291** (1977) 21

[An 76] C.G. Anderson *et al.*, Nucl. Phys. **A268** (1976) 205

[An 78] C.G. Anderson *et al.*, Nucl. Phys. **A309** (1978) 141

[Ar 83] H.F.R. Arciszewski *et al.*, Nucl. Phys. **A410** (1983) 531

[BAR 88] T. Bengtsson, S. Åberg and I. Ragnarsson, Phys. Lett. B **208** (1988) 39

[BB 36] H.A.Bethe and R.F.Bacher, Rev. Mod. Phys. **8** (1936) 82

[BCS 57] J. Bardeen, L.N. Cooper and J.R. Schrieffer, Phys. Rev. **108** (1957) 1175

[Be 59] S.T. Belyaev, Matt. Fys. Medd. Dan. Vid. Selsk. **1959** No. 11

[Be 75] R. Bengtsson *et al.*, Phys. Lett. B **57** (1975) 301

[Be 79] R. Bengtsson, S. Frauendorf., Nucl. Phys. **A327** (1979) 139

[Be 80] G.F. Bertsch, Phys. Lett B **95** (1980) 157

[Be 81] T. Bengtsson *et al.*, Phys. Scr. **24** (1981) 200

[Be 84] R. Bengtsson and J.D. Garrett, in "Collective Phenomena in Atomic Nuclei", International Rev. of Nucl. Phys. Vol.2 (World Scientific, 1984, Singapore) 194

[Be 86] T. Bengtsson *et al.*, Phys. Scr. **34** (1986)

[Be 87] M.A. Bentley *et al.*, Phys. Rev. Lett. **59** (1987) 2141

[Be 88] M.A. Bentley, Ph.D Thesis, University of Liverpool (1988)

[Be 88a] T. Bengtsson *et al.*, Phys.Lett. **B208** (1988) 39

[Be 91] M.A. Bentley, *et al.*, J. Phys. **G17** 1991 481

[Bj 80] Bjornholm, S., Lynn, J. E., Rev. Mod. Phy. **52** (1980) 725

[Bl 66] A.E. Blaugrund, Nucl. Phys. **A88** (1966) 501

[Bl 79] J. Blomqvist, Z. Phys. **A290** (1979) 337

[BM 53] A. Bohr and B .R. Mottelson, Matt. Fys. Medd. Dan. Vid. Selsk. **27** (1953) No. 16

[BM 69] A. Bohr and B.R. Mottelson, *Nuclear Structure Volume I* (1969) Benjamin, New York

[BM 74] A. Bohr and B.R. Mottelson, Phy. Scr. **10A** (1974) 13

[BM 75] A. Bohr and B.R. Mottelson, *Nuclear Structure Volume II* (1975) Benjamin, New York

[BM 81] A. Bohr and B.R. Mottelson, Phys. Scr **24** (1981) 71

[BMP 58] A. Bohr, B. Mottelson and D. Pines, Phys. Rev. **110** (1958) 936

[Bo 36] N. Bohr, Nature, **344** (1936) 137

[Bo 58] N.N. Bogoliubov, Sov. Phys. **JETP** **7** (1958) 41

[Br 79] Broda, R., Kleinheinz, P., Lunardi, S. and Blomqvist, J., Symp. on High Spin Phenomena in Nuclei, Argonne.

[BR 85] T. Bengtsson and I. Ragnarsson, Nucl. Phys. **A436** (1985) 14

[BW 52] J.M. Blatt and V.F. Weisskopf, *Theoretical Nuclear Physics* (1952) New York: Wiley

[By 90] T. Byrski *et al.* Phy. Rev. Lett. **64** (1990) 1650

[Ce 79] Cerkaski, M., Dudek, J., Rozmej, P., Szymanski, Z. and Nilsson, S.G., Nuc. Phys. **A315** (1979) 269

[Ch 87] R.R. Chasman, Phys. Lett. B **187** (1987) 219

[Ch 67] Chepurnov, V. A. Yad. Faz. **6** (1967) 955

[CPS 74] S. Cohen, F. Plasil and W.J. Swiatecki, Ann. Phys. **82** (1974) 557

[Cu 69] W.M. Currie *et al.*, Nucl. Phys. **A134** (1969) 325

[Cu 88] D. Curien, Ph. D Thesis, Centre de Recherches Nucléairs, Strasbourg, France

[Da 69] Damgaard, J., Pauli, H.C., Pashkevich, V.V., and Strutinsky, V.M. Nucl. Phys. **A135** (1969) 432

[De 78] M.A. Deleplanque *et al.*, Phys. Rev. Lett. **41** (1978) 1105

[De 88] M.A. Deleplanque *et al.*, Phys. Rev. Lett. **60** (1988) 1626

[De 89] M.A. Deleplanque *et al.*, Phys. Rev. Lett. C **39** (1989) 1651

[DN 85] J. Dudek and W. Nazarewicz, Phys. Rev C **31** (1985) 298

[Do 80] Døssing, T.,*et al.*, Proc. Int. Conf. on Nucl. Behaviour at High Angular Momentum, Strasbourg. (1980)

[Do 81] Døssing, T., *et al.*, Phy. Scr. **24** (1981) 258

[Du 81] J. Dudek *et al.*, Phys. Rev. C **23** (1981) 920

[Du 82] J. Dudek *et al.*, Phys. Rev. C **26** (1982) 1712

[Du 87] J. Dudek, *Proc. Winter Meeting on Nuclear Physics, Bormio, Italy* (1987)

[Du 87] J. Dudek, Phys. Rev. Lett.C **59** (1987) 1405

[Du 88] J. Dudek *et al.*, Phys. Rev. C **38** (1988) 940

[DW 78] Dudek, J. Werner, T. J. Phys. **G4** (1978) 1543

[DW 88] J. Dudek and T. Werner, *JIHIR doc. 88/01* (1988)

[En 74] R. Engfer, *et al.*, Atomic and Nuclear Data Tables **14** (1974) 509

[Fa 89] P. Fallon *et al.*, Phys. Lett. B **218** (1989) 137

[Fo 81] Folkmann, F., Garrett, G.D., Hagemann, G.B., Harakeh, M.N., Herskind, B., Hillis, D.L., Ogaza, S., Emling, H., Grosse, E., Schwalm, D., Simon, R.S. and Tjølm, P.O., Nuc. Phys. **A361** (1981) 242

[FP 80] Faessler, A. and Ploszajczak, M., Z. Phy. **A295** 87

[Ga 85] J. Garrett, Journ. Phys. Soc. **Jap. 54** (1985) 456

[GG 67] J.R. Grover and J. Gilat, Phys. Rev. (1967) 157

[Ha 77] Haenni, D. R. and Sugihara, T. T., Phys. Rev **C16** (1977) 120

[Gu 67] C. Gustafson *et al.* Arkiv Fysik **36** (1967) 449

[Ha 79] B. Haas*et al.*, Phys. Lett. **84B** (1979) 178.

[Ha 81] B. Haas*et al.*, Nuc. Phys. **A362** (1981) 254.

[Ha 83] B. Haas, IL NUOVO CIMENTO **81A, N.1** (1983) 159

[Ha 88] B. Haas *et al.*, Phys. Rev. Lett. **60** (1988) 503

[He 80] B. Herskind, J.de Phys. 41 (1980) C10-106

[He 88] B. Herskind *et al.*, Phys. Rev. Lett. **59** (1988) 2416

[HJS 49] O. Haxel *et al.*, Phys. Rev. **75** (1949) 1766

[Ho 78] P.E. Hodgson, *Nuclear Heavy Ion reactions* (1978) Oxford, p2

[Ho 86] D. Howe, Ph.D Thesis, University of Liverpool (1986)

[Ho 83] Horn, D., Towner, I.S., Hausser, O., Andrews, H.R., Lone, M.A. and Taras, P., Phys. Rev. Lett. **50** 1447

[Ho 86a] Horn, D., Towner, I.S., Hausser, O., Ward, D., Andrews, H. R., Lone, M.A., Sharpey-Schafer, J.F., Rud, N. and Taras, P., (1986)

[In 54] Inglis, D.R. Inglis, Phys. Rev. **96** (1954) 1059

[In 55] Inglis, D.R. Inglis, Phys. Rev. **97** (1955) 701

[Ja 74] C.W.de Jager, *et al.*,Atomic and Nuclear Data Tables **14** (1974) 479

[Ja 74a] Jansen, J.F.W., de Meier, R.J., Sujkowski, Z., Chmielewska, d. and Grabowski, J. Proc. Int. Conf. on Nucl. structure spectroscopy, Amsterdam (1974)

[Ja 79] Jansen, J.F.W., de Voigt, M.J.A., Sujkowski, Z. and Chmielewska, D. Nuc. Phys. **A321** (1979) 365.

[Je 90] N.A.Jelley "Fundamentals of Nuclear Physics", Cambridge, (1990)

[JHR 72] A. Johnson, H. Ryde and A. Hjorth, Nucl. Phys. **A179** (1972) 753

[Jo 71] A. Johnson *et al.*, Phys. Lett. **B34** (1971) 605

[Jo 89] J. K. Johansson *et al.*, Phys. Rev. Lett. **62** (1989) 2200

[JRS 71] A. Johnson, H. Ryde and J. Starkier, Phys. Lett. **34B** (1971) 605

[Kh 78] T.L. Khoo, *et al.*, Phys. Rev. Lett. 41 (1978) 1027

[Kl 78] Kleinheinz, P., Ogawa, M., Broda, R., Daly, P.J., Haeni, D., Beucher, M. and Kleinrahm, A., Z. Phys. **A286** (1978) 27

[Kl 52] P. Klingenberg, Rev. Mod. Phys. **24** (1952) 63

[Kl 79] Kleinheinz, P., Broda, R., Daly, P.J., Lunardi, S., Ogawa, M. and Blomqvist, J., Z. Phys. **A290** (1979) 279

[Kr 73] K. S. Krane *et al.*, Nucl. Data Tables **11** (1973) 352

[Kr 87] K. S. Krane "Introductory Nuclear Physics", Wiley, (1987)

[Le 59] R.B. Leighton "Principles of Modern Physics", Mcgraw Hill, 1959

[Le 79] Leander, G., Andersson, C.G., Nilsson, S.G., Ragnarsson, I., Almberger, J., Døssing, T. and Neergaard, K. Proc. Symp. High Spin Phenomena in nuclei, Argonne.

[Li 63] J. Lindhard *et al.*, K. Dan. Vidensk. Selsk. Matt. Phys. Medd. **33** (1963) No. 14

[Li 82] J.S. Lilley. Phys. Scr. **25** (1982) 435

[LS 78] C.M. Lederer and V.S. Shirley, **Table of Isotopes 7th Edition**

[LVH 70] K.E.G. Löbner *et al.*, Nuclear Data Tables **A7** (1970) 495

[Ma 49] M.G. Mayer, Phys. Rev. **75** (1975) 1969

[Me 79] Merdinger, J.C., Beck, F.A., Byrski, T., Gehringer, C., Vivien, J.P., Bozek, E. and Styczen, J. Phys. Rev.Lett.**42** (1979) 23

[MG 63] H. Morinaga and P.C. Gugelot, Nucl. Phys. **46** (1963) 210

[Mo 87] J.N. Mo, *et al.*, Nucl. Phys. **A472** (1987) 295

[Mo 88] J.D. Morrison, Ph.D Thesis, University of Liverpool (1988)

[MV 60] B.R. Mottelson and Valatin, Phys. Rev. Lett. **5** (1960) 511

[Na 80] Nagai, Y., Styczen, J., Piiparinen, M. and Kleinheinz, P. **vol 1, 71** (1980) proc. Int. Conf. on Nucl. Behaviour at High Angular Momentum, Strasbourg.

[Na 88] W. Nazarewicz, *Contemporary Topics in Nuclear Structure Physics,* (World Scientific, 1988) 467

[Na 90] W. Nazarewicz, P.J.Twin, P.Fallon and J.D.Garrett, Phy. Rev. Lett. **64** (1990) 1654

[Ne 81] J.O. Newton, B. Herskind, R.M. Diamond, E.L. Dines, J.E. Draper, K.H. Lindenberger, C. Schuck, S. Shih and F. Stephens, Phys. Rev. Lett. **46** (1981) 1383

[Ni 55] S.G. Nilsson, Matt. Fys. Medd. Dan. Vid. Selsk. **29** (1955) No. 16

[Ni 69] S.G. Nilsson *et al.*, Nucl. Phys. **A131** (1969) 1

[No 85] P.J. Nolan *et al.*, Nucl. Instr. and Meth. **A236** (1985) 95

[No 86] P.J. Nolan, Proc. of the International Nuclear Physics Conference, Harrogate (1986) 155

[NPS 76] K. Neegard, V.V Pashkelvich and S. Frauendorf, Nucl. Phys. **A262** (1976) 61

[No 83] P.J. Nolan *et al.*, Phys. Lett. **B128** (1983) 285

[NT 88] P.J. Nolan and P. J. Twin, Ann. Rev. Nucl. Part. Sci. **38** (1988) 533

[NS 70] L.C. Northcliffe and R.F. Schilling, Nucl. Data Tables **7A** (1970) 233

[NS 79] P.J. Nolan and J.F. Sharpey-Schafer, Reports on Progress in Physics **42** (1979) 1

[NSD 87] W. Nazarewicz, Z. Szymanski and J. Dudek, Phys. Lett. B **196** (1987) 404

[NWJ 85] W. Nazarewicz, R. Wyss and A. Johanson, Phys. Rev. **C31** (1985) 298

[NWJ 88] W. Nazarewicz, R. Wyss and A. Johanson, Phys. Lett. B **225** (1988) 208.

[NWJ 89] W. Nazarewicz, R. Wyss and A. Johanson, Nuc. Phys. **A503** (1989) 285

[Ny 86] B.M. Nyako *et al.*, Phys. Rev. Lett. **56** (1986) 2680

[Pi 79] Piiparinen, M., Lunardi, S., Kleinheinz, P., Backe, H. and Blomqvist, J., Z. Phys. **A290** (1979) 337

[Po 62] S.M.Polikanov *et al.*, Sov. Phys. **JETP 15** (1962) 1016

[PP 80] Peter Ring and Peter Schuck, The Nuclear Many-Body Problem (Springer-Verlag) (1980)

[Pr 75] M.A. Preston *et al.*, Structure of the Nucleus (Addison-Wesley) (1962) 1016

[Ra 78] I. Ragnarsson *et al.*, Phys. Rev. **45** (1978) 1

[Ra 80] I. Ragnarsson *et al.*, Nucl. Phys. **A347** (1980) 287

[RA 86] I. Ragnarsson and S. Åberg, Phys. Lett. B **180** (1986) 191

[Ra 88] G.E. Rathke *et al.*, Phys. Lett. B **209** (1988) 177

[RFP 78] Rösel, F., Fries, H. M., and Pauli, H. C. Atomic Data and Nuclear Data Tables Numbers 2-3 **21** (1978)

[Ri 88] M.A. Riley *et al.*, Phys. Rev. Lett. **60** (1988) 553

[RNS 78] I.Ragnarsson, S.G.Nilsson and R.K.Sheline, Phy. Rep. **45** (1978) 1

[Ro 67] Rost, E. Phys. Lett. **26B** (1967) 184

[Ro 88] N. Rowley, *private communication*

[Sc 85] C. Schuck *et al.*, Contribution to the XXXIII International Meeting on Nuclear Physics BORMIO, January 21 - 26, 1985

[Si 77] Simon, R.S., Banascik, M.V., Diamond, R.M., Newton, J.O. and Stephens F.S. Nuc. Phys. **A290** (1977) 253

[Si 87] J. Simpson *et al.*, J. Phys. G **13** (1987) 847

[Sh 72] R.K.Sheline, I. Ragnarsson and S.G. Nilsson, Phys. Lett. **B41** (1972) 115

[SLD 65] F.S. Stephens, N.L. Lark and R.M. Diamond, Nuc. Phys. **63** (1965) 82

[Sp 72] H.J.Specht *et al.*, Phys. Lett. **B41** (1972) 43

[SS 72] F.S. Stephens and R.S Simon, Nucl. Phys. **A183** (1972) 257

[SS 88] J. F. Sharpey-Schafer and J. Simpson, Prog. Part. Nucl. Phy. **21** (1988) 293

[St 65] V.M. Strutinsky, Sov. J. Nucl. Phys. **3** (1966) 449

[St 67] V.M. Strutinsky, Nucl. Phys. **A95** (1967) 420

[St 68] V.M. Strutinsky, Nucl. Phys. **A122** (1968) 1

[Su 81] A.W. Sunyar, Physica Scripta, **24** (1981) 288

[Sz 83] Z. Szymański, *Fast Nuclear Rotations*, (Oxford Studies in Physics 1983) section 3.2

[Ta 62] I. Talmi, Rev. Mod. Phys. **34** (1962) 704

[Tr 79] Trautmann, W., Sharpey-Schafer, J.F., Andrews, H.R., Haas, B., Hauser, O., Taras, P., and Ward, D., Phys. Rev. Lett. **43** (1979) 991

[Tr 82] Trautmann, W., Sharpey-Schafer, J.F., Andrews, H.R., Haas, B., Hauser, O., Taras, P., and Ward, D., Nucl. Phys. **A378** (1982) 141

[Tw 83] P.J. Twin, Nucl. Phys. **A409** (1983) 343

[Tw 86] P.J. Twin *et al.*, Phys. Rev. Lett. **58** (1986) 503

[Vo 83] de Voigt, Dudek and Szymański, Rev. of Mod. Phys. **55** (1983)

[We 35] C.F. von Weizsäker, Z. Phys. **96** (1935) 431